

# SOX - Towards the Detection of Sterile Neutrinos in Borexino

Beta Spectrum Modeling, Monte Carlo Development and Sensitivity Studies for the Sterile Neutrino Search in Borexino

Dissertation  
zur Erlangung des Doktorgrades  
des Fachbereichs Physik  
der Universität Hamburg

vorgelegt von  
Mikko Meyer  
aus Hamburg

Hamburg  
2016

Gutachter der Dissertation: Prof. Dr. Caren Hagner  
Dr. Björn Wonsak

Gutachter der Disputation: Prof. Dr. Caren Hagner  
Prof. Dr. Peter Hauschildt  
Prof. Dr. Dieter Horns (Vorsitz)  
Dr. Björn Wonsak  
Prof. Dr. Michael Wurm

Datum der Disputation: 30. 11. 2016

## Abstract

Several experiments have reported anomalies in the neutrino sector which might be explained by the existence of a fourth (sterile) neutrino with a squared mass difference of about  $1 \text{ eV}^2$  to the other three active neutrinos. The SOX project is part of the experimental program of the BOREXINO experiment and seeks for a clarification of the observed anomalies. For that purpose an artificial antineutrino source ( $^{144}\text{Ce}$ – $^{144}\text{Pr}$ ) and possibly neutrino source ( $^{51}\text{Cr}$ ) will be deployed underneath the large low background detector BOREXINO. The detector provides both energy and vertex resolution to observe a possible oscillation signature within the detector volume. The calculation of the antineutrino spectrum is based on existing theoretical models and was performed within this thesis. The modeling includes several sub-leading corrections particularly such as finite size of the nucleus, screening of the atomic electrons and radiative effects. Related to this work, dedicated Monte Carlo generators have been developed to simulate the inverse beta decay reaction and the (anti)neutrino elastic scattering off electrons. Based on a profile likelihood analysis, the sensitivity to the sterile neutrino search of the SOX project was evaluated. The results obtained from this analysis confirm that the currently allowed parameter regions for sterile neutrinos can be tested at 95% confidence level. Finally, an alternative concept for the sterile neutrino search is presented which is based on a cyclotron and a Beryllium target near BOREXINO (BOREXINO+IsoDAR).

## Zusammenfassung

Eine Reihe von Experimenten in der Neutrinophysik haben Anomalien beobachtet, die sich möglicherweise durch die Einführung eines vierten, eines sogenannten sterilen Neutrinos mit einer quadratischen Massendifferenz von  $1 \text{ eV}^2$  zu den drei aktiven Neutrinos, erklären ließen. Das SOX-Projekt ist Teil des experimentellen Forschungsprogramms des BOREXINO-Experimentes und widmet sich der Aufklärung der beobachteten Anomalien. Zu diesem Zweck wird eine Antineutrinoquelle ( $^{144}\text{Ce}$ – $^{144}\text{Pr}$ ) und möglicherweise auch eine Neutrinoquelle ( $^{51}\text{Cr}$ ) unterhalb des großen, mit Flüssigszintillator gefüllten, BOREXINO-Detektors installiert. Der Detektor bietet sowohl eine präzise Energie- als auch Vertexp Auflösung um ein mögliches Oszillationsmuster innerhalb des Detektorvolumens abzubilden. Die theoretische Berechnung des Antineutrinospektrums basiert auf bestehenden theoretischen Modellen und wurde im Rahmen dieser Dissertation durchgeführt. Die Modellierung umfasst eine Vielzahl von Korrekturen, die z.B. die endliche Ausdehnung des Kernes, Abschirmungseffekte der Elektronen sowie Strahlungseffekte umfassen. Darüber hinausgehend wurden Monte-Carlo-Generatoren entwickelt, die die physikalischen Interaktionen über den inversen Beta-Zerfall sowie der elastischen Streuung der Neutrinos bzw. Antineutrinos an Elektronen simulieren. Basierend auf einer sogenannten *profile likelihood* Analyse wurde die Sensitivität des SOX-Projektes in Hinblick auf die sterile Neutrinosuche evaluiert. Die Resultate dieser Studie zeigen, dass der derzeitige erlaubte Parameterraum für sterile Neutrinos bei einem Konfidenzlevel von 95% getestet werden kann. Abschließend wird ein alternatives Konzept zur Suche nach sterilen Neutrinos vorgestellt. Dieses als BOREXINO+IsoDAR bezeichnete Konzept basiert auf einem Zyklotron und einem Berylliumziel in der Nähe des BOREXINO Detektors.



*Steure mutiger Segler! Es mag der Witz dich verhöhnen,  
Und der Schiffer am Steu'r senken die lässige Hand.  
Immer, immer nach West! Dort muß die Küste sich zeigen,  
Liegt sie doch deutlich und liegt schimmernd vor deinem Verstand.  
Traue dem leitenden Gott und folge dem schweigenden Weltmeer,  
Wär' sie noch nicht, sie stieg jetzt aus den Fluten empor.  
Mit dem Genius steht die Natur im ewigem Bunde,  
Was der eine verspricht, leistet die andre gewiß.*

KOLUMBUS. - Friedrich Schiller.



---

<b>1</b>	<b>Introduction</b>	<b>13</b>
<b>2</b>	<b>Neutrino Physics</b>	<b>17</b>
2.1	Neutrinos in the Standard Model . . . . .	17
2.2	Leptonic Mixing and Neutrino Masses . . . . .	18
2.3	Neutrino Oscillations . . . . .	18
2.3.1	General Neutrino Mixing Formalism in Vacuum . . . . .	19
2.3.2	Neutrino Oscillations in Matter and MSW Effect . . . . .	22
2.4	Results of the Last Two Decades: Three Flavor Oscillations . . . . .	23
2.4.1	Solar Neutrinos . . . . .	24
2.4.2	Atmospheric Neutrinos . . . . .	29
2.4.3	Geo-Neutrinos . . . . .	31
2.4.4	Supernova Neutrinos . . . . .	31
2.4.5	Reactor Neutrinos . . . . .	33
2.4.5.1	Reactor Experiments and $\theta_{13}$ . . . . .	33
2.4.5.2	Double Chooz and $\theta_{13}$ . . . . .	34
<b>3</b>	<b>Sterile Neutrinos and Mixing Freedom</b>	<b>41</b>
3.1	Number of Active Neutrinos . . . . .	41
3.2	Introduction to Sterile Neutrinos . . . . .	42
3.3	Sterile Neutrino Mixing Formalism . . . . .	43
3.4	Anomalies in the Neutrino Sector and Hints for Sterile Neutrinos . . . . .	44
3.4.1	LSND Anomaly . . . . .	45
3.4.2	Constraints from KARMEN and MiniBooNE . . . . .	46
3.4.3	The Gallium Anomaly . . . . .	47
3.4.4	The Reactor Antineutrino Anomaly . . . . .	48
3.4.5	Global Analysis . . . . .	51
3.4.6	Experimental Perspectives . . . . .	51

<b>4</b>	<b>Borexino and SOX</b>	<b>55</b>
4.1	Detector Design . . . . .	55
4.1.1	Inner Detector . . . . .	55
4.1.2	Outer Detector . . . . .	57
4.1.3	Liquid Scintillator Purification . . . . .	57
4.2	Neutrino Detection in Borexino . . . . .	58
4.3	Physics Program . . . . .	60
4.3.1	Solar ${}^7\text{Be}$ Neutrino Flux Measurement . . . . .	60
4.3.2	Solar ${}^8\text{B}$ Neutrinos . . . . .	61
4.3.3	Solar pep and CNO Neutrinos . . . . .	61
4.3.4	Solar pp Neutrinos . . . . .	63
4.3.5	Geo-Neutrinos . . . . .	64
4.4	The SOX Project . . . . .	64
4.4.1	$\nu_e$ and $\bar{\nu}_e$ Emitters as Probes for the Neutrino Anomalies . . . . .	65
4.4.2	${}^{144}\text{Ce}$ and ${}^{51}\text{Cr}$ at Borexino . . . . .	65
4.4.3	${}^{144}\text{Ce}$ $\bar{\nu}_e$ Source Production . . . . .	68
4.4.4	Transportation of the $\bar{\nu}_e$ Source . . . . .	69
4.4.5	${}^{51}\text{Cr}$ $\nu_e$ Source Production . . . . .	69
4.4.6	Transportation of the $\nu_e$ Source . . . . .	71
4.4.7	Time Schedule of the SOX Experiment . . . . .	71
<b>5</b>	<b>Source Properties</b>	<b>73</b>
5.1	Radioactive Decay . . . . .	73
5.2	Antineutrino Source . . . . .	74
5.2.1	Beta Decay Classification . . . . .	74
5.2.2	Beta Spectrum Modeling . . . . .	75
5.2.3	Discussion of Potential Antineutrino Emitters . . . . .	80
5.2.4	Antineutrino Spectrum Modeling of ${}^{144}\text{Pr}$ . . . . .	81
5.2.5	Antineutrino Spectrum Modeling of ${}^{144}\text{Ce}$ – ${}^{144}\text{Pr}$ . . . . .	81
5.2.6	${}^{144}\text{Ce}$ – ${}^{144}\text{Pr}$ Spectrum Error Discussion . . . . .	83
5.2.7	Comparison to Beta Spectroscopy Results . . . . .	85
5.3	Neutrino Source . . . . .	87
5.3.1	Discussion of Potential Neutrino Emitters . . . . .	89
5.3.2	Source Characteristics of ${}^{51}\text{Cr}$ and ${}^{37}\text{Ar}$ . . . . .	89
5.4	Summary . . . . .	90

<b>6</b>	<b>Monte Carlo Simulation</b>	<b>93</b>
6.1	Software Structure . . . . .	93
6.1.1	Detector Model . . . . .	95
6.2	Particle Generators . . . . .	96
6.2.1	Position Generation . . . . .	96
6.2.2	Solar Neutrino Generator . . . . .	99
6.2.3	Radioactive Decay Generator . . . . .	99
6.2.4	The Sterile Antineutrino Generator . . . . .	100
6.2.5	The Sterile Neutrino and Antineutrino Scattering Generator . . . . .	100
6.3	Simulation of the Optical Processes . . . . .	102
6.3.1	Scintillation Light . . . . .	104
6.3.2	Cherenkov Light . . . . .	104
6.3.3	Photon Tracking . . . . .	105
6.4	Electronic Simulation . . . . .	105
6.5	Monte Carlo Validation . . . . .	105
6.5.1	Calibration Data from an $^{241}\text{Am}-^9\text{Be}$ Source . . . . .	107
6.5.2	Energy and Neutron Capture Time from Borexino Data . . . . .	108
6.6	Summary . . . . .	109
<b>7</b>	<b>Towards the Detection of Sterile Neutrinos</b>	<b>111</b>
7.1	Expected Number of Interactions . . . . .	111
7.2	Background . . . . .	116
7.2.1	Background for the SOX+Ce Phase . . . . .	116
7.2.2	Background for SOX+Cr Phase . . . . .	118
7.3	Event Selection . . . . .	120
7.3.1	IBD Selection for SOX+Ce . . . . .	120
7.3.2	$\nu_e e^-$ Scattering Selection for SOX+Cr . . . . .	121
7.4	Sensitivity . . . . .	122
7.4.1	The Profile Log-Likelihood Method . . . . .	122
7.4.2	Sensitivity of the SOX+Ce Project . . . . .	125
7.4.3	Sensitivity of the SOX+Cr Project . . . . .	132
7.4.4	Sensitivity Comparison . . . . .	132
<b>8</b>	<b>Outlook: Borexino + IsoDAR</b>	<b>135</b>
8.1	The IsoDAR Concept . . . . .	135
8.1.1	Ion Source and Injection System . . . . .	135
8.1.2	Cyclotron . . . . .	136
8.1.3	Target Design and $\bar{\nu}_e$ Production . . . . .	137
8.2	Event Prediction and Sensitivity . . . . .	138
8.3	Summary and Discussion of the Borexino+IsoDAR Project . . . . .	139

---

<b>9 Conclusion</b>	<b>143</b>
<b>A Theoretical Antineutrino Modeling</b>	<b>149</b>
A.1 Tables for the Antineutrino Spectrum Modeling . . . . .	149
<b>B Additional Information for SOX</b>	<b>151</b>
B.1 $\chi^2$ Distribution and $\chi^2_{n,\alpha}$ Quantile . . . . .	151
B.2 Old Gallex Source . . . . .	152
B.3 Cerium Source in the Center of Borexino . . . . .	153
<b>C Double Chooz</b>	<b>155</b>
C.1 Reactor Physics and $\bar{\nu}_e$ Production . . . . .	155
C.2 Double Chooz Detector . . . . .	157
C.3 Oscillation Analysis . . . . .	158
C.4 Summary and Conclusion . . . . .	160
<b>D Cross-Section Overview</b>	<b>161</b>

## LIST OF ABBREVIATIONS

---

$^{37}\text{Ar}$	Argon-37 (EC, neutrino emitter)
CC	Charged Current
$^{144}\text{Ce}$	Cerium-144 ( $\beta^-$ , antineutrino emitter)
C.L.	Confidence Level
CNO	Carbon-Nitrogen-Oxygen fusion cycle
$^{51}\text{Cr}$	Chromium-51 (EC, neutrino emitter)
EC	Electron Capture
FADC	Flash Analog-to-Digital Converter
GUT	Grand Unified Theory
$M_{\odot}$	One solar mass ( $(1.98855 \pm 0.00025) \times 10^{30}$ kg)
MC	Monte Carlo
MSW	Mikheyev-Smirnov-Wolfenstein
NC	Neutral Current
pc	Parsec (1 pc = 3.26 light-years)
PMT	Photomultiplier tube
$^{144}\text{Pr}$	Praseodymium-144 ( $\beta^-$ , antineutrino emitter)
SM	Standard Model
SN	Supernova
SNO	Sudbury Neutrino Observatory
SSM	Standard Solar Model



Frederick Reines had to wait almost 40 years to receive what is widely regarded as the highest honor in his field, the Nobel Prize in Physics. On December 10, 1995, Reines stepped forward and after a short honorable bow, received the Nobel diploma and medal from the hands from Carl XVI Gustaf, King of Sweden. Together with Clyde L. Cowan (1919-1974), Reines had achieved what was considered impossible for a long time: the detection of neutrinos.

Back in 1951 Frederick Reines, a young physicist at Los Alamos, decided to take a sabbatical-in-residence from his duties to look for a question of fundamental interest. As he later recalled [99]:

“I moved to a stark empty office, staring at a blank pad for several months searching for a meaningful question worthy of a life’s work.”

The question being worth a life’s work was the first detection of the neutrino. Wolfgang Pauli had postulated the existence of the neutrino already in 1930 to save the energy conservation law. However, the cross-section, the chance to detect the neutrino, was so small that twenty years later, the neutrino was still undetected. Already at the beginning Pauli had to admit that he had done a terrible thing. “I have postulated a particle that cannot be detected” (see [99]). In fact, the idea of searching for the elusive neutrinos was a big challenge and Reines soon looked for a collaborator to work on this problem [108]:

“The idea of searching for the elusive neutrino had, in fact, occurred to me as early as 1947, but the opportunity did not present itself. I was now determined to do it, and formed an extremely fruitful collaboration with Clyde Cowan, another Los Alamos staff member.”

The natural choice for Reines and Cowan, both members of the Manhattan Project, was the use of a nuclear bomb as a neutrino source. As they concluded, such a device would produce an “extraordinarily intense pulse of neutrinos” which could easily be separated from background processes [99]. However, after they had recognized that the reduction of background might also be achieved by using the coincident nature of the inverse beta decay reaction, they decided that the reactor at Hanford, Washington, would be more appropriate [108]. They soon transferred to the recently established Savannah River reactor facility. After a great variety of tests, they were convinced by their experimental findings and concluded they had indeed detected the neutrino. They soon sent a telegram to Pauli [99]:

“We are happy to inform you that we have definitely detected neutrinos from fission fragments by observing inverse beta decay of protons. Observed cross section agrees well with expected six times ten to minus forty four square centimeters.”

Pauli responded the same night<sup>1</sup> [99]:

“Thanks for the message. Everything comes to him who knows how to wait.  
Pauli” .

Since those days when the detection of neutrinos have been regarded as being practically impossible, “the field of neutrino physics has rapidly grown” [168, p. 1]. Neutrino oscillations are well established and helped to solve the solar neutrino problem<sup>2</sup>. Many properties like the mixing parameters have been measured over the past years. Solar, reactor, atmospheric and accelerator neutrinos have been measured and their properties have been determined with great precision. A milestone was reached in 2014 when the BOREXINO experiment announced the first direct detection of the pp neutrinos, the neutrinos from the main reaction which powers the Sun.

However, many questions concerning the properties of neutrinos remain unanswered [168, p. 1]. The absolute masses of neutrinos, the mass ordering as well as their electromagnetic properties and their nature itself being Dirac or Majorana particle is still unknown [168, p. 1]. Among these unknown properties, CP violation in the leptonic sector and the quest for sterile neutrinos are the next questions to be solved.

The existence of sterile neutrinos has been discussed for several decades. In contrast to the three known active neutrinos, sterile neutrinos do not interact via any known force, except gravity. The present thesis shall be devoted to this topic (chapter 3). The BOREXINO detector and the SOX project is summarized in chapter 4. The thesis will pursue the objective of presenting a detailed study to show the potential of the BOREXINO experiment to search for sterile neutrinos. Secondly, it will pave the way towards the detection of sterile neutrinos in BOREXINO. Considering the parameter space currently favored by global fits, sterile neutrino oscillations are expected at short distances (centimeters to meters) assuming neutrino energies of about 1 MeV. The name SOX (short distance neutrino oscillation with BOREXINO) was chosen accordingly. The search for sterile neutrinos at BOREXINO is expected to start at the end of 2017 by deploying a high intense  $\bar{\nu}_e$  source underneath the detector. The theoretical modeling of the  $\bar{\nu}_e$  spectrum, including several sub-leading corrections, was performed within this thesis (chapter 5). The precise knowledge is an important parameter for the  $\bar{\nu}_e$  flux prediction, Monte Carlo simulations and for the sensitivity studies. To simulate the inverse beta decay reaction, a Monte Carlo generator which simulates the source induced  $\bar{\nu}_e$  was developed within this thesis (chapter 6). The generator is complemented by a second generator to simulate the  $\nu_e$  and  $\bar{\nu}_e$  elastic scattering off electrons induced by artificial neutrino sources (chapter 6). Both generators are part of the official BOREXINO software. Simplified and fast-running versions of these generators were used to evaluate the sensitivity for the sterile neutrino search for different scenarios (section 7.4.2). The thesis ends with the proposal of a new experimental setup at BOREXINO using a cyclotron and Beryllium target near BOREXINO (chapter 8). Many of these techniques and methods developed within the framework of this thesis will find their direct application as soon as the SOX experiment starts. In case of a positive signal, SOX will demonstrate the existence of sterile neutrinos and will open a brand new era in particle physics and cosmology. In case of a negative signal, SOX will end a long-standing debate on this topic. The main part of the thesis is focused on the search of sterile neutrinos using an artificial antineutrino source. Additionally, studies assuming a neutrino source ( $^{51}\text{Cr}$ ) are incorporated as well. Other work performed by the author in the framework of the OPERA (section 2.4.2) and DOUBLE CHOOZ experiment (cosmogenic

<sup>1</sup>Unfortunately, the original message never reached Cowan and Reines.

<sup>2</sup>Over several decades the amount of detected neutrinos was in great disagreement to the number of neutrinos expected from theoretical solar models.

background analyses) is briefly summarized at the beginning of this thesis (section 2.4.5.2) and in the appendix.



The knowledge about neutrino physics has constantly grown over the past years [168, p. 3]. Following the detection of the neutrino in 1956 by Reines and Cowan, “particle physics went through a spectacular flowering which culminated in the formulation of the Standard Model” [141, p. 17]. The confirmation of neutrino oscillations by SUPER-KAMIOKANDE and the solution of the solar neutrino problem by SNO have recently been awarded with the Nobel Prize in Physics (2015) underlining the importance of this research field. Neutrino oscillation has proven that neutrinos have mass and moreover that they break the fundamental law of lepton number conservation.

This chapter gives an introduction into the field of neutrino physics. Particular focus will be given to the neutrino oscillation mechanism and recent discoveries. Work done by the author in the framework of other experiments than BOREXINO is also briefly summarized.

## 2.1 Neutrinos in the Standard Model

The *Standard Model* (SM) of particle physics is a compilation of laws, theories and observations [141]. Within the framework of the SM all particles and the forces between them are described with high accuracy. From the mathematical point of view, the SM is a so-called gauge theory based on the local symmetry group  $SU(3) \times SU(2) \times U(1)$ .  $SU(3)$  belongs to the color group of quantum electrodynamics (QCD) and is generated by eight massless gluons that mediate the strong interaction [212]. The weak isospin  $SU(2)$  and the hypercharge section  $U(1)$  is unified within the Glashow-Weinberg-Salam (GWS) model corresponding to a  $SU(2) \times U(1)$  group. Elementary particles are divided into left handed fields arranged as doublets under  $SU(2)$  transformation and right handed singlets for right handed fields [212]. The weak interaction has three massive mediators also known as gauge bosons. Two of them have an electric charge ( $W^\pm$ ) while one of them is electrically neutral ( $Z^0$ ). Within the GWS model, photons are the mediator of the electromagnetic force with  $U(1)$  being the weak hypercharge symmetry group. In the construction of this theory all particles are massless to guarantee gauge invariance [212]. To incorporate the observed masses of the heavy gauge bosons ( $Z^0$  and  $W^\pm$ ) the Higgs mechanism has to be introduced to allow spontaneous symmetry breaking. The Higgs boson was only recently discovered (July 2012) by the CMS<sup>1</sup> and ATLAS<sup>2</sup> collaborations at the LHC<sup>3</sup> at a mass of about 125 – 126 GeV [83, 5].

Standard Model particles are separated into fermions (spin-1/2 particles) and bosons (integer-spin). The fermions within the SM are divided into different classes of particles. Six of them are the so-called leptons ( $e^-, \mu^-, \tau^-, \nu_e, \nu_\mu, \nu_\tau$ ) while six of them are called quarks ( $u, d, c, s, t, b$ ). In addition to the fermions, twelve bosons are constituents of the SM (eight

---

<sup>1</sup>CMS: Compact Muon Solenoid.

<sup>2</sup>ATLAS: A Toroidal LHC Apparatus.

<sup>3</sup>LHC: Large Hadron Collider

gluons, photon,  $Z^0$  and  $W^\pm$ ). The heavy gauge bosons do only couple to left-handed fermion fields and right-handed anti-fermion fields. Neutrino interactions with other fermions take place either through the exchange of a  $W^\pm$  boson (CC interaction) or through the exchange of the neutral  $Z^0$  (NC interaction) [141].

## 2.2 Leptonic Mixing and Neutrino Masses

To incorporate the experimentally observed neutrino mass into the SM, it is convenient to assume that neutrinos are Dirac particles and that right-handed neutrinos exist in nature [141]. The Dirac equation for a free fermion is derived by the Euler-Lagrangian. Assuming neutrinos to be Dirac particles, the SM Lagrangian can be modified by an additional term

$$-\mathcal{L}_{m_\nu}^D = m_\nu \bar{\nu}\nu = m_\nu (\bar{\nu}_L \nu_R + \bar{\nu}_R \nu_L), \quad (2.1)$$

where  $\bar{\nu}\nu$  is invariant under Lorentz transformation. As it can be seen from this equation, the Dirac mass term includes left-handed neutrinos as well as right-handed neutrinos. The  $V - A$  coupling nature of the weak sector only involves chirally left-handed states. The neutrino masses arise then from the coupling with the Higgs field, e.g. in [141, p. 27], and is given by  $h^\nu v/\sqrt{2}$ , in terms of a Yukawa coupling constant ( $h^\nu$ ) and the Higgs vacuum expectation value ( $v$ ). Although this formalism provides mass to neutrinos, it does not explain the lightness of the neutrinos [141, p. 27].

The see-saw model is one of the expansions of the SM and provides light neutrinos in a natural way. Each light left-handed neutrino  $\nu_L$  gains a super-heavy right handed Majorana partner. The Lagrangian is then modified by an additional Majorana term  $\mathcal{L}_{m_\nu}^M$  [141, p. 29]:

$$-\mathcal{L}_{m_\nu} = -\mathcal{L}_{m_\nu}^M - \mathcal{L}_{m_\nu}^D = \frac{m_R}{2} \overline{(\nu_R^0)^c} \nu_R^0 + m_D \overline{\nu_R^0} \nu_L^0 + h.c. \quad (2.2)$$

where  $c$  denotes the charge conjugation. By diagonalizing, the observable mass eigenstates can be obtained [176]:

$$-\mathcal{L} = \frac{1}{2} (\bar{\nu}_L, \overline{N_L^c}) \begin{pmatrix} 0 & m_D \\ m_D & m_R \end{pmatrix} \begin{pmatrix} \nu_R^c \\ N_R \end{pmatrix} + h.c. \quad (2.3)$$

In the view of GUT<sup>4</sup>-models, the light Dirac-mass  $m_D$  can be identified as the mass of a charged fermion, while the heavy Majorana mass can be identified with the GUT mass scale  $m_R \approx m_{GUT}$  [141, p. 30].

## 2.3 Neutrino Oscillations

The term *neutrino oscillation* [176, 54, 70, 142] is understood to mean the oscillating transition of different neutrino flavors  $\nu_\alpha \longleftrightarrow \nu_\beta$  ( $\alpha, \beta = e, \mu, \tau, \dots$ ). In this context the lepton number is not conserved  $L_\alpha \neq L_\beta$ . In addition, it is necessary that different neutrinos have different masses.

In the standard model (SM) neutrinos are considered to be massless<sup>5</sup>.

Bruno Pontecorvo suggested the possibility of neutrino oscillations, although he predicted a different kind of neutrino oscillations<sup>6</sup>, which was later modified by Maki, Nakagawa and

<sup>4</sup>GUT: Grand Unified Theory

<sup>5</sup>This is based more or less on assumptions.

<sup>6</sup>Pontecorvo suggested originally  $\nu \rightarrow \bar{\nu}$  transitions.

Sakata to the form well known today. In view of many experiments that have been carried out in the past decades, today neutrino oscillations are well established. Neutrino oscillations can be described by a wave packet treatment [142], using a specific, cohesive and clear quantum field approach. The following sections are based on a wave plane approximation, which yield same results.

### 2.3.1 General Neutrino Mixing Formalism in Vacuum

In order to derive the neutrino oscillation probabilities, a wave plane approximation is applied.<sup>7</sup> The oscillation formalism is based on the idea that the flavor eigenstates  $|\nu_\alpha\rangle$  ( $\alpha = e, \mu, \tau, \dots$ ) are linear combinations of the mass eigenstates  $|\nu_i\rangle$  ( $i = 1, 2, 3, \dots$ ):

$$|\nu_\alpha\rangle = \sum_j U_{\alpha j} |\nu_j\rangle, \quad |\bar{\nu}_\alpha\rangle = \sum_j U_{\alpha j}^* |\nu_j\rangle \quad (2.4)$$

where  $U$  denotes the neutrino mixing matrix called Pontecorvo-Maki-Nakagawa-Sakata (PMNS) mixing matrix. The mixing matrix  $U = (u_{kl})_{(k,l) \in n \times n}$  with  $n \in \mathbb{N}$  is approximately a unitary matrix ( $U^\dagger U = 1$ ) and can be described by  $(n-1)^2$  independent parameters with  $\frac{1}{2}n(n-1)$  rotation angles (Euler angles) and  $\frac{1}{2}(n-1)(n-2)$  phases<sup>8</sup>. In general, an arbitrary unitary matrix is parametrized by the product

$$U = \prod_{a < b} R(\theta_{ab}) = \prod_{a < b} R_{ab}, \quad (2.5)$$

where the matrix  $R_{ab} = (r_{pq})_{(p,q) \in n \times n}$  describes an arbitrary complex rotation in the  $ab$  plane [175, 120]. In general, the entries of  $R_{ab}$  are given in analogy to the Givens rotation principle by

$$R_{ab}(\theta_{ab}, \delta_h) = \begin{cases} \cos \theta_{ab} & p = q = a, b \\ 1 & p = q \neq a, b \\ \sin \theta_{ab} e^{-i\delta_h} & p = a; q = b \\ -\sin \theta_{ab} e^{i\delta_h} & p = b; q = a \\ 0 & \text{otherwise} \end{cases} \quad (2.6)$$

$\delta_h$  is a Dirac  $CP$ -Violating phase which is only zero if  $U$  is real.

In order to describe the time dependent propagation the state  $\nu_i$  is developed by its proper time  $\tau_i$  according to the Schrödinger equation

$$i \frac{\partial}{\partial \tau_i} |\nu(\tau_i)\rangle = \mathcal{H}^\nu |\nu(\tau_i)\rangle \quad (2.7)$$

where  $\mathcal{H}^\nu$  denotes the Hamiltonian in the mass eigenstates representation. The solution is given by

$$|\nu_i(\tau)\rangle = e^{-im_i\tau} |\nu_i(0)\rangle, \quad (2.8)$$

which becomes

$$|\nu_i(t)\rangle = e^{iE_i t + ipx} |\nu_i\rangle = e^{-iE_i t + ipt} |\nu_i\rangle, \quad (2.9)$$

in the laboratory frame where  $t$  denotes the starting time of the propagation,  $p$  the momentum,  $x$  the position of the neutrino and  $E_i$  the energy of the mass-eigenstate  $i$ . Neutrinos

<sup>7</sup>For the following section please also note [159, p. 9-12].

<sup>8</sup>If neutrinos are considered as Majorana particles, additional parameters are expected (e.g. Majorana phases). In this section only rotational matrices are assumed.

move approximately with the speed of light which yield  $x \approx t$  (using natural units with  $c = 1$ ). Using the approximations  $p \gg m_i$  and  $E \approx p$  it follows that:

$$E_i \approx \sqrt{p^2 + m_i^2} \approx p + \frac{m_i^2}{2p} \approx E + \frac{m_i^2}{2E} \quad (2.10)$$

The time dependent development of a pure flavor state  $|\nu_\alpha\rangle$  at the time  $t = 0$  is given by

$$|\nu_\alpha(t)\rangle = \sum_i U_{\alpha i} e^{-iE_i t + i p t} |\nu_i\rangle = \sum_i U_{\alpha i} U_{\beta i} e^{-iE_i t + i p t} |\nu_\beta\rangle \quad (2.11)$$

The probability  $P(\nu_\alpha \rightarrow \nu_\beta)$  that a neutrino with flavor  $\alpha$  oscillates into a neutrino with flavor  $\beta$  is derived by

$$P(\nu_\alpha \rightarrow \nu_\beta) = |\langle \nu_\beta | \nu_\alpha \rangle|^2 = \left| \sum_i U_{\alpha i} U_{\beta i}^* e^{-iE_i t + i p t} \right|^2 \quad (2.12)$$

For relativistic particles  $L \approx t$  and  $E_i \gg m_i$  is assumed so that

$$E_i t - p_i t \approx (E_i - p_i) L = \frac{E_i^2 - p_i^2}{E_i + p_i} L = \frac{m_i^2}{E_i + p_i} L \approx \frac{m_i^2}{2E} L. \quad (2.13)$$

For the oscillation probability the following equation applies<sup>9</sup>:

$$\begin{aligned} P(\nu_\alpha \rightarrow \nu_\beta) &= \left| \sum_i U_{\alpha i} U_{\beta i}^* e^{-i \frac{m_i^2}{2E} L} \right|^2 = \left( \sum_i U_{\alpha i} U_{\beta i}^* e^{-i \frac{m_i^2}{2E} L} \right) \left( \sum_j U_{\alpha j} U_{\beta j}^* e^{i \frac{m_j^2}{2E} L} \right) \\ &= U_{\alpha 1} U_{\beta 1}^* U_{\alpha 1}^* U_{\beta 1} + U_{\alpha 2} U_{\beta 2}^* U_{\alpha 2}^* U_{\beta 2} + \dots + U_{\alpha n} U_{\beta n}^* U_{\alpha n}^* U_{\beta n} \\ &+ U_{\alpha 1} U_{\beta 1}^* U_{\alpha 2}^* U_{\beta 2} e^{-i \frac{(m_1^2 - m_2^2)}{2E} L} + U_{\alpha 2} U_{\beta 2}^* U_{\alpha 1}^* U_{\beta 1} e^{-i \frac{(m_2^2 - m_1^2)}{2E} L} \\ &+ U_{\alpha 1} U_{\beta 1}^* U_{\alpha 3}^* U_{\beta 3} e^{-i \frac{(m_1^2 - m_3^2)}{2E} L} + U_{\alpha 3} U_{\beta 3}^* U_{\alpha 1}^* U_{\beta 1} e^{-i \frac{(m_3^2 - m_1^2)}{2E} L} \\ &+ \dots + U_{\alpha 1} U_{\beta 1}^* U_{\alpha n}^* U_{\beta n} e^{-i \frac{(m_1^2 - m_n^2)}{2E} L} + U_{\alpha n} U_{\beta n}^* U_{\alpha 1}^* U_{\beta 1} e^{-i \frac{(m_n^2 - m_1^2)}{2E} L} \\ &+ U_{\alpha 2} U_{\beta 2}^* U_{\alpha 3}^* U_{\beta 3} e^{-i \frac{(m_2^2 - m_3^2)}{2E} L} + U_{\alpha 3} U_{\beta 3}^* U_{\alpha 2}^* U_{\beta 2} e^{-i \frac{(m_3^2 - m_2^2)}{2E} L} \\ &+ \dots \\ &+ U_{\alpha, n-1} U_{\beta, n-1}^* U_{\alpha n}^* U_{\beta n} e^{-i \frac{(m_{n-1}^2 - m_n^2)}{2E} L} + U_{\alpha n} U_{\beta n}^* U_{\alpha, n-1}^* U_{\beta, n-1} e^{-i \frac{(m_n^2 - m_{n-1}^2)}{2E} L} \\ &= \sum_i |U_{\alpha i} U_{\beta i}^*|^2 + 2\Re \sum_{j>i} U_{\alpha i} U_{\beta i}^* U_{\alpha j}^* U_{\beta j} e^{-i \frac{\Delta m_{ij}^2}{2E} L} \\ &= \delta_{\alpha\beta} - 2\Re \sum_{j>i} U_{\alpha i} U_{\beta i}^* U_{\alpha j}^* U_{\beta j} + 2\Re \sum_{j>i} U_{\alpha i} U_{\beta i}^* U_{\alpha j}^* U_{\beta j} e^{-i \frac{\Delta m_{ij}^2}{2E} L} \\ &= \delta_{\alpha\beta} - 2\Re \sum_{j>i} U_{\alpha i} U_{\beta i}^* U_{\alpha j}^* U_{\beta j} \left( 1 - e^{-i \frac{\Delta m_{ij}^2}{2E} L} \right) \end{aligned} \quad (2.14)$$

where  $\Delta m_{ij}^2$  represents the neutrino squared mass difference

$$\Delta m_{ij}^2 = m_i^2 - m_j^2. \quad (2.15)$$

<sup>9</sup>For the following derivation please notice [176, 54] and particularly [191].

It was used that

$$z + z^* = 2\Re(z) \quad (2.16)$$

and

$$\delta_{\alpha\beta} = \delta_{\alpha\beta} \cdot \delta_{\beta\alpha} = \left( \sum_i U_{\alpha i} U_{\beta i}^* \right) \left( \sum_j U_{\alpha j} U_{\beta j}^* \right) \quad (2.17)$$

$$= \sum_i |U_{\alpha i} U_{\beta i}^*| + 2\Re \sum_{j>i} U_{\alpha i} U_{\beta i}^* U_{\alpha j}^* U_{\beta j} \quad (2.18)$$

The last term of the preceding equation can be transformed to<sup>10</sup>

$$\begin{aligned} & -2\Re \sum_{j>i} U_{\alpha i} U_{\beta i}^* U_{\alpha j}^* U_{\beta j} \left( 1 - e^{-i \frac{\Delta m_{ij}^2}{2E} L} \right) \\ &= -2 \sum_{j>i} \Re U_{\alpha i} U_{\beta i}^* U_{\alpha j}^* U_{\beta j} \left( 1 - \cos \left( \frac{\Delta m_{ij}^2}{2E} L \right) + i \sin \left( \frac{\Delta m_{ij}^2}{2E} L \right) \right) \\ &= -2\Re (U_{\alpha i} U_{\beta i}^* U_{\alpha j}^* U_{\beta j}) \left( 1 - \cos \left( \frac{\Delta m_{ij}^2}{2E} L \right) \right) + 2 \sum_{j>i} \Im (U_{\alpha i} U_{\beta i}^* U_{\alpha j}^* U_{\beta j}) \sin \left( \frac{\Delta m_{ij}^2}{2E} L \right) \\ &= -4\Re (U_{\alpha i} U_{\beta i}^* U_{\alpha j}^* U_{\beta j}) \sin^2 \left( \frac{\Delta m_{ij}^2}{4E} L \right) + 2 \sum_{j>i} \Im (U_{\alpha i} U_{\beta i}^* U_{\alpha j}^* U_{\beta j}) \sin \left( \frac{\Delta m_{ij}^2}{2E} L \right) \end{aligned}$$

Therefore the oscillation probability is given by

$$\begin{aligned} P(\nu_\alpha \rightarrow \nu_\beta) &= \delta_{\alpha\beta} - 4 \sum_{j>i} \Re (U_{\alpha i} U_{\beta i}^* U_{\alpha j}^* U_{\beta j}) \sin^2 \left( \frac{\Delta m_{ij}^2}{4E} L \right) \\ &\quad + 2 \sum_{j>i} \Im (U_{\alpha i} U_{\beta i}^* U_{\alpha j}^* U_{\beta j}) \sin \left( \frac{\Delta m_{ij}^2}{2E} L \right) \end{aligned} \quad (2.19)$$

The matrix elements  $U_{\alpha\beta}$  are responsible for the oscillation amplitude while the squared mass differences  $\Delta m_{ij}^2$  determine the oscillation frequency for an experiment-specific baseline and energy. Three points are important to realize:

- Neutrino oscillations only occur, if at least one neutrino mass is non-zero ( $m_i \neq 0$ ).
- The squared mass differences must be distinct ( $\Delta m_{ij}^2 \neq 0$ ). Otherwise there are no neutrino oscillations.
- If the mixing matrix  $U$  is not real, i.e.  $\delta \neq 0$ , different oscillation probabilities for neutrinos and antineutrinos occur. Since  $P(\nu_\alpha \rightarrow \nu_\beta)$  and  $P(\bar{\nu}_\alpha \rightarrow \bar{\nu}_\beta)$  are related by CP operation, a different oscillation will lead to CP violation in the leptonic sector.

The possibility of CP violation is an important aspect in our understanding of the matter-antimatter asymmetry in the universe and was originally motivated by the discovery of CP violation by *J.H. Christenson, J.W. Cronin, V.L. Fitch* and *R. Turlay* in the neutral kaon system [84].<sup>11</sup>

<sup>10</sup>Using the following relations:  $\Re(z_1 z_2) = \Re(z_1) \Re(z_2) - \Im(z_1) \Im(z_2)$  and  $\cos(2a) = 1 - 2 \sin^2(a)$

<sup>11</sup>J.W. Cronin and V.L. Fitch both received the Nobel Prize in Physics in 1980.

### 2.3.2 Neutrino Oscillations in Matter and MSW Effect

When neutrinos propagate through matter, the oscillation probability changes mainly due to the coherent forward scattering, which was first realized by *Lincoln Wolfenstein* in 1978 [205]. The evolution of the transition amplitude in the flavor state is given by the Schrödinger equation, as described in Ref. [176]:

$$i \frac{d}{dt} |\nu(t)\rangle = \mathcal{H}_0 |\nu\rangle, \quad \mathcal{H}_0 = U \left[ 1 + \frac{m^2}{2p} \right] \quad (2.20)$$

By replacing the free Hamiltonian  $\mathcal{H}_0$  by the effective Hamiltonian  $\mathcal{H}_{eff} = \mathcal{H}_0 + V$  ( $V$  represents the matrix of matter-induced neutrino potentials), the  $CC$  and  $NC$  interaction between the neutrinos and matter (electrons, protons and neutrons) are incorporated [31]. One can deduce that the contribution due to elastic neutrino-quark-scattering has no physical influence on the oscillation in neutral matter ( $e\mu\tau$ - universality via  $Z^0$  exchange). An additional term comes from the  $CC$  interaction between the neutrinos and electrons, which results in an additional effective potential  $V = \pm\sqrt{2}G_F N_e$  (the " + " sign applies for antineutrinos, while for neutrinos the opposite sign has to be used). Therefore the evolution equation becomes:

$$i \frac{d}{dt} |\nu(t)\rangle = \left[ U \frac{m^2}{2E} U^\dagger \pm \sqrt{2}G_F N_e \beta \right] |\nu\rangle, \quad (2.21)$$

where  $G_F$  denotes the Fermi constant and  $N_e$  the electron density (see also [176]). If constant matter density is assumed, the total Hamiltonian can be diagonalized. The eigenvalues describe the effective masses. The effective difference of squared masses  $\Delta m_m^2$  and the effective mixing angles  $\theta_m$  are then given by [212, p. 222]

$$\tan(2\theta_m) = \frac{\Delta m^2 \sin 2\theta}{\Delta m^2 \cos 2\theta - A} \quad (2.22)$$

$$\Delta m_m^2 = \sqrt{(\Delta m^2 \cos(2\theta) - A)^2 + ((\Delta m^2) \sin(2\theta))^2} \quad (2.23)$$

The quantity  $A$  is defined by

$$A = 2E (V_e - V_x). \quad (2.24)$$

It should be pointed out that even massless neutrinos acquire non-vanishing effective masses in matter [205]. The oscillation length in matter is given by [212, p. 223]

$$L^{osc} = \frac{L_0^{osc} \Delta m^2}{\sqrt{(\Delta m^2 \cos 2\theta - A)^2 + ((\Delta m^2) \sin(2\theta))^2}}, \quad (2.25)$$

where  $L_0^{osc} = 4\pi E / \Delta m_{ij}^2$  represents the vacuum oscillation length. The oscillation length in matter has a resonant point at

$$L_R^{osc} = \frac{L_0^{osc}}{\sin 2\theta}. \quad (2.26)$$

The maximum resonance occurs, if  $A = \Delta m^2 \cos 2\theta$ , which means that  $\theta_{mR} = 45^\circ$ . The resonant amplification of neutrino oscillations in matter is called MSW (*Mikheyev-Smirnov-Wolfenstein*) effect [162].

## 2.4 Results of the Last Two Decades: Three Flavor Oscillations

Today, most of the neutrino oscillation data can be well explained with three active neutrinos [141, 176, 212]. In the common picture, the three neutrino flavors ( $\nu_e$ ,  $\nu_\mu$ ,  $\nu_\tau$ ) are linear combinations of the three mass eigenstates ( $\nu_1$ ,  $\nu_2$ ,  $\nu_3$ ) separated by the two squared mass differences of  $\Delta m_{21}^2 = 8 \times 10^{-5} \text{ eV}^2$  and  $\Delta m_{31}^2 = 2.4 \times 10^{-3} \text{ eV}^2$  [160]. Three independent neutrino mixing angles  $\theta_{12}$ ,  $\theta_{23}$  and  $\theta_{13}$  define the oscillation amplitudes and are used to parametrize the neutrino mixing matrix. The transformation between the neutrino flavors and the mass eigenstates can be expressed through the following mixing formalism:

$$\begin{pmatrix} \nu_e \\ \nu_\mu \\ \nu_\tau \end{pmatrix} = \begin{pmatrix} U_{e1} & U_{e2} & U_{e3} \\ U_{\mu1} & U_{\mu2} & U_{\mu3} \\ U_{\tau1} & U_{\tau2} & U_{\tau3} \end{pmatrix} \begin{pmatrix} \nu_1 \\ \nu_2 \\ \nu_3 \end{pmatrix}.$$

The mixing matrix  $U$  is given by  $U = R_{23}(\theta_{23})R_{13}(\theta_{13}, \delta)R_{12}(\theta_{12})M(\phi_1, \phi_2)$ . Following Givens rotation principle, multiplied with an additional matrix to incorporate a possible Majorana character of the neutrinos, this becomes:

$$\begin{aligned} U &= \underbrace{\begin{pmatrix} 1 & 0 & 0 \\ 0 & c_{23} & s_{23} \\ 0 & -s_{23} & c_{23} \end{pmatrix}}_{\text{atmospheric}} \underbrace{\begin{pmatrix} c_{13} & 0 & s_{13}e^{-i\delta} \\ 0 & 1 & 0 \\ -s_{13}e^{i\delta} & 0 & c_{13} \end{pmatrix}}_{\text{reactor}} \underbrace{\begin{pmatrix} c_{12} & s_{12} & 0 \\ -s_{12} & c_{12} & 0 \\ 0 & 0 & 1 \end{pmatrix}}_{\text{solar}} \\ &\quad \times \underbrace{\begin{pmatrix} e^{-\phi_1} & 0 & 0 \\ 0 & e^{-\phi_2} & 0 \\ 0 & 0 & 1 \end{pmatrix}}_{\text{Majorana}}, \\ &= \begin{pmatrix} c_{12}c_{13} & s_{12}c_{13} & s_{13}e^{i\delta} \\ -s_{12}c_{23} - c_{12}s_{23}s_{13}e^{-i\delta} & c_{12}c_{23} - s_{12}s_{23}s_{13}e^{-\delta} & s_{23}c_{13} \\ s_{12}s_{23} - c_{12}c_{23}s_{13}e^{-i\delta} & c_{12}s_{23} - s_{12}c_{23}s_{13}e^{-\delta} & c_{23}c_{13} \end{pmatrix} \times \begin{pmatrix} e^{-\phi_1} & 0 & 0 \\ 0 & e^{-\phi_2} & 0 \\ 0 & 0 & 1 \end{pmatrix} \end{aligned} \quad (2.27)$$

where  $s_{ab} \equiv \sin \theta_{ab}$ ,  $c_{ab} \equiv \cos \theta_{ab}$ .  $\phi_1$  and  $\phi_2$  are the Majorana CP phases, which do not affect the neutrino oscillation. However, the nature of the neutrino being Dirac or Majorana particle is still unknown. If neutrinos are Dirac particles, the last matrix can be neglected. The knowledge of the mixing parameters and squared mass differences was gained in a series of experiments conducted over many years [207]. The two independent squared mass differences,  $\Delta m_{12}^2$  and  $\Delta m_{23}^2$  control the solar and atmospheric neutrino oscillations while  $\Delta m_{13}^2$  drives the oscillation length for reactor neutrino experiments [141]. The solar mixing angle  $\theta_{12} \simeq 35^\circ$  is mainly fixed by the  $^8\text{B}$  neutrino measurement performed by the SNO and SUPER-KAMIOKANDE experiments [207]. The squared mass difference  $\Delta m_{12}^2$  is often associated to these solar neutrino measurements, although the most accurate determination was actually performed by the reactor-based experiment KAMLAND. SUPER-KAMIOKANDE has also provided the most precise measurement of the atmospheric mixing angle  $\theta_{23} \simeq 43^\circ$ . However, it remains an open question whether it is truly maximal. The associated squared mass difference  $\Delta m_{23}^2$  was determined by the MINOS experiment. [207]

Since  $\Delta m_{31}^2 \gg \Delta m_{21}^2$ , many experiments can be described by a two-flavor scheme. In this case the mixing matrix  $U$  is considered to be a  $2 \times 2$  rotation matrix without a complex Dirac phase and with only one rotation angle  $\theta$ :

$$U = \begin{pmatrix} \cos \theta & \sin \theta \\ -\sin \theta & \cos \theta \end{pmatrix} \quad (2.28)$$

parameter	best fit $\pm 1\sigma$	$2\sigma$ range	$3\sigma$ range
$\Delta m_{21}^2$ [ $10^{-5}$ eV $^2$ ]	$7.60^{+0.19}_{-0.18}$	7.26–7.99	7.11–8.18
$ \Delta m_{31}^2 $ [ $10^{-3}$ eV $^2$ ] (NH)	$2.48^{+0.05}_{-0.07}$	2.35–2.59	2.30–2.65
$ \Delta m_{31}^2 $ [ $10^{-3}$ eV $^2$ ] (IH)	$2.38^{+0.05}_{-0.06}$	2.26–2.48	2.20–2.54
$\sin^2 \theta_{12}/10^{-1}$	$3.23 \pm 0.16$	2.92–3.57	2.78–3.75
$\theta_{12}/^\circ$	$34.6 \pm 1.0$	32.7–36.7	31.8–37.8
$\sin^2 \theta_{23}/10^{-1}$ (NH)	$5.67^{+0.32}_{-1.28}$	4.13–6.23	3.92 – 6.43
$\theta_{23}/^\circ$	$48.9^{+1.9}_{-7.4}$	40.0–52.1	38.8–53.3
$\sin^2 \theta_{23}/10^{-1}$ (IH)	$5.73^{+0.25}_{-0.43}$	4.32–6.21	4.03–6.40
$\theta_{23}/^\circ$	$49.2^{+1.5}_{-2.5}$	41.1–52.0	39.4–53.1
$\sin^2 \theta_{13}/10^{-2}$ (NH)	$2.34 \pm 0.20$	1.95–2.74	1.77–2.94
$\theta_{13}/^\circ$	$8.8 \pm 0.4$	8.0–9.5	7.7–9.9
$\sin^2 \theta_{13}/10^{-2}$ (IH)	$2.40 \pm 0.19$	2.02–2.78	1.83–2.97
$\theta_{13}/^\circ$	$8.9 \pm 0.4$	8.2–9.6	7.8–9.9
$\delta/\pi$ (NH)	$1.34^{+0.64}_{-0.38}$	0.0–2.0	0.0–2.0
$\delta/^\circ$	$241^{+115}_{-68}$	0–360	0–360
$\delta/\pi$ (IH)	$1.48^{+0.34}_{-0.32}$	0.0–0.14 & 0.81–2.0	0.0–2.0
$\delta/^\circ$	$266^{+61}_{-58}$	0–25 & 146–360	0–360

**Table 2.1:** Three neutrino oscillation data from Ref. [106]. For  $\Delta m_{31}^2$ ,  $\sin^2 \theta_{23}$ ,  $\sin^2 \theta_{13}$ , and  $\delta$  the upper (lower) row corresponds to normal (inverted) neutrino mass ordering. Please note that a local minimum in the first octant,  $\sin^2 \theta_{23} = 0.467$  with  $\Delta\chi^2 = 0.28$  with respect to the global minimum has been identified.

The survival probability is given according to Eq. (2.19) by

$$P(\nu_\alpha \rightarrow \nu_\beta) = \delta_{\alpha\beta} - 4 |U_{\alpha 2}^* U_{\beta 2} U_{\alpha 1} U_{\beta 1}^*| \sin^2 \left( \frac{\Delta m^2 L}{4E} \right). \quad (2.29)$$

The corresponding matrix elements are given by Eq. (2.28). Inserting these elements leads to

$$P(\nu_\alpha \rightarrow \nu_\beta) = 1 - \sin^2(2\theta) \sin^2 \left( \frac{\Delta m^2 L}{4E} \right) \quad (2.30)$$

$$= 1 - \sin^2(2\theta) \sin^2 \left( 1.267 \frac{\Delta m^2 L [\text{m}]}{E [\text{MeV}]} \right). \quad (2.31)$$

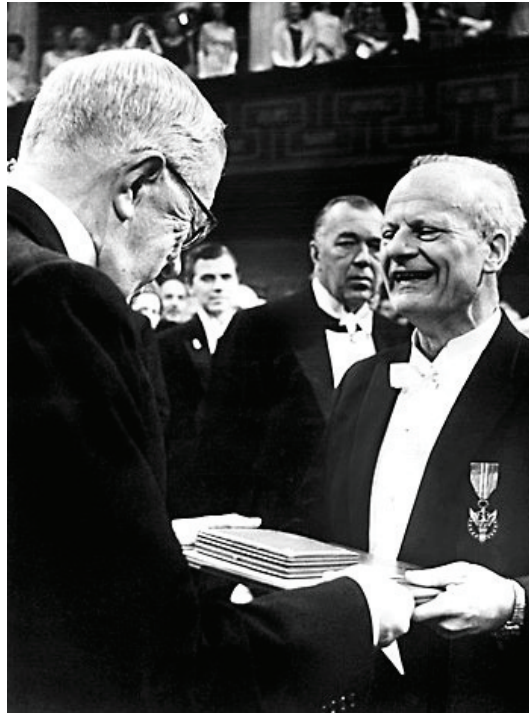
The most recent results on the mixing parameters are summarized in Table 2.1.

### 2.4.1 Solar Neutrinos

#### Historical Prologue

The fundamental process behind the energy production in stars was first proposed by Carl-Friedrich von Weizsäcker in 1937, a former student of Werner Heisenberg at the University of Leipzig, in which four protons are converted into Helium. The basic step of the reaction is the fusion of two Hydrogen atoms into Deuterium, which occurs in 99.76% of the time. The complete fusion process is referred to as pp chain.

In 1937, Charles Critchfield studied the “problem of calculating the cross-section for the reaction  $p + p \rightarrow d + e^+ + \nu_e$  under stellar conditions in order to see whether the cyclic



(a)



(b)

**Figure 2.1:** (a): Hans Bethe receiving the Nobel Prize in Physics from His Majesty the King Gustaf VI Adolf of Sweden. The ceremony was held on December 10, the anniversary of Nobel's death. Photo taken from [www.nobelprize.org](http://www.nobelprize.org). (b): Physics conference in Copenhagen. The conference was held probable in 1937 about the same time when Carl-Friedrich von Weizsäcker proposed the fundamental process behind the energy production in stars. Von Weizsäcker is sitting in the third row (second on the left side). Photo from the the estate of Friedrich Hund. Online available at [200].

reaction [...] could account for the luminosity of the sun” [179, p. 345]. This problem was closely linked to nucleosynthesis which attracted a lot of physicist at that time, including George Gamow and Subrahmanyan Chandrasekhar. Hans Bethe got involved in this topic during the annual Washington Conference on Theoretical Physics which started on March 17, 1938 [179, p. 345]. Bethe had already attended the first conference in 1935 and also the following conferences in 1936 and 1937, “but when invited to the 1938 meeting he first declined because he was not interested in the topic for that year, the stellar energy generation. The topic had been chosen by Gamow. It was only after Teller’s urging that Bethe agreed to come to the conference” [179, p. 345]. It was during that conference that Bethe developed a deeper interest in the energy production of stars. He was more and more convinced that the reaction proposed by von Weizsäcker was the most likely source for stellar energy. “Upon hearing Critchfield’s interest in the reaction, Bethe proposed that they collaborate. Before the conference’s end Bethe was able to report that the reaction [...]  $[p + p \rightarrow d + e^+ + \nu_e]$  together with the chain of reactions [...] could account for energy production in the Sun” [179, p. 347-347]. However, Bethe soon recognized that the so-called pp chain could explain the energy production of our Sun, but not of heavier bright stars [179]. From astronomical observations, it was followed that “the amount of observed radiation - their luminosity - increases very rapidly with increasing mass“ [179, p. 347]. For much heavier stars a process with a much stronger temperature dependence than the pp chain was needed. “Since the  $T$  dependence is determined by the Coulomb barrier Bethe inferred the necessity of involving heavier nuclei in the energy-generating process” [179, p. 347]. The energy production process developed from these assumptions was a cyclic reaction which involved carbon, oxygen and nitrogen as catalyst. The term CNO pays tribute to these elements. The temperature dependence of this reaction is  $T^{18}$  compared to  $T^4$  as given by the pp chain and thus accounts “for the sharp increase of luminosity with slight increases in core temperature” [179, p. 350]. Although Bethe was tremendously busy during the months following the Washington Conference, he managed to write up a paper he was going to publish with Critchfield on the pp chain [179]. In a letter to Critchfield Bethe wrote:

“In writing up the paper, I found that it would be rather in-homogeneous if the proton process and the discussion of the other reactions in stars were put into the same paper. The proton calculations are very explicit and quantitative, the rest is only qualitative and partly speculative. It would be much easier to write it as two separate papers. In this case, I think I should not make you share the responsibility for my speculations about the other processes, so I would suggest publishing part II alone whereas you would, of course, have to be the senior author on the proton paper. Is this alright with you? Please let me know soon because writing up of the papers depends on your decision. Perhaps you [should] discuss this question with Teller, I am sending him a copy of this letter” [179, p. 351].

Critchfield agreed, but insisted on having “Bethe and Critchfield” on the author list [179]. The paper was finally published in *Physical Review* the same year [72]. Bethe published separately another paper where he introduced the carbon-nitrogen-oxygen cycle (CNO) titled “*Energy production in stars*” [71]. The conclusion of the paper was rapidly accepted and in 1967 Bethe was awarded the Nobel Prize in Physics [179] (see Figure 2.1a). Critchfield and von Weizsäcker did not receive this prestigious award.

Solar neutrinos have been measured over several decades to study the stellar physics. As a well-defined neutrino source, the Sun also allows to study the fundamental properties of neutrinos like the mass ordering, flavor mixing and the MSW effect. Solar neutrino experiments like HOMESTAKE, GALLEX, SAGE, SNO and BOREXINO have provided a deep insight

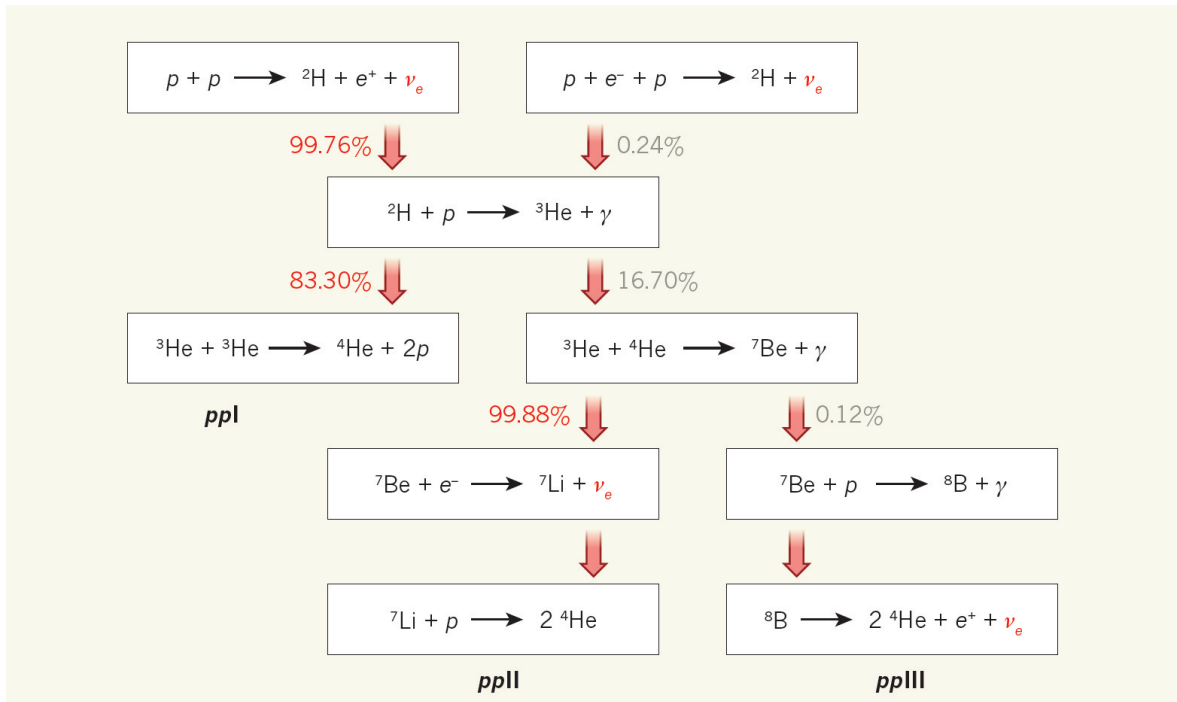


**Figure 2.2:** Neutrinos from the pp chain. Figure taken from [129].

into the stellar interior. Only recently, BOREXINO announced the first direct detection of the primary neutrinos from the pp chain, more than 80 years after the first prediction by von Weizsäcker and Bethe.

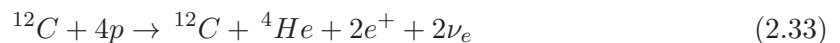
### Production of Solar Neutrinos

The neutrino production in our Sun is dominated by the pp chain. Only one percent of the solar energy is expected to come from the CNO cycle. However, as pointed out previously, this reaction is the dominant process in heavier stars with a mass of more than 1.5 solar masses and older stars. To the present date, no CNO neutrinos have ever been observed by any experiment. The pp chain consists of three branches, named pp-I, pp-II and pp-III. The total net reaction is given by



with a total energy release of 26.7 MeV. The different pp branches are depicted in Figure 2.2.

The second reaction for the fusion to  ${}^4\text{He}$  is the carbon-nitrogen-oxygen cycle (CNO). The energy production is achieved with the participation of  ${}^{12}\text{C}$  which is the most abundant heavy element in normal stellar conditions [91]:



The total released energy is equal to the energy of the pp chain. The contribution of the CNO cycle to the luminosity of the Sun is in the order of one percent in the standard solar model (SSM). At the end of the Sun's lifetime the core temperature will increase and a contribution of 30% to the solar energy budget is expected. The CNO cycle has two sub-cycles named CN cycle and NO cycle. The reaction of the CN cycle are given by:



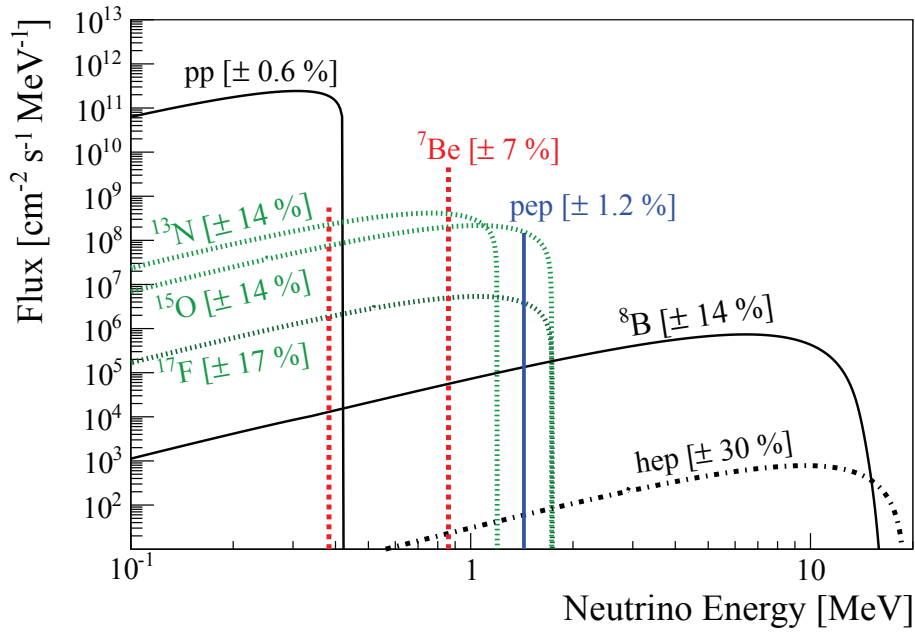
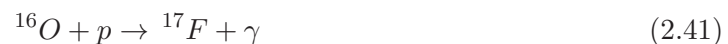


**Figure 2.3:** Solar Neutrino Fluxes [181]. Figure was taken from [66].



The  $\gamma$  de-excitation of  $^{16}\text{O}^*$  is the first step of the CN cycle:



The energy spectrum of the CNO neutrinos and from the three different branches of the pp chain are depicted in Figure 2.3. The neutrino fluxes were originally calculated by John Bahcall and his collaborators and later continued by M. Pinsonneault and A. Serenelli (BPS). The metallicity<sup>12</sup> of the Sun is an important input parameter to the flux prediction. The exact metal content of the Sun is still under discussion since current measurements and solar models do not provide a cohesive picture. Adopting newly determined solar abundances “has proven challenging for SSMs because the agreement with helioseismic data that existed previously has been lost” [180]. The measurement of the CNO flux could help to solve this puzzle as the predicted flux is naturally very sensitive to metal content of the Sun.

<sup>12</sup>Metallicity is defined as the mass fraction of elements other than Hydrogen and Helium with respect to the total mass.

### 2.4.2 Atmospheric Neutrinos

Atmospheric neutrinos are produced in cosmic-ray air showers. Among these air showers, charged pions and kaons are produced. “Charged pions decay into muons” and neutrinos “with a branching ratio of almost 100%” while “kaons decay into muons” and their associated neutrinos in only 63% of all cases [178, p. 33]. “The relative contribution of pions and kaons to the neutrino and muon production determines the flavor composition, energy spectrum and angular distribution of atmospheric neutrinos and muons” [178, p. 33]. The oscillations of atmospheric neutrinos have been measured by a number of experiments (KAMIOKANDE, IMB, SOUDAN 2, FREJUS and NUSEX). In recent years, SUPER-KAMIOKANDE has provided a detailed study of the atmospheric neutrinos and has proven neutrino oscillations with high accuracy. The water Cherenkov detector of SUPER-KAMIOKANDE allows to separate between electron and muon neutrinos. Additionally, its technique allows to determine the flight direc-

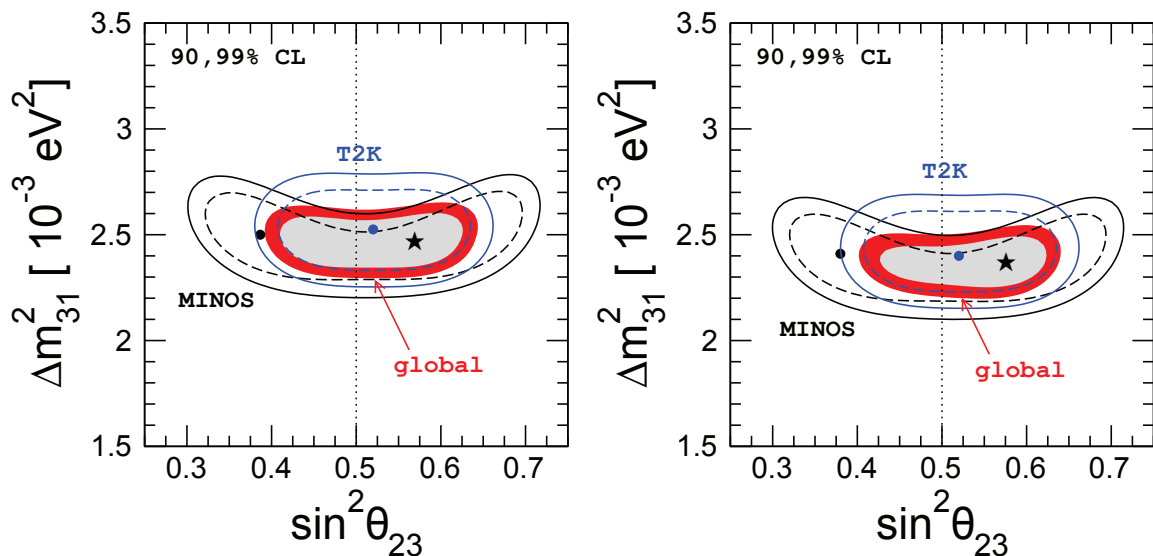


**Figure 2.4:** Allowed parameter space from separate analysis of MINOS and T2K data. The left (right) plot corresponds to the normal (inverted) mass ordering. The global analysis has incorporated all available data, including recent results from SUPER-KAMIOKANDE. Figure taken from [106].

tion of the neutrino. The results showed a significant zenith angle deficit of the atmospheric muon neutrinos while the number of observed electron neutrinos was within theoretical expectations. The disappearance as a function of the zenith angle (and equivalent to that, to the baseline<sup>13</sup>) of the muon neutrinos was finally attributed to  $\nu_\mu \rightarrow \nu_\tau$  transitions. The same oscillation parameters ( $\Delta m_{23}^2, \sin^2(2\theta_{23})$ ) are also approachable via neutrino accelerator experiments like MINOS and T2K. The allowed parameter space is depicted in Figure 2.4. Currently, OPERA is the only neutrino experiment operating in appearance mode in this sector. OPERA has reported the observation of five  $\nu_\tau$  events which amounts to a significance of about  $5\sigma$  [22, 23].

As part of a campaign to reduce the background level of the OPERA experiment and to improve the sensitivity for the  $\nu_\tau$  appearance search, more sophisticated methods are currently developed including the so-called angular matching method (AMM) [21]. “The estimation of the large-angle muon scattering background which was formerly based on conservative assumptions has been recently updated [150] and reduced to a level where charm decays now contribute for about 95% of the background in the muonic channel. This allows for a more

<sup>13</sup>Muon neutrinos coming from below have to cross the entire diameter of the earth. Their baseline is therefore significantly larger compared to *downward going* muon neutrinos.

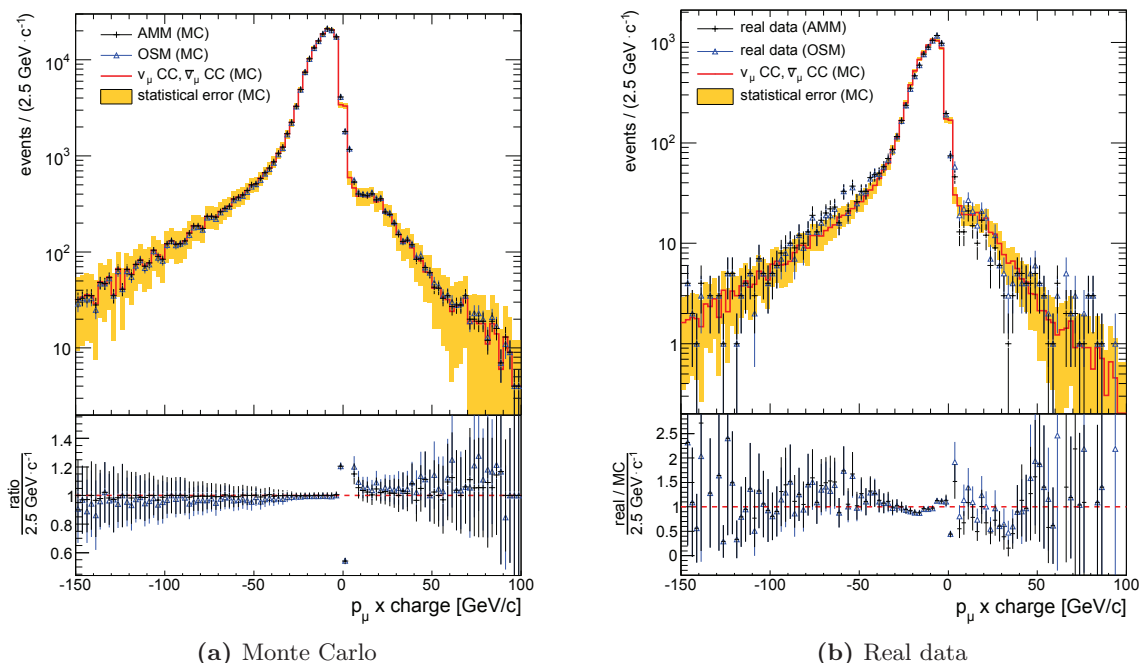


**Figure 2.5:** Top of each plot: Reconstructed muon charge sign multiplied with the muon momentum  $p_\mu$ . The red band shows the theoretical expectation obtained from the Monte Carlo truth information. The performance of the new algorithm (AMM) is shown as black dots while the old method (OSM) is indicated by blue triangles. In (a) only MC data was used while in (b) the MC truth is compared to real data. The bottom of each plot shows the ratio between the MC truth and the reconstructed data points. Figures have partly previously been published in [21].

significant role of the AMM algorithm in improving the sensitivity of the experiment” [21]. The basic principle of the AMM was originally presented as an outlook of my diploma thesis [159] while the performance was evaluated within my PhD research and was accepted for publication by JINST [21]. The AMM ensures a small number of misidentified muon charge signs and provides a stable and reliable determination of the  $\mu^+/\mu^-$  fraction over a wide momentum range (see Figure 2.5). Figure 2.5b shows the reconstructed momentum times charge sign distributions of the simulated CC processes compared to real data. Within the selected momentum range  $150 \text{ GeV}/c < p_\mu \times \text{charge} < 100 \text{ GeV}/c$ , the ratio of  $\mu^+$  and  $\mu^-$  is estimated to  $N_{\mu^+}/(N_{\mu^+} + N_{\mu^-}) = (3.7 \pm 0.2 \text{ (stat.)})$  for the new AMM and  $(4.5 \pm 0.2 \text{ (stat.)})$  for the old algorithm (called OSM).  $N_{\mu^-}$  is the number of muons and  $N_{\mu^+}$  the number of antimuons. For the Monte Carlo truth this ratio is  $(3.5 \pm 0.1 \text{ (stat.)})$ , assuming binomial errors. Figure 2.5a shows the performance of both algorithms using only simulated data. While the muon and antimuon ratio is equal for the AMM, the old method reaches a value as low as  $(3.9 \pm 0.2 \text{ (stat.)})$ . “In the momentum range relevant for the OPERA main analysis, the impurity is kept below 0.5%” [21]. The method was already applied for the event selection to analyze the  $\nu_\mu/\bar{\nu}_\mu$  neutrino velocity [19] and was used to determine the muon charge ratio at the LNGS [125]. For more details, the reader is referred to the separate publication “*Determination of the muon charge sign with the dipolar spectrometers of the OPERA experiment*” [21]. To summarize, the AMM algorithm provides a stable and reliable determination of the muon charge sign for both Monte Carlo and real data while the old algorithm significantly deviates with respect to the  $N_{\mu^+}/(N_{\mu^+} + N_{\mu^-})$  fraction, if real and Monte Carlo data is compared. Considering the fraction of misidentified muon charge signs, the improvement for the  $\nu_\tau$  analysis corresponds to about 40%. For high energetic muon penetrating both

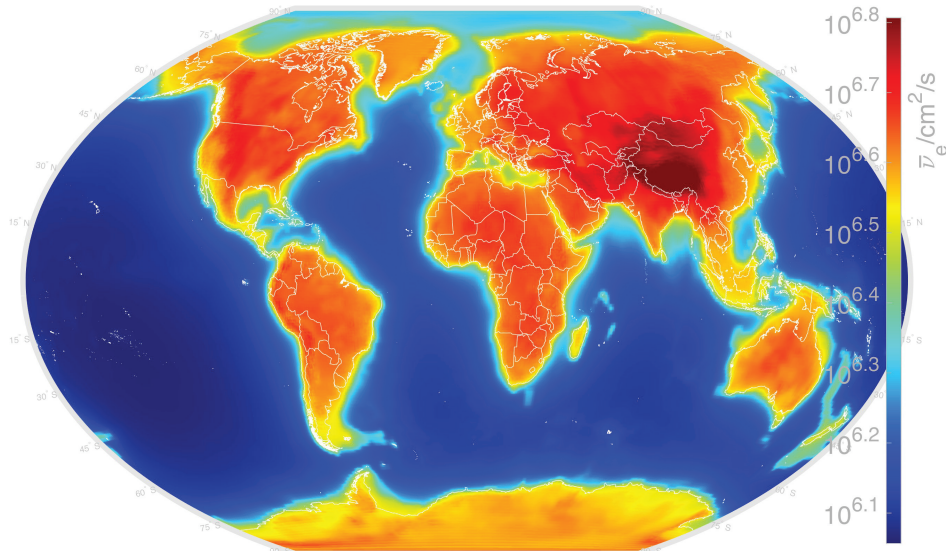


**Figure 2.6:** Expected geo-neutrinos worldwide. Figure taken from [190].

spectrometers, the improvement corresponds to one order of magnitude.

### 2.4.3 Geo-Neutrinos

The earth radiates more energy than it absorbs [97]. The origin of the heat flow radiated away has been studied by the observation of so-called geo-neutrinos. The first measurement of geo-neutrinos was published in 2005 by the KAMLAND collaboration. Geo-neutrinos are  $\bar{\nu}_e$  originating from the radioactive decays of nuclei along the natural Uranium and Thorium chains. The heat generated by these beta decays “contributes to the mantle convection and plate tectonics [...]”. Measuring the amount and location the Thorium and Uranium provides fundamental information on the formation and thermal evolution of our planet” [98]. At least 50% of the heat flow from the Uranium and Thorium chains is assumed to come from the Earth mantle and crust. So far, a potential Geo-reactor in the Earth’s core could not be confirmed. The rest of the heat flow is provided by the crystallization of the liquid outer core. To the present day, only KAMLAND and BOREXINO have reported the measurement of geo-neutrinos. As the detection was performed via the inverse beta decay which has a threshold of  $\sim 1.8$  MeV, only geo-neutrinos originating from the Uranium and Thorium decay chains have been observed. In Japan, KAMLAND measured the  $\bar{\nu}_e$  flux to be  $(3.4 \pm 0.8) \times 10^6 \text{ cm}^2\text{s}^{-1}$  [115, 190] while in Italy the BOREXINO experiment measured the  $\bar{\nu}_e$  flux to be  $(4.3 \pm 1.3) \times 10^6 \text{ cm}^2\text{s}^{-1}$  [190]. In BOREXINO, the null observation of geo-neutrinos is rejected with more than  $5\sigma$  [26]. The global expected geo-neutrino flux including all  $\bar{\nu}_e$  above the IBD threshold is shown in Figure 2.6 [190].

### 2.4.4 Supernova Neutrinos

Supernova (SN) explosions are among the most energetic events in the universe [139]. Historically, supernovae are divided in two different classes based on whether spectral hydrogen lines have been observed (Type-I) or not (Type-II). From the neutrino physics point of view core-collapse supernovae (Type-IIa) are especially interesting as about 99% of their energy is released in the form of neutrinos [139]. The progenitor star must have a mass of at least  $8M_{\odot}$ . The following explosion may then carry away an energy of about  $10^{46}$  J within ten



**Figure 2.7:** SN1987A in the Large Magellanic Cloud. About 20 neutrinos were registered on the 23th of February. It was the first time that neutrinos from a supernova explosion were detected. Credit: ESO

seconds. From observations of nearby galaxies, about 1-3 SNe are expected within a century in our galaxy. So far, only neutrinos from one SN have been observed. On the 23th of February in 1987 a supernova explosion in the Large Magellanic Cloud at a distance of about 51.4 kpc (168,000 light-years) from the Earth was observed both with optical telescopes and neutrino detectors. Although only about 20 neutrinos have been collected by three different experiments, the supernova named SN1987A promoted greatly the understanding of core-collapse supernovae. The progenitor star was identified as Sanduleak (SK -69° 202), a blue super-giant. Figure 2.7 shows a photo from this rare SN event. The underlying process of the SN explosion can be divided into different stages: Right after the core bounce and with the beginning of the accretion phase, neutrinos are thermally created. The sudden  $\nu_e$  burst is dominated by the neutronization which last only about 20 ms. Mostly  $\nu_e$  are created during this stage. During the following accretion phase the energies and luminosity of the neutrinos increase. The cooling phase is characterized by roughly exponential decrease of the neutrino luminosity over time. The flavor content of all neutrinos is approximately the same with a small extent in the  $\nu_{\mu,\tau}$  content. [139]

SNe could be used to address many fundamental properties of neutrinos like measurement of the neutrino velocity, mass and mass ordering [139]. A high-statistic signal enabling a flavor and time resolved analysis could also help in the theoretical modeling of SNe.

#### 2.4.5 Reactor Neutrinos

Reactor  $\bar{\nu}_e$  have been used since the beginning of neutrino observations. Over the past years, many reactor experiments contributed to the understanding of the fundamental properties of neutrinos. But only recently, three reactor experiments (DOUBLE CHOOZ, RENO and DAYA BAY) were able to close a long-standing gap in neutrino oscillations physics. In 2011/2012, all experiments confirmed a non-vanishing mixing angle  $\theta_{13}$  with great significance [11, 40, 30]. With a 43,000 t-GW<sub>th</sub>-day live-time exposure in 55 days, 10416 (80376) electron antineutrino candidates were detected by the DAYA BAY experiment [40]. Based upon these statistics, DAYA BAY was able to determine the last unknown mixing angle to be  $\sin^2(2\theta_{13}) = 0.092 \pm 0.016(\text{stat.}) \pm 0.005(\text{syst.})$  [40]. The significance for  $\theta_{13}$  being non-zero corresponded to 5.2 standard deviations [40].

In general, two different approaches can be used to determine the mixing angle  $\theta_{13}$ . One possibility is to measure  $\theta_{13}$  in reactor disappearance experiments. The other possibility is to use accelerator experiments by searching for  $\nu_{\mu} \longleftrightarrow \nu_e$  oscillations in appearance mode. The following section will focus on reactor experiments. Particular focus will be given to the evaluation of the cosmogenic background processes.

##### 2.4.5.1 Reactor Experiments and $\theta_{13}$

In order to be sensitive to a specific oscillation parameter, the neutrino energy and baseline have to be chosen accordingly. Taking into account the mean antineutrino energy of  $\langle E \rangle = 3 \text{ MeV}$  from reactor neutrinos and the value of  $\Delta m_{31}^2$ , the detector should be placed  $\sim 1 - 1.5 \text{ km}$  from the reactor core. To minimize systematic uncertainties of the neutrino flux and spectrum, all current reactor experiments use near detectors to measure the almost non-oscillated rate [191] (see also Figure 2.8). Both, near and far detectors are built identically to guarantee equal detection efficiencies. Among the current experiments, DOUBLE CHOOZ was the first experiment which started data taking, but the last one which took the near detector into operation. So far, all published analyses from DOUBLE CHOOZ had to rely on a precise theoretical prediction of the  $\bar{\nu}_e$  flux (see also appendix C.1).

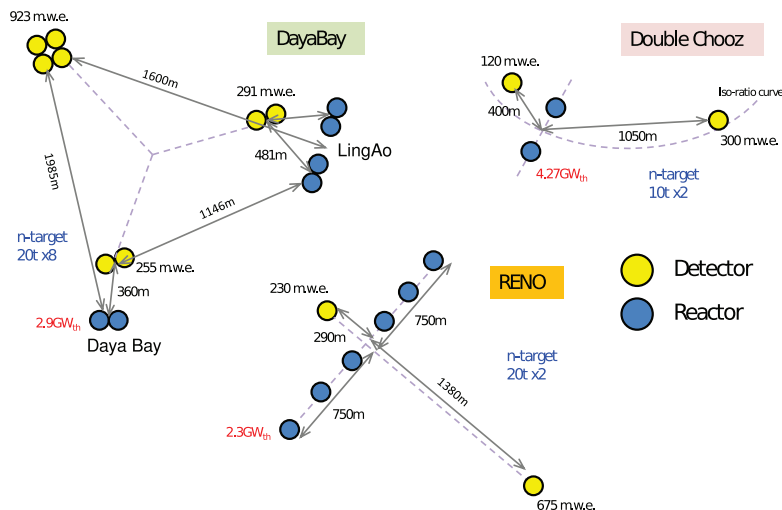


**Figure 2.8:** Experimental layout of the three running reactor experiments. The figure was taken from [126].

The former experiments CHOOZ [44] and PALO VERDE [73] had found no evidence for  $\bar{\nu}_e$  disappearance at 90% C.L.. Presently, three reactor experiments have measured the mixing angle  $\theta_{13}$ : DOUBLE CHOOZ, RENO and DAYA BAY. The detection of the reactor  $\bar{\nu}_e$  is performed via the inverse beta decay reaction. All experiments use a similar detector layout consisting of cylindrical detectors filled with gadolinium-doped liquid scintillator. However, the number of used detectors and reactor cores are different. DOUBLE CHOOZ uses a simple layout consisting of two reactor cores and two detectors while RENO uses four  $2.8 \text{ GW}_{th}$  and two  $2.66 \text{ GW}_{th}$  reactors and two detectors. The DAYA BAY experiment was designed to measure even a nearly vanishing mixing angle and uses accordingly six  $2.9 \text{ GW}_{th}$  reactors and six detectors grouped in two near halls and one far hall [191] (see also Figure 2.8). Unlike DOUBLE CHOOZ and RENO, the DAYA BAY detectors are located within a water tank to shield the detectors against radiation.

To determine the mixing angle  $\sin^2 2\theta_{13}$  DAYA BAY compares the reconstructed positron energy observed in the far site with the expectation derived from the measurement in the near halls [41]. The most recent result for the allowed regions in the  $(\Delta m_{ee}^2, \sin 2\theta_{13})$  plane are shown in Figure 2.9 [41]. The best fit corresponds to  $|\Delta m_{ee}^2| = (2.42 \pm 0.11) \times 10^{-3} \text{ eV}^2$  and  $\sin^2 2\theta_{13} = 0.084 \pm 0.005$  [41].

#### 2.4.5.2 Double Chooz and $\theta_{13}$

The analyses of all three reactor experiments are similar. To provide a further insight into the most important aspects, the analyses chain of the DOUBLE CHOOZ (DC) experiment is shortly summarized. Work done by the author in context of this experiment is incorporated as well. A more detailed account can be found in appendix C. The structure and argumentation line of this section follows Ref. [126] and [12].

**Data Analysis** The DC data analysis is based on a detailed reactor flux prediction as outlined in section C.1 as well as on a precise background evaluation. To minimize the background level, a  $\bar{\nu}_e$  candidate selection based on the coincidence nature of the inverse beta decay (IBD) reaction was performed. The signal consists of the positron annihilation

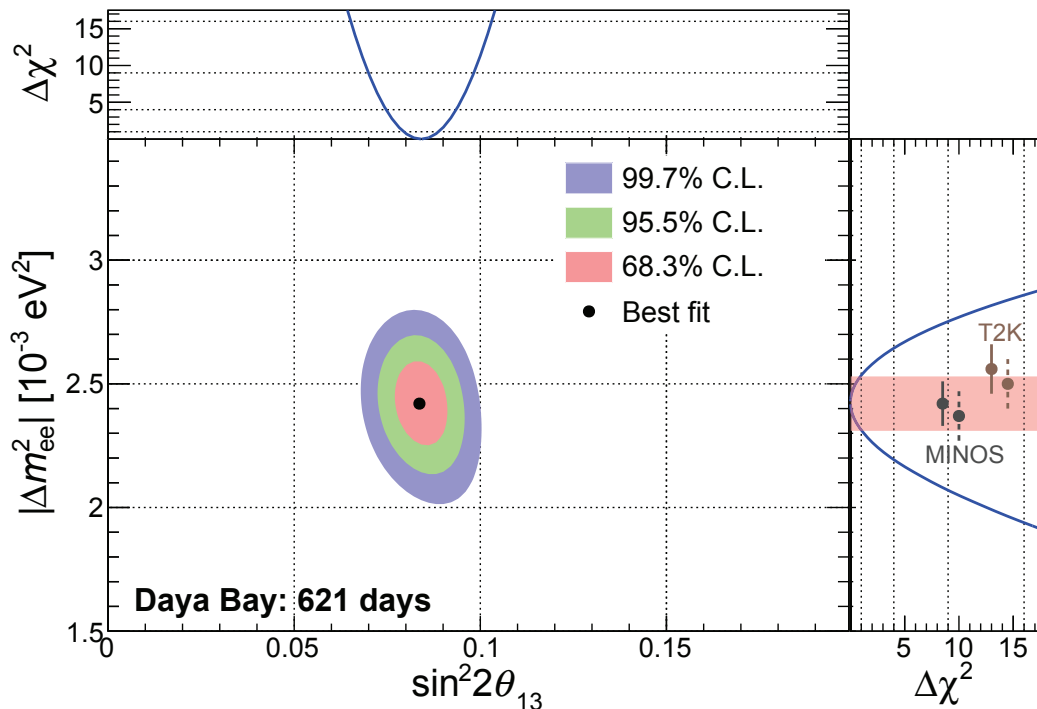


**Figure 2.9:** Allowed regions for  $\sin^2 2\theta_{13}$  and the effective squared mass difference  $|\Delta m_{ee}^2|$ . The measurement  $|\Delta m_{ee}^2|$  was consistent with measurement of  $\Delta m_{32}^2$  from the Minos and T2K experiments, converted to  $|\Delta m_{ee}^2|$  assuming the normal (solid) and inverted (dashed) mass ordering. Plot taken from Ref. [41].

(prompt signal) and the neutron capture (delayed signal). Depending on the detection channel, the neutron is either registered to have been captured on gadolinium releasing a 8 MeV de-excitation energy peak or on hydrogen. The latter reaction releases a visible energy of about 2.2 MeV. The exact selection cuts for the different analysis phases have been reported in Ref. [11, 12, 16] for the Gd-channel analysis and in Ref. [14, 18] for the hydrogen-channel analysis.

**Background** Two major categories of background have been identified: accidental and correlated background. These two categories are discussed in the following.

**Accidental Background** The  $\bar{\nu}_e$  selection was optimized to select the two correlated events of the IBD reaction. However, it may happen that two uncorrelated events are passing the selection cuts accidentally. The time distribution of these events is expected to be flat in contrast to the neutron capture time profile of the IBD reaction. Most of the so-called *accidentals* are products of  $\gamma$ -quanta from radioactive decays and have energies below 3 MeV. The only noteworthy decays which contribute at higher energies are  $\beta$  decays from  $^{214}\text{Bi}$  (Q-value of 3.27 MeV) and  $^{208}\text{Tl}$  (Q-value of 5.0 MeV) [126]. Due to the large contribution of accidentals at low energies, the use of gadolinium is particularly advantageous as the delayed energy window around 8 MeV strongly reduces this kind of background. In addition, the neutron capture time is lowered to  $\sim 30 \mu\text{s}$  compared to  $\sim 300 \mu\text{s}$  for the hydrogen-channel analysis.

**Correlated Background** One major source of background is the correlated background. Within this class, two separated events from a common physical process are expected. Unlike

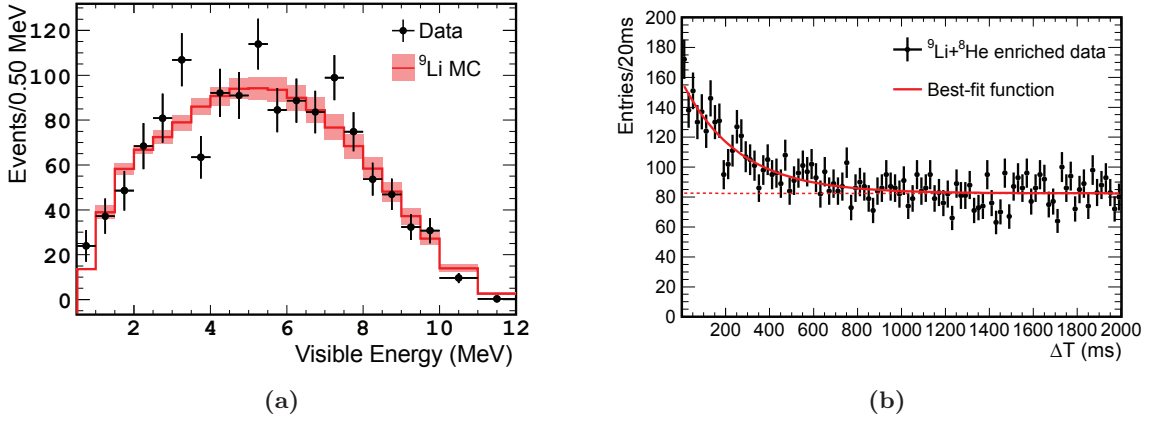


**Figure 2.10:**  ${}^9\text{Li}+{}^8\text{He}$  energy spectrum and muon time correlation. Figures taken from [16].

reactor  $\bar{\nu}_e$  their time and space correlation might be different. However, several events might pass the  $\bar{\nu}_e$  selection criteria. Most of the correlated background is muon-induced [126]. Three relevant classes of background have been identified with respect to the  $\theta_{13}$  analysis [126, 11, 12, 16, 14, 18]:

- $\beta - n$  decays of  ${}^9\text{Li}$  and  ${}^8\text{He}$
- Fast neutrons
- Stopping muons decay

${}^9\text{Li}$  and  ${}^8\text{He}$  belong to the class of muon-induced background and are produced by muon spallation on  ${}^{12}\text{C}$  which is naturally present in any organic liquid scintillator. The  $\beta$  decay of  ${}^9\text{Li}$  is accompanied by the emission of two  $\alpha$  particles and a neutron in 50.8% of the cases [126]. The  $\beta - n$  of  ${}^8\text{He}$  is accompanied by a neutron (BR: 16%) or a neutron, an  $\alpha$  particle and a triton [126]. The life-times of these isotopes are  $\tau = 257$  ms for  ${}^9\text{Li}$  and  $\tau = 172$  ms for  ${}^8\text{He}$ , respectively. These numbers are too long to remove this background on any event-by-event basis as the loss of live-time would be too large. The  ${}^9\text{Li}/{}^8\text{He}$  content can be extracted by fitting the time correlation between identified muons ( $E_{vis} > 600$  MeV) and IBD candidates:

$$f(\Delta t_{\mu-IBD}) = \frac{A}{\tau_{Li}} e^{-\Delta t_{\mu-IBD}/\tau_{Li}} + B. \quad (2.44)$$

The time difference between the parent muon and the IBD candidate is denoted as  $\Delta t_{\mu-IBD}$ . The  ${}^8\text{He}$  content was neglected during the first analysis [11]. For the following analyses a  ${}^9\text{Li}+{}^8\text{He}$  likelihood was developed. Figure 2.10a shows the  ${}^9\text{Li}+{}^8\text{He}$  spectrum selected by this method. More details can be found in Ref. [12, 16].

Fast neutrons are the second most important correlated background. They are produced by cosmic muon spallation in the surrounding rock of the DC detector. The prompt signal can be mimicked by proton recoils in the liquid scintillator while the delayed signal is mimicked by the capture of the thermalized neutron (see Figure 2.11).

Fast neutrons can be identified if they deposit energy in the inner veto (IV<sup>14</sup>). Their contribution to the prompt energy spectrum is assumed to be flat. For a selection and study of this background a  $\bar{\nu}_e$  selection was developed (see also section 7.3.1).

<sup>14</sup>More details about the detector can be found in appendix C

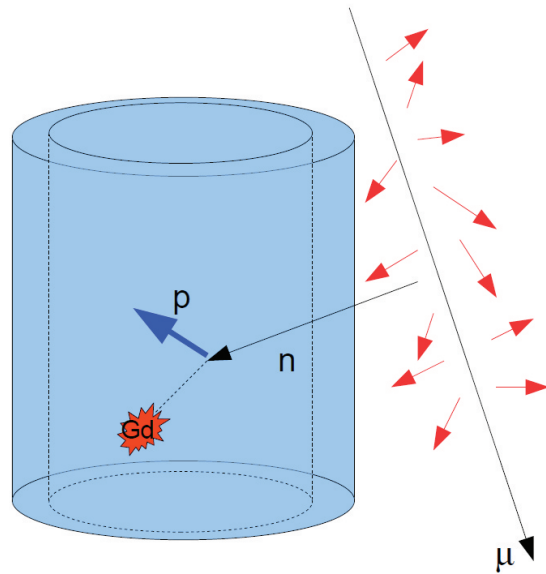


**Figure 2.11:** Fast neutron background in the DOUBLE CHOOZ detector. Fast neutrons are produced by cosmic muon spallation in the surrounding rock of the DC detector. The prompt signal can be mimicked by proton recoils while the delayed signal is mimicked by the capture of the thermalized neutron.

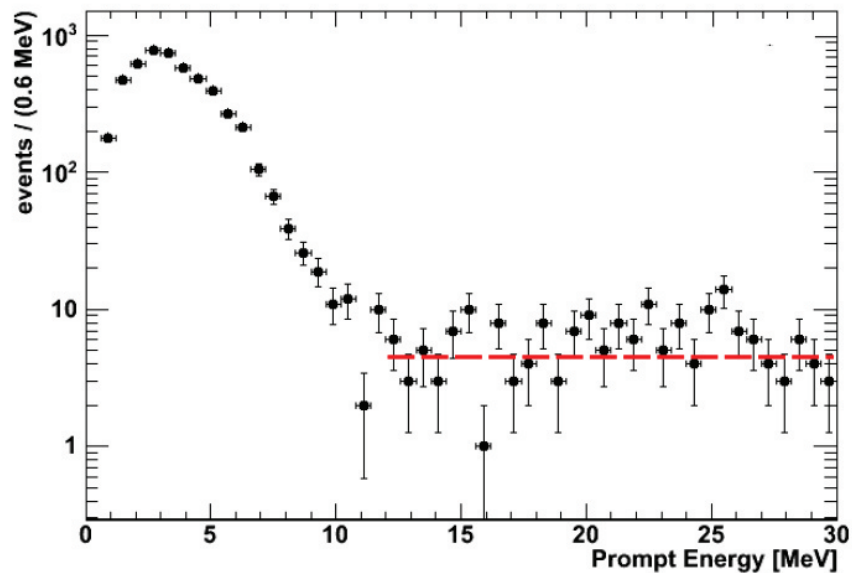


**Figure 2.12:** Fast Neutron content. In order to evaluate the fast neutron background the prompt energy window was opened to 30 MeV and extrapolated to lower energies.

To estimate the fast-n content, the prompt energy window was opened to 30 MeV (see Figure 2.12). Since the amount of accidentals can safely be ignored above 12 MeV, it was possible to evaluate the pure fast-n content. Using the first data set of IBD candidates, the background was extrapolated to the energy region of interest and determined to  $R_{\mu n} = (0.93 \pm 0.36(\text{stat.})) \text{ d}^{-1}$ . The current, official analysis, uses slightly different cuts (details can be found in Ref. [16]) and the background is estimated to  $R_{\mu n} = 0.604 \pm 0.501$  [16]<sup>15</sup>.

Stopping muons can mimic the IBD reaction by decaying within the DC detector. The prompt signal is originating from the energy deposition of the muons while the delayed signal is induced by the electron or positron following the decay of the muon:

$$\mu^- \rightarrow e^- + \bar{\nu}_e + \nu_\mu \quad (2.45)$$

$$\mu^+ \rightarrow e^+ + \nu_e + \bar{\nu}_\mu \quad (2.46)$$

The decay has a well known time correlation of  $\tau = 2.197 \mu\text{s}$ . During the first phase of the

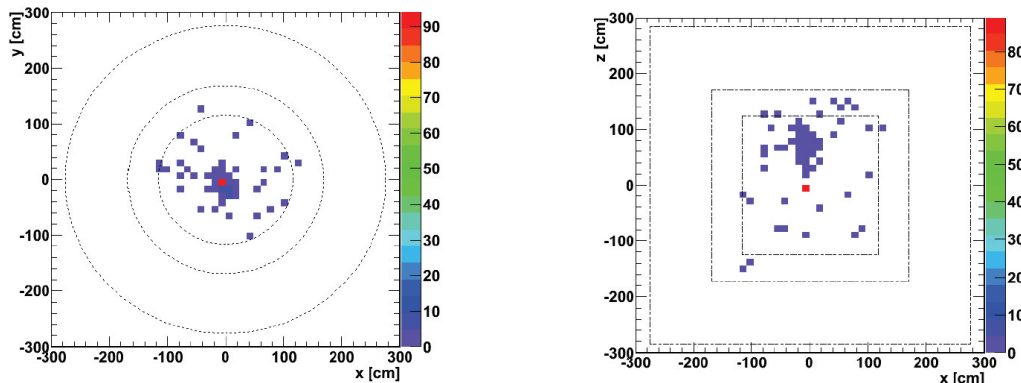


**Figure 2.13:** Stopping Muons entering the DOUBLE CHOOZ detector through the chimney.

DC data analysis, the amount of stopping muons was rather unexpected. The DC detector is equipped with plastic scintillators, the so-called outer veto (OV), to identify muons. At the beginning a small area was unequipped. The so-called chimney is located at the top-center of the detector to allow the insertion of calibration sources inside the detector. Before the additional top-OV was installed, muons were able to pass inside and produced a non-negligible amount of background (see Figure 2.13).

**Oscillation Analysis** To extract the neutrino oscillation parameter  $\theta_{13}$  the predicted number of IBD candidates was compared with the actual measurement. The data deficit is accordingly directly linked to the neutrino oscillation parameter  $\theta_{13}$  assuming the two flavor approximation framework and a squared mass difference of  $\Delta m_{31}^2 = 2.44_{-0.1}^{+0.009} \times 10^{-3} \text{ eV}^2$ . DC has used three different data analysis techniques: *Rate+Shape*, *rate only* and the *Reactor Rate Modulation* (RRM) (see appendix C for more details). In total, three analyses using the Gd-channel have been used to determine  $\theta_{13}$ . These analyses are complemented by two

<sup>15</sup>For the first data set, the official fast neutron and stopping muon rate was determined to  $R_{\mu n} = 0.82 \pm 0.38$  [11].

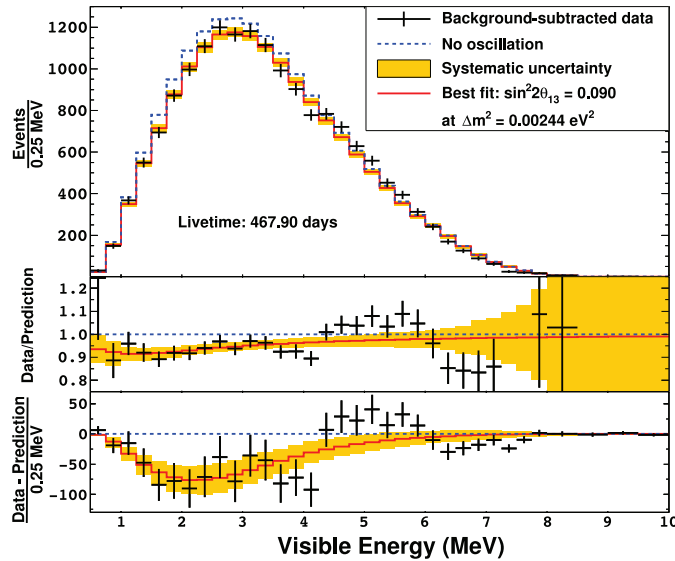


**Figure 2.14:** Rate+Shape analysis to extract the mixing angle  $\theta_{13}$ . The Figure was reproduced in Ref. [126].

Background rate ( $\text{d}^{-1}$ )	Gd-I	Gd-II	H-II	Gd-III
${}^9\text{Li}+{}^8\text{He}$	$2.3 \pm 1.2$	$1.25 \pm 0.54$	$2.8 \pm 1.2$	$0.97^{+0.41}_{-0.16}$
Fast-n, Stopping- $\mu$	$0.82 \pm 0.38$	$0.67 \pm 0.20$	$2.50 \pm 0.47$	$0.604 \pm 0.501$
Accidental	$0.33 \pm 0.03$	$0.261 \pm 0.002$	$73.45 \pm 0.16$	$0.070 \pm 0.003$
${}^{13}\text{C}(\alpha, n){}^{16}\text{O}$	-	-	-	$< 0.1$
${}^{12}\text{B}$	-	-	-	$< 0.03$
Correlated light noise	-	-	$0.32 \pm 0.07$	-

**Table 2.2:** Background contributions for different analysis stages of the DOUBLE CHOOZ detector. Taken from [126].

hydrogen-channel analyses. The first publication using the near detector is expected to be published within this year (2016). Depending on the IBD selection channel and procedure, different amounts of background events are expected. Table 2.2 summarizes the expected background level for the different analyses.

The most precise value for the mixing angle  $\theta_{13}$  is based on a rate+shape analysis and is given by  $\sin^2 2\theta_{13} = 0.090$  [16] (see Figure 2.14). An increase in the sensitivity is expected in the years following 2016 when both detectors are fully operational.



Several observed anomalies in the neutrino sector might be explained by the existence of one or more sterile neutrinos. The most prominent hints for sterile neutrinos have been obtained by accelerator experiments (LSND [27] and MINIBOONE [141]), radioactive source experiments (GALLEX [43, 124] and SAGE [7, 8, 9]) and by reactor experiments at short baselines (*reactor anomaly* [155]). These experiments are discussed in greater detail in section 3.4. Cosmological data had also first favored the existence of a fourth sterile neutrino while current results are fully consistent with the three observed active neutrinos [20]. From the experimental point of view, each of the anomalies might have its own, individual explanation. Most of the anomalies are based on a deficit in their count rate. The characteristic oscillation pattern induced by possible sterile neutrinos remains unobserved [6].

From the theoretical point of view “the existence of sterile neutrinos is a rather natural consequence of neutrinos having non-zero mass” [6]. Despite the question whether light sterile neutrinos exist or not, the fundamental consequences are too large to be ignored. Every anomaly taken for itself might be regarded as not significant, but at least they point to the same direction. A global analysis confirms the anomaly at  $3\sigma$  [116]. At the same time, a number of experiments are in conflict with this interpretation. Among other proposed experiments, the SOX project will address this question trying to solve this long-standing debate.

### 3.1 Number of Active Neutrinos

The number of light active neutrinos ( $m_\nu < m_{Z^0}/2$ ) was determined by several LEP<sup>1</sup> experiments with great precision during the nineties of the last century. ALEPH<sup>2</sup>, DELPHI<sup>3</sup>, L3 and OPAL<sup>4</sup> have measured the hadron production cross-section around the  $Z^0$  resonance. The gauge boson  $Z^0$  decays into fermion-anti-fermion pairs with the partial decay width  $\Gamma_f$ :

$$\Gamma_{Z^0} = \sum_f \Gamma_f \quad (3.1)$$

The sum incorporates all possible final states like the decay into hadrons, charged leptons and neutrinos. Considering universality of the weak interaction ( $\Gamma_e = \Gamma_\mu = \Gamma_\tau$  and  $\Gamma_{\nu_e} =$

<sup>1</sup>LEP: Large Electron–Positron Collider

<sup>2</sup>ALEPH: Apparatus for LEP Physics

<sup>3</sup>DELPHI: Detector with Lepton, Photon and Hadron Identification

<sup>4</sup>OPAL: Omni Purpose Apparatus at LEP

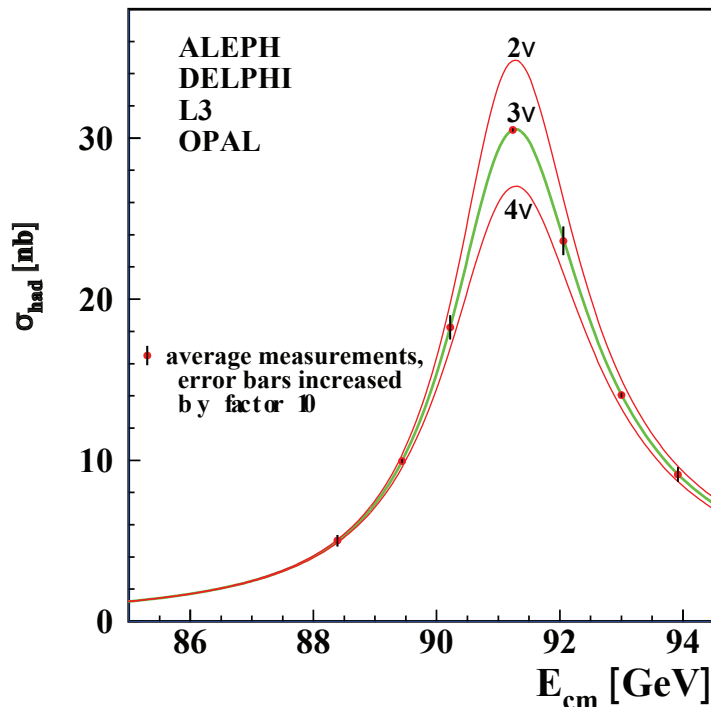


**Figure 3.1:**  $Z^0$  resonance. The different lines correspond to the theoretical expectation for two, three and four neutrinos, respectively. Figure taken from [174]

$\Gamma_{\nu_\mu} = \Gamma_{\nu_\tau}$ ), the invisible decay width<sup>5</sup> is given by [176]

$$\Gamma_{inv} = \Gamma_Z - \Gamma_h - 3\Gamma_l \quad (3.2)$$

The invisible decay width  $\Gamma_{inv}$  is the product of the neutrino decay width  $\Gamma_\nu$  and the number of active neutrinos.

$\Gamma_Z$ ,  $\Gamma_h$  and  $\Gamma_l$  are directly accessible via measurements while  $\Gamma_\nu$  can be calculated within the SM framework (details can be found in several textbooks like Ref. [176] and [212]).

The results of all experiments agree with great precision and the combined analysis provides a number highly compatible with three [176]:

$$N_\nu = 2.991 \pm 0.016 \quad (3.3)$$

Figure 3.1 shows the result of this fit. As a comparison the theoretically expected curves for two and four neutrino families have been added.

### 3.2 Introduction to Sterile Neutrinos

A sterile neutrino is a hypothetical lepton which does not interact via any known forces of the SM, except gravitation. The terminus *sterile* refers to that property. In principle, sterile neutrinos can have any mass. Within this thesis, we focus on relatively light sterile neutrinos that mix significantly with the three active neutrinos [6].

Sterile neutrinos are represented as a  $SU(2)$  singlet (or right-handed) with respect to the strong and weak interaction. Such particles are defined by having no electric charge, hypercharge and weak isospin (which prohibits as a consequence any coupling on the  $Z^0$  boson).

<sup>5</sup>Invisible decay width refers to the fact that the neutrinos can not directly be observed, only their contribution to the  $Z^0$  decay width.

However, they may participate in Yukawa interactions involving the Higgs boson and the well-known leptons which allows mixing with the three standard neutrinos via the Higgs mechanism.

### 3.3 Sterile Neutrino Mixing Formalism

The neutrino oscillation framework was already presented in section 2.3.1. In case of additional sterile neutrinos, the matrix  $U$  has to be expanded along with the introduction of further squared mass differences (see Figure 3.2). Since the SOX experiment will perform a disappearance experiment, special attention is paid to the  $\bar{\nu}_e$  disappearance mode. For the mathematical derivation it is assumed that the sterile neutrino is much heavier than the other massive states ( $|\Delta m_{41}| \gg |\Delta m_{31}^2| \gg |\Delta m_{21}^2| > 0$ ). For the following derivation, one additional sterile neutrino is assumed. According to Eq. (2.4), the flavor eigenstates  $|\nu_\alpha\rangle$  ( $\alpha = e, \mu, \tau, s$ ) are related to the mass eigenstates by a  $4 \times 4$  mixing matrix  $U$ , which is parametrized by the matrix product as defined in Eq. (2.5):

$$U = R_{34}(\theta_{34}, 0) R_{24}(\theta_{24}, 0) R_{14}(\theta_{14}, 0) R_{23}(\theta_{23}, \delta_3) R_{13}(\theta_{13}, \delta_2) R_{12}(\theta_{12}, \delta_1), \quad (3.4)$$

where  $R_{ab}(\theta_{ab}, \delta_h)$  is defined as in Eq. (2.6). The mixing matrix elements are therefore given by

$$\begin{aligned} U_{e1} &= c_{12}s_{13}c_{14} \\ U_{e2} &= c_{13}c_{14}s_{12}e^{-i\delta_1} \\ U_{e3} &= c_{14}s_{13}e^{-i\delta_2} \\ U_{e4} &= s_{14} \\ U_{\mu 1} &= -c_{23}c_{24}s_{12}e^{i\delta_1} - c_{12} \left[ c_{24}s_{23}s_{13}e^{i(\delta_2-\delta_3)} + c_{13}s_{14}s_{24} \right] \\ U_{\mu 2} &= c_{12}c_{23}c_{24} - s_{12}e^{-\delta_1} \left[ c_{24}s_{23}s_{13}e^{i(\delta_2-\delta_3)} + c_{13}s_{14}s_{24} \right] \\ U_{\mu 3} &= c_{13}c_{24}s_{23}e^{-i\delta_3} - s_{13}s_{24}s_{14}e^{-i\delta_2} \\ U_{\mu 4} &= c_{14}s_{24} \\ U_{\tau 1} &= s_{12}e^{i\delta_1} \left[ c_{34}s_{23}e^{i\delta_3} + c_{23}s_{24}s_{34} \right] - c_{12} \\ &\quad \times \left[ -c_{13}c_{24}s_{13}s_{34} + s_{13}e^{i\delta_2} \left( c_{23}c_{34} - s_{23}s_{24}s_{34}e^{-i\delta_3} \right) \right] \\ U_{\tau 2} &= -c_{12} \left[ -c_{34}s_{23}e^{-i\delta_3} + c_{23}s_{24}s_{34} \right] - s_{12}e^{-i\delta_1} \\ &\quad \times \left[ c_{13}c_{24}s_{14}s_{34} + s_{13}e^{i\delta_2} \left( c_{23}c_{34} - s_{23}s_{24}s_{34}e^{-i\delta_3} \right) \right] \\ U_{\tau 3} &= -c_{24}s_{13}s_{14}s_{34}e^{-i\delta_2} + c_{13} \left[ c_{23}c_{34} - s_{23}s_{24}s_{34}e^{-i\delta_3} \right] \\ U_{\tau 4} &= c_{14}c_{24}s_{34} \\ U_{s1} &= s_{12}e^{i\delta_1} \left[ c_{23}c_{34}s_{24} - s_{23}s_{34}e^{i\delta_3} \right] - c_{12} \\ &\quad \times \left[ c_{13}c_{24}c_{34}s_{14} - s_{13}e^{i\delta_2} \left( c_{23}s_{34} + c_{34}s_{23}s_{24}e^{-i\delta_3} \right) \right] \\ U_{s2} &= -c_{12} \left[ c_{23}c_{34}s_{24} + s_{23}s_{34}e^{i\delta_3} \right] - s_{12}e^{-i\delta_1} \\ &\quad \times \left[ c_{13}c_{24}c_{24}s_{14} - s_{13}e^{i\delta_2} \left( c_{23}s_{34} + c_{34}s_{23}s_{24}e^{-i\delta_3} \right) \right] \\ U_{s3} &= -c_{24}c_{34}s_{13}s_{14}^{-i\delta_2} - c_{13} \left[ c_{23}s_{34} - c_{34}s_{23}s_{24}e^{-i\delta_3} \right] \\ U_{s4} &= c_{14}c_{24}c_{34} \end{aligned}$$

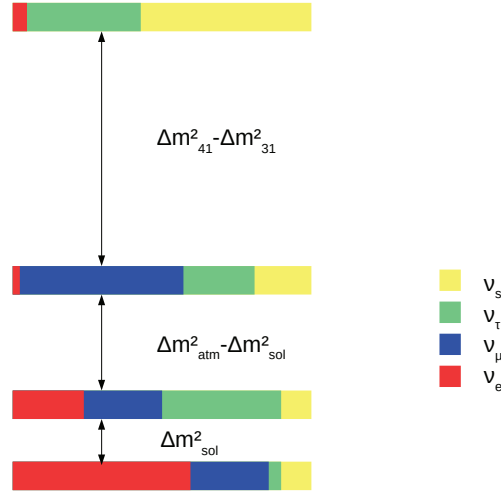


**Figure 3.2:** Conceptual drawing for the four neutrino mass spectra for the normal ordering and one additional sterile neutrino.

(3.5)

The oscillation disappearance probability for the 3+1 model is derived by using Eq. (2.19). In disappearance mode all imaginary parts vanish<sup>6</sup>:

$$\begin{aligned}
 P(\bar{\nu}_e \rightarrow \bar{\nu}_e) &= 1 - 4 \left[ (c_{12}c_{13}c_{14}c_{13})^2 \cdot \sin^2(\Delta_{12}^2) + (c_{12}c_{13}c_{14}c_{14}s_{13})^2 \cdot \sin^2(\Delta_{13}^2) \right. \\
 &\quad + (c_{12}c_{13}c_{14}s_{14}) \cdot \sin^2(\Delta_{14}^2) + (c_{12}c_{14}s_{12}c_{14}s_{13})^2 \cdot \sin^2(\Delta_{23}^2) \\
 &\quad \left. + (c_{13}c_{14}s_{12}s_{14})^2 \cdot \sin^2(\Delta_{24}^2) + (c_{14}s_{13}s_{14})^2 \cdot \sin^2(\Delta_{34}^2) \right] \quad (3.6)
 \end{aligned}$$

Since  $|\Delta m_{i4}^2|$  ( $i = 1, 2, 3$ )  $\gg |\Delta m_{12}^2|$ ,  $|\Delta m_{13}^2|$ ,  $|\Delta m_{23}^2|$  and  $\Delta m_{14}^2 \approx \Delta m_{24}^2$ ,  $\Delta m_{34}^2$  Eq. (3.6) becomes:

$$\begin{aligned}
 P(\bar{\nu}_e \rightarrow \bar{\nu}_e) &\approx 1 - 4 \left[ (c_{12}c_{13}c_{14}s_{14})^2 + (c_{13}c_{14}s_{12}s_{14})^2 + (c_{14}s_{13}s_{14})^2 \right] \cdot \sin^2(\Delta_{14}^2) \\
 &= 4c_{14}^2s_{14}^2 [c_{13}^2(c_{12}^2 + s_{12}^2) + s_{13}^2] \cdot \sin^2(\Delta_{14}^2) \\
 &= 1 - \sin^2(2\theta_{14}) \cdot \sin^2(\Delta_{14}^2), \quad (3.7)
 \end{aligned}$$

which is equal to the simplified two-flavor oscillation approximation. In the short-baseline case, matter effects can safely be ignored.

### 3.4 Anomalies in the Neutrino Sector and Hints for Sterile Neutrinos

Most neutrino oscillation data can be well explained within the framework of three active neutrinos. However, several neutrino experiments have reported anomalies which are inconsistent with the standard scenario. These anomalies have particularly been observed at short

<sup>6</sup>We will use the following abbreviated form  $\Delta_{ij}^2 \equiv \Delta m_{ij}^2 \frac{L}{4E}$

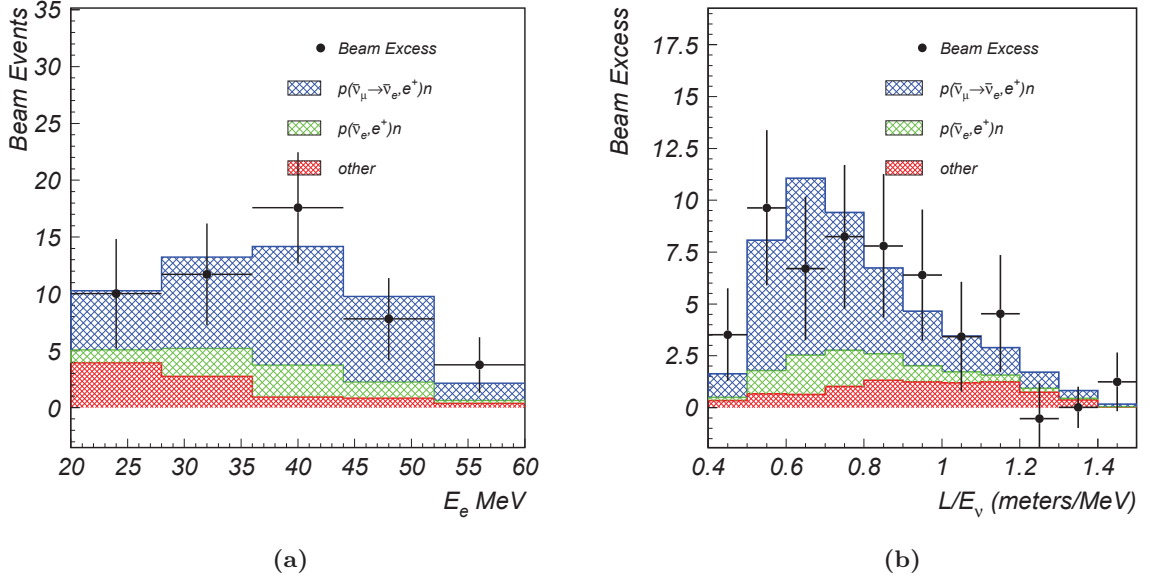


**Figure 3.3:** LSND  $\bar{\nu}_e$  event excess. The left panel (a) shows the observed data and the expected background.  $E_e$  is the energy of the positron. The right panel shows the corresponding  $L/E_\nu$  dependence, where  $L$  is the reconstructed baseline and  $E_\nu$  the reconstructed antineutrino energy. The small event excess visible in (b) can be attributed to sterile neutrino oscillations with  $\Delta m_{41}^2 \sim 1 \text{ eV}^2$  and  $\sin^2 2\theta_{\mu e} \sim 0.003$  [141]. Plots taken from [27].

baselines. The existence of sterile neutrinos with a relatively large squared mass difference in the order of  $1 \text{ eV}^2$  might explain these observations. Global analyses have confirmed the anomaly at  $3\sigma$  [116], although other experiments have found no such evidence. The following sections will review (see also [6]) the most prominent experimental hints for sterile neutrinos including critical remarks on the analysis and claimed sensitivity.

### 3.4.1 LSND Anomaly

The LSND<sup>7</sup> experiment was one of the first experiments which reported inconsistencies with the three active neutrino scenario. The experiment was designed to search for  $\bar{\nu}_\mu \rightarrow \bar{\nu}_e$  oscillations using a high intense 800 MeV proton beam, an absorber and a cylindrical 167 t liquid scintillator tank [50]. Within the absorber, a large number of pions were produced. While  $\pi^-$  were mainly absorbed, most of the neutrinos were produced from  $\pi^+ \rightarrow \mu^+ \nu_\mu$  and  $\mu^+ \rightarrow e^+ \bar{\nu}_\mu \nu_e$  decays [50]. The detector was equipped with 1220 8-inch Hamamatsu PMTs allowing the detection of events via their scintillation as well as Cherenkov light [50]. The main detection channel applied for the analysis was the inverse beta decay (IBD) reaction which allowed to suppress the background. For the primary  $\bar{\nu}_\mu \rightarrow \bar{\nu}_e$  oscillation search, an event excess was observed (see Figure 3.3). Based on the results of a  $(\sin^2 2\theta, \Delta m_{41}^2)$  likelihood analysis an allowed region from  $\Delta m_{41}^2 \simeq 0.2 - 2.0 \text{ eV}^2$  complemented with allowed regions around  $\Delta m_{41}^2 \simeq 7 \text{ eV}^2$  was found (see Figure 3.4) [27]. As it can be seen from Figure 3.4, the allowed region for  $\sin^2 2\theta_{14}$  spans a wide region depending on the associated squared mass difference. [6]

<sup>7</sup>LSND: Liquid Scintillator Neutrino Detector

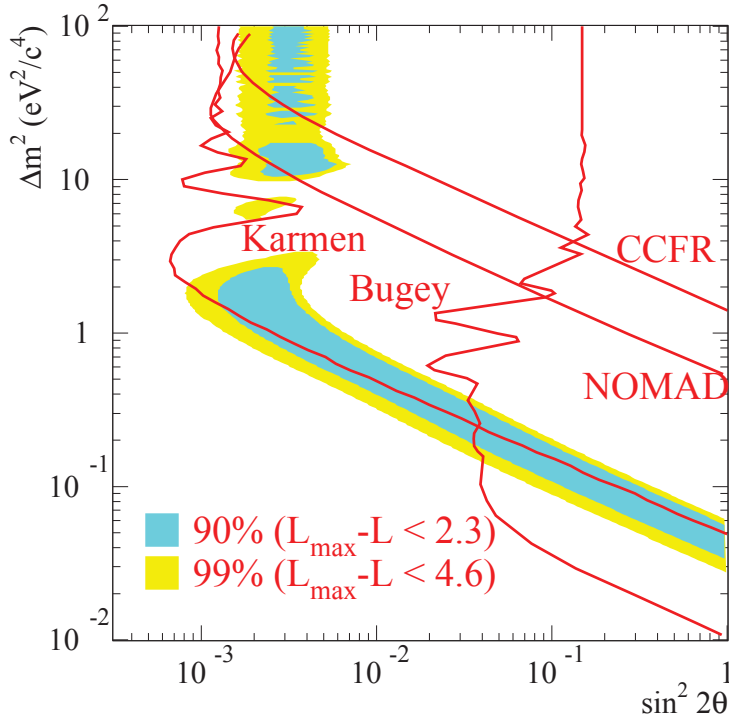


**Figure 3.4:** Allowed regions for sterile neutrino parameters obtained from the LSND experiment. In addition, exclusion limits from other accelerator and reactor experiments are shown. Taken from [27].

### 3.4.2 Constraints from KARMEN and MiniBooNE

The KARMEN<sup>8</sup> experiment used a similar approach. Protons were accelerated to 800 MeV and interacted within a Ti-D<sub>2</sub>O target producing  $(0.0448 \pm 0.0030) \pi^-$  per incident proton [6, 78]. A liquid scintillator calorimeter was used which had a total mass of 56 t. The baseline was almost half as long as the baseline of LSND (17.7 m instead of 30 m) covering slightly different  $\Delta m^2$  values. Event selection was performed in the same way as in LSND. In contrast to LSND, KARMEN did not find any significant event excess. The observed events are fully compatible with the estimated background of  $15.8 \pm 0.5$  events. KARMEN was able to rule out the parameter space with  $\Delta m_{41}^2 > 10 \text{ eV}^2$  (see also Figure 3.4). However, regions with  $\Delta m_{41}^2 < 1 \text{ eV}^2$  and around  $7 \text{ eV}^2$  are still consistent with LSND using a combined analysis. [6]

MINIBOONE is a follow-up experiment of LSND and KARMEN. One of the scientific objectives is to address the neutrino anomaly as observed by LSND [6]. The MINIBOONE experiment is located at Fermilab and uses a 8 GeV proton accelerator pointing at a magnetic horn coupled with a 71 cm Be target [28]. The produced kaons and pions decay in a 50 m long pipe. The spherical liquid scintillator detector is located 541 m downstream of the target. MINIBOONE has performed dedicated neutrino oscillation studies searching for  $\nu_e$  and  $\bar{\nu}_e$  appearance [28]. The results reported for the  $\nu_e$  analysis showed an excess at low reconstructed neutrino energies ( $E_\nu^{QE} < 475 \text{ MeV}$ ) which is comparable to the LSND excess, although the shape needs more complicated oscillation models with CP violation to be consistent with the LSND data [6]. A similar analysis was performed using the  $\bar{\nu}_e$  appearance

<sup>8</sup>KARMEN: KARlsruhe Rutherford Medium Energy Neutrino experiment

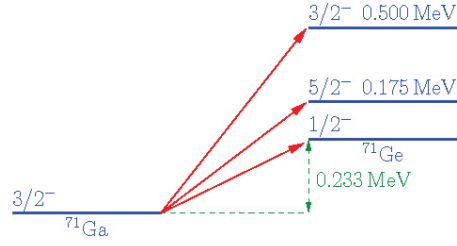


**Figure 3.5:** Nuclear levels for the Gallium Detection. Description and figure taken from [6].

mode. The results obtained from this study are consistent with the LSND anomaly. [6]

Further studies were initiated to study  $\nu_\mu$  and  $\bar{\nu}_\mu$  disappearance at MINIBOONE as well as SciBOONE, both operating in the same beamline. However, the current data points to  $\Delta m_{41}^2 = 17.5 \text{ eV}^2$  which is incompatible to the appearance results. [6]

### 3.4.3 The Gallium Anomaly

Mainly in the 1990s, two solar neutrino experiments performed calibration campaigns with radioactive sources to test their detection efficiencies.<sup>9</sup> GALLEX performed two calibration campaigns using  $^{51}\text{Cr}$  as an intense EC neutrino source [43, 124]. The Russian-American experiment SAGE conducted their two calibration phases using both  $^{51}\text{Cr}$  and  $^{37}\text{Ar}$  [7, 8, 9]. The decay of  $^{51}\text{Cr}$  and  $^{37}\text{Ar}$  produces mono-energetic neutrinos via EC:



The SOX experiment will possibly refurbish the old GALLEX source. More details about these sources are given later in chapter 5. The neutrinos produced by these sources were captured by  ${}^{71}\text{Ga}$  which is identical to the solar neutrinos,  $\nu_e + {}^{71}\text{Ga} \rightarrow {}^{71}\text{Ge} + e^-$ . The measured neutrino flux was compared to theoretical calculations. The averaged ratio (measured/predicted) is given by [6]:

$$R_B = 0.86 \pm 0.05 \quad (3.10)$$

The measured events account for a  $2.8\sigma$  effect compared to the theoretical prediction assuming the cross-section as calculated by *Bahcall* [53]. However, the ratio as given in (3.10) does not include any uncertainties on the cross-section [6] which have been reported to be large in Ref. [127, 128]. Only the cross-section from the ground state of  ${}^{71}\text{Ga}$  to the ground state of  ${}^{71}\text{Ge}$  is known precisely as stated in the review on light sterile neutrinos [6]. Reactions involving excited states (Figure 3.5) are associated with big uncertainties. Neglecting all excited transitions yields a ratio of  $R = 0.91 \pm 0.05$  which corresponds to a  $1.7\sigma$  deficit [118]. Other cross-section calculations as performed by *Haxton* [128] are bench-marked to experimental results. The predicted cross-section accounts to  $\sigma_H({}^{51}\text{Cr}) = (63.9 \pm 6.8) \times 10^{-46} \text{ cm}^2$  compared to  $\sigma_B({}^{51}\text{Cr}) = (58.1_{-1.6}^{+2.1}) \times 10^{-46} \text{ cm}^2$  from *Bahcall*. The average ratio is then given by  $R_H = 0.76_{-0.08}^{+0.09}$ . According to Ref. [6] the associated uncertainties are relatively large and yield a similar significance of  $2.7\sigma$ .

Similar to the LSND and MINIBOONE results, the Gallium anomaly might be explained by short baseline oscillations induced by sterile neutrinos. Assuming one additional neutrino, the best fit values for the oscillation parameters are given by

$$\sin^2(2\theta_{14,bf}) = 0.50 \quad (3.11)$$

<sup>9</sup>The  ${}^{37}\text{Ar}$  source experiment was performed in the 2000s.

and

$$\Delta m_{41,bf}^2 = 2.24 \text{ eV}^2. \quad (3.12)$$

The effect of the Gallium anomaly is incorporated in Figure 3.8 of the global analysis. It may be noteworthy that other explanations based on quantum de-coherence in neutrino oscillations are reported in the literature as well [102].

In terms of sterile neutrino models the Gallium anomaly requires oscillations with  $\sin^2 2\theta_{14} \gtrsim 0.07$  and a squared mass difference of  $\Delta m_{41}^2 \geq 0.35 \text{ eV}^2$  at 95% C.L. [6].

### 3.4.4 The Reactor Antineutrino Anomaly

Over the past years, several experiments have measured reactor  $\bar{\nu}_e$ . For many years, the results have been considered to be consistent with the mixing of the three standard neutrinos ( $\nu_e, \nu_\mu, \nu_\tau$ ) separated by the two squared mass differences of  $\Delta m_{31}^2 = 2.4 \times 10^{-3} \text{ eV}^2$  and  $\Delta m_{21}^2 = 8 \times 10^{-5} \text{ eV}^2$  [147].

In 2011, the Saclay reactor group announced their reactor  $\bar{\nu}_e$  flux results obtained in preparation for the DOUBLE CHOOZ experiment. The new calculation predicted a  $\bar{\nu}_e$  flux which is a few percent higher than previous studies [163]. The re-analysis of the observed  $\bar{\nu}_e$  rate compared to the predicted  $\bar{\nu}_e$  rate for 19 published experiments at short distances ( $< 100 \text{ m}$ ) resulted in a deficit of about 6% [155]. A detailed study revealed three major effects which contributed to the observed deficit: change of the neutron life-time, re-evaluation of the  $\bar{\nu}_e$  spectrum including higher-order corrections at the branch level and so-called off equilibrium effects.

### Re-Evaluation of the Neutron Life-Time

Over the past decades the neutron life-time has changed tremendously from  $\tau_n = 885.7 \text{ s}$  in 2004 to  $\tau_n = (880.3 \pm 1.1) \text{ s}$  as given by the current PDG average (2014). The neutron mean life-time is directly linked to the cross-section of the detection reaction of the  $\bar{\nu}_e$  on free protons (IBD) [6]. Within the  $V - A$  theoretical framework the mean cross-section per fission (see also appendix C.1)

$$\sigma_f^{pred} = \int_0^\infty S_{tot} \sigma_{V-A}(E_{\bar{\nu}}) dE \quad (3.13)$$

is depending on the  $\bar{\nu}_e$  spectra  $S_{tot}$  as well as on the IBD cross-section  $\sigma_{V-A}$ . This quantity is inversely proportional to the neutron life-time:

$$\sigma_{V-A}[\text{cm}^2] = \frac{857 \times 10^{-43}}{\tau_n} p_e [\text{MeV}] E_e [\text{MeV}] \times (1 + \delta_{fs} + \delta_{WM} + \delta_{rad}), \quad (3.14)$$

where  $p_e$  represents the momentum and  $E_e$  the kinetic energy of the electron. The last factor incorporates several corrections (more details can be found in section 5.2.2). The current value for the neutron life-time is lower than the previous value and resulted therefore in an increase of the mean cross-section per fission.

### Re-Evaluation of the $\bar{\nu}_e$ Spectra

The fission products of Uranium and Plutonium consist of several hundred nuclei with different end-points [6]. The  $\bar{\nu}_e$  spectrum is the sum of all these  $\beta$  branches including all possible

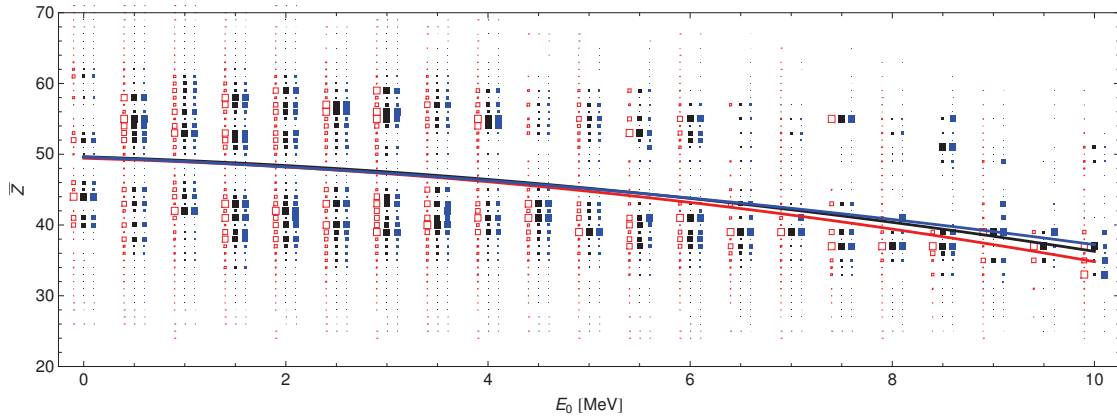


**Figure 3.6:** Effective nuclear charge depending on the end-point energy of the fission fragments of  $^{235}\text{U}$ . For the complete reactor spectrum, which is composed of several hundreds beta branches, virtual branches are assumed. The effective nuclear charge is an important input parameter and derived from data sets (color coded). Figure taken from [132], where more details are reported.

transitions weighted by their fission yield of the parent nucleus [6]. The direct calculation (or *ab-initio* approach) is impossible as too many  $\beta$ -branches are involved and the nuclear data sets are incomplete and may include systematic errors, especially for transitions with large end-points ( $E_0 > 4\text{ MeV}$ ). In the common approach, the  $\bar{\nu}_e$  spectra are converted from the total  $\beta$ -spectrum of each isotope which had been measured in the 1980s at ILL [177, 195, 123] for  $^{235}\text{U}$ ,  $^{239}\text{Pu}$  and  $^{241}\text{Pu}$  and recently in Garching [122]. Since not all single branches are known, the conversion procedure is based on 30 virtual branches fitted on the data [6]. Virtual branches have been described by

$$S_{\text{virtual}}(Z, A, E_e) = K \times F(Z, A, E_e) \times p_e E_e (E_e - E_0)^2 \times (1 + \delta) \quad (3.15)$$

with  $Z$  and  $A$  the charge and atomic number of the parent nucleus.  $E_0$  is the end-point of each branch. For the charge number  $Z$  an effective or mean charge is chosen in connection to the end-point energy,  $Z(E_0) = 49.5 - 0.7E_0 - 0.09E_0^2$ . The last factor  $(1 + \delta)$  accounts for several sub-leading corrections.

In a second approach, only few virtual branches are used in addition to the modeling based on nuclear data. The new antineutrino spectrum modeling lead to an increase of the predicted  $\bar{\nu}_e$  rate of about 3%. Further studies have been presented in Ref. [132] based on the ILL conversion procedure. It was shown that results could be achieved with minimum bias by using only virtual branches with a “judicious choice of the effective nuclear charge” [6]. Figure 3.6 shows the effective nuclear charge depending on the end-point energy  $E_0$ . Both recently published results by *Mueller et al.* [163] and *Huber* [132] are in agreement and predicted an  $\bar{\nu}_e$  deficit of about 3%. In Ref. [132], sub-leading corrections to the  $\bar{\nu}_e$  spectrum modeling have been implemented. The effect is stated to account for a change in the  $\bar{\nu}_e$  rate between 1% and 1.4% depending on the isotope [132, 6].

### Off Equilibrium Effects

The data obtained from the ILL measurement was taken shortly after irradiation (12 hours to 1.8 days). The typical timescale in a reactor experiment is in the order of several month. Since several  $\beta$  decaying isotopes have half-lives of several days, an off equilibrium effect is present. This effect is taken into account by modeling the time evolution using the MURE and FISPAC simulation packages [6]. Unfortunately, the total effect of the so-called off equilibrium effect on the  $\bar{\nu}_e$  rate was not provided in Ref. [163].

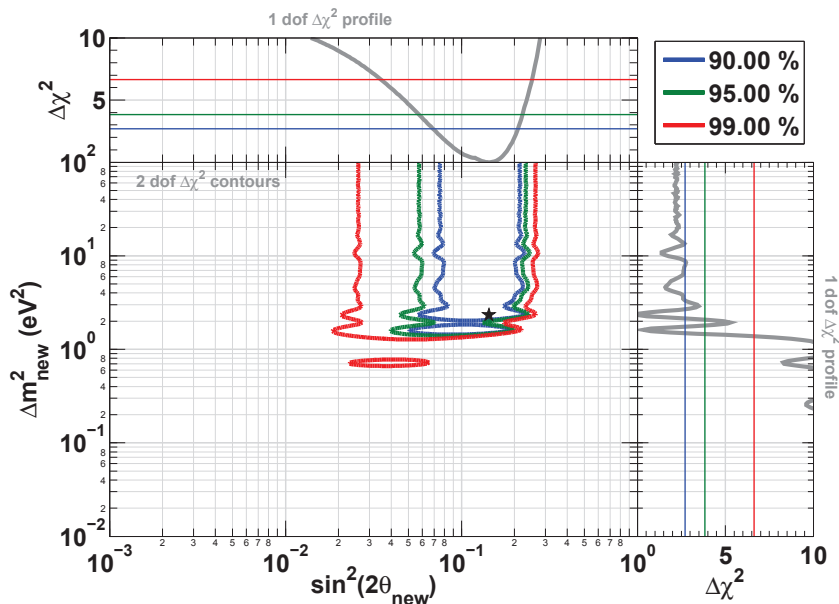


**Figure 3.7:** Allowed contours for the mixing parameters  $\sin^2 \theta_{14}$  and  $\Delta m_{41}^2$  obtained from the analysis of the short-baseline reactor experiments. Figure taken from [155].

### Summary

A re-evaluation of the  $\bar{\nu}_e$  spectra was performed yielding an increase of the expected  $\bar{\nu}_e$  rate for nuclear reactor experiments of about 3%. The shift can be attributed to the precise modeling of sub-leading corrections to Fermi theory which had previously been neglected [6].

### Sterile Neutrinos as an Explanation of the Reactor Anomaly

The  $\bar{\nu}_e$  deficit might be explained by a fourth sterile neutrino with relatively large squared mass difference. For short baselines, the oscillation formula can be approximated within the two flavor neutrino scenario. In Ref. [155] a *rate only* and *rate+shape* analysis was performed. Figure 3.7 shows the fit in the  $(\sin^2 2\theta_{14}, \Delta m_{41}^2)$  plane for the rate+shape analysis. The analysis favors  $\Delta m_{41}^2 > 1 \text{ eV}^2$  at 95% C.L. and a mixing angle of about  $\sin^2 2\theta_{14} \approx 0.15$ . It may be noteworthy that the ILL experiment may have found an indication for a spectral distortion in their measured positron spectrum [6]. The result is consistent with the found fit parameters in other reactor experiments. In contrast to the BUGEY-3 experiment the reactor core at the ILL Grenoble research plant is small preventing any washout of oscillation effects due to geometric effects.

### Critical Discussion of the Reactor Anomaly

Although two independent groups have claimed the observation of a total  $\bar{\nu}_e$  deficit of about 6%, the results have to be critically discussed. The authors have tried to model the  $\bar{\nu}_e$  reactor spectra as accurately as possible by implementing a number of sub-leading corrections including a correction to account for the weak magnetism effect. At least three aspects have to be considered to be problematic:

- Correct modeling of the weak magnetism

- Forbidden shape factors
- Unknown sub-leading corrections

The first two aspects are long known, but were only recently pointed out again by *Hayes et al.* [130]. The weak magnetism (WM) does only occur in transitions with angular momentum change. The WM correction takes the interference of the magnetic moment of the vector current  $\vec{J}_V = \vec{\nabla} \times \vec{\mu}$  with the spin distribution  $\vec{\Sigma}$  of the axial current into account. This has been neglected in the studies of *Mueller et al.* [163] and *Huber* [132]. In Ref. [132] the weak magnetism uncertainty of 100% is assumed without any justification. Experimental results partly differ even from that number.

Forbidden transitions (see also section 5.2.1) introduce so-called shape factors. Of the 6000  $\beta$  transitions about 1500 are classified as forbidden transitions which introduces additional shape factors, including a modified weak magnetism treatment (see Ref. [130] for more details). The effect has been studied for allowed transitions and non-unique first forbidden transitions with different operators depending on the  $\Delta J$  and the parity change of the transition. Based on the assumption of unknown transitions a difference in shape and in magnitude of about 4% was reported.

The uncertainty reported by *Hayes et al.* [130] is therefore in the order of the reactor anomaly. Although some ingredients have to be studied in greater detail (in fact the treatment of the effective charge is based on old assumptions), the  $\sim 3\sigma$  claim of the reactor anomaly group may have to be revised.

### 3.4.5 Global Analysis

The neutrino anomalies which have been observed might be explained by a fourth sterile neutrino. A number of global analyses have been conducted to determine the mixing parameters within different sterile neutrino scenarios (one, two or more sterile neutrinos). 3+2 and other models can be ruled out by cosmology. Results of these studies have been reported in Ref. [116].

Among the neutrino oscillation data, the MiniBooNE data adds some tension into the global analysis. In Ref. [116], two separate analyses have been used. In the so-called total global analysis (“TotGLO”) all available data is incorporated while the pragmatic analysis (“Pr-GLO”) omits the MiniBooNE results. The global fit is shown in Figure 3.8. The best fit results are shown in Table 3.1.

$\frac{\Delta m_{41,bf}^2}{1.6 \text{ eV}^2}$	$\sin^2 2\theta_{e\mu,bf}$	$\sin^2 2\theta_{ee,bf}$	$\sin^2 2\theta_{\mu\mu,bf}$
	0.0014	0.11	0.050

**Table 3.1:** Best fit results of the global analysis [116].

The SOX experiment will mainly address the  $\bar{\nu}_e$  disappearance anomaly.

### 3.4.6 Experimental Perspectives

Within the next years, several experiments will search for light sterile neutrinos. These experiments can be divided into accelerator, reactor,  $\beta$  decay mass measurement and radioactive source experiments. The summary follows explicitly Ref. [117].

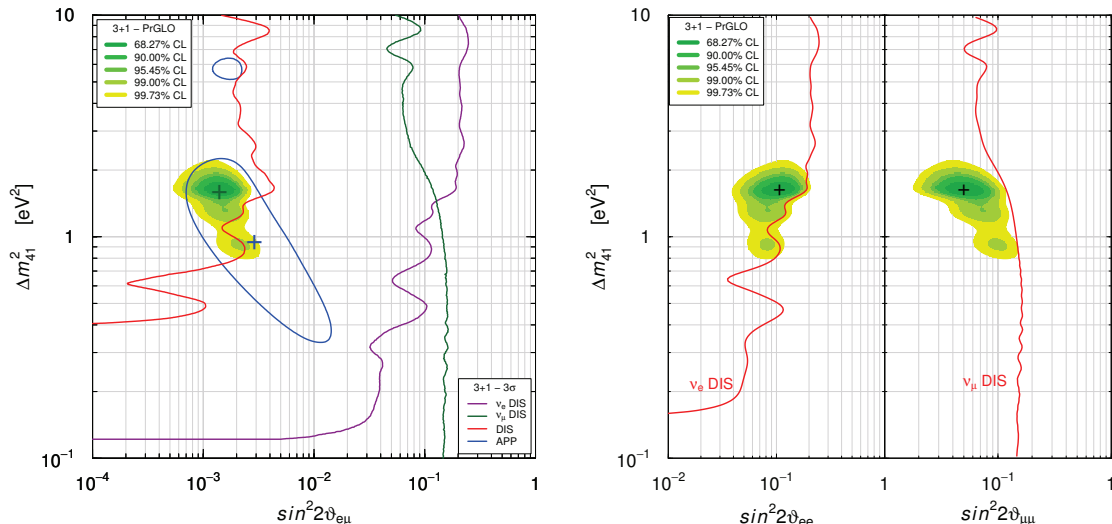


**Figure 3.8:** Global analysis of the neutrino anomalies for different detection channels. The left plot corresponds to the short baseline  $\nu_e \rightarrow \nu_\mu$  appearance mode. The disappearance channel (neutrino disappearance and muon disappearance) is depicted on the right side. The best fit point is indicated by a cross. Plots taken from Ref. [116].

### Accelerator Experiments

Several accelerator experiments have been proposed to search for sterile neutrinos in different channels ( $\bar{\nu}_e/\nu_e$  disappearance,  $\bar{\nu}_\mu \rightarrow \bar{\nu}_\mu/\nu_\mu \rightarrow \nu_\mu$  appearance and  $\bar{\nu}_\mu/\nu_\mu$  disappearance). Some of these experiments will use  $\beta$  beams from a low-energy neutrino factory ( $\bar{\nu}_e/\nu_e$  disappearance). Currently, only upper limits exist for  $\nu_\mu$  and  $\bar{\nu}_\mu$  disappearance experiments which makes it especially important to gain insight into this field.

### Reactor Experiments

Reactors are strong  $\bar{\nu}_e$  sources and several experiments have been proposed at short distances of about 10 m. Their energy resolution is particularly important to observe possible distortions in the detected positron spectrum induced by additional sterile neutrinos. NUCIFER is already operating and STEREO will start its measurement very soon. The sensitivity is strongly suppressed by the large  $\gamma$  and neutron background. STEREO like other proposals may have the possibility to observe a distance-dependent  $\bar{\nu}_e$  oscillation. PROSPECT and CARR will use two detectors while another proposal will use a movable detector (DANSS).

### $\beta$ Decay Mass Measurements

A further possibility to search for an eV-scale neutrino are  $\beta$ -decay mass experiments. The most sensitive results on the electron neutrino mass have been provided by  $\beta$  decay end-point measurements conducted at Tritium decay experiments,  ${}^3\text{H} \rightarrow {}^3\text{He} + e^+ + \bar{\nu}_e$ . The effective neutrino mass  $m_\beta$  is given by

$$m_\beta^2 = \sum_{k=1}^3 |U_{ek}|^2 m_k^2 \quad (3.16)$$

An additional neutrino state would result in a kink in the kinetic energy spectrum of the emitted electron at  $Q - m_k$  below the end-point. The KATRIN experiment is currently scheduled to start its operation in 2016 and aims at a sensitivity of 0.2 eV at 90% C.L. for  $m_\beta$  in

five years [117]. Sensitivity studies for possible sterile neutrinos have been reported in Ref. [157].

### Radioactive Source Experiments

The neutrino anomalies might also be tested by using intense radioactive sources placed near or inside a large low background detector. These experiments are particularly attractive as it may be possible to observe an energy- and distance-dependent neutrino flux. Several experiments have been proposed over the past years. The radioactive source experiments can be performed by using either monochromatic neutrino sources like  $^{51}\text{Cr}$  or  $^{37}\text{Ar}$ , or by using intense  $\bar{\nu}_e$  sources like  $^{144}\text{Ce}$ ,  $^{106}\text{Ru}$  or  $^{90}\text{Sr}$  [160]. The source geometry should be as compact as possible to observe the characteristic oscillation pattern. By using monochromatic neutrino sources,  $\nu_e$  disappearance can be measured as a function of distance.

In case of  $\bar{\nu}_e$  sources with a continuous  $\beta$ -spectrum, a precise vertex and energy resolution is required to resolve the  $L/E$  oscillation pattern.

Currently, two experimental setups are under preparation. The SAGE experiment intends to use  $^{51}\text{Cr}$  while the SOX project will use the  $^{144}\text{Ce}$   $\bar{\nu}_e$  source.

The potential of the SOX experiment was studied within this thesis.

A summary of several projects in preparation or proposed is given in Table 3.2. For a complete overview see Ref. [117].

Source Experiments	neutrino	source	$E$ (MeV)	$L$ (m)	status
SAGE	$\nu_e$	$^{51}\text{Cr}$	0.75	$\lesssim 1$	in preparation
CeSOX	$\bar{\nu}_e$	$^{144}\text{Ce}$	1.8 – 3	5 – 12	in preparation
CrSOX	$\nu_e$	$^{51}\text{Cr}$	0.75	5 – 12	proposal
Daya Bay	$\bar{\nu}_e$	$^{144}\text{Ce}$	1.8 – 3	1.5 – 8	proposal
JUNO	$\bar{\nu}_e$	$^{144}\text{Ce}$	1.8 – 3	$\lesssim 32$	proposal
Reactor Experiments	$P_{th}$ (MW)	$M_{target}$ (tons)	$L$ (m)	Depth (m.w.e.)	status
Nucifer (FRA)	70	0.8	7	13	operating
Stereo (FRA)	57	1.75	9 – 12	18	in preparation
DANSS (RUS)	3000	0.9	10 – 12	50	in preparation
SoLid (BEL)	45 – 80	3	6 – 8	10	in preparation
PROSPECT (USA)	85	3, 10	7 – 12, 15 – 19	few	in preparation
NEOS (KOR)	16400	1	25	10 – 23	in preparation
Neutrino-4 (RUS)	100	1.5	6 – 11	10	proposal
Poseidon (RUS)	100	3	5 – 8	15	proposal
Hanaro (KOR)	30	0.5	6	few	proposal
CARR (CHN)	60	$\sim 1$	7, 11	few	proposal
Accelerator Exp.	$P$ (MW)	$M_{target}$ (tons)	$E$ (MeV)	$L$ (m)	status
SBN (USA)	$> 0.09$	112, 89, 476	$\sim 800$	110, 470, 600	in preparation
J-PARC MLF (JPN)	$\sim 1$	50	$\sim 40$	20	proposal
KPipe (JPN)	$\sim 1$	684	$\sim 236$	32 – 152	proposal
nuPRISM (JPN)	$\sim 1$	4000 – 8000	200 – 1000	1000 – 2000	proposal
IsoDAR-KamLAND	0.6	1000	$\sim 6.5$	10 – 22	proposal
IsoDAR-JUNO (CHN)	0.6	20000	$\sim 6.5$	20 – 100	proposal
OscSNS (USA)	1.4	450	$\sim 40$	50 – 70	proposal

**Table 3.2:** Main features of future source, reactor and accelerator experiments and their status. This table is reproduced from Ref. [117]. For more information about each project please see Ref. [117] and the references therein.

The main purpose of the BOREXINO experiment is the real-time detection of solar neutrino fluxes. The proposal of the experiment dates back to the 1980s. However, data taking started only as early as May 2007 after a long time of testing which included the construction of a prototype (CTF<sup>1</sup>) and the development of new methods and procedures to reach the extremely high level of radio-purity needed for the the low-energy neutrino measurement.

To the present date (2015/2016), BOREXINO has measured many different neutrino fluxes, including the <sup>7</sup>Be [66], <sup>8</sup>B [57], pep [61] and only recently the pp neutrino fluxes [67]. BOREXINO is going to address two major challenges within the coming years. After the completion of the first phase of data taking, BOREXINO has set the most stringent limit on the CNO flux. Within the next data taking phase, BOREXINO will try to improve the CNO flux limit or even to measure CNO neutrinos for the first time. The second priority task is the SOX project which intends to test the fourth sterile neutrino hypothesis at squared mass differences of about 1 eV<sup>2</sup>.

The first section of the present chapter describes the general detector layout, including all sub-systems. Section 4.2 summarizes the different detection techniques for neutrinos and antineutrinos, respectively. The section following this description is devoted to the scientific achievements of BOREXINO. In the last section the SOX project is described.

## 4.1 Detector Design

BOREXINO is a large volume liquid scintillator detector located in Hall C of the Laboratori Nazionali del Gran Sasso (LNGS). The detector (shown in Figure 4.1 and 4.2) is described in detail in Ref. [36, 59, 35]. Purification techniques and plants are summarized in Ref. [69, 37]. At the underground laboratory, the muon flux is reduced significantly with respect to the surface. The Gran Sasso mountain massive provides a shielding of about 3800 m.w.e. which reduces the muon flux by a factor of 10<sup>6</sup>.

The detector is divided into two sub-detectors [207, 172]. Both parts are intersected by the spherical support structure. The support structure is called *stainless steel sphere* (SSS) and has a diameter of 13.7 m. Most of the PMTs are mounted on the SSS to detect the scintillation light originating from physical processes. The two sub-detectors are reviewed in the following.

### 4.1.1 Inner Detector

The centerpiece of the inner detector (ID) is the spherical inner nylon vessel of 8.5 m diameter which contains 280 t of liquid scintillator. The liquid scintillator is a mixture of pseudocume

---

<sup>1</sup>CTF: counting test facility



**Figure 4.1:** The BOREXINO detector is located at Hall C at the LNGS. In 2015 an insulation layer was installed to shield against temperature changes in the underground laboratory. The interior consists of several spherical nylon vessels. The innermost target region contains liquid scintillator with a small amount of PPO. BOREXINO has started data taking in May 2007. Figure taken from [198].

(1,2,4-trimethylbenzene,  $C_6H_3(CH_3)_3$ ) as solvent and 1.5 g/l PPO (2,5-Diphenyloxazole). The scintillator has an electron density of  $(3.307 \pm 0.003) \times 10^{29}$  per metric ton [172] and the proton density has been estimated as  $\rho_H = 5.3 \times 10^{28} \text{ m}^{-3}$ .

The light attenuation length corresponds to  $\lambda_{att} = 8 \text{ m}$  at 420 nm. The scintillation volume is  $320 \text{ m}^3$ . Depending on the analysis, a software cut might be applied to reduce background processes originating from the outside. Steel and nylon pipes are connected to the vessel poles for fluid handling operations [172]. The innermost vessel is surrounded by 1040 t shielding liquid, called buffer. The buffer is filled with scintillator complemented by 5 g/l of demethylphalate (DMP) as a quencher. The density of the buffer was chosen to be similar to the inner vessel liquid to avoid hydro-static pressure and to ensure similar refraction indices for both liquids<sup>2</sup>. The DMP solvent assures that external  $\gamma$ -radiation is suppressed. [207, 172]

Based upon the experience obtained with the prototype of BOREXINO (CTF), it was decided to install a second nylon sphere, the outer vessel (OV), which divides the buffer at a radius of 5.5 m. The purpose of this layer is to stop radon gas diffusion emanating from the PMTs toward the inner vessel [172]. The nylon membrane has a thickness of  $125 \mu\text{m}$  [172].

<sup>2</sup>This is especially important for the light tracking and vertex determination.

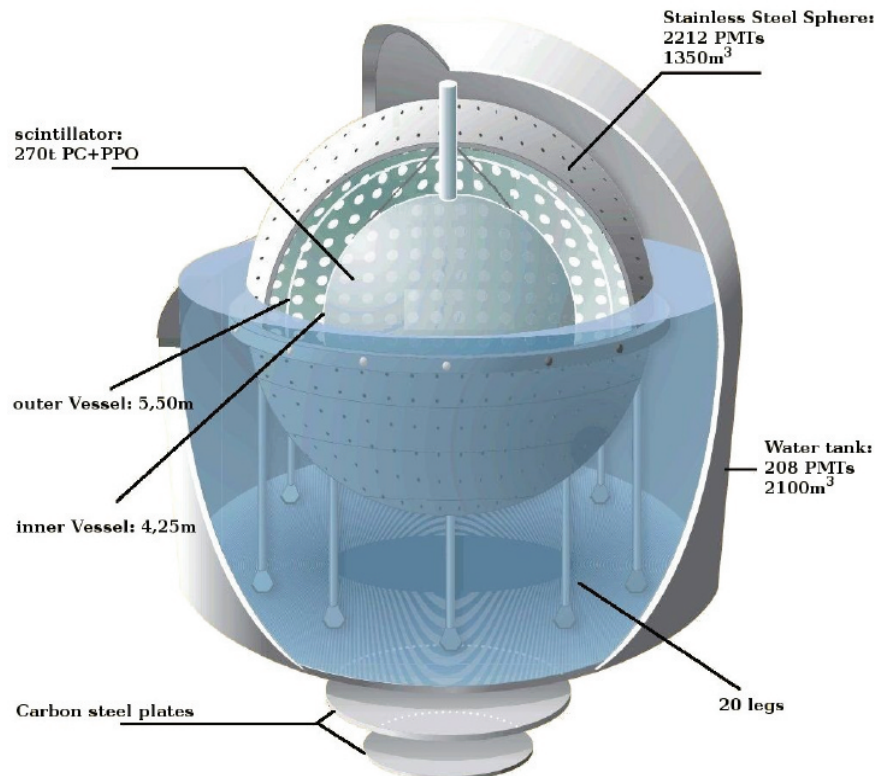


**Figure 4.2:** BOREXINO Detector. The target contains liquid scintillator. 2,212 inward facing PMTs had originally been installed on the so-called stainless steel sphere. Figure taken from [59].

All components are housed in the SSS [172] which serves as a support structure for the PMTs (see Figure 4.2). 20 legs are attached to the SSS for stabilization which are welded to the external water tank floor [172]. The SSS contains 2212 8-inch ETL-9351 inward facing PMTs. 1838 PMTs are equipped with Winston cones to increase the optical coverage of the inner vessel (IV, see Figure 4.2) to 30%. These PMTs are particularly sensitive to light with wavelengths between 350 nm and 500 nm [172]. The photocathode quantum efficiency is 21%. The observed photo-electron-yield is about 550 pe/MeV [207]. Over the past years many channels have stopped working which reduced the total number of PMTs to about 1500 at the end of 2015.

#### 4.1.2 Outer Detector

The outer detector (OD) contains 2.1 kt of ultra-pure water to shield the ID against external  $\gamma$ -radiation and to identify atmospheric muons. The OV (outer veto) has 208 additional PMTs in order to detect the Cherenkov light. Most of the OD surface is covered with highly reflective Tyvek foil. [77]

#### 4.1.3 Liquid Scintillator Purification

BOREXINO uses several devices to purify the liquid scintillator. This includes filtration, vacuum distillation, water extraction and nitrogen stripping. Filtration is necessary to avoid small particles entering the IV. Vacuum distillation separates impurities with higher boiling points than the liquid scintillator [172]. In order to remove polar molecules and metal ions

from the liquid scintillator, water extraction is performed. Nitrogen stripping has proven to be an effective way to remove gases like Oxygen (which would quench the light output) and radioactive noble gases like Radon, Krypton and Argon [172]. More details can be found in Ref. [69].

## 4.2 Neutrino Detection in Borexino

In BOREXINO, neutrinos are detected by means of their elastic scattering via the charged and neutral current processes:

$$\nu_x + e^- \rightarrow \nu_x + e^- \quad (4.1)$$

Only for electron neutrinos charged current interactions, mediated by the  $W^\pm$  boson, are possible. As a consequence, the cross-section for the other flavors is smaller as they are only mediated by the  $Z^0$  boson. At the lowest order in perturbation theory, the  $\nu_e e^-$  cross-section is given by:

$$\frac{d\sigma}{dE} = \frac{\sigma_e}{m_e} \left[ g_l^2 + g_r^2 \left( 1 - \frac{T_e}{E_\nu} \right)^2 - g_l g_r \frac{m_e T_e}{E_\nu^2} \right], \quad (4.2)$$

where

$$\sigma_e = \frac{2G_F^2 m_e^2}{\pi \hbar^2} = 88.06 \times 10^{-46} \text{ cm}^2 \quad (4.3)$$

and

$$g_l = \pm \frac{1}{2} + \sin^2 2\theta_W. \quad (4.4)$$

The visible energy in BOREXINO is the recoil energy of the electron which is given by

$$T_e = E'_\nu - E_\nu \quad (4.5)$$

where

$$E'_\nu = \frac{E_\nu}{1 + \frac{E_\nu}{m_e c^2} (1 - \cos \theta)} \quad (4.6)$$

In elastic scattering  $\theta$  denotes the deflection angle of the incoming neutrino with respect to the original direction. The maximum kinetic energy of the electron is given by

$$T_e^{max} = \frac{E_\nu}{1 + \frac{m_e c^2}{2E_\nu}}. \quad (4.7)$$

For the mono-energetic  ${}^7\text{Be}$  neutrinos with an energy of 862 keV the maximum kinetic energy corresponds to 665 keV. The kinematic is analogously to the Compton scattering process and the recoil spectrum exhibits the characteristic Compton shoulder at the given end-point.

The total cross-section relevant for the interaction prediction is obtained by integrating the differential cross-section over its energy up to the maximum kinetic energy. For the  ${}^{51}\text{Cr}$  interaction prediction the total cross-section  $\sigma_{CC+NC} = 22.5 \times 10^{-42} \text{ cm}^2$  from Ref. [164] is used which includes radiative effects.

A second detection channel can be used for antineutrinos, the inverse beta decay (IBD) reaction,  $\bar{\nu}_e + p \rightarrow e^+ + n$ . This technique has already been used by many experiments and was used by BOREXINO for the geo-neutrino analysis. Compared to the elastic scattering reaction, the cross-section is two orders of magnitude larger. The total cross-section was derived by Vogel and Beacom. The inverse beta decay is often referred to as the golden channel in neutrino physics, because of its relatively large cross-sections and good background suppression due to the coincidence signal. In this section the formalism of *Vogel and Beacom*

is followed [194]. The derivation is based on an expansion of the cross-section on the proton to the first order in nucleon mass in order to study the cross-section's angular dependence (see also Ref. [107]). The matrix element of this reaction is given by the expression [194]

$$\mathcal{M} = \frac{G_F \cos \theta_C}{\sqrt{2}} \left[ \bar{u}_n \left( \gamma_\mu f - \gamma_\mu \gamma_5 g - \frac{i f_2}{2M} \sigma_{\mu\nu} q^\nu \right) u_p \right] \times [\bar{u}_\nu \gamma^\mu (1 - \gamma_5) v_e], \quad (4.8)$$

where  $f = 1$  and  $g = 1.26$  represent the vector and axial-vector coupling constants.  $\cos \theta_C = 0.974$  represents the cosine of the Cabbibo angle. The variation of the form factor due to their dependence on the transferred four-momentum is neglected, since it is a effect of  $\mathcal{O}(E_\nu^2/M^2)$ . At zeroth order the differential cross-section is therefore given by

$$\left( \frac{d\sigma}{d\cos\theta} \right)^{(0)} = \frac{\sigma_0}{2} \left[ (f^2 + 3g^2) + (f^2 - g^2) v_e^{(0)} \cos\theta \right] E_e^{(0)} p_e^{(0)}, \quad (4.9)$$

where the positron energy at zeroth order  $E_e^{(0)}$ , the positron momentum  $p_e^{(0)}$  and velocity  $v_e$  are ( $M_n$  : neutron mass,  $M_p$  : proton mass,  $m_e$  : positron mass)

$$E_e^{(0)} = E_\nu - \Delta = E_\nu - (M_n - M_p), \quad (4.10)$$

$$p_e^{(0)} = \sqrt{\left(E_e^{(0)}\right)^2 - m_e^2} \quad (4.11)$$

$$v_e^{(0)} = p_e/E_e. \quad (4.12)$$

The normalizing constant  $\sigma_0$  is

$$\sigma_0 = \frac{G_F^2 \cos^2 \theta_C}{\pi} (1 + \Delta_{inner}^R), \quad (4.13)$$

including the energy-independent inner radiative corrections with  $\Delta_{inner}^R \simeq 0.024$  (see [194] and references therein). The total cross section is finally given by

$$\sigma_{tot}^{(0)} = \sigma_0 (f^2 + 3g^2) E_e^{(0)} p_e^{(0)} = 0.0952 \left( \frac{E_e^{(0)} p_e^{(0)}}{1\text{MeV}^2} \right) \times 10^{-42} \text{ cm}^2. \quad (4.14)$$

This can also be written as

$$\sigma_{tot}^{(0)} = \frac{2\pi^2}{f^R m_e^5 \tau_n} E_e^{(0)} p_e^{(0)}, \quad (4.15)$$

since the energy-independent inner radiative corrections affect the neutron beta decay rate in the same way.  $\tau_n$  denotes the neutron life-time and  $f^R = 1.7152$  the phase factor, respectively. At first order in  $1/M$ , the positron energy depends upon the scattering angle  $\theta$  and is [194]

$$E_e^{(1)} = E_e^{(0)} \left[ 1 - \frac{E_\nu}{M} (1 - v_e^{(0)} \cos\theta) \right] - \frac{(\Delta^2 - m_e^2)}{2M} \quad (4.16)$$

The differential cross section at first order is therefore given by

$$\left( \frac{d\sigma}{d\cos\theta} \right)^{(1)} = \frac{\sigma_0}{2} \left[ (f^2 + 3g^2) + (f^2 - g^2) v_e^{(1)} \cos\theta \right] E_e^{(1)} p_e^{(1)} - \frac{\sigma_0}{2} \left[ \frac{\Gamma}{M} \right] E_e^{(0)} p_e^{(0)}, \quad (4.17)$$

where

$$\begin{aligned}
\Gamma = & 2(f + f_2)g \left[ \left( 2E_e^{(0)} + \Delta \right) \left( 1 - v_e^{(0)} \cos \theta \right) - \frac{m_e^2}{E_e^{(0)}} \right] \\
& + (f^2 + g^2) \left[ \Delta \left( 1 + v_e^{(0)} \cos \theta \right) + \frac{m_e^2}{E_e^{(0)}} \right] \\
& + (f^2 + 3g^2) \left[ \left( E_e^{(0)} + \Delta \right) \left( 1 - \frac{\cos \theta}{v_e^{(0)}} \right) - \Delta \right] \\
& + (f^2 - g^2) \left[ \left( E_e^{(0)} + \Delta \right) \left( 1 - \frac{\cos \theta}{v_e^{(0)}} \right) - \Delta \right] v_e^{(0)} \cos \theta. \tag{4.18}
\end{aligned}$$

The threshold for the inverse beta decay is

$$E_\nu^{thres} = \frac{(M_n + m_e)^2 - M_p^2}{2(M_n + m_e)} = 1.803 \text{ MeV} \tag{4.19}$$

in the center of momentum frame and

$$E_\nu^{thres} = \frac{(M_n + m_e)^2 - M_p^2}{2M_p} = 1.806 \text{ MeV} \tag{4.20}$$

in the laboratory frame (proton at rest). In Ref. [185] an approximation was presented which yields similar results with deviations of only 1/1000 up to 60 MeV:

$$\sigma = p_e E_e E_\nu^{-0.07056 + 0.02018 \ln E_\nu - 0.001953 \ln^3 E_\nu} \times 10^{-43} \text{ cm}^2. \tag{4.21}$$

### 4.3 Physics Program

The  $^7\text{Be}$ ,  $^8\text{B}$  and pep neutrino measurements have been completed in 2014 when BOREXINO announced the first direct detection of the pp neutrinos originating from the primary reaction that powers the Sun. The analysis of BOREXINO data allows to investigate the transition from matter dominated oscillations to vacuum oscillations. BOREXINO has provided constraints on the Mikheyev–Smirnov–Wolfenstein large-mixing angle (MSW-LMA) solution.

In addition to the solar neutrino program, BOREXINO has set limits on several exotic physics events like the electron decay time [24], the heavy sterile neutrino mixing in the  $^8\text{B}$  decay [64] and the search for solar axions in the  $p(d, ^3\text{He})\alpha$  reaction [62].

Alongside KAMLAND, BOREXINO is the only experiment which has reported the observation of geo-neutrinos [58].

Future efforts of the BOREXINO collaboration are centered on the first CNO measurement and the SOX project which is going to test the sterile neutrino hypothesis (see section 3.4).

#### 4.3.1 Solar $^7\text{Be}$ Neutrino Flux Measurement

In 2008, BOREXINO reported a direct measurement of the  $^7\text{Be}$  neutrino flux with an uncertainty of 10% [48]. As the  $^7\text{Be}$  neutrinos are mono-energetic, the measured recoil spectrum in BOREXINO features the characteristic Compton shoulder (see Figure 4.3). The fiducial

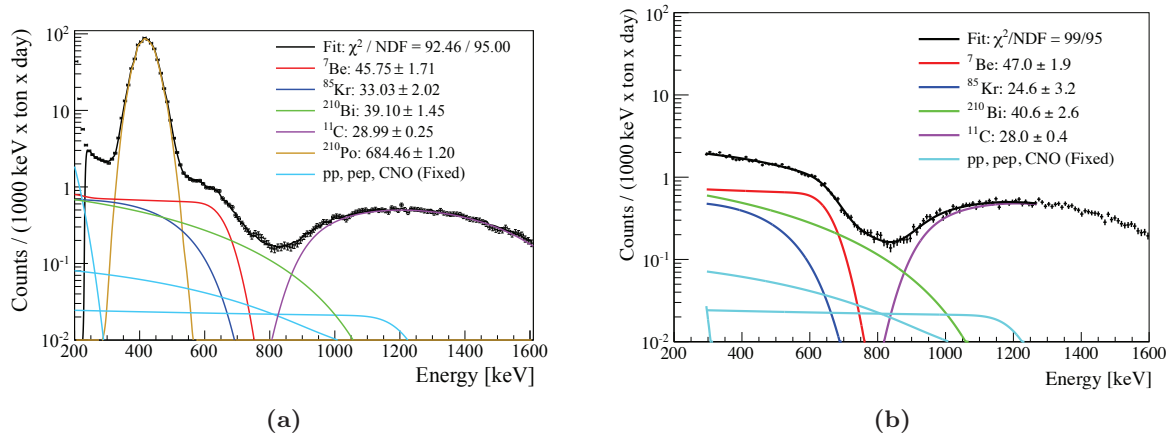


**Figure 4.3:** Energy spectrum for the  ${}^7\text{Be}$  analysis. Two different analyses have been carried out. For the analysis shown on the left side, the Polonium decay was fitted together with all other contributions. For a second analysis (shown on the right), a  $\alpha$  subtraction was performed. Both analyses yield the same results. The characteristic Compton shoulder of the  ${}^7\text{Be}$  electron recoil spectrum is clearly visible and allows a robust analysis. Figure taken from Ref. [66].

volume<sup>3</sup> was limited to 100t to suppress muons and external  $\gamma$ -rays. Further background processes are induced by the radioactive decay of  ${}^{85}\text{Kr}$  and  ${}^{210}\text{Bi}$ . The  ${}^7\text{Be}$  flux was retrieved by fitting background components together with the  ${}^7\text{Be}$  recoil spectrum. The light yield was left as a free parameter. BOREXINO has recently published the final results from the first phase of data taking [66]. The  ${}^7\text{Be}$  flux was determined with a precision of better than 5% [66]. The experimental uncertainty is therefore smaller than the uncertainty from the Standard Solar Model predictions. The corresponding survival probability is depicted in Figure 4.4. A detailed discussion can be found in Ref. [66].

#### 4.3.2 Solar ${}^8\text{B}$ Neutrinos

The solar  ${}^8\text{B}$  neutrinos have already been measured in great accuracy by SNO and SUPER-KAMIOKANDE above 5 MeV. BOREXINO, taking advantage of the low-energy threshold of liquid scintillator detectors, was able to measure the  ${}^8\text{B}$ - $\nu$  spectrum down to 3 MeV. The  ${}^8\text{B}$  background is similar to the background of the  ${}^7\text{Be}$ - $\nu$  analysis. At low energies, the radioactive decay of  ${}^{208}\text{Tl}$  in the detector bulk has been identified as the major source of background. The mean value for  ${}^8\text{B}$  neutrinos above 3 MeV was measured to  $75 \pm 13$  counts [57]. The measurement of the  ${}^8\text{B}$  neutrinos at low energies is particularly interesting in order to test the large mixing angle solution (LMA) of the MSW effect. The energy of those neutrinos covers the region from vacuum to matter dominated oscillations. The neutrino survival probability for the MSW-LMA prediction is shown in Figure 4.4 together with different measurements.

#### 4.3.3 Solar pep and CNO Neutrinos

In October 2011, BOREXINO reported the first evidence of the pep solar neutrinos [61]. The result was achieved by adopting novel data analysis techniques for background reduction. The dominant background in the energy range of interest (1 – 2 MeV) has been identified as the cosmogenic  ${}^{11}\text{C}$   $\beta^+$  emitter. The  ${}^{11}\text{C}$  production rate due to muon spallation is

<sup>3</sup>The volume used for the analysis is often reduced to avoid background processes. The fiducial volume is equal to the volume which is in fact used for the analysis.

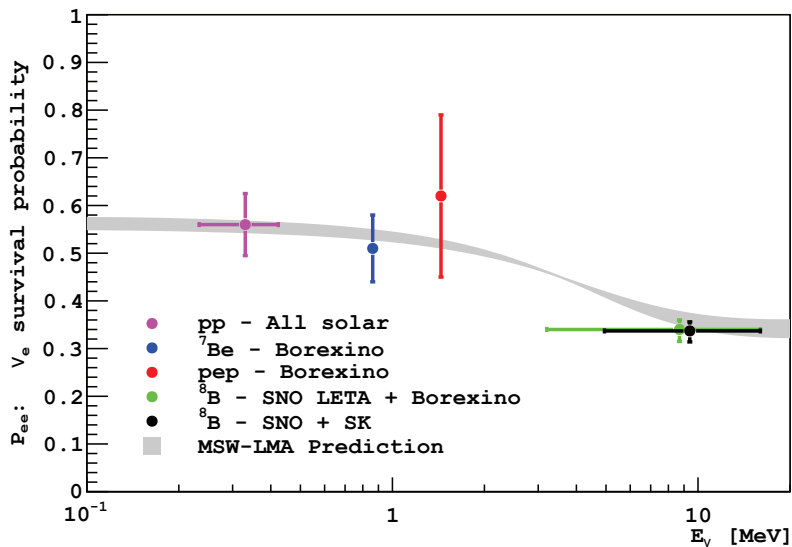


Figure 4.4: Electron neutrino survival probability. Figure taken from [66].

about  $\sim 27 \text{ counts} \cdot (\text{d} \cdot 100 \text{ t})^{-1}$ . The lifetime of  $^{11}\text{C}$  is relatively large with 29.4 min. The  $^{11}\text{C}$  background was reduced by the application of a space and time veto. This method applied is called threefold coincidence (TFC) method and was originally introduced by M. Deutsch (see Figure 4.5). The method is based on an event-by-event selection by linking the following three signals [154]:

- **Prompt muon signal**
- **First delayed signal:** Following the reaction of the muon on the  $^{12}\text{C}$  nuclei,  $\mu + ^{12}\text{C} \rightarrow \mu + ^{11}\text{C} + \text{n}$ , the emitted neutron is thermalized and finally captured on hydrogen. The characteristic 2.223 MeV  $\gamma$ -ray is detected by the PMTs.
- **Second delayed signal.**  $^{11}\text{C}$  atoms, which are created along the muon trajectory, undergo  $\beta^+$  decays [154]:



By identifying each step,  $^{11}\text{C}$  candidates are selected and further processed for the analysis. The surviving  $^{11}\text{C}$  content is further reduced by pulse shape discrimination techniques. This method is based on a boosted-decision-tree and uses small pulse shape differences between  $e^+$  and  $e^-$ .

The most recent result based on the presented techniques has been reported in Ref. [66], see also Figure 4.6. The measured pep interaction rate is given by [66]:

$$R(\text{pep}) = 3.1 \pm 0.6 \text{ (stat.)} \pm 0.3 \text{ (sys.) cpd/100 t} \quad (4.23)$$

The CNO rate was fitted simultaneously. The current limit is given by

$$R(\text{CNO}) < 7.9 \text{ cpd/100 t} \quad (4.24)$$

at 95% C.L.. The ability to measure the CNO- $\nu$  content is mostly limited by the background process from the decay of  $^{210}\text{Bi}$  which has a similar spectral shape as the CNO- $\nu$ . During the

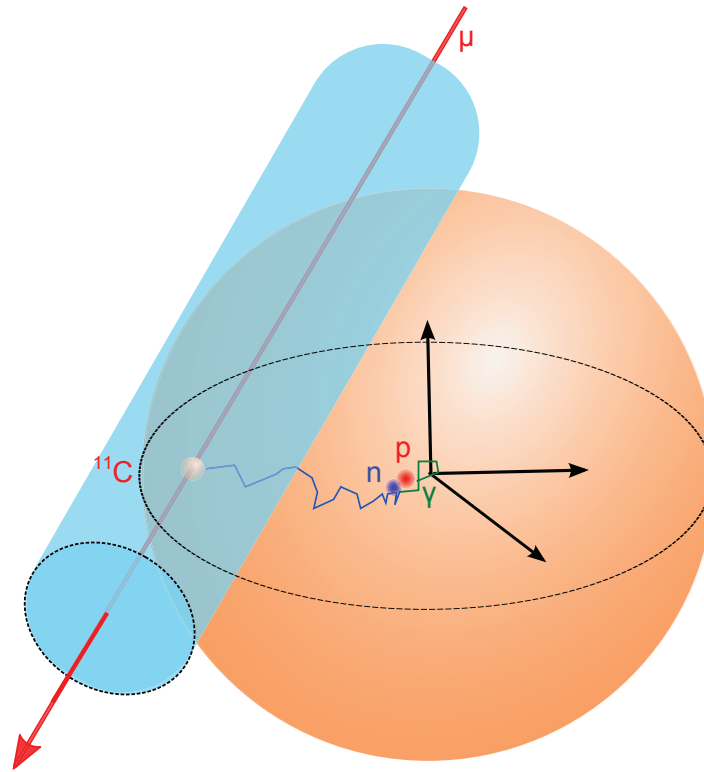


**Figure 4.5:** Threefold coincidence method (TFC method) for  $^{11}\text{C}$  identification and reduction. The isotope production is assumed along the muon track. In combination with the neutron vertex point, a sub-volume can be excluded for several half-lives of the isotopes. The minimum volume, which has to be excluded, corresponds to the intersection area between the cylinder and a sphere around the neutron capture vertex.

first phase a  $^{210}\text{Bi}$  content more than ten times higher than the expected CNO- $\nu$  content was measured. The measurement of the CNO content is particularly important as it may help to solve the solar metallicity problem [181]. The predicted CNO rate is naturally linked to the metallicity of the Sun. The high metallicity (GS98) model predicts a flux 40% higher than the Low Metallicity Model (AGSS09) [181].

For the second phase of data taking, BOREXINO has put its focus towards a more stringent limit on the CNO flux or even to measure the flux directly. Future analyses will try to measure the  $^{210}\text{Bi}$  content by looking at the  $^{210}\text{Po}$  rate ( $^{210}\text{Bi}$  is the successor of the  $^{210}\text{Po}$  isotope) [192, 193]. Current efforts have been limited by temperature effects on the  $^{210}\text{Po}$  rate. To address this problem, BOREXINO has decided to thermally isolate the water tank (see Figure 4.1).

#### 4.3.4 Solar pp Neutrinos

Most recently, BOREXINO reported the first direct detection of the pp neutrinos [67]. Two major challenges had to be addressed:  $^{14}\text{C}$  pile-up and liquid scintillator purification. The liquid scintillator purification had been addressed long before the experiment started data taking. To minimize the  $^{14}\text{C}$  content inside BOREXINO, deep underground petroleum was used. Although the  $^{14}\text{C}$  was reduced by a factor of 1000, the  $^{14}\text{C}$  marks the largest and most problematic background for the pp analysis. Due to the large content two separate  $^{14}\text{C}$  radioactive decays may be registered as one event. The overlap of both events results in an energy pile-up (two energy depositions are registered as one energy deposition). This effect was modeled

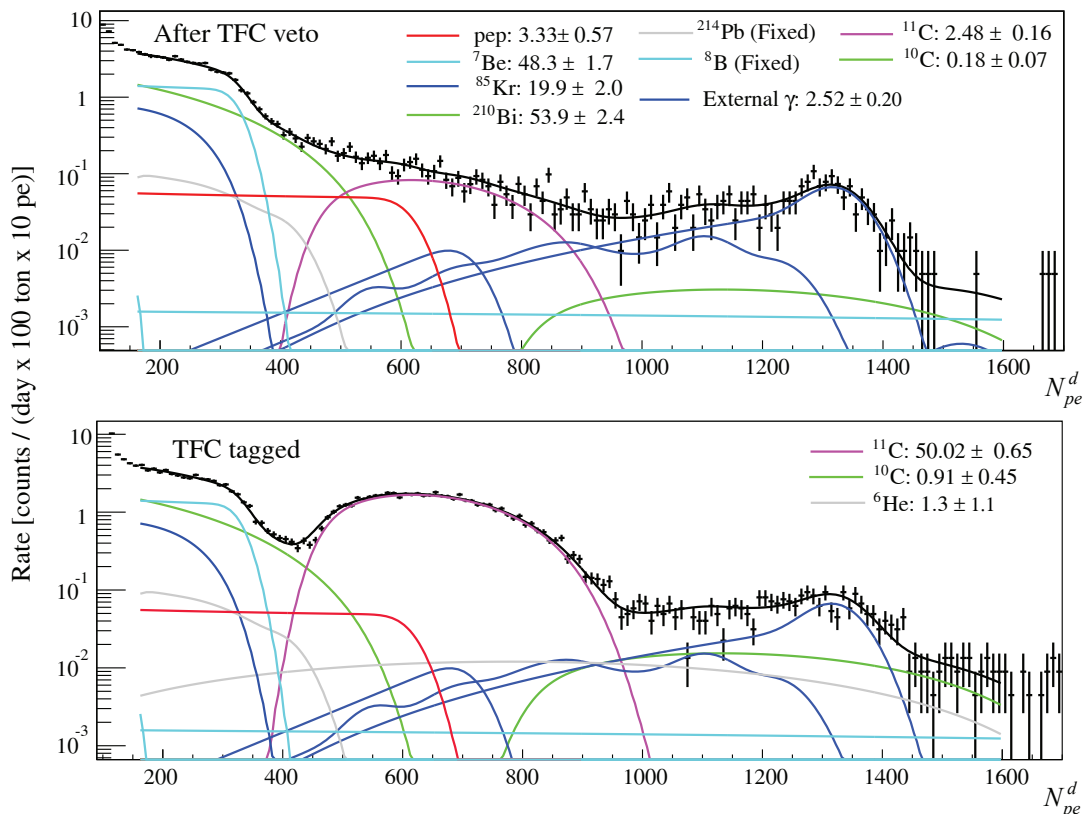


**Figure 4.6:** Energy spectrum for the CNO analysis. The top panel shows the total spectrum after the subtraction of the TFC-vetoed events while the bottom panel shows all TFC tagged events. Figure taken from Ref. [66].

by creating an artificial pile-up of two separated events via the reconstruction software. In total, BOREXINO has determined the pp rate to  $144 \pm 13(\text{stat.}) \pm 10(\text{sys.})$  cpd/100 t. This corresponds to a measured pp flux of  $(6.6 \pm 0.7) \times 10^{10} \text{ cm}^{-2} \text{ s}^{-1}$  which is in good agreement with the SSM prediction of  $5.98 \times 10^{10} \text{ cm}^{-2} \text{ s}^{-1}$  [67].

#### 4.3.5 Geo-Neutrinos

Over the past years, BOREXINO has published several results on geo-neutrinos. The most recent publication is based on 2056 days of data taking. The null-observation of geo-neutrinos with BOREXINO has a significance of  $5.9\sigma$  [26].

### 4.4 The SOX Project

The idea of testing non-standard neutrino properties with an artificial neutrino or antineutrino source dates back to the beginning of the 1990s. The BOREXINO proposal (also known as the *Borex yellow book* [81]) already included a short section about *laboratory neutrino physics* and examined the possibility to search for a neutrino magnetic moment with a  $^{90}\text{Sr}$   $\bar{\nu}_e$  experiment. Following studies were presented in Ref. [136, 134] and were complemented by studies concerned with the search for an additional neutrino species, so called sterile neutrinos [135, 136]. As a complement to the  $^{90}\text{Sr}$   $\bar{\nu}_e$  source, the  $^{51}\text{Cr}$   $\nu_e$  was discussed in context of a BOREXINO laboratory experiment.

After the reactor anomaly was published around 2010, the focus on a possible source experiment at the BOREXINO detector gained momentum. Originally it was discussed to deploy a  $^{51}\text{Cr}$  source underneath the detector. This phase was known as phase A of the experiment [65]. Later phases could have included a  $^{144}\text{Ce}$   $\bar{\nu}_e$  source inside the water tank or at the center of the detector. A similar project was planned at the KAMLAND detector using the  $^{144}\text{Ce}$   $\bar{\nu}_e$  source [114]. However, due to technical and administrative limitations at KAMLAND, the so called CELAND project was abandoned [105]. Subsequently, the Saclay group, which had been granted money for the production of the  $^{144}\text{Ce}$  source, transferred to BOREXINO. As a consequence, the SOX project shifted their experimental setup towards the deployment of this antineutrino source underneath the detector. Depending on the scientific results, this might be followed by an installation of the source inside the water tank. The  $^{51}\text{Cr}$  remains an option after the first phase.

#### 4.4.1 $\nu_e$ and $\bar{\nu}_e$ Emitters as Probes for the Neutrino Anomalies

The idea of testing the observed neutrino anomalies with an artificial  $\nu_e$  or  $\bar{\nu}_e$  emitter near or inside a large low-background detector is particularly attractive. A radioactive source like  $^{144}\text{Ce}$ – $^{144}\text{Pr}$  or  $^{51}\text{Cr}$  features energies which enable a test of the neutrino anomalies with high sensitivity at the  $(\sin^2 2\theta_{14}, \Delta m_{41}^2)$  parameter space currently favored by global fits. Within the  $(3+1)$  sterile neutrino oscillation model, oscillation lengths of few centimeters to meters are expected assuming  $\Delta m_{41}^2$  of about  $1 \text{ eV}^2$  at the given source energies of about 1 MeV. A large liquid scintillator detector with an unprecedented low background is the ideal candidate to search for the characteristic oscillation pattern. The position resolution of the BOREXINO detector is about 15 cm at 1 MeV and the energy resolution is  $6\%/\sqrt{E}$  [169]. Both properties are therefore precise enough to resolve the distinct oscillation signature. This concept has the additional advantage that the radioactive source is relatively compact, a prerequisite to resolve the oscillation pattern. Compared to other accelerator and short baseline reactor experiments, the source induced background is easier manageable (at least if the source is deployed outside the detector).

The concept of deploying an intense  $\nu_e$  or  $\bar{\nu}_e$  source at a large low background detector is a long standing idea. The option to use the isotope pair  $^{144}\text{Ce}$ – $^{144}\text{Pr}$  instead of  $^{90}\text{Sr}$ – $^{90}\text{Y}$  was recently brought back to attention [88]. The SOX project is based on this proposal by *Cribier et al.* [88].

#### 4.4.2 $^{144}\text{Ce}$ and $^{51}\text{Cr}$ at Borexino

The search for possible light sterile neutrinos at BOREXINO will be performed by using a  $\sim 100 \text{ kCi}$  ( $3.7 \text{ PBq}$ ) intense  $\bar{\nu}_e$  source ( $^{144}\text{Ce}$ – $^{144}\text{Pr}$ ) and possibly a monochromatic neutrino source like  $^{51}\text{Cr}$ . The isotope pair  $^{144}\text{Ce}$ – $^{144}\text{Pr}$  will be used during the first phase of the experimental setup. The parent nucleus  $^{144}\text{Ce}$  has a long half-life of 284.5 days which allows production and transportation. The  $Q$  value is well below the IBD threshold while the daughter nucleus  $^{144}\text{Pr}$  has a  $Q$  value of 2997.5 keV. An artificial antineutrino source deployed underneath the detector (see Figure 4.7) will result in a time and space dependent (anti)neutrino flux. The characteristic oscillation pattern for the  $^{144}\text{Ce}$   $\nu_e$  source is shown in Figure 4.8.

$^{51}\text{Cr}$  is an electron capture source,  $^{51}\text{Cr} + e^- \rightarrow ^{51}\text{V} + \nu_e$ , featuring four monochromatic neutrino lines. The most dominant transition has a BR of 81.6% and features a neutrino energy of 747 keV. The energy is similar to the 862 keV  $\nu_e$  from the radioactive decay of  $^7\text{Be}$  in the Sun [160]. The activity of the  $^{51}\text{Cr}$  neutrino source will be in the order of 5 – 10 MCi.

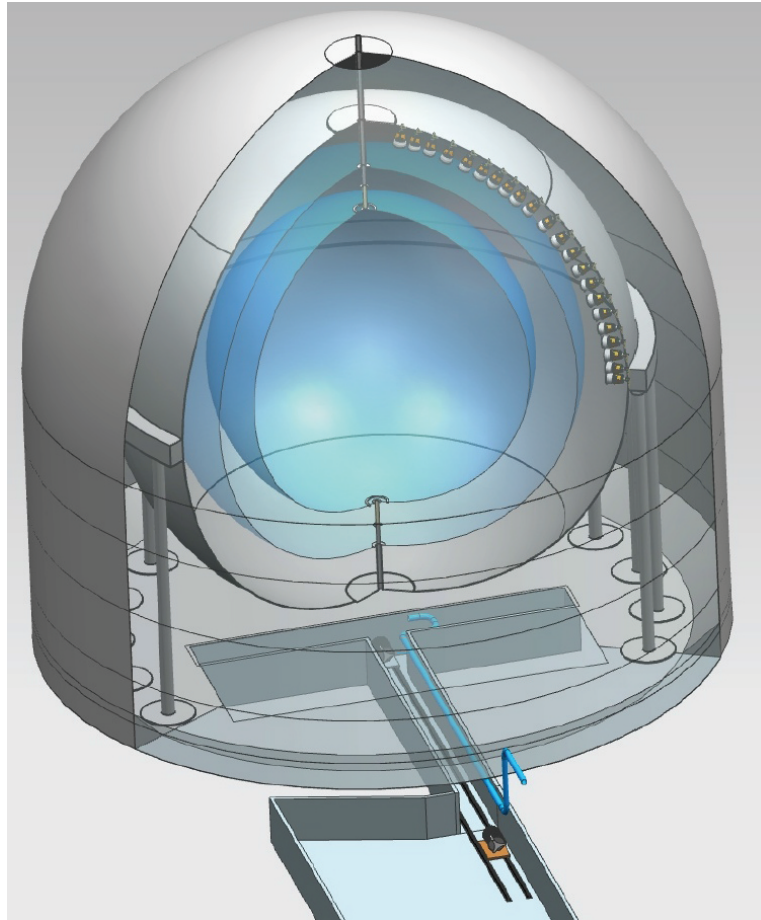


**Figure 4.7:** SOX concept. During the first phase of the experimental setup an artificial antineutrino source will be deployed underneath the BOREXINO detector. The source distance to the detector center will be approximately 8.51 m. Figure credit: BOREXINO collaboration.

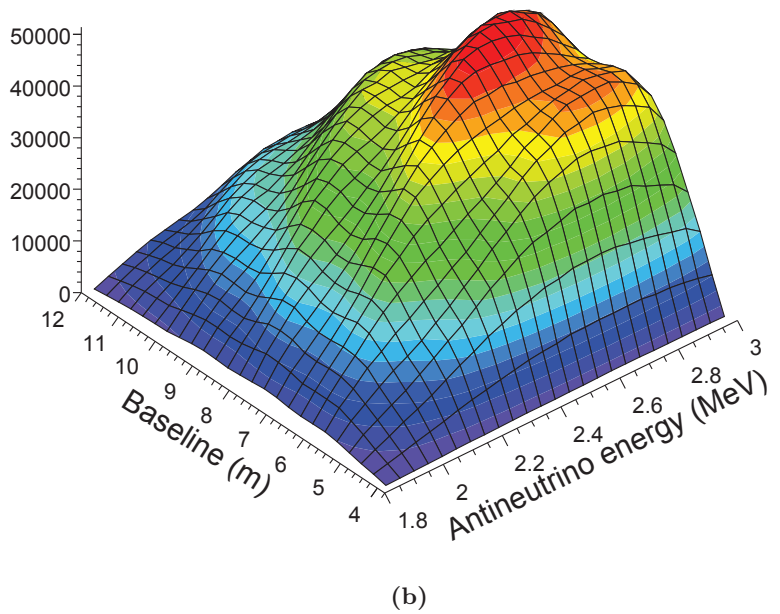
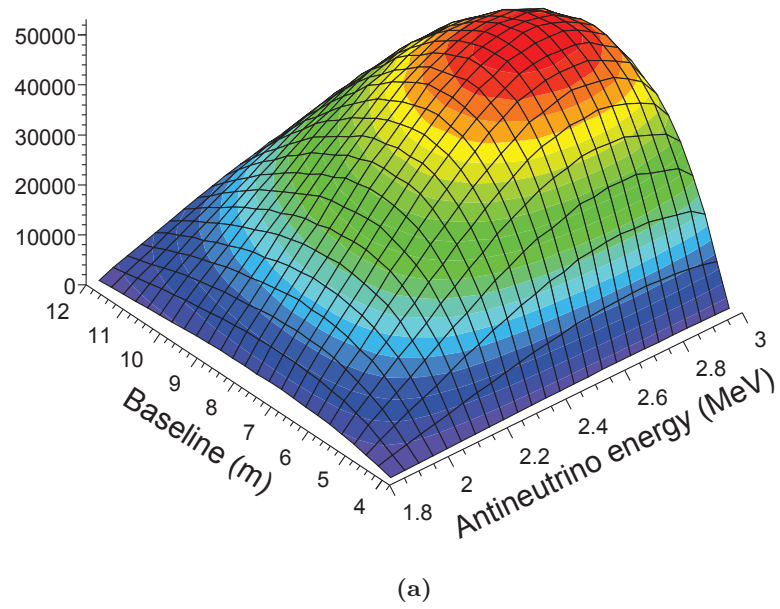


**Figure 4.8:** Expected signal for a  $^{144}\text{Ce}$ – $^{144}\text{Pr}$  source underneath the BOREXINO detector without (a) and with sterile neutrino induced oscillation (b). The mixing parameters are  $\sin^2 2\theta_{14} = 0.15$  and  $\Delta m_{41}^2 = 2.5 \text{ eV}^2$ . Please note that the event rate is not realistic.

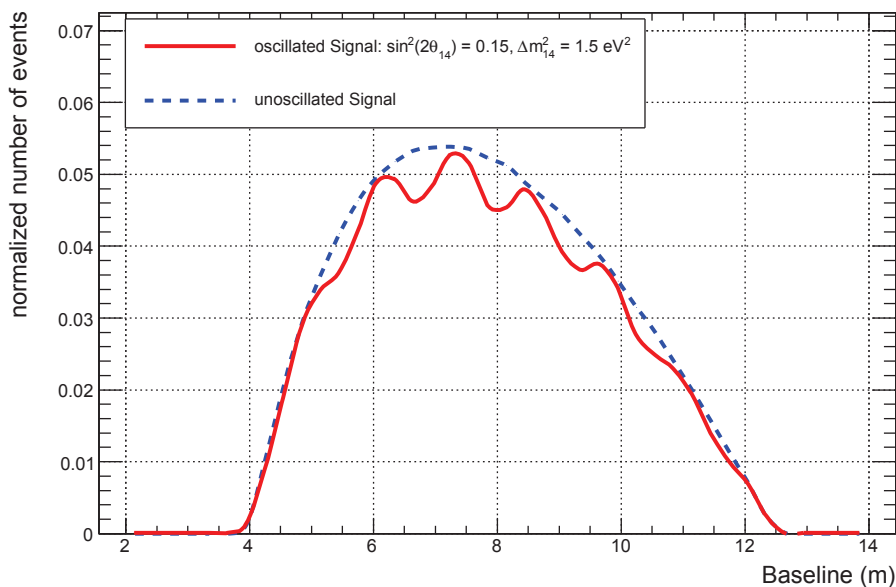


**Figure 4.9:** Expected signal for the  $^{51}\text{Cr}$  source.

The source characteristics of both sources are reviewed in detail in the following chapter. The characteristic oscillation pattern for the  $^{51}\text{Cr}$  source is shown in Figure 4.9. Due to the fact that the neutrinos are mono-energetic, the oscillation pattern becomes visible by reconstructing the baseline of all events.

During the first phase of the SOX project, the old ICARUS pit will house the source directly underneath the BOREXINO detector. The width of this tunnel is only about 1 m and will allow to host the source only 8.51 m from the detector center.

The SOX project will be conducted in Hall C of the LNGS. The experiment will require several modifications and changes around the BOREXINO detector. Most importantly a rail system and an operations building has to be installed to allow source handling and transportation underneath the detector (see Figure 4.7). The source will be housed inside a calorimeter to determine the source activity via its heat release. Two calorimeter are currently under development (one from the TUM/Genoa group and one from the Saclay group). The small building will allow operations connected to these measurements.

The first phase of the experimental setup does not require any changes to the BOREXINO detector itself. Originally, it was discussed to place the  $\bar{\nu}_e$  emitter inside the water tank or in the center of the detector which would have allowed a much higher  $\bar{\nu}_e$  flux. However, any operation might risk to contaminate the detector which would then interfere with any solar neutrino analysis, the main purpose of the experiment.

#### 4.4.3 $^{144}\text{Ce}$ $\bar{\nu}_e$ Source Production

The production of the Cerium source will be performed at the “Federal State Unitary Enterprise Mayak Production Association” (hereafter simply called Mayak). Mayak is a spent nuclear fuel reprocessing facility located 150 km south-east of Yekaterinburg (Russia). [105]

$^{144}\text{Ce}$  is a fission product of Uranium and Plutonium. The reprocessing of spent nuclear fuel involves several steps, including the chemical purification, called PUREX process, which is based on liquid-liquid extraction ion exchange. [105, 114]

	Isotopic composition of natural Cr (%)	Isotopic composition of the enriched Cr (%)	Thermal neutron capture cross-section (barn)
$^{50}\text{Cr}$	4.35	38.6	15.9
$^{52}\text{Cr}$	83.8	60.7	0.76
$^{53}\text{Cr}$	9.5	0.7	18.2
$^{54}\text{Cr}$	2.35	<0.3	0.36

**Table 4.1:** Isotope composition and thermal neutron cross-sections of natural Chromium. Table was taken from [86].

The PUREX process extracts Uranium, Plutonium and Nonylphenole. After this purification process, the “remaining raffinate is concentrated and evaporated” [105] and further processed. Impurities like  $^{137}\text{Cs}$  are removed subsequently. Other contaminants like  $^{90}\text{Sr}$  are removed by precipitation. The remaining concentrate of rare-earth and transplutonic elements is diluted in nitric acid and poured in a 500 m long pipeline. Following the pipeline, a chromatography facility is connected which contains one sorption and two separation columns with  $\text{H}^+$  or  $\text{Ni}_2^+$ . [105]

The Cerium is finally extracted from the separation column and diluted in a solution. During the last step, the Cerium material is precipitated and calcinated into a powder of Cerium-oxide,  $\text{CeO}_2$ . This powder is pressed into pallets with a density of  $4 - 6 \text{ g/cm}^3$  and inserted into a capsule. [105]

#### 4.4.4 Transportation of the $\bar{\nu}_e$ Source

The transportation of the source from Mayak to the detector site is a non-trivial task which involves many certifications and permissions. The Cerium source will be transported by train from Mayak to the Kapitolve station, close to the St. Petersburg harbor. After the source is stored onto a dedicated vessel, the responsibility is taken over by CEA<sup>4</sup>. The ship journey to Le Havre (France) will last approximately two weeks. Hereafter, the source transportation will continue via truck to the LNGS in Italy. A short stop at CEA Saclay for inspection is being considered as well. [105]

The total transportation time is expected to last about three weeks which corresponds to an activity loss of about 3% [105]. Further details about the shielding and other related information can be found in the CELAND paper [114] and in Ref. [105].

#### 4.4.5 $^{51}\text{Cr} \nu_e$ Source Production

For the SOX+Cr phase the old GALLEX source will be refurbished. The production process was described in detail in Ref. [86]. Natural Chromium consists of four stable isotopes. Their abundances and thermal neutron capture cross-sections are given in Table 4.1.  $^{51}\text{Cr}$  is produced by neutron irradiation at a nuclear reactor,  $^{50}\text{Cr} (^{50}\text{Cr} + n \rightarrow ^{51}\text{Cr} + \gamma)$ . Neutron activation of  $^{52}\text{Cr}$  and  $^{54}\text{Cr}$  produces stable isotopes. In order to reach the desired activity an enriched  $^{50}\text{Cr}$  sample has to be used. [86]

The  $^{50}\text{Cr}$  enrichment of the Chromium source was conducted by the Kurchatov Institute in Moscow (Russia). Isotope separation was achieved by means of a gas centrifuge. For that purpose, volatile chromyl fluoride,  $\text{CrO}_2\text{F}_2$ , was used. Afterwards, the enriched  $\text{CrO}_2\text{F}_2$  was

<sup>4</sup>CEA: Commissariat à l’énergie atomique et aux énergies alternatives

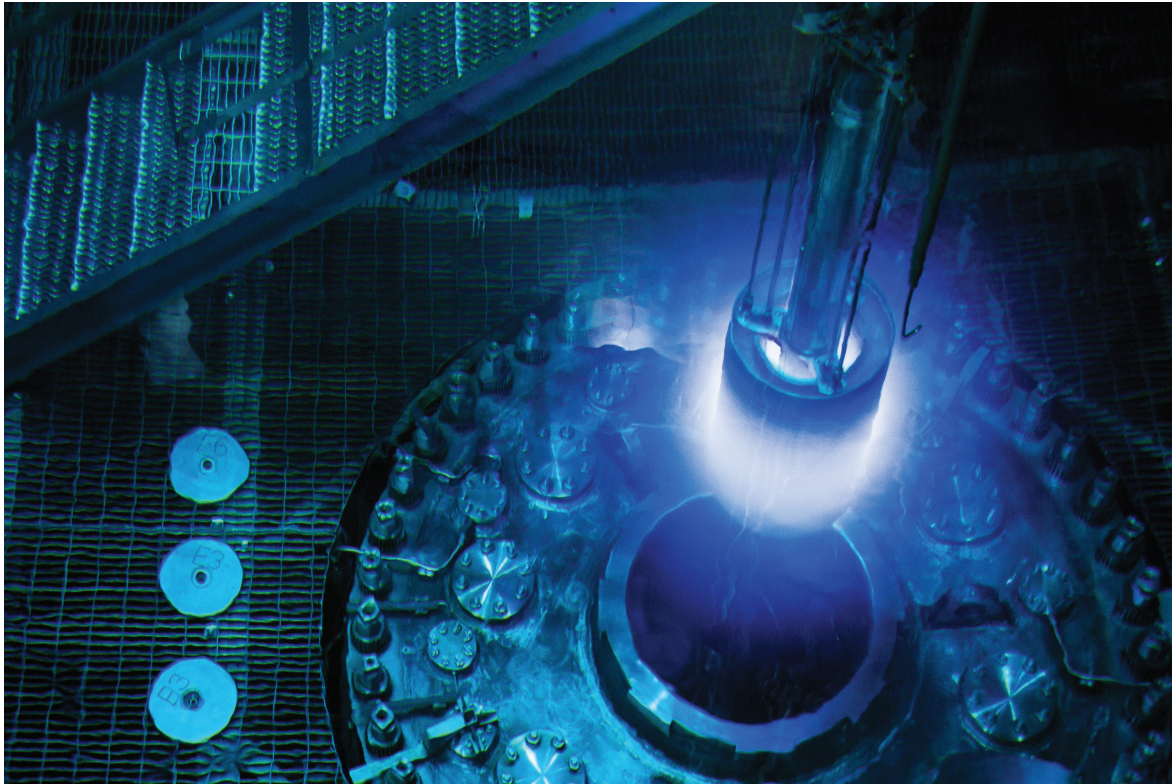


**Figure 4.10:** HFIR Refueling in July 2015. The photo shows the removal of a HFIR fuel element. For the production of the  $^{51}\text{Cr}$  neutrino source, the  $^{50}\text{Cr}$  raw material would enter this research facility for neutron irradiation. Image credit: Genevieve Martin/ORNL

hydrolyzed in water (in the form of ice),  $\text{CrO}_2\text{F}_2 + \text{H}_2\text{O} \rightarrow \text{CrO}_3 + 2\text{HF}$ . The Chromium trioxide,  $\text{CrO}_3$ , was then finally delivered to Saclay. [86]

Chromium metal was produced in Saclay by means of an electrolysis. The resulting Chromium tubes were manually broken into small, irregular shaped chips about  $1\text{ mm}^3$  in volume. For the GALLEX experiment, the Chromium irradiation was performed at Silo  (Grenoble, France). In total, GALLEX performed two calibration campaigns with  $^{51}\text{Cr}$  sources. The observed deficit has already been reviewed in context of the chapter about the neutrino anomalies (see section 3.4). After the GALLEX experiment was completed, the enriched Chromium was stored in Saclay. In preparation of the SOX+Cr project, the source was inspected at Nucleo (Casaccia, Rome).<sup>5</sup> A first and preliminary Chromium content analysis was performed with 0.1238 g material which was dissolved in 1 ml ultra pure Hydrochloric acid. The isotopic abundance of  $^{50}\text{Cr}$  relative to the total sample was estimated to  $37.8\% \pm 0.7\%$  while the  $^{53}\text{Cr}$  content was determined to  $0.7\% \pm 0.7\%$  which is in agreement with the results published by the GALLEX collaboration in 1996 [170]. The  $^{52}\text{Cr}$  and  $^{54}\text{Cr}$  was measured to  $61.5\% \pm 1.1\%$  and  $0.021\% \pm 0.001\%$  [170].

The neutron irradiation in context of the SOX+Cr project can either be performed in Mayak or at the High Flux Isotope Reactor at the Oak Ridge National Laboratory (Tennessee, USA, see Figure 4.10). The HFIR generally runs for approximately 26 days operating at 85 MW. Preliminary studies have been performed to evaluate the expected activity at the HFIR complex. These studies are based on the MCNP simulation code completed with a detailed HFIR model. Under conservative assumptions an activity as high as 5.5 MCi from so-called

<sup>5</sup>A picture of the storage barrel and small Chromium fragments can be found in the Appendix (Figure B.1).

back-to-back double cycle irradiation can be expected [76]. Further studies and feasibility studies from technical experts at ORNL are expected when the projects get approved.

#### 4.4.6 Transportation of the $\nu_e$ Source

The transportation of the  $^{51}\text{Cr}$  after irradiation is one of the critical aspects of the SOX+Cr project as the half-life is only about 27.7 days. After the end of neutron bombardment, the Chromium source will soon enter the calorimeter. The exact logistics are still under discussion. At the detector site, the source will enter the tunnel together with the calorimeter. First results are expected after three month of data taking.

#### 4.4.7 Time Schedule of the SOX Experiment

Following the transfer of the CEA Saclay group with their ERC<sup>6</sup> grant for the  $\bar{\nu}_e$  source production, the focus of the SOX project has shifted towards the SOX+Ce phase. The deployment of a 3 – 5 PBq  $^{144}\text{Ce}$  source is planned between November 2017 and February 2018. First results on the clarification of the observed antineutrino anomalies are expected in 2018. Depending on the results and the funding situation, the SOX+Ce phase might be followed by a second deployment inside the water tank or the deployment of the Chromium source inside the tunnel underneath the BOREXINO detector.

---

<sup>6</sup>ERC: European Research Council



The search for possible light sterile neutrinos can be performed by using either electron capture sources like  $^{51}\text{Cr}$  or  $^{37}\text{Ar}$  with monochromatic neutrino lines or by using intense antineutrino sources ( $^{144}\text{Ce}$ ,  $^{106}\text{Ru}$  or  $^{90}\text{Sr}$ ) with a continuous  $\beta^-$  and antineutrino spectrum [146]. The size of the source used by an experiment should be as compact as possible to observe the characteristic (anti)neutrino oscillation pattern [146]. The BOREXINO experiment will use a  $^{144}\text{Ce}$ – $^{144}\text{Pr}$  antineutrino source and possibly a  $^{51}\text{Cr}$  neutrino source [160]. The calculation of the  $\bar{\nu}_e$  spectrum was performed within this thesis and is outlined in section 5.2.2. In order to achieve the high precision needed for the SOX experiment several sub-leading corrections have been implemented. The  $\bar{\nu}_e$  spectrum shape will serve as an important input for the antineutrino MC generator, sensitivity studies and as a bench-mark for the experimental  $\bar{\nu}_e$  spectrum modeling. Currently, an experimental setup from the Saclay group and the Technical University of Munich is under preparation. The combination of theoretical and experimental studies will then allow to model the antineutrino spectrum with a uncertainty as low as 1% w.r.t the IBD interactions.

$^{51}\text{Cr}$  is an electron capture source featuring four monochromatic neutrino lines. The source properties are summarized in section 5.3.

## 5.1 Radioactive Decay

For the SOX project, the  $\beta^\pm$  and electron capture (EC) decays are relevant.<sup>1</sup> The basic decay processes are therefore in the following form [212]:

$$\beta^- : {}^A_Z X \rightarrow {}^A_{Z+1} Y + e^- + \bar{\nu}_e \quad (5.1)$$

$$\beta^+ : {}^A_Z X_N \rightarrow {}^A_{Z-1} Y + e^+ + \nu_e \quad (5.2)$$

$$EC : {}^A_Z X + e^- \rightarrow {}^A_{Z-1} Y + \nu_e \quad (5.3)$$

The latter two processes are energetically forbidden for free protons and only occur in bound states of the nuclei.

The  $Q$  value is defined as the mass difference between the mother and daughter atom. For the three mentioned processes they are summarized as follows [212]:

$$Q_{\beta^-} = \{[m(Z, A) - Zm_e] - [m(Z+1) - (Z+1)m_e] - m_e\} c^2 + B \quad (5.4)$$

$$Q_{\beta^+} = \{[m(Z, A) - Zm_e] - [m(Z-1, A) - (Z-1)m_e] + m_e\} c^2 + B \quad (5.5)$$

$$Q_{EC} = \{[m(Z, A) - Zm_e] + m_e - [m(Z-1, A) - (Z-1)m_e + m_e]\} c^2 + B \quad (5.6)$$

<sup>1</sup>Within this thesis, decay is defined as a transition accompanied with the release of energy.

Transition Type	$\log ft$	$L_\beta$	$\Delta\pi$	Fermi $\Delta J$	Gamow-Teller $\Delta J$
super-allowed	2.9-3.7	0	0	0	0
allowed	4.4-6.0	0	0	0	0,1
first-forbidden	6-10	1	1	0,1	0,1,2
second forbidden	10-13	2	0	1,2	1,2,3
third-forbidden	>15	3	1	2,3	2,3,4

**Table 5.1:** Transition classification. Table taken from [2].

where  $m$  is the atomic mass and  $B$  represents the binding energy which is released. For  $\beta^-$  decay this may be written as  $B = \sum_{i=1}^Z B_i - \sum_{i=1}^{Z+1} B_i$ . The  $Q$  value is equal to

$$Q = E_e + E_\nu, \quad (5.7)$$

for  $\beta^-$  decays, where  $E_e$  denotes the kinetic energy of the electron and  $E_\nu$  the energy of the antineutrino. The EC and  $\beta^+$  decay are sometimes competing depending on the  $Q$  value of the reaction. If  $Q < 2m_e c^2$ ,  $\beta^+$  decay does not appear.

## 5.2 Antineutrino Source

The section provides all relevant aspects in context of the antineutrino source. The first part summarizes general aspects followed by the theoretical modeling of the  $\beta$  spectrum. This modeling includes several sub-leading corrections. The section ends with the error discussion and gives further information about the experimental efforts which have gained more importance due to the theoretical discussion triggered by this and other studies.

### 5.2.1 Beta Decay Classification

Beta transitions are classified according to the initial and final nuclear state quantum numbers [95, 144].

In Fermi (a) transitions the spin of the neutrino and electron are anti-parallel, which corresponds to vector current transitions. Gamow-Teller (b) decays are axial current transitions (spins are parallel).

$$\begin{array}{ccc|ccc}
 \uparrow & \rightarrow & \uparrow + \downarrow & \uparrow & \rightarrow & \downarrow + \uparrow\uparrow \\
 +\frac{1}{2} & & +\frac{1}{2} & +\frac{1}{2} & & -\frac{1}{2} & +1 \\
 n & & p & n & & p & e, \bar{\nu} \\
 & & (a) & & & (b) & 
 \end{array} \quad (5.8)$$

In terms of the interaction Hamiltonian  $\hat{\mathcal{H}}_{int}$ , the probability amplitude from parent to daughter nucleus forms two possible final states:

$$\hat{\mathcal{H}}_{int} = \begin{cases} \hat{1}\hat{\tau} & \text{Fermi decay} \\ \hat{\sigma}\hat{\tau} & \text{Gamow-Teller decay} \end{cases} \quad (5.9)$$

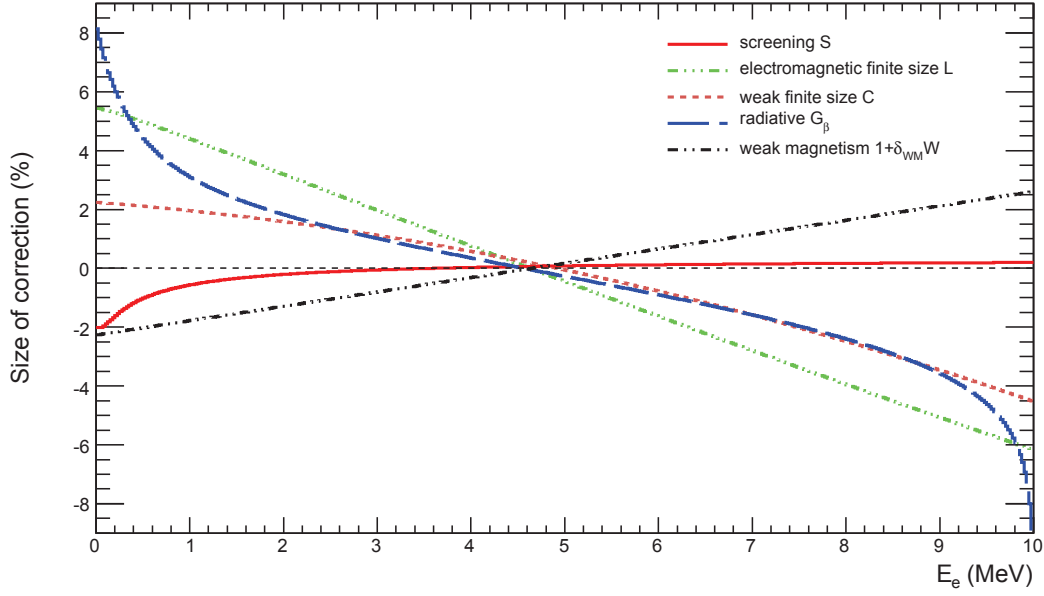


**Figure 5.1:** Relative size of various electron spectrum corrections depending on the electron kinetic energy  $E_e$  for a hypothetical allowed  $\beta$  decay with  $Z=46$ ,  $A=117$  and  $Q = 10$  MeV.

where  $\hat{\tau}$  is the isospin transition matrix and  $\hat{\sigma}$  is the rotational matrix which changes the parity of the parent nucleus from  $0 \rightarrow 1$ . The isospin formalism was first proposed by Heisenberg and is based on the idea that proton and neutron can be treated as two different isospin states of the same nucleon. In Fermi decays the isospin is conserved, while in Gamow-Teller decays the isospin remains unchanged or change by  $\pm 1$ . For forbidden decays the nuclear matrix elements introduce a so-called form factor which alters the beta spectrum.

For a  $n^{\text{th}}$  forbidden  $\beta$  branch  $\Delta J = n$  defines non unique and  $\Delta J = n + 1$  defines unique decays. If  $\Delta J = 0$ , the transition is called allowed. For Fermi transition of the type  $0^+ \rightarrow 0^+$ , the transition is called super-allowed. This classification is directly linked to the decay time and historically the classification was done in terms of the logarithm of the parent nucleus half life  $\log ft$ . The observed selection rules are summarized in Table 5.1.

### 5.2.2 Beta Spectrum Modeling

The  $\beta$  spectrum for a  $n^{\text{th}}$  forbidden ( $n = 0$  for allowed) decay is given by [3]

$$N_{\beta}^0(W) = K S_n W p (W - W_0)^2 F(Z, W), \quad (5.10)$$

where  $S_n$  is the shape factor,  $K$  is a normalization constant,  $Z$  is the atomic number,  $W = E_e/m_e + 1$  is the total energy of the  $\beta$  particle in units of electron mass,  $p = \sqrt{W^2 - 1}$  is the momentum of the  $\beta$  particle, and  $W_0 = Q/m_e \pm 1$  is the maximum  $\beta^{\mp}$  particle energy.  $E_e$  is the kinetic energy of the  $\beta$  particle and  $Q$  is the end-point of the  $\beta$  spectrum.  $F(Z, W)$  is the well-known Fermi function which is the leading QED correction to the  $\beta$  spectrum shape:

$$F(Z, W) = 2(\gamma + 1) (2pR)^{2(\gamma-1)} e^{\pi\alpha ZW/p} \frac{|\Gamma(\gamma + i\alpha ZW/p)|^2}{\Gamma(2\gamma + 1)^2}. \quad (5.11)$$

The Fermi function accounts for the quantum mechanical interaction between the Coulomb field and the electron wave function [1]. It should be emphasized that approximations of the

Fermi function yield large uncertainties for nuclei with large  $Z$  and have to be considered inappropriate for an accurate  $\bar{\nu}_e$  spectrum modeling. The nuclear radius  $R$  depends on  $A$  and can be determined with the Elton formula [100]:

$$R = 0.0029A^{1/3} + 0.0063A^{-1/3} - 0.017A^{-1} \quad (5.12)$$

in units of  $m_e c^2$ .

The shape factors  $S_n$  for forbidden decays are listed as follows:

$$S_n = \begin{cases} p_\nu^2 + p^2 & \text{first unique, second nonunique} \\ p_\nu^4 + \frac{10}{3}p_\nu^2 p^2 + p^4 & \text{second unique, third nonunique} \\ p_\nu^6 + 7p_\nu^2 p^2 + 7p^4 p_\nu^2 + p^6 & \text{third unique, fourth nonunique} \end{cases} \quad (5.13)$$

For precision studies a number of additional effects have to be considered. The modified  $\beta$  spectrum then becomes:

$$N_\beta(W) = K p^2 (W - W_0)^2 F(Z, W) L_0(Z, W) C(Z, W) S(Z, W) G_\beta(Z, W) (1 + \delta_{WM} W) \quad (5.14)$$

The associated antineutrino spectrum is obtained by taking into account the energy conservation  $W_\nu = W_0 - W$  and correct radiative correction  $G_\beta \rightarrow G_\nu$ . In the following the different corrections are summarized and shortly discussed. The size of each of these correction factors for a hypothetical  $\beta$  decay is shown in Figure 5.1 (electron spectrum) and Figure 5.2 (antineutrino spectrum).

To check the calculation the same example as in [132] was used.<sup>2</sup> The spectrum evaluation was written in C++ in the ROOT environment. For the calculation of the complex  $\Gamma$  function the GNU Scientific Library (GSL) was implemented. The corrections which have to be applied are listed in the following; we here particularly follow the summary of *Huber* [132] which is mainly based on the works of *Wilkinson* [201, 202], *Sirlin* [183], *Behrens and Bühring* [56].<sup>3</sup> This summary is complemented by a discussion of potential antineutrino emitters (section 5.2.3) and the calculation of the  $^{144}\text{Ce}-^{144}\text{Pr}$  antineutrino spectrum (section 5.2.4 and 5.2.5). The error discussion is provided in section 5.2.6.

### Electromagnetic Finite Size Correction $L_0$

The Fermi function is derived by solving the Dirac equation for a point-like nuclear charge [202]. A realistic treatment and evaluation of the spectral shape must evaluate the electron and positron wave functions as solutions of the Dirac equation in the extended charge distribution of the nucleus [202]. The electromagnetic finite size correction  $L_0$  is the result of the numerical integration of the Dirac equation:

$$L_0(Z, W) = 1 + 13 \frac{(\alpha Z)^2}{60} - WR\alpha Z \frac{41 - 26\gamma}{15(2\gamma - 1)} - \alpha Z R \gamma \frac{17 - 2\gamma}{30W(2\gamma - 1)} + a_{-1} \frac{R}{W} + \sum_{n=0}^5 a_n (WR)^n + 0.41 (R - 0.0164) (\alpha Z)^{4.5}, \quad (5.15)$$

<sup>2</sup>Please note that in the work of *Huber* [132] the correction factors for the screening and the radiative corrections are wrongly reproduced.

<sup>3</sup>Please also note the independent work originally performed by *M. Durero* [95] in the framework of the CELAND project which is also based on the summary of *Huber*.

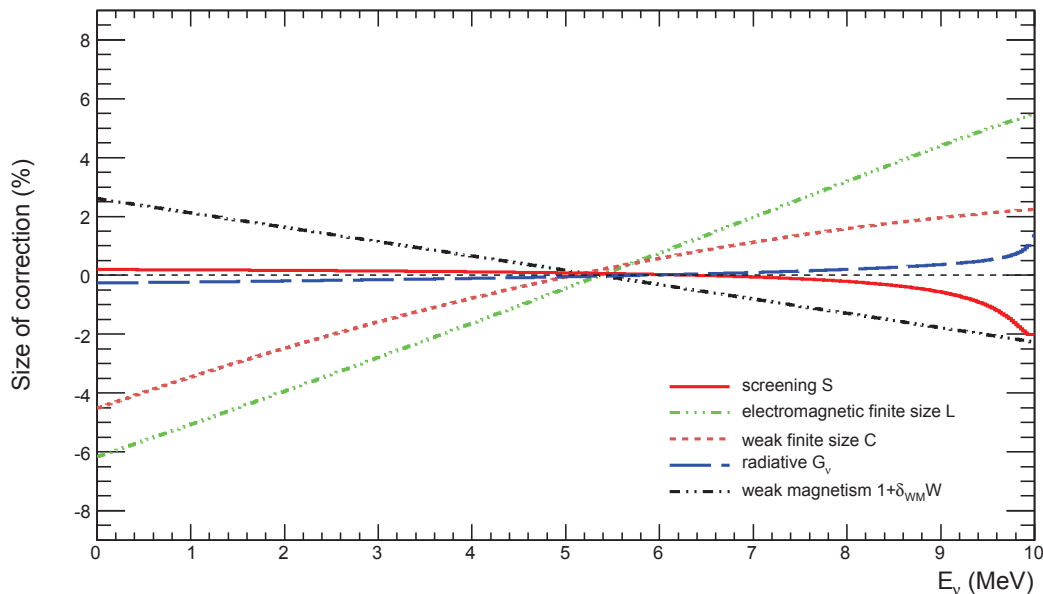


**Figure 5.2:** Relative size of various antineutrino spectrum corrections depending on the antineutrino energy  $E_\nu$  for a hypothetical allowed  $\beta$  decay with  $Z=46$ ,  $A=117$  and  $Q = 10$  MeV.

where  $a_n$  are given by

$$a_n = \sum_{x=1}^6 b_x (\alpha Z)^x \quad (5.16)$$

and the  $b_n$  are taken from Ref. [132] and reproduced in Table A.1 in Appendix A. Eq. (5.15) is only valid for electrons. If positrons ( $\beta^+$  decay) are considered the last term of Eq. (5.15) has to be changed from 0.41 to 0.22 and  $Z$  has to be replaced by  $|Z|$  [202].

### Weak-Interaction Finite Size Correction

The weak interaction finite size correction for Gamow-Teller decays is [132, 202]

$$C(Z, W) = 1 + C_0 + C_1 W + C_2 W^2 \quad (5.17)$$

with

$$C_0 = -\frac{233}{630} (\alpha Z)^2 - \frac{(W_0 R)}{5} + \frac{2}{35} W_0 R \alpha Z, \quad (5.18)$$

$$C_1 = -\frac{21}{35} R \alpha Z + \frac{4}{9} W_0 R^2, \quad (5.19)$$

$$C_2 = -\frac{4}{9} R^2 \quad (5.20)$$

The weak interaction finite size correction is the result of the convolution of the lepton and nucleon wave functions [202]. Analogous to the electromagnetic correction mentioned above it takes into account the finite size of the nucleus. For super-allowed Fermi vector transitions the correction terms have to be modified.

### Screening Correction

The screening correction  $S(W, Z)$  takes into account the electrons in the atomic bound states that screen the positive charge of the nucleus [132, 187]:

$$S(Z, W) = \frac{\bar{W}}{W} \left( \frac{\bar{p}}{p} \right)^{2\gamma-1} e^{\pi(\bar{y}-y)} \frac{|\Gamma(\gamma + i\bar{y})|^2}{|\Gamma(\gamma + iy)|^2}, \quad (5.21)$$

where  $\bar{W} = W - V_0$ ,  $\bar{p} = \sqrt{\bar{W}^2 - 1}$ ,  $y = \alpha ZW/p$ ,  $\bar{y} = \alpha Z\bar{W}/\bar{p}$  and  $\tilde{Z} = Z - 1$ .  $V_0$  is the screening potential and can be parametrized [132] as

$$V_0 = \alpha \tilde{Z}^{4/3} N(\tilde{Z}) \quad (5.22)$$

The Fermi function is effectively shifted by this additional potential. The screening correction is only valid for  $W > V_0$ . Otherwise it is set to  $S(Z, W) = 1$ , since the square root would become negative. From the physical point of view, this “may be interpreted as the deceleration of the emitted electrons by the screening effects of the electron shell down to such low energies that the  $\beta$  decay cannot be observed” [187, p. 31]. The screening potential is derived from numerical calculations. Within this thesis the relativistic Hartee Fock ansatz is used.  $N(\tilde{Z})$  is calculated by linear interpolation of the values in Table A.2 in Appendix A, following the description in [132].

### Radiative Corrections

The  $G_\beta$  factor arises from the emission of real and virtual photons in the  $\beta$  decay process. These corrections are expressed as photon loops in the associated Feynman diagrams for  $\beta$  decay (see Figure 5.3). Due to the fact that only charged leptons radiate photons, the correction term differs for the electron and antineutrino spectrum [163]. This also implies that the electron spectrum is affected more than the antineutrino spectrum. This means that the end-point energy  $E_0 = E_e + E_\nu$  is expanded by an additional term  $E_\gamma$  which represents the energy of the radiated photon [163].

The radiative correction term  $g_\beta$  for the electron spectrum is given by [183]:

$$g_\beta = 3 \ln M_n - \frac{3}{4} + 4 \left( \frac{\tanh^{-1} \beta}{\beta} - 1 \right) \times \left( \frac{W_0 - W}{3W} - \frac{3}{2} + \ln [2(W_0 - W)] \right) \\ + \frac{4}{\beta} L \left( \frac{2\beta}{1 + \beta} \right) + \frac{1}{\beta} \tanh^{-1} \beta \left( 2(1 + \beta^2) + \frac{(W_0 - W)^2}{6W^2} - 4 \tanh^{-1} \beta \right) \quad (5.23)$$

$L(x)$  is the Spence function, defined as  $L(x) = \int_0^x dt/t \ln(1-t)$  [132]. The complete correction is then given by

$$G_\beta(Z, W) = 1 + \frac{\alpha}{2\pi} g_\beta. \quad (5.24)$$

For the calculation of the antineutrino spectrum shape, the compact form derived by *Sirlin* is used [183]:

$$h_\nu = 3 \ln M_N + \frac{23}{4} - \frac{8}{\hat{\beta}} L \left( \frac{2\hat{\beta}}{1 + \hat{\beta}} \right) + 8 \left( \frac{\tanh^{-1} \hat{\beta}}{\hat{\beta}} - 1 \right) \ln(2\hat{W}\hat{\beta}) \\ + 4 \frac{\tanh^{-1} \hat{\beta}}{\beta} \left( \frac{7 + 3\hat{\beta}^2}{8} - 2 \tanh^{-1} \beta \right), \quad (5.25)$$

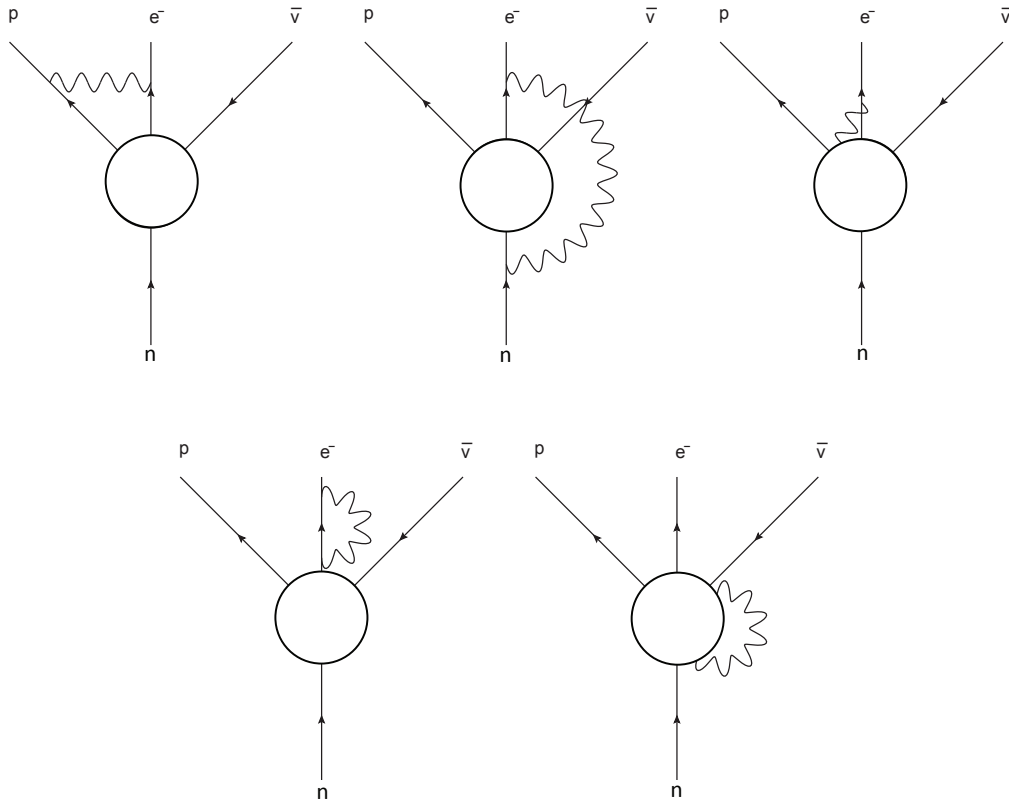


**Figure 5.3:** Feynman diagrams for radiative corrections. Figure taken from [95].

where  $\hat{\beta} = p/W_\nu$  and  $p = \sqrt{W_\nu^2 - 1}$  and  $W = W_0 - W_\nu$ . Analogous to the electron correction, the complete expression is given by [132]

$$G_\nu(Z, W_\nu) = 1 + \frac{\alpha}{2\pi} h_\nu. \quad (5.26)$$

It is important to notice that the radiative corrections are especially high for  $\beta$  decays with a high endpoint  $Q$  in the energy spectrum (see Figure 5.1) [183]. Radiative corrections are also especially important for the calculation of the neutron life-time and for precision tests of the standard model like the verification of the unitarity of the Cabibbo-Kobayashi-Maskawa (CKM) matrix [183].

### Weak Magnetism Correction $1 + \delta_{WM}W$

The weak magnetism correction is given by

$$1 + \delta_{WM}W, \quad (5.27)$$

with

$$\delta_{WM} = \frac{4}{3} \frac{b}{Mc} m_e, \quad (5.28)$$

where  $c$  is the Gamow-Teller matrix element,  $b = \sqrt{2}\mu$  with  $\mu$  being the magnetic transition moment and  $M = A \cdot N$  the mass of the nucleus [132]. In the impulse approximation it is

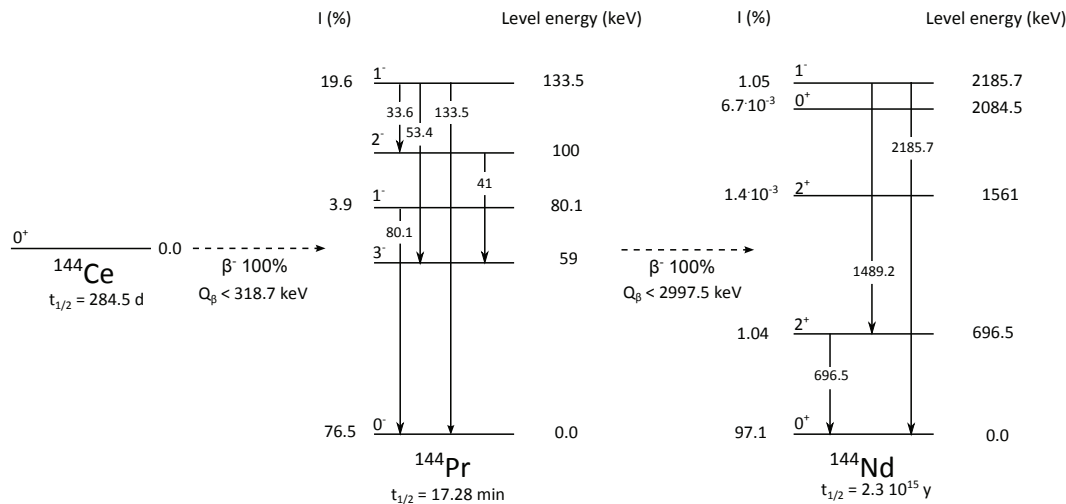


**Figure 5.4:** Simplified decay scheme of  $^{144}\text{Ce}$ – $^{144}\text{Pr}$ .  $^{144}\text{Ce}$  decays with a half life of  $\sim 285$  days, followed by the decay of  $^{144}\text{Pr}$ . The figure layout and data was adopted from [112].

assumed that the magnetic moment is given entirely by the intrinsic anomalous magnetic moments of the proton  $\mu_p$  and the neutron  $\mu_n$  [132]:

$$w = \frac{b}{Mc} \simeq \frac{\mu_p - \mu_n}{M_n} \left| \frac{C_V}{C_A} \right| \quad (5.29)$$

If the orbital angular momentum is neglected  $dN/dE = 4/3 w = 0.5\% \text{ MeV}^{-1}$  is valid for all Gamow-Teller decays. This approximation is supported by the measured values  $dN/dE$  for several  $\beta$  decays with small  $A$  [132].

### 5.2.3 Discussion of Potential Antineutrino Emitters

The deployment of an artificial antineutrino source was discussed since the beginning of the BOREXINO experiment. A suitable  $\bar{\nu}_e$  source must have a long half-life to allow the production and transportation of the source as well as a high  $Q$  value (above the IBD threshold) [146]. In addition, technical challenges in the production have to be taken into account. Four possible isotope pairs have been reported in the literature (see [146] and references therein):  $^{144}\text{Ce}$ – $^{144}\text{Pr}$ ,  $^{106}\text{Ru}$ – $^{106}\text{Rh}$ ,  $^{90}\text{Sr}$ – $^{90}\text{Y}$  and  $^{42}\text{Ar}$ – $^{42}\text{K}$ . “The first three are common fission products from nuclear reactors that can be extracted from spent fuel rods” [146]. In the past predominantly  $^{90}\text{Sr}$ – $^{90}\text{Y}$  was discussed by BOREXINO as a feasible option [136, 134, 135]. This is attributable to the fact that Strontium sources are widely used by the medical industry and several 10 kCi sources have already been produced industrially for heat generation [88]. However,  $^{90}\text{Y}$  has the smallest  $Q$  value of 2.28 MeV which would limit the number of emitted  $\bar{\nu}_e$  above the IBD threshold. In contrast to  $^{106}\text{Ru}$ , the chemical extraction of  $^{144}\text{Ce}$  from spent nuclear fuel is easier and the  $Q$  value of the Praseodymium is higher compared to Yttrium ( $Q_{^{144}\text{Pr}} = 2.995 \text{ MeV}$ ). Cerium is present at the level of 5.5% and 3.7% in the fission products of Uranium and Plutonium, respectively [114]. Considering the production perspective and the high  $\beta$  endpoint, Cerium is considered to be the best choice [114]. The production of  $^{42}\text{Ar}$  was withdrawn due to the high technical challenges in the production. In fact,  $^{42}\text{Ar}$  can only be produced through double neutron capture on stable  $^{40}\text{Ar}$  [112, 114].

“Cerium is mostly produced by the decay of  $^{144}\text{Cs}$  and is abundantly produced in the fission of  $^{235}\text{U}$  and  $^{239}\text{Pu}$ ” [114]. The exact content is naturally linked to the irradiation history and

neutron spectrum [114]. In order to reach the desired sensitivity for sterile neutrino searches, an activity of about 100 kCi has to be reached.

#### 5.2.4 Antineutrino Spectrum Modeling of $^{144}\text{Pr}$

$^{144}\text{Ce}$  undergoes 100%  $\beta^-$  decay to  $^{144}\text{Pr}$ . The end-point energy of  $^{144}\text{Ce}$  is as low as 318.6 keV which is below the IBD threshold. The half-life of  $^{144}\text{Ce}$  is 284.5 d compared to 17.28 min of  $^{144}\text{Pr}$ . The interaction rate in BOREXINO is therefore driven by the Cerium decay while the antineutrinos above the IBD threshold are delivered by the decay of Praseodymium.

$^{144}\text{Pr}$  undergoes 100%  $\beta^-$  decay to various excited states and predominantly to the ground state of  $^{144}\text{Nd}$ . The dominant decay is from the ground state  $0^-$  while the branching ratio of  $^{144}\text{Pr}$  from the excited  $3^-$  state to  $^{144}\text{Nd}$  is as low as  $10^{-6}\%$  and therefore negligible. A simplified decay scheme is shown in Figure 5.4. The complete data set including transition probabilities and energy end-points is shown in Table A.3. The eight dominant  $\beta$  branches have been included for the theoretical modeling. Only two of these  $\beta$  branches exhibit endpoint energies above the IBD threshold. The dominant  $^{144}\text{Pr}$  transition is a  $0^- \rightarrow 0^+$  non-unique first forbidden transition. The electron and  $\bar{\nu}_e$  spectrum of  $^{144}\text{Pr}$  is displayed in Figure 5.5a and 5.5b, respectively. Two discontinuities are visible in Figure 5.5b at 811 keV and 2301 keV corresponding to the endpoints of the two  $\beta$  branches with branching ratios of 1.05% and 1.04%, respectively. The other branches have only a minor impact on the spectrum shape. All branches drawn separately are shown in Figure 5.6. The theoretical modeling of the  $\bar{\nu}_e$  spectrum is based on Fermi's theory of  $\beta$  decay as outlined in the previous section. In addition, several sub-leading corrections particularly such as finite size, screening of the atomic electrons and radiative effects have been considered. The size of each of these corrections can be in the order of a few percent as seen in Figure 5.7 and 5.8. The calculations of these corrections are generally assumed to be known with high accuracy and often treated without theoretical errors. Weak magnetism is expected to be negligible as the dominant  $^{144}\text{Pr}$  has no angular momentum change [130]. The dominant uncertainty arises then from the screening correction and possibly from shape factors of the first non-unique forbidden transitions of  $^{144}\text{Pr}$  as further discussed in section 5.2.6.

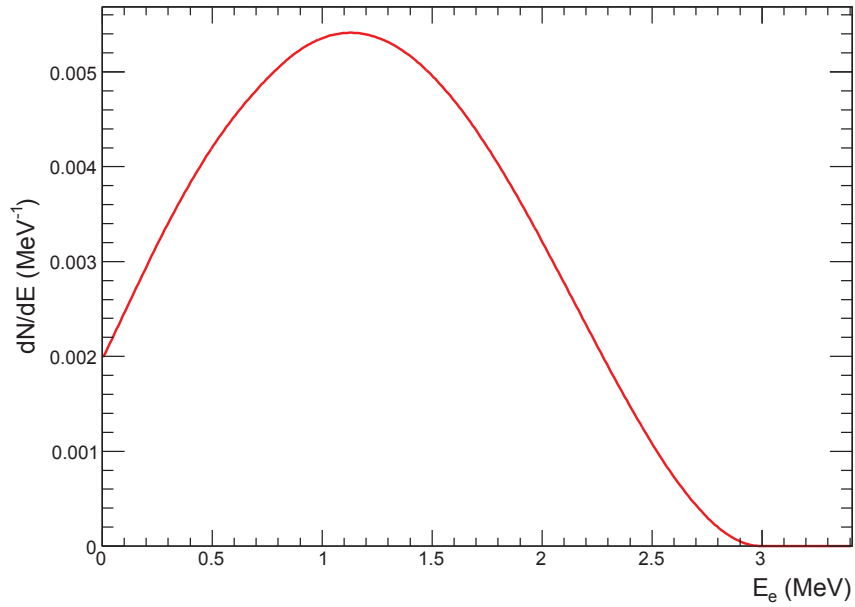
Further experimental studies are foreseen to constrain the error of these corrections. For these measurements the inversion from the measured spectrum into the corresponding antineutrino spectrum is straightforward, if nuclear recoil effects are neglected [132]. Any uncertainties are therefore symmetric, except of the radiative corrections. As shown in Figure 5.7 and 5.8, radiative corrections to the electron spectrum have a higher amplitude. The adjustment and conversion to the  $\bar{\nu}_e$  spectrum might be the crucial point in this analysis.

#### 5.2.5 Antineutrino Spectrum Modeling of $^{144}\text{Ce}-^{144}\text{Pr}$

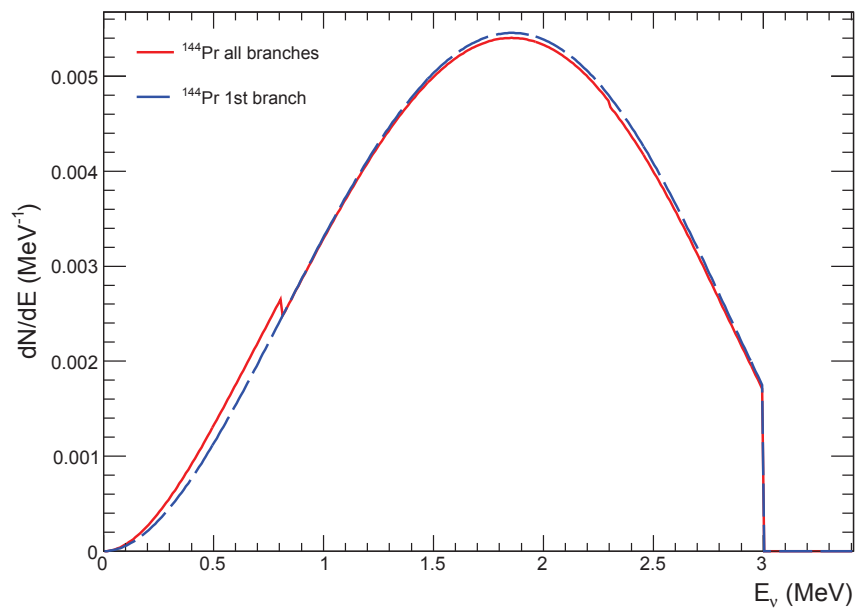
The most important part of the theoretical antineutrino spectrum modeling concerns the  $^{144}\text{Pr}$  spectrum as only this isotope delivers  $\bar{\nu}_e$  above the IBD threshold. However, the source combined activity of both  $^{144}\text{Ce}$  and  $^{144}\text{Pr}$  is directly linked to the mean released energy. This value has to be known precisely as an input parameter for the calorimetric activity measurement.<sup>4</sup> From this point of view, the modeling of the Cerium part is important for any rate based analysis.<sup>5</sup>

<sup>4</sup>Please note that the heat contribution comes not only from  $\beta$ 's but also from  $\gamma$ 's. For all contributions please see Table A.3 in Appendix A.

<sup>5</sup>Accordingly, other isotope contaminants of the  $^{144}\text{Ce}-^{144}\text{Pr}$  source might play a role. The developed framework for the  $\bar{\nu}_e$  spectrum modeling can incorporate this as well once the contaminants have been identified via mass spectroscopy.



(a)



(b)

**Figure 5.5:** Electron spectrum (a) and antineutrino spectrum (b) of  $^{144}\text{Pr}$ . The calculation of both spectra incorporates several sub-leading corrections particularly such as finite size, screening of the atomic electrons and radiative effects.

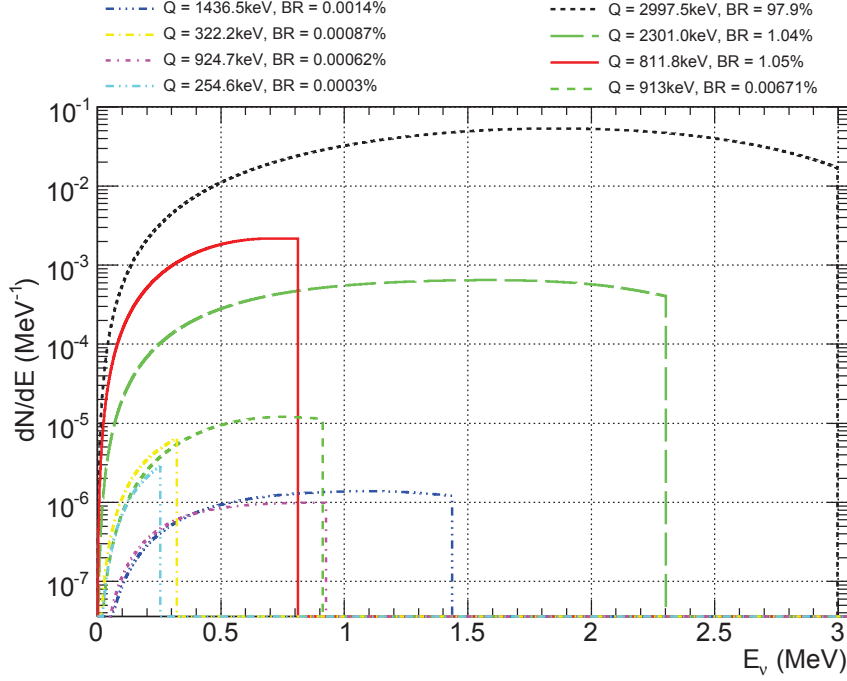


**Figure 5.6:** Relative contribution of all eight dominant  $\bar{\nu}_e$  spectra of  $^{144}\text{Pr}$  in logarithmic scale. The endpoint energy  $Q$  and branching ratio (BR) is provided at the top of the figure. Please note that only two branches exhibit endpoint energies above the IBD threshold. The discontinuities visible in the total  $\bar{\nu}_e$  spectrum can be identified as the endpoints of the two  $\beta$  branches with branching ratios of 1.05% and 1.04%, respectively.

$^{144}\text{Ce}$  undergoes 100%  $\beta^-$  decay to  $^{144}\text{Pr}$ . Three  $\beta$  branches have been identified which are classified as first forbidden non-unique transitions. The dominant transition has a branching ratio of 76.9% with an end-point of 318.6 keV. The complete data set of  $^{144}\text{Ce}$  is summarized in Table A.3. Figure 5.9 shows the electron and  $\bar{\nu}_e$  spectrum including three  $^{144}\text{Ce}$  branches together with the five dominant branches of  $^{144}\text{Pr}$  assuming secular equilibrium. In analogy to the previous study, all sub-leading effects outlined in section 5.2.2 have been implemented.

It may be worthwhile to mention that the theoretical modeling of the  $^{144}\text{Ce}$  spectrum may be especially important as the experimental effort might be limited due to the equipment used at these low energies and due to limitations in the achievable source purity. From the experimental point of view it is unlikely that the apparatus alone will be able to measure the entire  $\beta$  spectrum, especially at low kinetic energies where both contributions from  $^{144}\text{Ce}$  and  $^{144}\text{Pr}$  are overlapped. The energy scale and experiment efficiency might also be difficult to measure.

### 5.2.6 $^{144}\text{Ce}$ – $^{144}\text{Pr}$ Spectrum Error Discussion

To reach the best possible sensitivity for the sterile neutrino search, an antineutrino flux uncertainty of 1% or better is desired. The calculation outlined in the previous section is generally regarded to be known with high precision. Following Ref. [132], theoretical errors can safely be ignored. An error propagation conducted in Ref. [95] confirms this assumption and has determined the error on the IBD rate to be less than 0.40%. Considering 7100 IBD interactions, this amounts to less than 30 events compared to  $\sim 85$  events arising from the statistical error. According to Ref. [114] and [95], the biggest uncertainty on the IBD rate was originally expected from the weak magnetism correction. This assumption follows Ref.

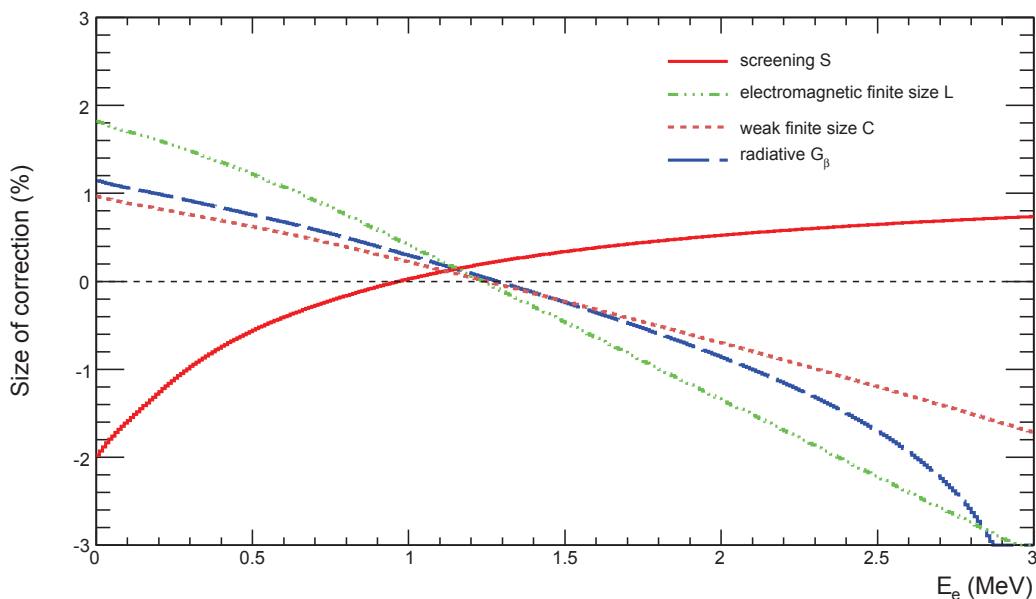


**Figure 5.7:** Relative size of various electron spectrum corrections depending on the electron energy for the  $^{144}\text{Pr}$  source.

[132] and [163]. However, as pointed out in section 5.2.4 following the study in [130], the dominant  $^{144}\text{Pr}$  transition has no angular momentum change. The weak magnetism plays therefore no significant role and can be neglected. The uncertainty of 0.4% given above takes this into account.

Triggered from the study of this thesis and the work presented in Ref. [95], additional corrections have been identified. In the previous calculation all transitions were approximated as allowed transitions. However, forbidden transitions introduce an additional shape factor  $\Psi$  which is depending on the specific matrix element.<sup>6</sup> The calculation of the matrix element is strongly model dependent and the exact definition of the shape factor has to be regarded as speculative. In [94], the effects of different matrix elements on the IBD rate were studied. Taking into account the values of the matrix elements found in the literature, the uncertainty might be negligible or amount to an uncertainty of more than 10% in the IBD rate. Additional, other effects are discussed in the literature (electron exchange effect, meson exchange effect) which lack a precise theoretical description. Partly, attempts have been made to measure these effects in different experiments. However, the obtained data provides no cohesive description.

Two  $\beta$  spectroscopy experiments are currently under preparation in Saclay and Munich to measure the spectral shape of  $^{144}\text{Ce}$  and  $^{144}\text{Pr}$ . Together with the theoretical  $\bar{\nu}_e$  modeling presented in this thesis, the best possible result will be pursued. In case of a high-precision measurement combined with the theoretical modeling, new insights in the theoretical modeling of forbidden transitions and matrix element calculations might be achieved.

In context of the SOX project, the question of interest is how these uncertainties affect the sensitivity for the sterile neutrino search. The result of this study are based on the profile likelihood method (section 7.4.1) and have been reported in Ref. [166]. These studies

<sup>6</sup>The shape factor for forbidden transitions is denoted  $\Psi$  within this thesis. The full correction then becomes  $N_\beta\Psi$  in which  $N_\beta$  includes all theoretically known corrections. Please note that this factor is often called  $C$  in the literature. However, to avoid ambiguities with the finite size correction, we have chosen  $\Psi$ .

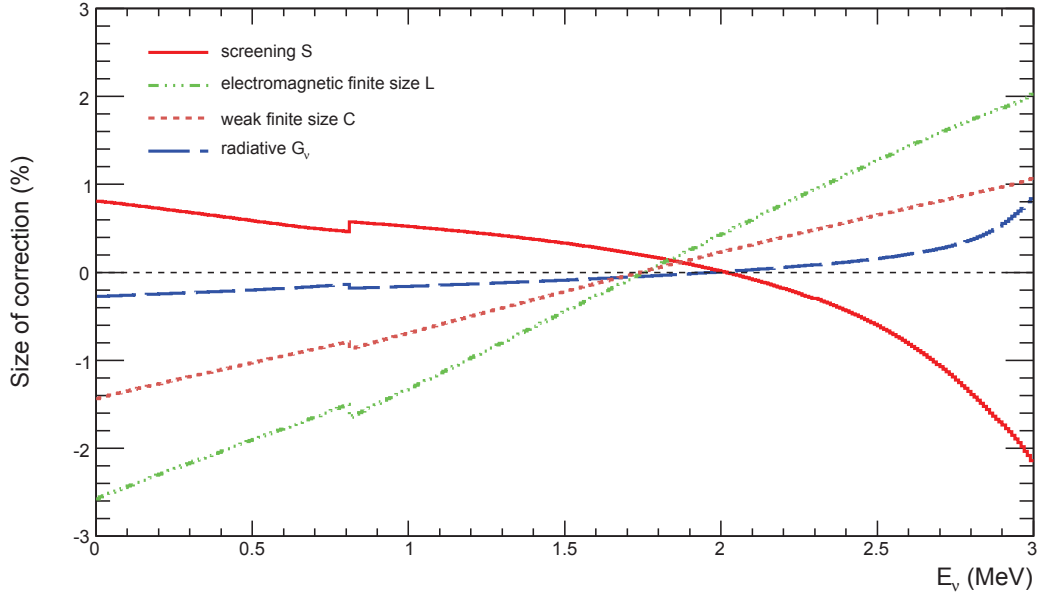


**Figure 5.8:** Relative size of various neutrino spectrum corrections for the  $^{144}\text{Pr}$  source.  $E_\nu$  is the antineutrino energy. This plot was already published by the author in Ref. [161].

incorporate the shape factor following the parametrization by *Behrens* and *Bühring* [56]:

$$\Psi = 1 + aW + \frac{b}{W} + cW^2, \quad (5.30)$$

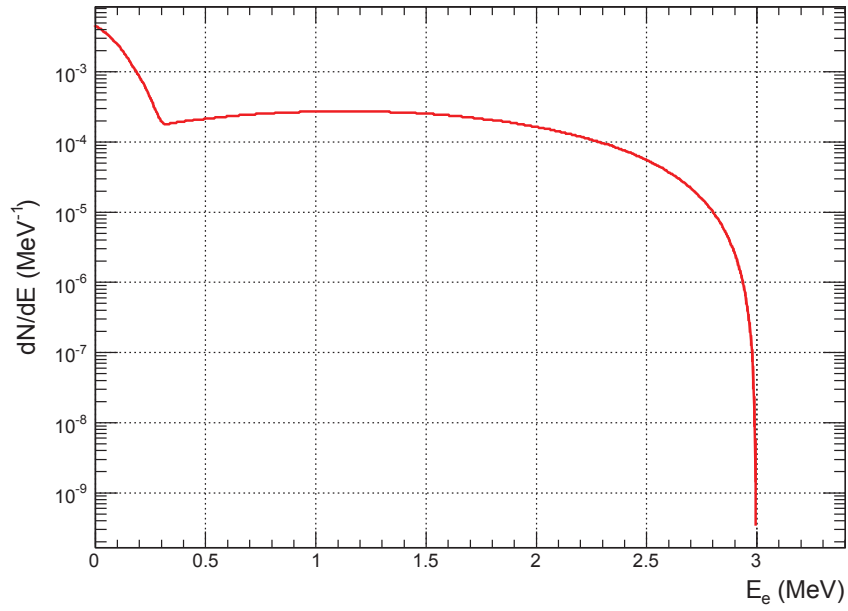
where  $W$  is the reduced energy while  $a$ ,  $b$  and  $c$  denote the measured experimental coefficients. According to [166], the factors  $a$  and  $c$  are not theoretically motivated leaving  $b$  as the factor of most interest. A fourth parameter, denoted as  $H$ , was included to account for the conversion heat power which is linked to the activity by  $A = H / \langle S_\beta(a, b, c) \rangle + \text{const}$ . The most recent result of these studies is shown in Figure 5.10.<sup>7</sup> It may be worthwhile to emphasize that the shape factors can hardly mimic any oscillation pattern induced by sterile neutrinos at  $\Delta m_{41}^2 \in [0.1, 0.8] \text{ eV}^2$  [166]. A so-called *shape only* analysis, where the normalization uncertainty of the inverse beta decay events is set to infinity (see section 7.4.1 for more details), is only weakly affected [166]. Studies performed later in this thesis always include exclusion limits for the shape-only case.

### 5.2.7 Comparison to Beta Spectroscopy Results

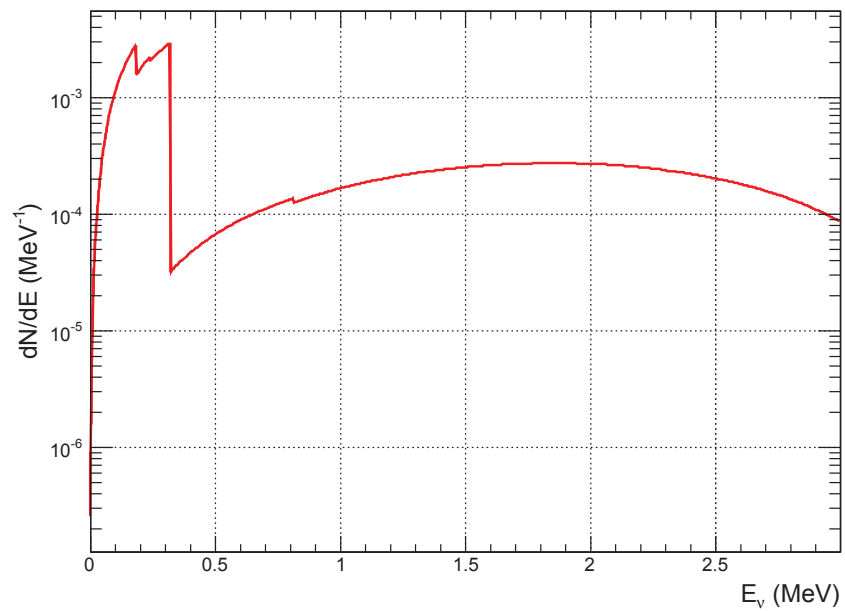
As mentioned in the previous section, two  $\beta$  spectroscopy experiments are under preparation. The apparatus developed in Munich was originally used for the determination of the antineutrino spectrum of the fission products of  $^{238}\text{U}$  (see Figure 5.11). The setup uses a  $\gamma$  suppressing electron telescope and consists of plastic scintillator coupled with a PMT and a multi-wire chamber for coincidence analysis [122]. The experimental setup is currently adopted for the Cerium and Praseodymium measurement.

The Saclay setup consists mainly of plastic scintillators and PMTs. The setup uses Hamamatsu R6231-100 photo-multiplier tubes with a quantum efficiency of about 35% and allows

<sup>7</sup>An updated version based on the presented spectrum calculation is under preparation.



(a)



(b)

**Figure 5.9:** Total electron (a) and  $\bar{\nu}_e$  (b) spectrum of  $^{144}\text{Ce}$ – $^{144}\text{Pr}$ . For the modeling secular equilibrium was assumed.

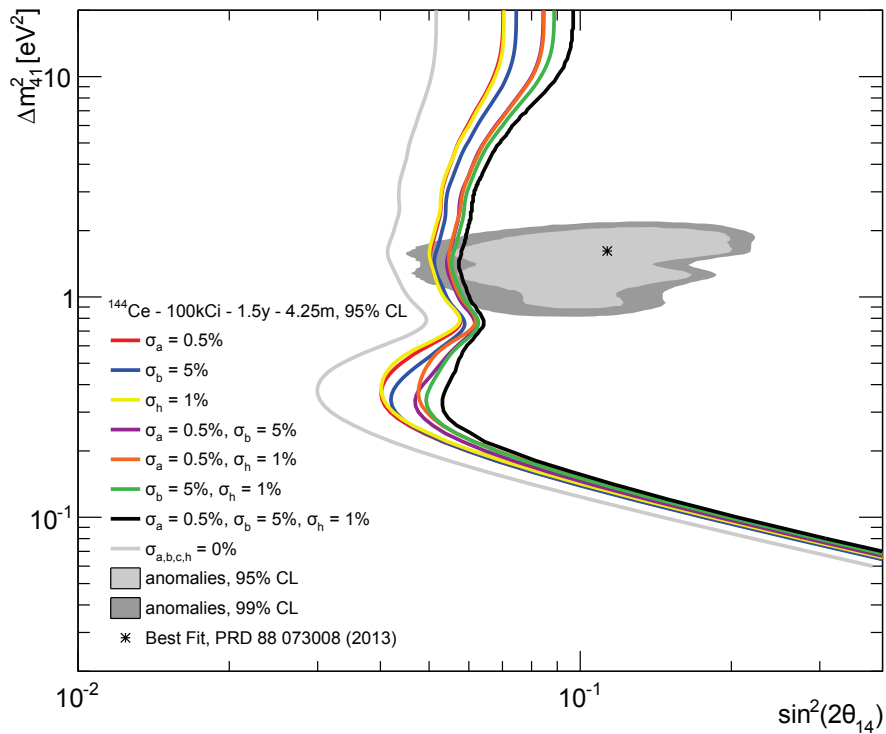


**Figure 5.10:** Impact of the shape factor uncertainty on the SOX sensitivity. Figure taken from [166].

a  $4\pi$  coverage of the electrons [45]. It has also a direct contact between the source and scintillator plastic allowing a low-energy threshold [45]. The experimental layout of the Saclay setup is depicted in Figure 5.12.

These measurements are needed not only from the theoretical point of view (determination of the matrix element dependent shape factor for forbidden transitions and possibly other effects) but also due to the great disagreement of past  $\beta$  spectroscopy results which are summarized in Ref. [39]. The shape factors presented in these studies account for several corrections excluding the QED-leading correction from the Fermi function. These measurements have mainly been conducted in the fifties, sixties and seventies of the past century. These shape factors are thus not equal to the shape factor of forbidden transitions, although this factor is included in it together with the other corrections (finite size etc.). These studies lack some details concerning whether and to what exact level the screening corrections is implemented. The results are summarized in Table 5.2. The studies have been performed by using mostly a magnetic spectrometer. The measurement of *Bosch et. al* is based on a scintillating crystal.

### 5.3 Neutrino Source

Two neutrino sources ( $^{51}\text{Cr}$  and  $^{37}\text{Ar}$ ) have already been produced and used in radio-chemical solar neutrino experiments. The following section will focus on these sources and summarize their properties.



**Figure 5.11:** A side view on the TUM experimental setup to measure the  $^{144}\text{Ce}$ – $^{144}\text{Pr}$  spectral shape. “The neutron beam enters the setup on the left and propagates horizontally through the cross piece. A target holder is inserted from the top, positioning the foils in the neutron beam. The multi-wire chamber is situated between the two yellow gas in - and outlet valves, 9 cm beneath the neutron beam. The lower part houses the scintillator and the photomultiplier, which looks towards the target position”. Text and Figure taken from [122].

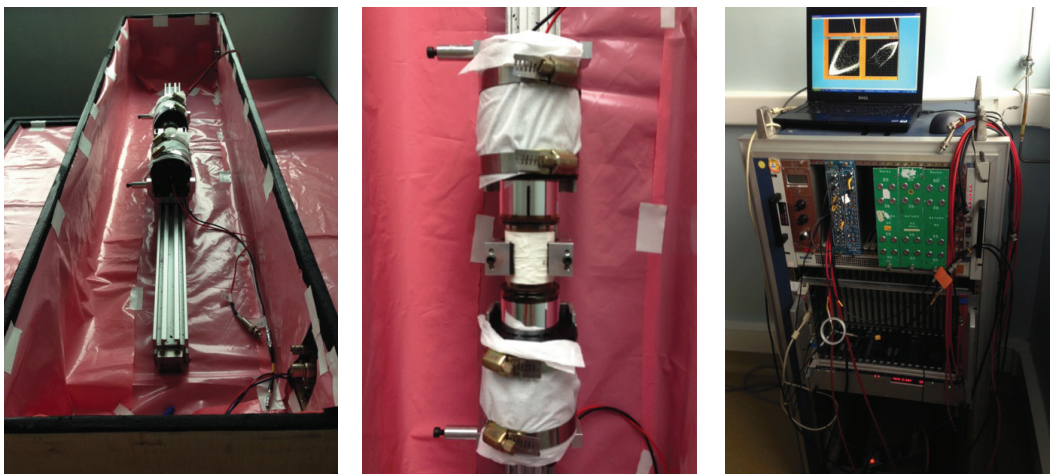


**Figure 5.12:** Saclay Apparatus to measure the  $^{144}\text{Ce}$ – $^{144}\text{Pr}$  spectral shape. Figure taken from [45].

Reference	Exp. setup	Shape factor	Endpoint $E_0$ [keV]
Laubitz (1956)	spectrometer	$1 - 0.058W - 0.389/W$	$2990 \pm 10$
Graham et al. (1958)	spectrometer	$1 + 0.0146W + 0.0283/W$	2984
Porter and Day (1956)	spectrometer	$1 + 0.028W + 0.091/W + 0.0041W^2$	2992
Daniel and Kaschl (1966)	spectrometer	$1 + 0.03W + 0.118/W + 0.008W^2$	$2996 \pm 3$
Nagarajan et al. (1971)	spectrometer	$1 + (0.0975 \pm 0.013)/W$	$3000 \pm 4$
Bosch et al. (1973)	scint. crystals	$1 + 0.33/W$	$3002 \pm 5$

**Table 5.2:** Past measurements of the shape factor. Summary taken from Ref. [39]. Please note that from the information available in the literature it is unclear whether the shape factor given in the table is equal to  $\Psi$  as defined within this thesis. It may include other corrections as well.

### 5.3.1 Discussion of Potential Neutrino Emitters

In the past, two different neutrino sources have been used. These sources are classified as electron capture sources and have previously been produced by the GALLEX and SAGE collaborations mainly in the nineties of the last century [43, 124, 7, 8, 9]. BOREXINO will possibly refurbish the old GALLEX source [170, 160, 169, 65]. From the technical point of view the production of these sources is challenging [112]. Both sources have to be produced by neutron irradiation inside nuclear reactors. The production of  $^{51}\text{Cr}$  is done through  $^{50}\text{Cr}(n, \gamma)^{51}\text{Cr}$  reactions while  $^{37}\text{Ar}$  can only be produced through  $^{40}\text{Ca}(\alpha, n)^{37}\text{Ar}$  reactions [112]. The high neutron flux for the last reaction makes it necessary to produce such a source inside a breeder reactor. In terms of half-life, heat release and  $\gamma$  shielding,  $^{37}\text{Ar}$  is easier to handle [112] since the neutrino emission of the  $^{51}\text{Cr}$  isotope is associated with the release of an 320 keV  $\gamma$  in 10% of all cases.  $^{37}\text{Ar}$  decays with a branching ratio of 100% directly to the ground state  $^{37}\text{Cl}$ . However, the technical challenge associated with the use of a breeder, makes Chromium the better choice, especially due to the fact that the old Chromium rods used by GALLEX were provided and could easily be refurbished.

Natural Chromium consists of four stable isotopes,  $^{50}\text{Cr}$ ,  $^{52}\text{Cr}$ ,  $^{53}\text{Cr}$  and  $^{54}\text{Cr}$  (see Table 4.1) [86]. The isotopic abundance of  $^{50}\text{Cr}$  amounts to only 4.35%. Since  $^{53}\text{Cr}$  has a relatively large thermal cross-section of 18.2 barn, enriched Chromium has to be used. For the GALLEX calibration campaign, an amount as high as 39.8% of  $^{50}\text{Cr}$  was achieved with a negligible amount of  $^{53}\text{Cr}$  at the level of less than one percent [86].

For the BOREXINO+Cr phase two reactors for irradiation are under discussion (Mayak in Russia or HFIR in the US). Since the detection of the  $\nu_e$  will be performed by the elastic scattering off electrons with an relatively small cross-section compared to the IBD, an activity as high as 7 – 10 MCi has to be reached. It seems feasible to reach at least 5 MCi with one irradiation [76]. The source experiment might therefore be performed twice to gain a similar sensitivity as could be reached by a 10 MCi neutrino source. Studies concerning the irradiation optimizations are currently under way.

Compared to the antineutrino source, the transportation time of the  $^{51}\text{Cr}$  is even more critical as the half-life is only 27.7 days.

### 5.3.2 Source Characteristics of $^{51}\text{Cr}$ and $^{37}\text{Ar}$

$^{51}\text{Cr}$  features four monochromatic neutrino lines. In 81.6% of the time it decays to the ground state of  $^{51}\text{V}$  and emits a 747 keV  $\nu_e$ , while in 8.5% of the time a 752 keV  $\nu_e$  is emitted depending whether the electron was captured from the innermost  $K$  or the second innermost  $L$  shell. In 9.9% of the time  $^{51}\text{Cr}$  decays to the first excited state of  $^{51}\text{V}$  followed by the

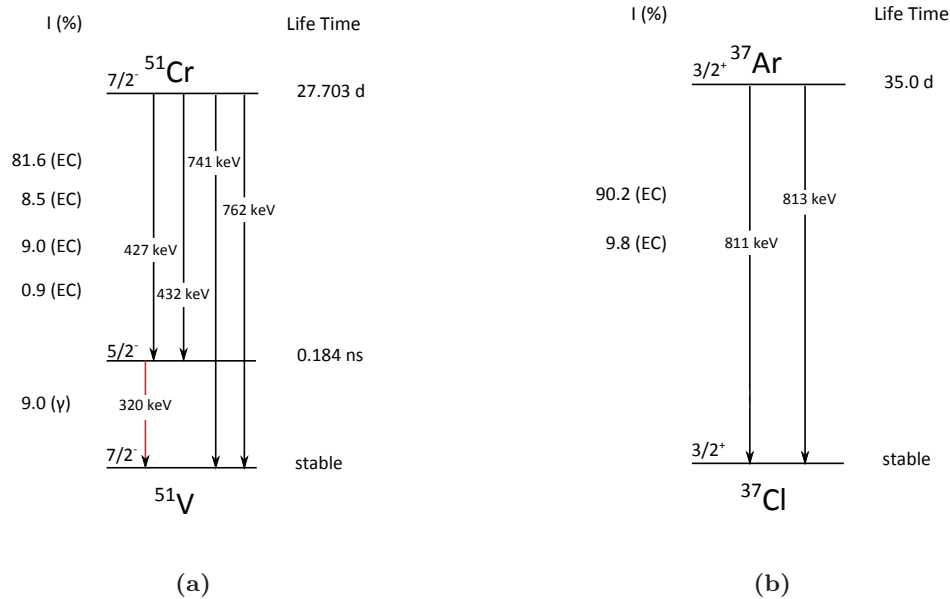


**Figure 5.13:** Decay scheme of  $^{51}\text{Cr}$  (a) and  $^{37}\text{Ar}$  (b). In 9.9% of all cases  $^{51}\text{Cr}$  decays to the first excited state of  $^{51}\text{V}$  followed by the emission of a 320 keV  $\gamma$  which has to be incorporated in the shielding design of the source. Both sources are EC emitters and thus producing mono-energetic neutrino lines.

emission of a 320 keV  $\gamma$ . This is associated with the emission of a 427 keV (432 keV)  $\nu_e$ . The dominant  $\nu_e$  line is very similar to the 0.862 MeV  $\nu_e$  from the radioactive decay of  $^7\text{Be}$  in the Sun which makes it an ideal calibration source for solar neutrino experiments [160].  $^{51}\text{Cr}$  has a half-life of 27.7 days.

$^{37}\text{Ar}$  decays with a half-life of 35 days into  $^{37}\text{Cl}$ . With a branching ratio of 90.2% a 823 keV  $\nu_e$  is released while in 9.8% off all cases a 811 keV  $\nu_e$  is released. The decay scheme of both sources is depicted in Figure 5.13.

## 5.4 Summary

The  $^{144}\text{Ce}$ – $^{144}\text{Pr}$  isotope pair was identified as the most suitable candidate for a BOREXINO source experiment. The theoretical modeling of the antineutrino spectral shape was performed within this thesis. Previous studies had focused on a  $^{90}\text{Sr}$ – $^{90}\text{Y}$  antineutrino emitter and a  $^{51}\text{Cr}$  source. However, the theoretical modelings did only include the Fermi function as the leading QED correction.<sup>8</sup> In this work it was shown that other sub-leading corrections can affect the antineutrino spectrum at a few percent level. The presented  $^{144}\text{Ce}$ – $^{144}\text{Pr}$  spectrum calculation is the most-precise theoretical modeling currently possible. Nevertheless, the theoretical uncertainties of forbidden transition might introduce an additional shape factor  $\Psi$  which makes it necessary to constrain this uncertainty in an experimental setup. For that purpose, two experiments are currently developed in Saclay and Munich. The effect on the sensitivity was studied in [166] and was summarized at the end of this chapter.

For a possible  $^{51}\text{Cr}$  source experiment all relevant properties have been summarized in this chapter. Since  $^{51}\text{Cr}$  is an electron capture source, no sophisticated theoretical calculations had to be performed. The challenges using a Chromium source are present at the event

<sup>8</sup>Past studies were based on approximation of the Fermi function. Unfortunately, these approximations are only valid for nuclei with small  $A$ . The modeling performed within this thesis uses the exact Fermi function.

---

selection and the background level estimation. In contrast to an antineutrino source where the IBD reaction allows to search for a coincident signal, the neutrino signal from a neutrino emitter arises from the neutrino scattering off electrons.



Like many modern experiments, BOREXINO relies on a precise and accurate modeling of the detector response. The “high precision measurement of the  ${}^7\text{Be}$  solar neutrino flux”, the “measurement of [the]  ${}^8\text{B}$  solar neutrinos with low energy threshold”, the direct measurement of the pep and recently the pp neutrinos were only possible due to a fundamental understanding of the detector behavior [91, p. 45]. This also involves investigations regarding the detector stability, energy calibration and the spatial reconstruction of the events [91]. The Monte Carlo simulation chain consist of several numerical codes in order to simulate the event generation, energy loss and the emulation of the electronic detector response [77]. The fundamental physics simulation is performed within the **Geant4** based framework **G4bx(2)**. This code was written in C++ and simulates the passage of particles through matter. The first version (**G4bx**) of this software package was already tuned and “reproduces the data with [an] accuracy of 1% or better for all quantities relevant for [the] data analysis” [91, p. 45]. The high precision of this modeling is achieved by and linked to several calibration campaigns with radioactive sources ( $\alpha$ ,  $\beta$ ,  $\gamma$  and neutron sources) for the fine-tuning of the full simulation output [77, 91]. **G4bx2** is the successor of this code and is currently under preparation. In the future all analyses are expected to be performed with this new simulation framework.

The full Monte Carlo simulation is one of the key elements of any analysis performed by the BOREXINO collaboration. As part of the **G4bx(2)** framework the geometry of the detector and so-called generators are implemented. The generator defines the physics input for the simulation. The SOX **Geant4** based generators for the upcoming analysis and search for sterile neutrinos were designed and developed within this thesis. The generators are namely the *sterile antineutrino generator* to simulate signals originating from the inverse beta decay, the *sterile antineutrino scattering generator* as well as the *sterile neutrino scattering generator*. The two latter ones are designed to simulate the scattering of the (anti)neutrinos on the electrons of the BOREXINO target. The calculation of the antineutrino spectral shape performed in section 5.2.4 serves as one of the important inputs for these generators. Other generators relevant for the upcoming analysis within the SOX project and for future solar measurements parallel to the SOX project are briefly summarized.

## 6.1 Software Structure

The simulation chain contains three major programs which are listed in the following:

- **G4Bx(2)** for setting up the geometry and material properties, simulating the energy loss, particle tracking and light propagation [77, 91].
- **Bx\_elec** for reproducing the electronics behavior and data collection [77]
- **Echidna** for data decoding and event reconstruction [77]

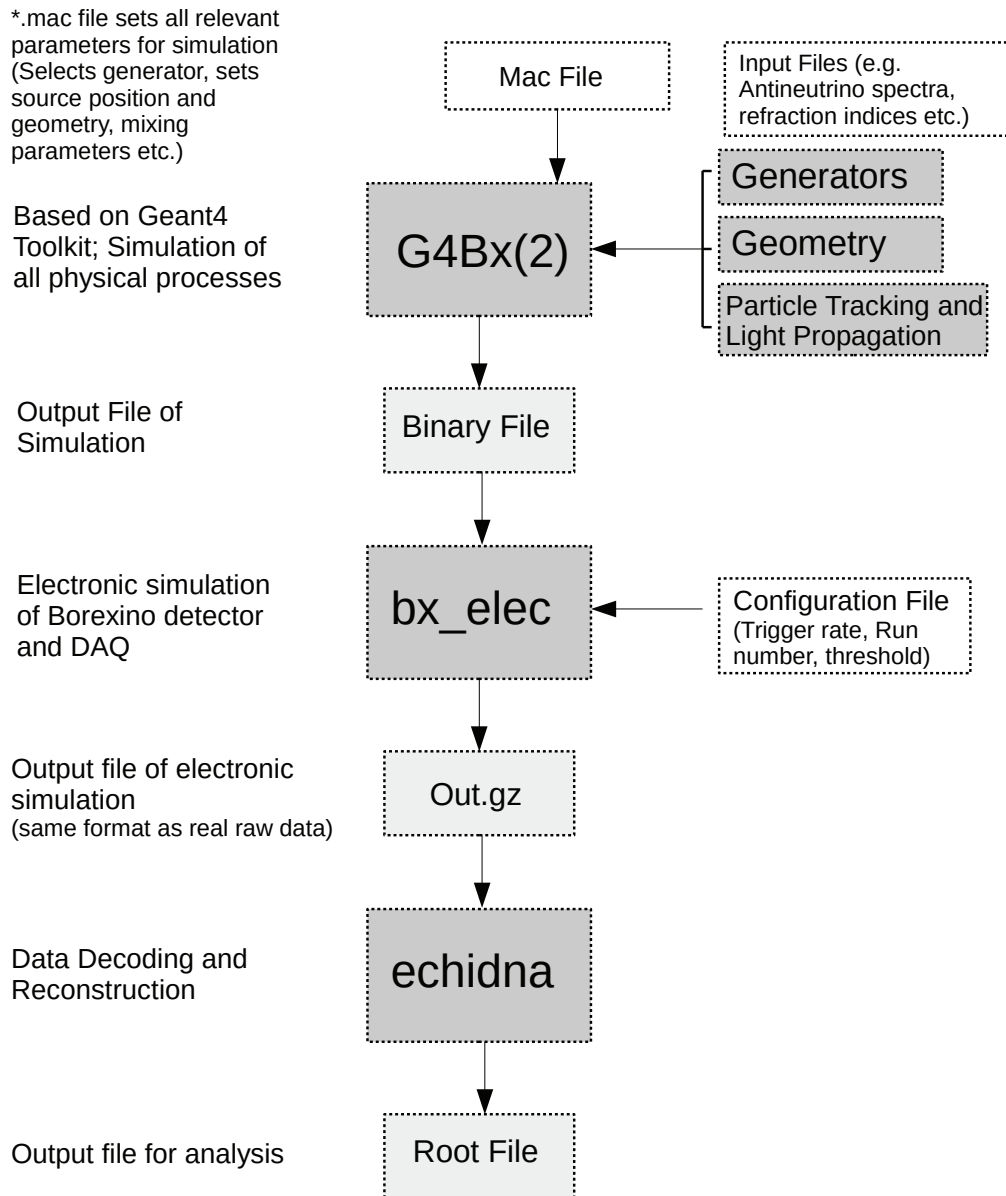
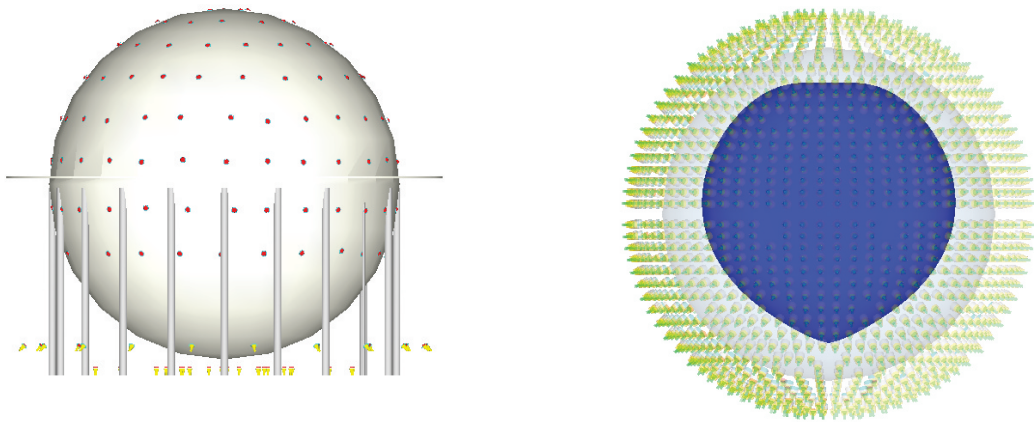


**Figure 6.1:** Software structure for the data processing. The so-called generators define the physics input of the simulation. The simulation itself is based on `Geant4` and uses a specific BOREXINO embedded simulation framework called `G4Bx(2)`. The spectrum calculation performed in chapter 5 serves as an important input parameter for the sterile neutrino generators.



(a) Stainless steel sphere and support structure. Depicted on the bottom are the PMTs which are part of the Cherenkov muon system. They are complemented by the PMTs installed upon the stainless steel pointing outwards.

(b) Interior view of the BOREXINO vessel. The deformation of the inner vessel (blue) is clearly visible. The PMTs pointing towards the vessel are shown in green/yellow.

**Figure 6.2:** View of the BOREXINO detector generated with `G4Bx2` and `OpenGL`. `OpenGL` is a programming interface for rendering three dimensional objects. It is implemented within the BOREXINO MC framework to define different geometrical objects.

The principle layout of the software structure is depicted in Figure 6.1. The simulation of all physical processes and the particle tracking is performed within the `G4Bx(2)` framework. The simulation input is set via a so-called `mac` file. This includes the setting of neutrino mixing parameters, detector geometries and other relevant aspects. Part of the `G4Bx(2)` framework are the generators. Depending on the setting in the `mac` file different physical processes can be selected. The output of the simulation chain has the same format as the real data recorded by the BOREXINO data acquisition system. The data is stored in a `ROOT` tree. The simulated tree contains additional so-called branches containing information of the original simulation. These variables are labeled throughout this thesis as true variables (e.g. true energy, true vertex etc.).

### 6.1.1 Detector Model

The detector description contains the modeling of the water tank, stainless steel sphere and the PMTs, including their surrounding structure [77, p. 87]. The geometry and material are implemented via `GDL` and are an accurate reproduction of the real BOREXINO detector in terms of the dimensions and material properties ([77, p. 87], see also Figure 6.2 and 6.3). This includes the modeling of liquids, namely water, the buffer as well as the liquid scintillator. Their physical parameters like reflectivity, absorption length and refraction index have previously been measured and implemented as part of the Monte Carlo tuning process. Similar to this, the physical parameters of the stainless steel sphere have been included.

The standard option for the inner vessel is a sphere with a diameter of 9.5 m. The deformation of the inner vessel can be selected according to a specific run period (see Figure 6.2b).

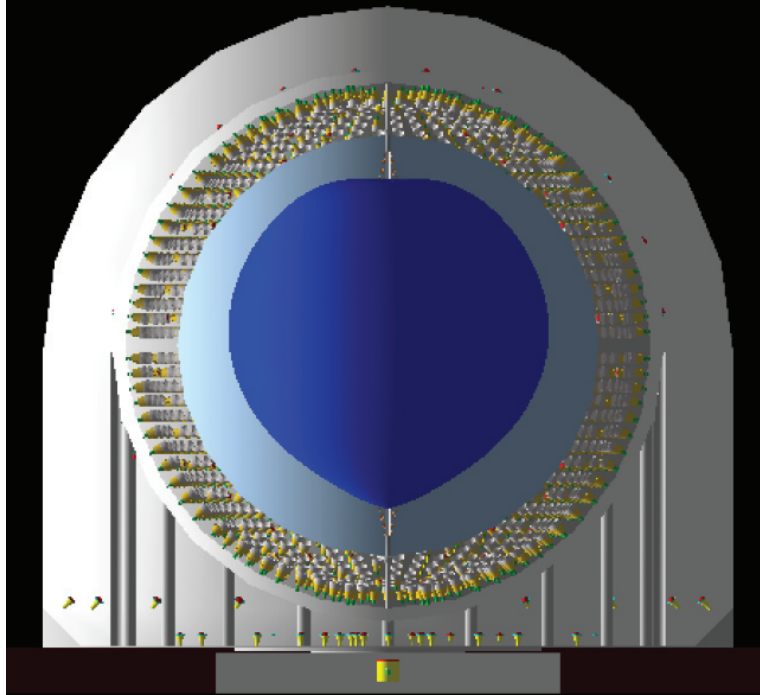


**Figure 6.3:** BOREXINO detector. The current geometry of the detector includes both tunnel and source geometry. Latter one is important for upcoming *Geant4* background simulations to validate the analytically performed calculations as well as to validate and *Tripoli-4* based background estimations. Plot courtesy by A. Caminata.

## 6.2 Particle Generators

As part of the *G4bx(2)* framework, several particle generators have been developed. This includes the solar neutrino generator to simulate the neutrino elastic scattering of each solar neutrino component as well as generators to simulate the decay of isotopes, calibration sources, geo-neutrinos and muons [91, p. 47]. Major ingredients of the generators are the spectra, cross-sections for different reactions and the vertex randomization.

The generators for the upcoming SOX analysis and search for sterile neutrinos were developed and designed within the work of this thesis. The sterile scattering generator includes options to simulate the  $^{51}\text{Cr}$  and  $^{37}\text{Ar}$  neutrino sources as well as the possibility to simulate the scattering of the  $^{144}\text{Ce}$ – $^{144}\text{Pr}$  source-induced antineutrinos off electrons. A second generator was developed to simulate the products of the inverse beta decay reaction of an antineutrino source such as the  $^{144}\text{Ce}$ – $^{144}\text{Pr}$   $\bar{\nu}_e$  source. Both generators are reviewed within the following sections. The vertex generation, similar for both sources, is reviewed within the first subsection. Other generators relevant for the analysis presented in the following chapter are summarized as well.

### 6.2.1 Position Generation

The position generation is one of the important ingredients of the developed Monte Carlo generators. It has to reflect the physical properties of the scintillator. Furthermore, the vertex reconstruction is used for many BOREXINO analyses. The reconstruction of the vertex is used for the definition of the fiducial volume, but may also play a significant role in different parts of the analysis chain. An accurate and reliable MC position generation, which reflects real data with high precision, is therefore mandatory. For the SOX project a position dependent

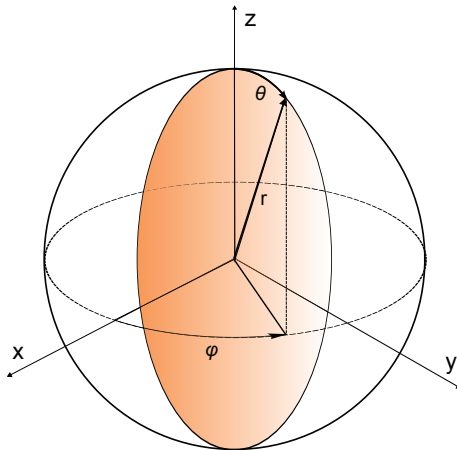


**Figure 6.4:** Coordinate system of the BOREXINO detector.

interaction rate as given by the oscillation probability is expected. The BOREXINO Monte Carlo environment includes the so-called *true* data set as well as the *reconstructed* data. True energy and position are used as input parameters for the electronic and physics simulation. The generation of true position and energy sets is part of the generators. For the SOX analysis, two sets of position vectors representing the space position  $(x, y, z)$  are required. One vector defines the decay point of the neutrino while the second vector defines the interaction position of the neutrino within the specified fiducial volume. The definition of the BOREXINO coordinate system is shown in Figure 6.4. The center of the detector is located at  $\vec{r} = \vec{0}$ .

The neutrino source can be placed at any desired position outside or inside the BOREXINO detector. The associated vector is defined as

$$\vec{r}_0 = \begin{pmatrix} x_0 \\ y_0 \\ z_0 \end{pmatrix}. \quad (6.1)$$

Within the selected source geometry, the decay point is uniformly randomized. The source position and geometry can be selected via a `macro` file. The compilation of the `G4Bx(2)` environment can therefore be avoided if changes of these parameters are conducted. Two different source geometries have been implemented (spherical and cylindrical geometry). A spherical source is parametrized via a spherical coordinate triplet and is given by

$$\begin{pmatrix} x_s \\ y_s \\ z_s \end{pmatrix} = r_s \begin{pmatrix} \sin \vartheta \cos \varphi \\ \sin \vartheta \sin \varphi \\ \cos \vartheta \end{pmatrix}, \quad (0 \leq \vartheta \leq \pi, 0 \leq \varphi \leq 2\pi), \quad (6.2)$$

where  $(x_s, y_s, z_s)$  are the Cartesian coordinates and  $r_s$  denotes the distance from the sphere center to a certain decay point (see Figure 6.5). For the upcoming SOX+Ce phase, Cerium oxide powder will be used. The decay point of the isotope within the sphere is therefore considered to be uniform. As part of the position randomization process a set of three random numbers between zero and one are generated,  $(z_1, z_2, z_3)$ . The random numbers are generated using `TRandom3` within the embedded `ROOT` framework. The position set is then given by

$$\begin{aligned} r_s &= R_S z_1^{1/3} \\ \varphi &= 2\pi z_2 \\ \vartheta &= \arccos(2z_3 - 1) \end{aligned} \quad (6.3)$$

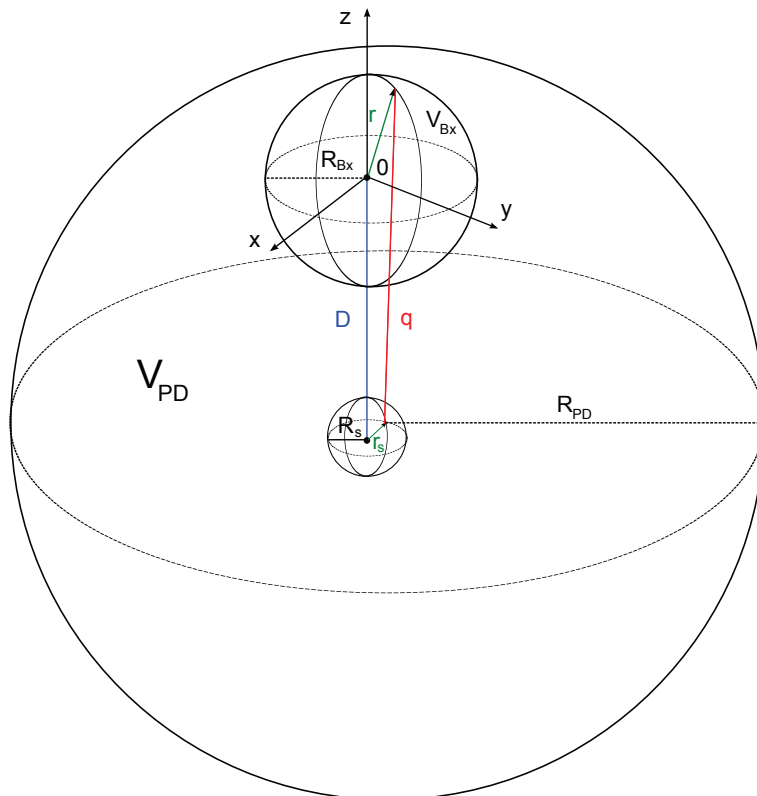


**Figure 6.5:** Vertex randomization for the sterile neutrino generators. The volume  $V_{Bx}$  represents the fiducial volume of the BOREXINO detector. At a distance of  $D$  the source is deployed. Vertices are generated within the volume  $V_{PD}$ . Only if the vertex is generated within the detector (within the volume  $V_{Bx}$ ) the event is stored and further processed.

The radius of the selected source is given by  $R_S$ . Cartesian coordinates are retrieved from the spherical coordinate triplet by the well known standard procedure.

However, for the upcoming SOX+Ce phase, the cylinder has been fixed as source geometry and is therefore the realistic choice. The coordinate triplet for the source is then given by

$$\begin{pmatrix} x_s \\ y_s \\ z_s \end{pmatrix} = \begin{pmatrix} R_c \cos \varphi \\ R_c \sin \varphi \\ z_s \end{pmatrix}, \quad (6.4)$$

where the source radius is given by  $R_c$ . With a given set of random numbers,  $(z_1, z_2, z_3)$ , the decay point is given by

$$\begin{pmatrix} r_c \\ \varphi \\ z \end{pmatrix} = \begin{pmatrix} r_c \sqrt{z_1} \\ 2\pi z_2 \\ h_c z_3 / 2 \end{pmatrix} \quad (6.5)$$

The decay point position in the detector framework is then the sum of the source position vector and the Cartesian coordinate triplet of the decay point.

The next important step is the generation of the neutrino interaction vertex. For that purpose two mathematical solids are defined. One of the solids  $V_{Bx}$  represents the active BOREXINO detector and is the strict subset of a sphere  $V_{PD}$  (see Figure 6.5). Starting from the decay point, the potential interaction point is isotropically randomized inside  $V_{PD}$ . The neutrino

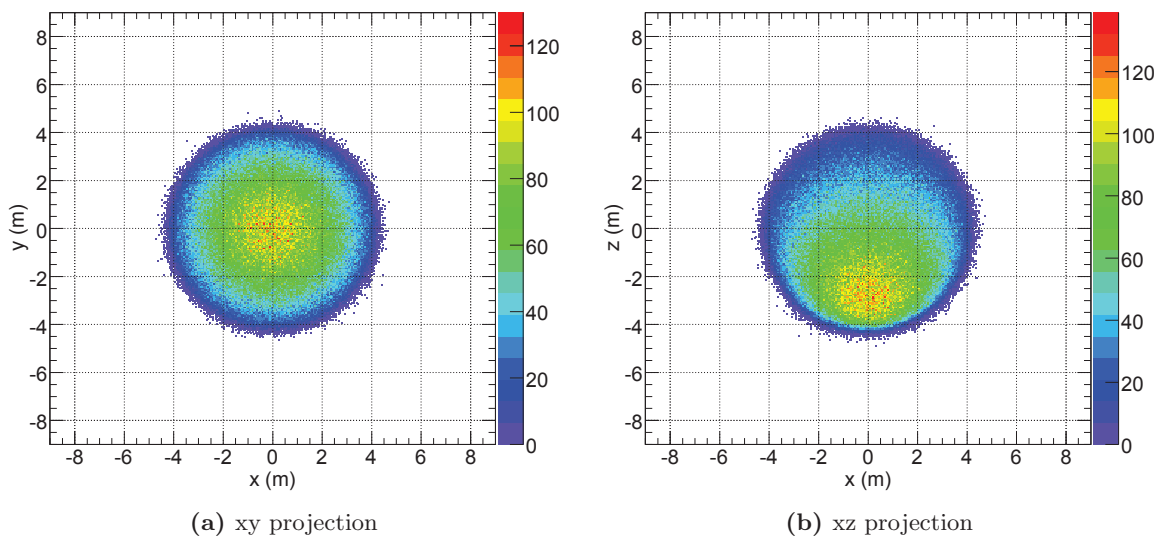


**Figure 6.6:** Reconstructed vertices for a source deployed 8.25 m underneath the BOREXINO detector.

baseline is given by  $q = R_{PD}z$  with  $z$  being a random number between zero and one. The associated parameters  $\varphi$  and  $\vartheta$  are computed analogous to Eq. (6.3). Only if the potential interaction position is inside the fiducial volume of the BOREXINO detector the position vector is returned. Taking the true neutrino energy and baseline into account, the event is only stored, if the oscillation probability allows it.

The reconstructed vertices in the  $xy$  and  $xz$  projections are shown in Figure 6.6. The influence of the source position is visible in the  $xz$  projection with an accumulation of events in the lower part of the detector.

### 6.2.2 Solar Neutrino Generator

The solar neutrino generator was developed to simulate elastic scattering interactions of all different solar neutrino components [91] such as pp,  ${}^7\text{Be}$ ,  ${}^8\text{B}$ , pep and CNO neutrinos. The neutrino spectra are based on the computations of *John Bahcall and collaborators* [52] (see also [91, p. 48]). The kinetic energy of the electrons is randomly extracted according to the differential cross-section which includes first order radiative corrections. The oscillation probability of the electron neutrinos ( $P_{ee}$ ) is calculated according to the LMA-MSW prediction [91]. Matter effects are included following Ref. [92]. The flavor conversion is computed taking into account the user defined input parameters of  $\theta_{Sun}$  and  $\Delta m_{Sun}^2$  (see also [91, p. 48]).

The vertex distribution is homogeneously distributed over the selected fiducial volume.

### 6.2.3 Radioactive Decay Generator

Within the G4bx(2) framework the radioactive decay generator called Radioactive Decay Module (RDM) was implemented. This generator is used to simulate the radioactive decay of isotopes via  $\alpha$ ,  $\beta^\pm$ ,  $\gamma$  emission and by electron capture [91]. The simulation model is data-driven and “uses the Evaluated Nuclear Structure Data File (ENSDF, [188])” [91, p. 48].

Complementing this, two additional radioactive decay generators are available. One of these generators was originally developed for the CTF<sup>1</sup>. The code is implemented within the old simulation framework `GeNeb` and was written in `FORTRAN`. A third generator is called `SCS` and is embedded in the `G4Bx(2)` framework. It is used to simulate individual user defined spectra for some nuclear decays such as the decay of <sup>11</sup>C and <sup>210</sup>Bi where several references in the literature are in disagreement. [91]

#### 6.2.4 The Sterile Antineutrino Generator

For the upcoming analysis within the SOX project, a sterile antineutrino generator was developed. The structure is based on the existing geo-neutrino generator and is part of the `G4bx(2)` framework.

The antineutrino spectrum convoluted with the inverse beta decay cross-section is embedded via an external `ROOT` file. The particular advantage of this procedure is that the spectrum can easily be replaced while no compilation of the actual generator is needed. With this generalization it is also possible to perform the simulation with other radioactive sources like <sup>90</sup>Sr. For future analyses the setting of the spectral shape factor is possible. Following reference [56] this is included using a polynomial function with three coefficients:

$$\Psi = 1 + \bar{a} \cdot E_\nu + \bar{b}/E_\nu + \bar{c} \cdot E_\nu^2, \quad (6.6)$$

where  $E_\nu$  is the kinetic energy of the antineutrino and  $\bar{a}$ ,  $\bar{b}$  and  $\bar{c}$  specific coefficients. The antineutrino energy is randomly extracted using `TRandom3` within the embedded `ROOT` framework. The oscillation effect due to sterile neutrinos is included according to the two flavor approximation. The oscillation parameters  $\sin^2 2\theta_{41}$  and  $\Delta m_{41}^2$  are given as input parameters. The true baseline  $L$  is taken into account as the absolute value of the vector sum of the decay and interaction position as described in the previous section.

The output of the sterile  $\bar{\nu}_e$  generator is shown in Figure 6.7a and 6.7b. The reconstructed energy and distance is compared to the expected theoretical values. Taking into account resolution effects and an energy calibration a good agreement was reached. Thus, the signal generated with the generator agrees well with the theoretical expectation.

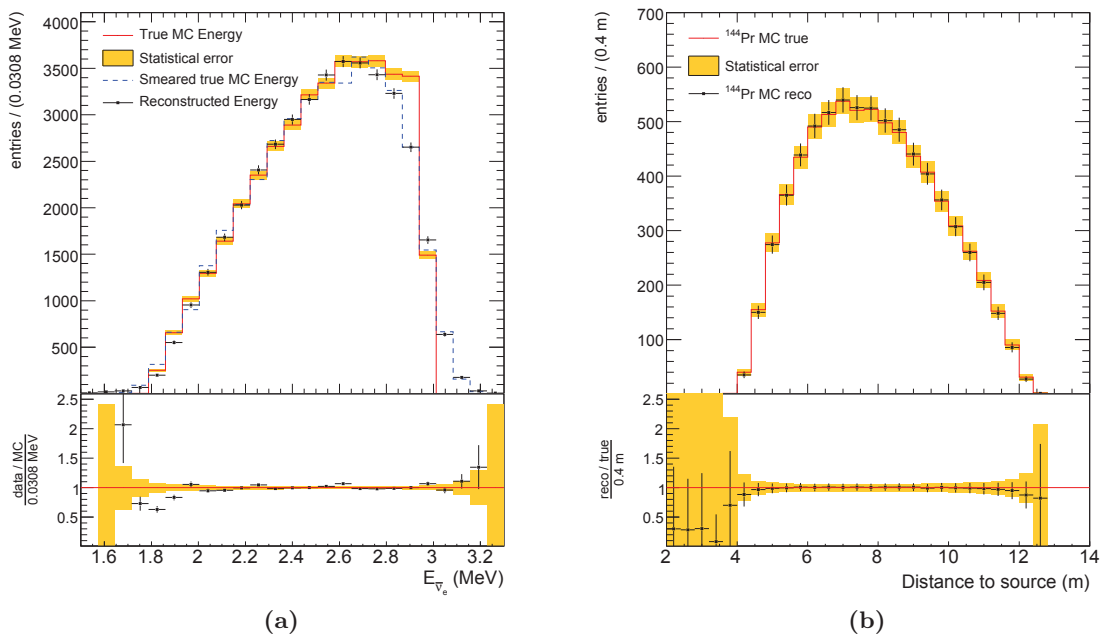
The neutron capture on hydrogen, followed by the emission of a 2.2 MeV  $\gamma$  is also taken into account. The positron and neutron capture are both space and time correlated. The validation of these aspects are outlined in section 6.5.

Figure 6.8 shows two simulated data sets with different mixing parameters. The null hypothesis corresponds to  $\sin^2 2\theta_{14} = 0$  and  $\Delta m_{41}^2 = 0 \text{ eV}^2$  while the oscillated signal assumes mixing parameters of  $\sin^2 2\theta_{14} = 0.15$  and  $\Delta m_{41}^2 = 1.0 \text{ eV}^2$ . To validate the oscillation output of the generator, the theoretical expectation was inserted (shown in blue). As it can be seen both, theoretical expectation and the reconstructed signal, agree well within the statistical uncertainty (see Figure 6.8 bottom).

#### 6.2.5 The Sterile Neutrino and Antineutrino Scattering Generator

In the elastic scattering channel, the neutrino or antineutrino respectively is scattered elastically off an electron. The detected spectrum is then derived by taking the scattering angle  $\theta$

<sup>1</sup>CTF: Counting test facility. The CTF was the prototype of the BOREXINO detector.



**Figure 6.7:** Output of the sterile  $\bar{\nu}_e$  generator. The unoscillated input signal (MC true) is shown in red while its associated statistical error is shown in orange. The reconstructed signal is shown as black dots. The data selection was performed as described in section 7.3.1. For this plot, the source was simulated 8.25 m underneath the detector center.

into account. The maximum recoil energy  $T$  of the electron is defined by its kinematics and is given by

$$T < \frac{2E_\nu^2}{m_e + 2E_\nu}, \quad (6.7)$$

if the neutrino is considered to be massless. The neutrino energy is given by  $E_\nu$  and the electron mass is given by  $m_e$ . As a consequence the recoil spectrum caused by mono-energetic neutrinos has a characteristic Compton shoulder (see Figure 6.9). The expected signal for a 10 MCi neutrino source is shown in Figure 6.9. The expected background is shown as well taking into account the latest measured background levels from phase one. An artificial neutrino source like  $^{51}\text{Cr}$  will feature a very similar recoil spectrum as the  $^7\text{Be}$  neutrinos from the Sun. The kinetic energy of the simulated electrons is randomly extracted according to the differential cross-section as shown in Ref. [133], which includes radiative corrections. The sterile scattering generator features the option to simulate either neutrino scattering off electrons as well as the scattering of antineutrinos off electrons. The user can choose between the following predefined spectra:

- Neutrino-electron scattering:  $^{51}\text{Cr}$  or  $^{37}\text{Ar}$
- Antineutrino-electron scattering:  $^{144}\text{Ce}$  or  $^{144}\text{Pr}$

As a further option, an arbitrary spectrum can be loaded via a ROOT or ASCII file. Again no compilation is needed. The shape factor for distortion of the continuous antineutrino spectrum is implemented according to Eq. (6.6). Similar to the sterile antineutrino generator for the inverse beta decay, the event position is randomly computed according to the settings of the mixing parameters in the two flavor approximation. The output of the  $\bar{\nu}_e$  scattering generator is shown in Figure 6.10.

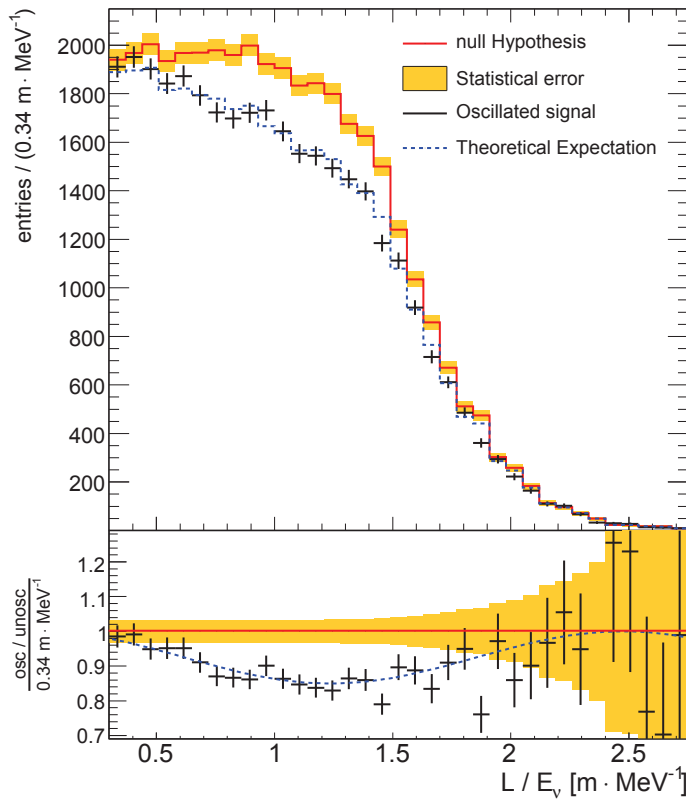


**Figure 6.8:** Output of the sterile  $\bar{\nu}_e$  generator. The reconstructed baseline is denoted as  $L$  while the reconstructed antineutrino energy is given by  $E_\nu$ . Two data sets have been simulated. The unoscillated signal is shown in red while its associated statistical error is shown in orange. The reconstructed oscillated signal is shown as black dots. The data selection was performed as described in section 7.3.1. The blue dashed line indicates the theoretical expectation to the given oscillation parameters. For this plot, the source was simulated in the center of the detector. The oscillation parameters are  $\sin^2(2\theta_{14}) = 0.15$  and  $\Delta m_{41}^2 = 1 \text{ eV}^2$ , respectively.

### 6.3 Simulation of the Optical Processes

Light in the BOREXINO detector is generated by two optical processes: scintillation light and Cherenkov light. The Cherenkov radiation was discovered in 1934 by Pavel Alekseyevich Cherenkov (1904-1990) while he observed a bottle of water near a radioactive source. Together with Igor Tamm and Ilya Frank, Cherenkov was awarded the Nobel Prize in Physics in 1956 “for the discovery and the interpretation of the Cherenkov effect” [167]. However, the phenomenon itself was noticed much earlier by Marie and Pierre Curie when they observed the “bluish glow seen in the dark from glass vessels containing salts of radium” [196, 89]. It was the systematic study of Cherenkov and the theoretical work of Tamm and Frank which brought light to this phenomenon. For BOREXINO, Cherenkov radiation plays a significant role in the detection of high-energetic muons penetrating the water tank.

However, for the energy range of interest ( $\sim 1 \text{ MeV}$ ) it only contributes at the level of 10% for an electron regarding the light generation [91]. The dominant process is therefore the scintillation process. Within G4Bx, optical photons originating from Cherenkov radiation as well as from the scintillation of the molecules are simulated. The exact amount of light was carefully measured and the tuning of simulation with real data is one of the important aspects of the Monte Carlo. This particularly includes the tuning of scintillation photon yield, the

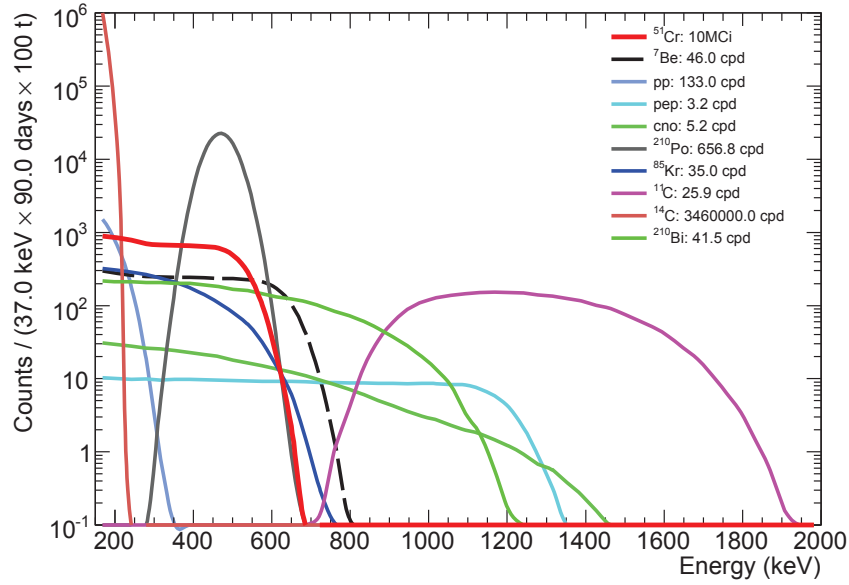


**Figure 6.9:** Visible recoil energy of a 10 MCi  $^{51}\text{Cr}$  neutrino source and visible energies of several background sources. The recoil spectrum of the  $^{51}\text{Cr}$  source was created by using the scattering MC generator.

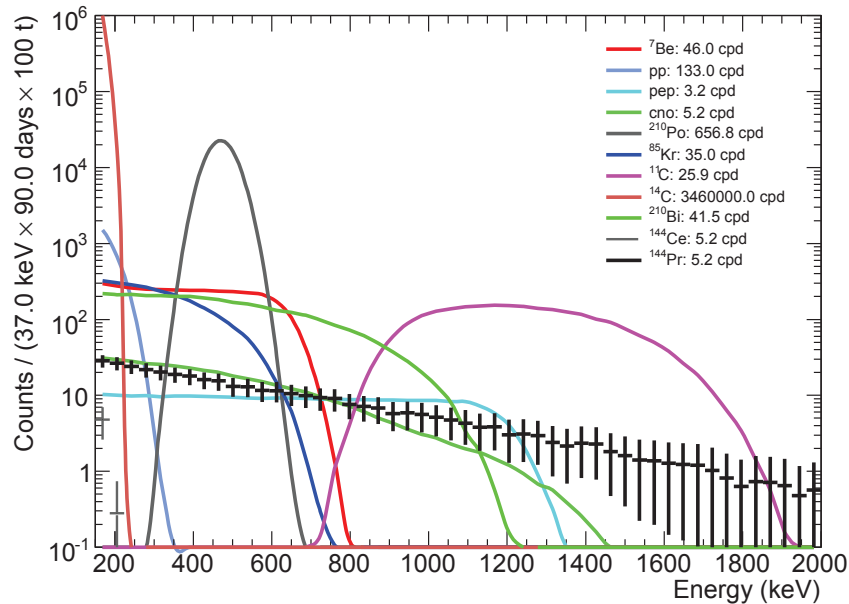


**Figure 6.10:** Visible energy obtained from simulations. The recoil spectra of the  $\bar{\nu}_e e^-$  elastic scattering off electrons was simulated using the developed generator. The  $\bar{\nu}_e e^-$  elastic scattering events are negligible for the first SOX sterile neutrino phase, but will be relevant for other studies like the measurement of the Weinberg angle and magnetic moment. Additionally, these spectra are relevant for the upcoming solar analysis, especially for the CNO background evaluation.

quenching effect, and the time distribution of the emitted scintillation light. [91]

### 6.3.1 Scintillation Light

The modeling of the scintillation light is based on a semi-empirical way as it is not possible to simulate all the scintillation processes *ab initio* (i.e. molecular level) which would also result in an inappropriate, large computing time [91, p. 50]. The used simplified model is based on the emitted light according to the spectra of the PC+PPO and PC+DMP mixtures. The time profile  $F(t)$  is modeled by the superposition of four exponential [77, p. 90]:

$$F(t) = \sum_i \frac{N_i}{\tau_i} e^{-t/\tau_i}, \quad (6.8)$$

where  $\tau_i$  is the time constant of component  $i$  and  $N_i$  the mean fraction of the emitted photons. The values of these parameters have been measured in the laboratory and are embedded within the **G4Bx** framework [77]. The mean number of the optical photons is computed from the energy loss of the primary particle taking into account the quenching effect [91]. The energy shift resulting from quenching is described by the Birks formula (see also [24]):

$$\frac{dL}{dx} = \frac{Y_0 \frac{dE}{dx}}{1 + kB \frac{dE}{dx}}, \quad (6.9)$$

where  $dL/dx$  is the number of photons emitted per unit path length and  $Y_0$  the light yield. The denominator in Eq. (6.9) quantifies the effect of ionization quenching. The variable pair  $kB$  is known as the Birks parameter. The mean number of emitted photons is obtained by integrating Eq. (6.9):

$$L(E) = L_0 \int_0^E \frac{dE}{1 + kB \frac{dE}{dx}} \quad (6.10)$$

The non-linearity in the energy reconstruction has to be properly modeled and accounted for the data analysis [91]. Within the **G4Bx** framework the mean number of scintillation photons is computed as the product of the initial kinetic energy, the scintillation light yield and the quenching factor  $Q(E)$  which is given by:

$$Q(E) = \frac{1}{E} \int_0^E \frac{dE}{1 + kB \frac{dE}{dx}} \quad (6.11)$$

The quenching factor is especially important for particles like protons and  $\alpha$  particles due to the high ionization per unit path length. The number of scintillation photons is then randomly computed according to Poisson statistics. [91]

### 6.3.2 Cherenkov Light

The Cherenkov light along the particle track is generated according to the Frank-Tamm law. The refraction index for PC+PPO has been measured and is implemented for different wavelengths. Ultraviolet Cherenkov photons which can not directly be detected by the PMTs are simulated as they are absorbed by the scintillator and re-emitted at higher wavelengths. [91]

### 6.3.3 Photon Tracking

In order to reach a high accuracy each photon is tracked individually in `G4Bx(2)`. While the photons propagate through their medium, they can either be absorbed and re-emitted by PPO molecules or might undergo Rayleigh scattering on the PC molecules. The interaction probability of each interaction strongly depends on the wavelength. At short wavelengths, the absorption by PPO molecules is expected to be dominant while at long wavelengths Rayleigh scattering processes are dominant. In addition, photons might be absorbed by DMP molecules inside the buffer or (to a lesser extent) by other materials such as the nylon vessel layer. The relevant attenuation lengths for these interactions have been obtained by measurements [91]. Details about the re-emission probabilities and their timing distribution can be found in Ref. [91]. The light propagation was already studied with the CTF and more information is available in [34]. The photon tracking also takes into account interactions at material boundaries such as the light reflection and refraction at all different materials (PMT structure, nylon vessel, stainless steel vessel). Photons are tracked until they are detected by PMTs with a given probability taking into account the wavelength dependent quantum efficiency or until they are absorbed by another material [91, 77].

## 6.4 Electronic Simulation

For an accurate modeling of the detector response the simulation of the BOREXINO electronics and triggering system have to be included. This is done by the `bx-elec` program which uses the binary output of the `G4Bx` simulation for further processing [77, p. 91]. The electronics simulation includes the PMT transit time spread and the emulation of after-pulses with a fixed probability of 2.5% [91, p. 53]. The after-pulse signal was measured for all PMTs in a dark room before installation [91].

The trigger system is emulated taking into account the trigger condition defined as 25 PMTs having to fire within 60 ns [77, p. 91]. The generated signal includes the gate of 16  $\mu$ s and consists of the scintillation signal and the dark noise background [77, p. 91]. The detector configuration of every single run can be reproduced by `bx-elec` with a specific number of working channels [77, p. 91]. The number of live PMTs of the simulated output is therefore equal to the number of PMTs of the actual measurement. The output format provided by the electronic simulation is equal to the real raw data. Further processing done by the reconstruction software `echidna` or `mach4` is independent from the origin of the data (simulated or real).

The tuning of the energy response was performed by using different radioactive sources. In Figure 6.11 the energy calibration obtained for numerous  $\gamma$ -emitters is shown. The tuning is performed for different energy estimators (see [91] for details) and is based on a  $\chi^2$  analysis of the  $\gamma$ -ray spectrum. The best fit values for  $(L_0, k_B)$  provide then the best accordance between Monte Carlo and real data [91].

## 6.5 Monte Carlo Validation

The Monte Carlo tuning and validation was conducted by using several calibration campaigns. In particular, several  $\gamma$  sources have been deployed inside the detector to measure different quantities such as the light yield and the quenching factor  $k_B$ . These measurements have been compared to the output of the Monte Carlo calibration generators. It may be worthwhile to emphasize that the  $\gamma$  source vial has fully been included in the simulation [66].

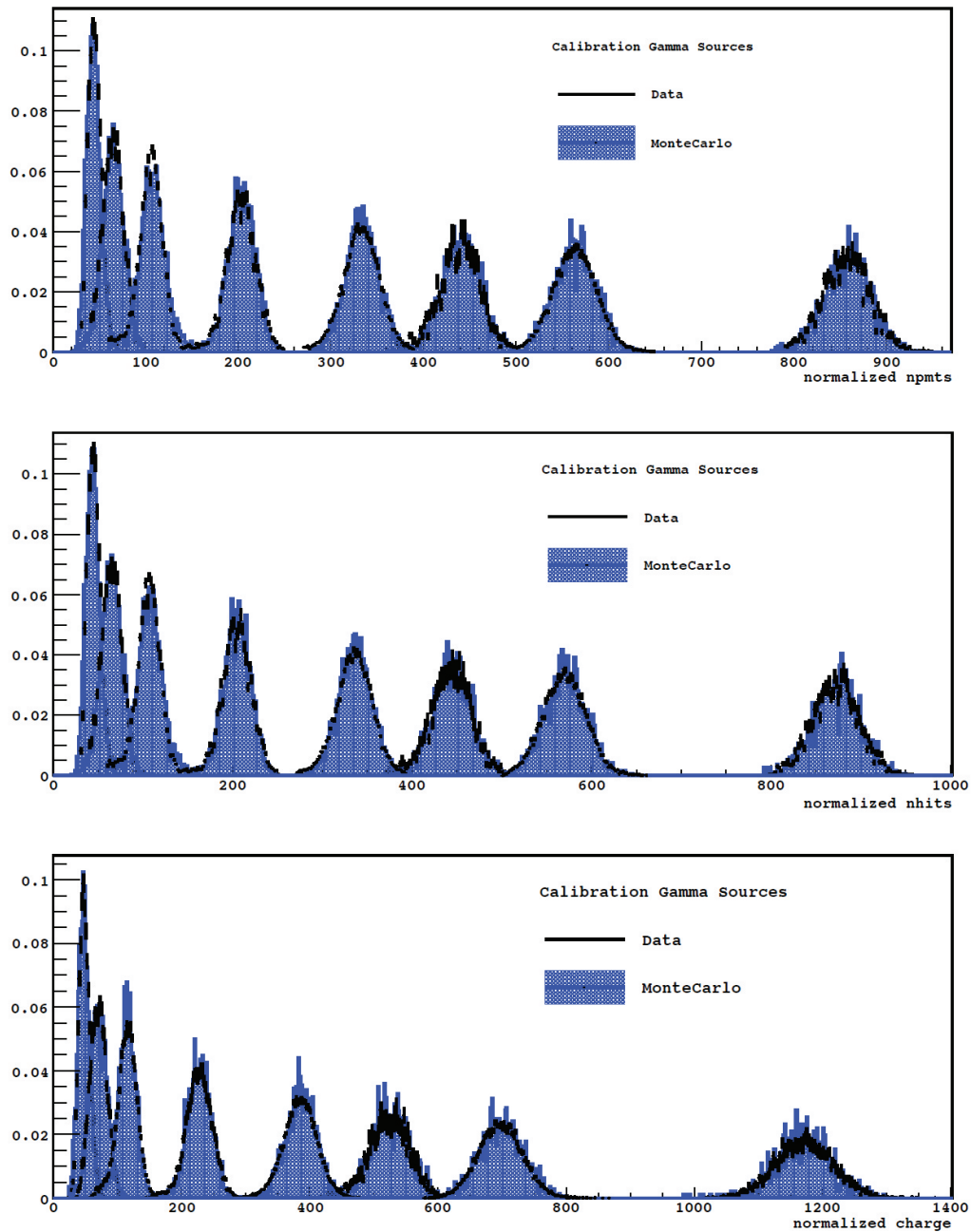


**Figure 6.11:** Energy spectrum of the calibration  $\gamma$ -ray sources in the center of the detector, in real and simulated calibration data. From left to right the peaks represent the  $\gamma$ -decays of  $^{57}\text{Co}$ ,  $^{139}\text{Ce}$ ,  $^{203}\text{Hg}$ ,  $^{85}\text{Sr}$ ,  $^{54}\text{Mn}$ ,  $^{65}\text{Zn}$ ,  $^{40}\text{K}$  and  $^{60}\text{Co}$ . **Top panel:** The energy is evaluated with the npmts energy estimator. **Central panel:** The energy is evaluated with the nhits energy estimator. **Bottom panel:** The energy is evaluated with the charge energy estimator. Text and Figure taken from [91].

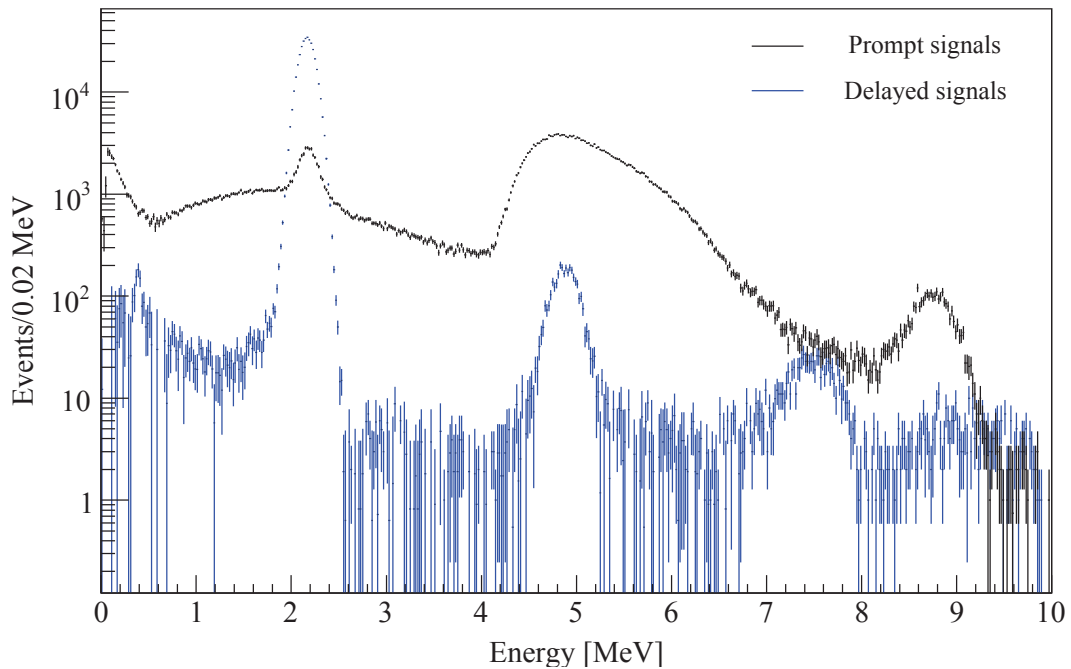


**Figure 6.12:** Energy spectrum of prompt and delayed signals of the  $^{241}\text{Am}-^9\text{Be}$  source registered by the BOREXINO detector. The data were collected in February 2009 and the source was placed close to the center of the detector. Text and Figure taken from [154].

Further tuning processes include studies regarding geometrical non-uniformity of the energy response with a Radon source. This was achieved by comparing the energy estimators of the  $^{214}\text{Po}$   $\alpha$ -peak of the data and the Monte Carlo. More information is available in Ref. [66].

In addition,  $\beta$  and neutron sources have been deployed inside BOREXINO. A detailed description of the calibration procedure can be found in Ref. [182, 91, 66, 154].

For the validation of the  $^{144}\text{Ce}-^{144}\text{Pr}$  antineutrino generator, data obtained from calibration campaigns using a  $^{241}\text{Am}-^9\text{Be}$  source is of particular interest as this source provides a time correlated and space correlated signal. The associated neutron capture on hydrogen can be used as a direct benchmark for the MC generated delayed signal of the antineutrino source.

### 6.5.1 Calibration Data from an $^{241}\text{Am}-^9\text{Be}$ Source

The BOREXINO collaboration has carried out three calibration campaigns in 2009 using a  $\sim 9.8\text{ Bq}$   $^{241}\text{Am}-^9\text{Be}$  source. Americium belongs to the class of radioactive transuranic elements and was first discovered in the framework of the Manhattan project in 1944. The discovery was leaked to the public by Glenn T. Seaborg in 1945 only five days prior to the official announcement at a meeting of the American Chemical society during a U.S. radio show for children (Quiz kids) [197].  $^{241}\text{Am}$  oxide in combination with Beryllium is widely used as an efficient neutron source:



Americium decays into a low- $Z$  element matrix, composed of an oxide- $^9\text{Be}$ -mixture [154]. The mean released neutron energy is  $\langle E \rangle = 4.05\text{ MeV}$  [154]. Americium decays into Neptunium

under the emission of an  $\alpha$  particle (Eq. 6.12). Through the following  $(\alpha, n)$  reaction of Beryllium, neutrons are produced.

The detected signal in BOREXINO is composed of two time and space correlated events. The prompt event is induced by the neutron irradiation. The excited state of a  $^{12}\text{C}^{(1)*}$  nucleus de-excites with a relaxation time of  $\tau \sim 6 \times 10^{-14}$  s accompanied by the emission of 4.439 MeV  $\gamma$ -rays [154]. As a result of the fast relaxation time, the  $\gamma$ -rays are instantly registered delivering the prompt signal. A second type of prompt signal may be induced from recoil protons in the calibration source holder [154]. The delayed signal is produced by the neutron capture on Hydrogen, Carbon or other materials. The neutron capture on Hydrogen is accompanied by a  $\gamma$  cascade at  $\sim 2.22$  MeV. Other, less dominant processes may result in  $\gamma$  energies of up to 9 MeV. [154]

### Analysis of the $^{241}\text{Am}-^9\text{Be}$ Energy Spectrum

The data selection and analysis of the  $^{241}\text{Am}-^9\text{Be}$  induced events was described in detail in Ref. [154]. Figure 6.12 shows the prompt and delayed signal obtained from the 2009 calibration runs. The prompt signal is composed of the  $\gamma$ -rays from recoil protons and of the 4.4 MeV peak originating from the relaxation of the  $^{12}\text{C}$  nuclei. The peak at 8.8 MeV is due to the superposition of two  $\gamma$ -rays registered as one signal. The delayed signal exhibits essentially three peaks at energies of 2.22 MeV, 4.94 MeV and 7.64 MeV. These peaks are correlated to the neutron capture on hydrogen,  $^{12}\text{C}$  and  $^{56}\text{Fe}$  atoms, respectively. The latter one has its origin due to the fact that the insertion arm for the calibration was manufactured from stainless steel. [154]

The essential use of the  $^{241}\text{Am}-^9\text{Be}$  source is to study the energy scale of the BOREXINO detector. Additional, the source may be used to calculate the neutron cross-section [154]. A detailed study of the energy scale was performed in [93]. According to [93] and [154], the energy (by means of the collected charge) scales almost linearly in the region from 2 MeV up to 9 MeV. The associated correction function expressed in the units of MeV is given by [154]

$$Q_{rec} [MeV] = -0.02(1) + 0.00209(1) \times Q_{rec} \quad (6.14)$$

The energy spectrum shown in Figure 6.12 was calibrated using this function.

### Estimation of the Neutron Capture Time

In Ref. [154], the neutron capture time was estimated. To exclude systematic errors, three different data sets with different source positions inside the fiducial volume were selected. More details can be found in Ref. [154], including the data selection procedure. The time profile distribution was fitted by the function  $f(t) = a + b \cdot e^{-t/\tau}$  [154]. Accidental background contributes as a flat component and was quantified to be less than 6% [154]. The capture time corresponding from the three data sets was estimated as [154]

$$\tau = (254.5 \pm 1.8) \mu\text{s} \quad (6.15)$$

This value is compared with the SOX MC in section 6.5.2.

### 6.5.2 Energy and Neutron Capture Time from Borexino Data

A similar cross-check was performed by using the normal `dst` BOREXINO data. The analysis was performed within the `Echidna` framework cycle 14. The data selection is based on the

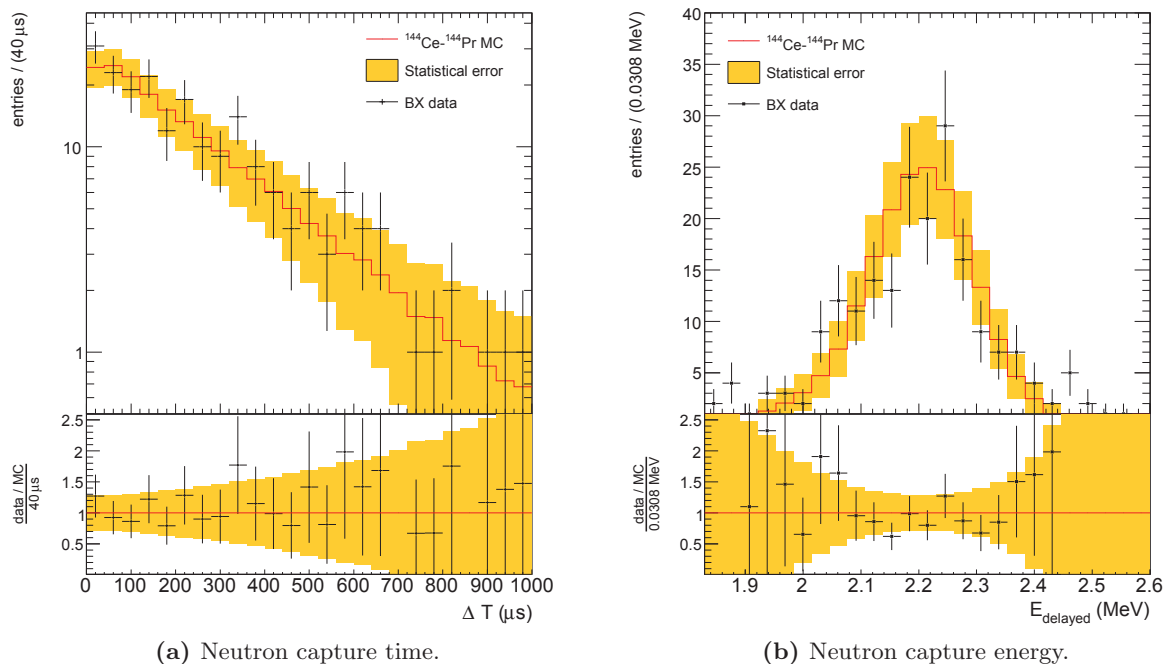


**Figure 6.13:** Monte Carlo validation. The neutron capture time and energy is compared to real data.

coincidence signal and is described in detail in section 7.3.1. The events selected by this technique are essentially geo-neutrinos and to a lesser extent cosmogenic induced neutrons. Compared to the analysis of the  $^{241}\text{Am}-^9\text{Be}$  data set, the statistic is relatively small.

The obtained data set was directly compared to the output of the SOX sterile  $\bar{\nu}_e$  MC generator and is shown in Figure 6.13. The associated time profile distribution was fitted following the exponential law as performed previously for the  $^{241}\text{Am}-^9\text{Be}$  calibration data. The capture time was estimated to be

$$\tau = (243.94 \pm 37.52) \mu\text{s}. \quad (6.16)$$

This result is in good agreement to the calibration data.

## 6.6 Summary

As part of the SOX project, two different generators have been developed to simulate the inverse beta decay reaction and the (anti)neutrino elastic scattering off electrons, respectively. Both simulation tools have been embedded into the existing framework of the BOREXINO software which already reproduces real data with an accuracy of 1% or better for all relevant parameters. The theoretical modeling of the  $\bar{\nu}_e$  spectrum performed in chapter 5 serves as an important input parameter. The software is currently used for other studies which are part of the SOX project and the solar neutrino program. The simulation of elastic scattering interactions induced by  $\bar{\nu}_e$  will become relevant for future solar neutrino analyses.



This chapter summarizes the calculation of neutrino and antineutrino interactions, respectively. The computation is performed analytically. Additionally, a Monte Carlo integration method is introduced to cross check the results.

Furthermore, the sensitivity for the SOX+Ce experiment is calculated. At the beginning the profile likelihood method is summarized. Two different approaches have been used. The so-called *shape+rate* analysis takes a normalization uncertainty of 1.5% into account. For the *shape only* analysis the normalization uncertainty was set to infinity. In that case the sensitivity is mostly driven by the distinct oscillation pattern of the (anti)neutrino flux. The impact of several experimental parameters is studied as well.

## 7.1 Expected Number of Interactions

The prediction of the IBD and neutrino scattering interactions relies on the precise knowledge of the source properties and detector characteristics. In the previous chapters important input parameters like the neutrino cross-section and the  $\bar{\nu}_e$  spectrum had been outlined. The expected number of  $\bar{\nu}_e$  events in a certain distance  $L$  is given by [88]:

$$\frac{d^2 N(L, E_\nu)}{dL dE_\nu} = \rho g \sigma(E_\nu) S(E_\nu) P(L, E_\nu) A_0 \int_{t_s}^{t_e} e^{-t/\tau} dt, \quad (7.1)$$

where  $\rho$  denotes the free proton density,  $g$  the geometric factor,  $\sigma$  the IBD cross-section,  $A_0$  the initial activity,  $t_s$  the start time and  $t_e$  the end time of the measurement.  $S(E_\nu)$  stands for the  $^{144}\text{Pr}$   $\bar{\nu}_e$  spectrum computed with the modeling as outlined in section 5.2.2.  $P(L, E_\nu)$  represents the two flavor oscillation probability as derived previously in section 3.3. The expected number of antineutrino interactions can be calculated analytically. Eq. (7.1) reduces then to

$$N_\nu = \rho A_0 \int_{t_s}^{t_e} e^{-t/\tau} dt \int_0^\infty S(E_\nu) \sigma(E_\nu) \int_K dV \frac{1}{4\pi q^2}, \quad (7.2)$$

where  $q$  is the distance as defined in Figure 7.1. In order to take the source position into account, the geometric factor  $g$  has to be introduced. The antineutrino flux decreases with  $q^{-2}$ . Secondly the geometry of the detector has to be taken into account. The calculation of the last integral then yields the geometric factor. The fiducial volume is treated as a sphere ( $K : x^2 + y^2 + z^2 = r^2$ ). Using spherical coordinates the volume element is given by  $dV = r^2 \sin \theta$ . If the point-like antineutrino source is deployed in the center of the detector,

the geometric factor is computed by integrating over the zenith and azimuth angles of the detector reference frame:

$$\int_K dV \frac{1}{4\pi r^2} = \int_0^{2\pi} d\varphi \int_{R_1}^{R_2} dr \int_0^{2\pi} d\theta \frac{1}{4\pi r^2} r^2 \sin \theta = R_2 - R_1, \quad (7.3)$$

where  $R_2$  denotes the radius of the fiducial volume and  $R_1$  the radius of the spherical volume which is not included in the analysis to reduce the source-induced background. Equation (7.3) makes clear that in case of no oscillations the number of interactions will be constant and independent of the distance  $r$  to the detector center. If the point-like source is assumed to be outside the fiducial volume, it is convenient to express the baseline  $q$  in terms of detector radius  $R$  and the source distance  $D$  (see Figure 7.1). According to the cosine law

$$q^2 = r^2 + D^2 - 2rD \cos \theta \quad (7.4)$$

this becomes

$$\int_K dV \frac{1}{4\pi q^2} = \frac{1}{2} \int_0^{R_{Bx}} dr \int_0^\pi d\theta \frac{r^2 \sin \theta}{r^2 + D^2 - 2rD \cos \theta} \quad (7.5)$$

The substitution  $\lambda = r/D$ , which means  $dr = D \cdot d\lambda$  leads to

$$\begin{aligned} \int_K dV \frac{1}{4\pi q^2} &= \frac{D}{2} \int_0^{R_{Bx}/D} d\lambda \int_0^\pi d\theta \frac{(\lambda D)^2}{(\lambda D)^2 + D^2 - 2\lambda D^2 \cos \theta} \sin \theta \\ &= \frac{D}{2} \int_0^{R_{Bx}/D} d\lambda \int_0^\pi d\theta \frac{\lambda^2}{\lambda^2 + 1 - 2\lambda^2 \cos \theta} \sin \theta \end{aligned} \quad (7.6)$$

A second substitution of the type  $\kappa = \cos \theta$  ( $d\theta = -d\kappa/\sin \theta$ ) simplifies the equation to the form

$$\int_K dV \frac{1}{4\pi q^2} = -\frac{D}{2} \int_0^{R_{Bx}/D} d\lambda \int_1^{-1} d\kappa \frac{\lambda^2}{\lambda^2 + 1 - 2\lambda^2 \cos \kappa}. \quad (7.7)$$

The solution of the last integral is given by

$$\begin{aligned} \int_1^{-1} d\kappa \frac{\lambda^2}{\lambda^2 + 1 - 2\lambda^2 \cos \kappa} &= -\lambda^2 \left[ -\frac{\ln(\lambda^2 - 2\lambda + 1)}{2t} + -\frac{\ln(\lambda^2 + 2\lambda + 1)}{2t} \right] \\ &= -\lambda^2 \left[ \frac{1}{\lambda} \ln \left( \frac{\lambda + 1}{1 - \lambda} \right) \right]. \end{aligned} \quad (7.8)$$

$$\begin{aligned} \int_K dV \frac{1}{4\pi q^2} &= \frac{D}{2} \int_0^{R_{Bx}/D} d\lambda \left[ \ln \left( \frac{\lambda + 1}{1 - \lambda} \right) \right] \lambda \\ &= \frac{D}{2} \left[ h - \frac{1}{2} \ln \left( \frac{1+h}{1-h} \right) + \frac{h^2}{2} \ln \left( \frac{1+h}{1-h} \right) \right] \\ &= \frac{D}{2} \left[ h - \frac{1-h^2}{2} \ln \left( \frac{1+h}{1-h} \right) \right], \end{aligned} \quad (7.9)$$

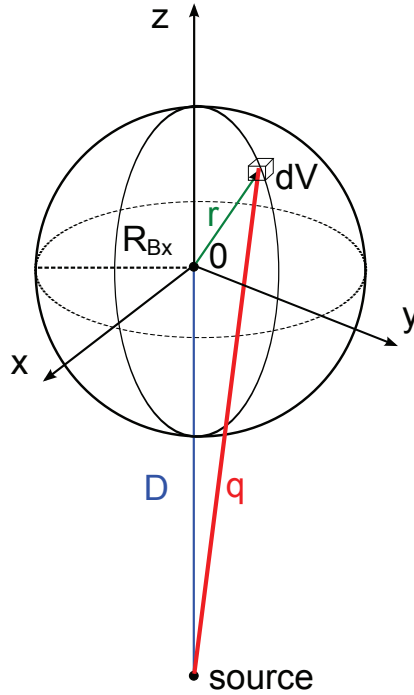


**Figure 7.1:** Fiducial volume integration for a point-like source. The mathematical formalism and details are reported in section 7.1. The BOREXINO detector is considered as a sphere with the fiducial volume radius  $R_{Bx}$ .  $D$  is the distance from the detector center to the source position. The distance from the detector center to a specific volume element  $dV$  is given by  $r$ .  $q$  is equal to the baseline and is the distance from the neutrino source to the volume element  $dV$ .

where  $h = R_{Bx}/D$ . It is worthwhile noting that the result for the geometric factor is equal to the factor presented in Ref. [136, 164]. An independent and similar derivation can also be found in Ref. [136].

For the  $^{51}\text{Cr}$  event prediction, the calculation of the neutrino scattering events is performed by using the neutrino-electron scattering cross-section weighted with the branching ratio of the different neutrino lines and taking into account the electron density.

### Activity and Target Mass

The overall active volume of BOREXINO consists of an inner nylon vessel of approximately  $321.555\text{ m}^3$  in a spherical volume of  $4.25\text{ m}$  radius. Depending on the source location and background conditions, the active volume is reduced. In case of using the  $^{51}\text{Cr}$  source the fiducial volume will be similar to the  $^7\text{Be}$  analysis of BOREXINO. Two calculations are performed. One calculation assumes a radius of  $3.3\text{ m}$  while for the second calculation a radius of  $3\text{ m}$  was assumed to suppress external background. The corresponding electron density for the target was measured to  $\rho_e = 3.307 \cdot 10^{29}\text{ m}^{-3}$  [36]. The antineutrino source will be placed underneath the detector or possibly inside the detector (either in the water tank or in the center of the detector). In order to reduce the source induced background a spherical volume cut of  $1.5\text{ m}$  around the source is applied. For the event calculation a free proton density of  $\rho_H = 5.3 \cdot 10^{28}\text{ m}^{-3}$  is assumed [25].

The activity of the Cerium source will be in the order of  $100\text{ kCi}$  while the activity of the Chromium source will be in the order of  $10\text{ MCi}$ .  $^{144}\text{Ce}$  decays into  $^{144}\text{Pr}$  with a half life of  $\sim 285$  days followed by the  $^{144}\text{Pr}$  decay into the stable  $^{144}\text{Nd}$  with a half life of  $\sim 17.3$  minutes.

The latter decay remains therefore in equilibrium at all times [114] and the differential equation simplifies to  $dN_{144Pr}/dt = -\lambda_{Ce}N_{144Pr}$ . The activity decreases according to an exponential decay law:

$$\mathcal{A}_0 \int_{t_s}^{t_e} e^{-t/\tau} dt = -\mathcal{A}_0 \tau e^{-t/\tau} \Big|_{t_s}^{t_e} = -\mathcal{A}_0 \tau \left[ e^{-t_e/\tau} - e^{-t_s/\tau} \right], \quad (7.10)$$

where the mean lifetime is correlated to the half life  $t_{1/2}$  by  $\tau = t_{1/2}/\ln(2)$ . The initial activity is given by  $\mathcal{A}_0$ .

The decay of Chromium into the stable Vanadium can be described analogously.

### Event Prediction for the $^{144}\text{Ce}$ – $^{144}\text{Pr}$ Antineutrino and $^{51}\text{Cr}$ Neutrino Source

Due to the much larger cross-section of the IBD, the activity of the  $^{144}\text{Ce}$  antineutrino source can be as low as  $\sim 100$  kCi. Compared to the Chromium source, the fiducial volume can be much larger since the coincidence signal allows an efficient way to suppress the external background. However, the monitoring of the vessel shape of BOREXINO has shown that the target volume is not perfect spherical. Due to the geometric dependence of the antineutrino flux which decreases with  $q^{-2}$ , the exact volume has to be determined precisely. The definition of the fiducial volume is therefore directly linked to calibration campaigns.

The transportation time will also be larger compared to the Chromium source ( $t_s = 30$  days), but is less critical due to the long half-life. Data taking will last approximately 1.5 years. For 100 kCi about 7100 IBD interactions are expected assuming a fiducial volume radius of 4 m (see also Figure 7.2).

The selection of the fiducial volume is one of the critical parts in the prediction of the number of neutrino and antineutrino interactions. For the Chromium neutrino source a fiducial volume radius  $r_{FV}$  of 3.3 m and 3.0 m is assumed. The chosen volume is similar to the one reported in Ref. [60] for the  $^7\text{Be}$  analysis. The cut is necessary to suppress the external background. The cross-section  $\sigma_e$  is obtained from the electroweak Standard Model including radiative corrections. The energy-integrated cross-section  $\sigma_e = 2.25 \times 10^{-49} \text{ m}^2$  is weighted with the branching ratio of the four neutrino energy lines and incorporates a minimum electron recoil energy of 250 keV to avoid  $^{14}\text{C}$  events (see Figure 7.3) [164]. The activity of the neutrino source decreases rather quickly. After 90 days of the measurement time, most  $\nu_e e^-$  scattering events have been collected (see Figure 7.2). This implies in particular that production and transportation time is critical. A transportation time of 5 days is assumed for the  $^{51}\text{Cr}$  neutrino source. According to Eq. (7.2) about 10,000 source-induced neutrino interaction are expected assuming a 10 MCi neutrino source (see Figure 7.2). However, it is still under discussion whether an activity of  $A_0 = 10$  MCi might be achievable. More realistic is the assumption of 5 MCi up to 7.5 MCi. In this scenario it should be discussed performing the source experiment twice. This could yield a similar interaction number, although the signal to background ratio would be worse.

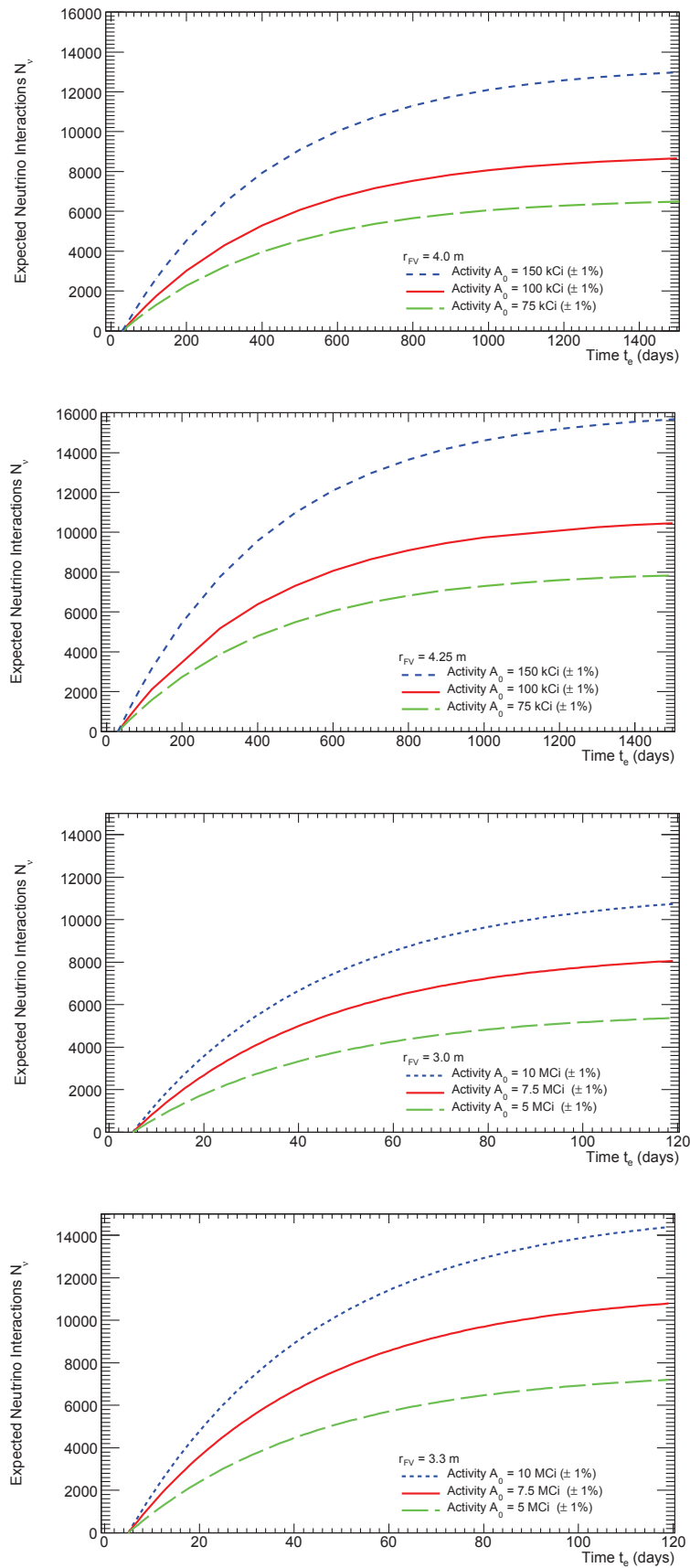


**Figure 7.2:** Integrated number of  $^{144}\text{Ce}$ - $^{144}\text{Pr}$ -antineutrino (two upper plots) and  $^{51}\text{Cr}$ -neutrino interactions under the assumption of full detection efficiency for different fiducial volumes.

## Monte Carlo Integration

The developed concept to simulate neutrino and antineutrino interactions within the **G4Bx(2)** framework was already summarized in chapter 6. A similar approach was used to predict the neutrino interactions within a specific fiducial volume. Compared to the full simulation, scintillation light and other details have been omitted. By analogy to section 6.2.1, two mathematical solids are defined where one of the solids (i.e. the fiducial volume) is a strict subset of a sphere:  $V_{Bx} \subset V_{PD}$ . At first, the decay point of the isotope is randomized. Based upon this the vertices are simulated isotropically around the decay point within the defined volume  $V_{PD}$ . The interaction number is then computed analytically according to Eq. (7.2) and Eq. (7.9). Only if the events are part of the solid  $V_{Bx}$  they are counted. In this way, different source and detector geometries can be tested.

## 7.2 Background

The following section summarizes the expected background for both phases of the experimental setup.

### 7.2.1 Background for the SOX+Ce Phase

The background for the SOX+Ce phase can be divided into external antineutrino and source-induced background. Background from internal radioactivity can be considered to be negligible thanks to the coincident signal of the  $\bar{\nu}_e$  as long as the  $\bar{\nu}_e$  source is deployed underneath the detector. The studies presented in this section have been previously reported in Ref. [114, 112, 63, 87] and are only briefly summarized:

- **External antineutrino background:** Reactor and geo-neutrinos are constantly detected and analyzed by BOREXINO. The most recent geo-neutrino paper of BOREXINO reports an observation of 77  $\bar{\nu}_e$  candidates over a period of 2056 days [26]. The total efficiency-corrected exposure for the present data set is 90744 t $\times$ y [26]. Other background processes like  ${}^9\text{Li}$ – ${}^8\text{He}$  correlated background, accidental, fast neutrons and other minor backgrounds have been estimated to be less than 0.65 events at 90% C.L. in the given data set which corresponds to an exposure of  $(5.5 \pm 0.3) \times 10^{31}$  proton  $\times$  y [26]. These sources of background will thus not play any significant role in the  ${}^{144}\text{Pr}$ -antineutrino measurement.
- **Source-induced background:** The presence of the antineutrino source itself could create additional background to the sterile neutrino search.  $\gamma$ -rays associated to the  $\beta^-$  decay of  ${}^{144}\text{Pr}$  [114] and neutrons predominantly caused from spontaneous fission have been identified as potential background processes [114, 112]:
  - $\gamma$ -rays and  $X$ -rays originate from all possible de-excitation modes of  ${}^{144}\text{Ce}$ – ${}^{144}\text{Pr}$  and other lanthanide or actinide contaminants [112]. The most serious  $\gamma$  background is the 2.185 MeV de-excitation  $\gamma$ -ray following the  $\beta^-$  decay of  ${}^{144}\text{Pr}$  [112]. The 2.185 MeV  $\gamma$  is the most-energetic  $\gamma$  line under consideration and drives accordingly the shielding thickness and background studies. For the study presented in Ref. [112] the TRIPOLI-4<sup>®</sup> Monte Carlo simulation code was used. This code was written mainly in C++ and calculates coupled neutron-photon propagation as

Isotope	Half-life [y]	BR to SF	Specific neutron activity (n/g)	$A/A(^{144}\text{Ce})$
$^{241}\text{Am}$	432	$4 \times 10^{-12}$	1.2	$5 \times 10^{-3}$
$^{242m}\text{Am}$	141	$4.7 \times 10^{-11}$	46	$10^{-4}$
$^{243}\text{Am}$	7370	$3.7 \times 10^{-11}$	0.72	$2 \times 10^{-4}$
$^{243}\text{Cm}$	29	$5.3 \times 10^{-11}$	$2.6 \times 10^2$	$2 \times 10^{-4}$
$^{244}\text{Cm}$	18	$1.4 \times 10^{-6}$	$1.2 \times 10^7$	$2 \times 10^{-2}$
$^{245}\text{Cm}$	8500	$6.1 \times 10^{-9}$	$1.1 \times 10^2$	$3 \times 10^{-6}$
$^{246}\text{Cm}$	4730	$3 \times 10^{-4}$	$1.0 \times 10^7$	$5 \times 10^{-7}$
$^{248}\text{Cm}$	$3.5 \times 10^4$	0.083	$4.3 \times 10^7$	$< 1 \times 10^{-7}$
$^{250}\text{Cm}$	9000	0.74	$1.5 \times 10^{10}$	-
$^{249}\text{Bk}$	320	$4.7 \times 10^{-10}$	$9.4 \times 10^4$	-
$^{248}\text{Cf}$	333	$2.9 \times 10^{-5}$	$5.4 \times 10^9$	-
$^{249}\text{Cf}$	351	$5 \times 10^{-9}$	$2.5 \times 10^3$	-
$^{250}\text{Cf}$	13	$8 \times 10^{-4}$	$1.1 \times 10^{10}$	-
$^{251}\text{Cf}$	898	$10^{-7}$	$2.0 \times 10^4$	-
$^{252}\text{Cf}$	2.65	0.030	$2.2 \times 10^{12}$	-

**Table 7.1:** Spontaneous fission (SF) properties of minor actinide isotopes with half-life  $> 0.5$  y [114].

well as the electron-photon cascade shower [75]. TRIPOLI-4 is widely used and is currently regarded as the state-of-the art program for neutron shielding studies and is comparable to the Los Alamos MCNPX code. An independent **Geant4** based calculation is currently under preparation.

For this study mono-energetic  $\gamma$ -rays were generated homogeneously and isotropically in the Cerium oxide source [112]. The shielding of the source was taken into account. The probability of a gamma to interact in the different detector layers as a function of its initial energy was investigated [112]. For instance, the number of gammas in the target per initial gamma in the energy range of 1 – 2.2 MeV was found to be less than  $10^{-18}$  [111]. The number of events after the IBD selection was found to be negligible. For the similar, but bigger CELAND proposal, an accidental event rate of  $2 \times 10^{-4}$  was found assuming an energy window of 1 ms [112].

- Actinide contaminants are considered to be important as a potential background source since they can undergo  $\alpha$  decay and spontaneous fission [112]. Fast neutrons are produced via the interaction of  $\alpha$  with light nuclei such as oxygen in the Cerium-oxide [112]. As described previously, fast neutrons can mimic the prompt and delayed signal. The most important contaminants are listed in Table 7.1.  $^{244}\text{Cm}$  is considered to be the most problematic isotope [112]. The background evaluation was conducted similar to the  $\gamma$  study described previously using the TRIPOLI-4 code. Details of this study were reported in Ref. [114, 112]. The probability for interactions inside the target is less than  $\sim 10^{-7}$  per neutron emitted and leads to an accidental rate of  $\sim 0.2$  IBD-like events per day, if a cut of  $> 2$  MeV for the delayed signal is applied. With respect to the correlated background an upper limit of  $10^{-4}$  IBD-like events was derived [112]. It is worth emphasizing that this background may well be neglected for the source deployment underneath the detector, but may be a serious problem for the source deployment inside the target of the detector. In this case a heavy shielding such as a balloon with boric water might be necessary. Taking into account the technical challenges, costs and background rate, this scenario might be unrealistic.

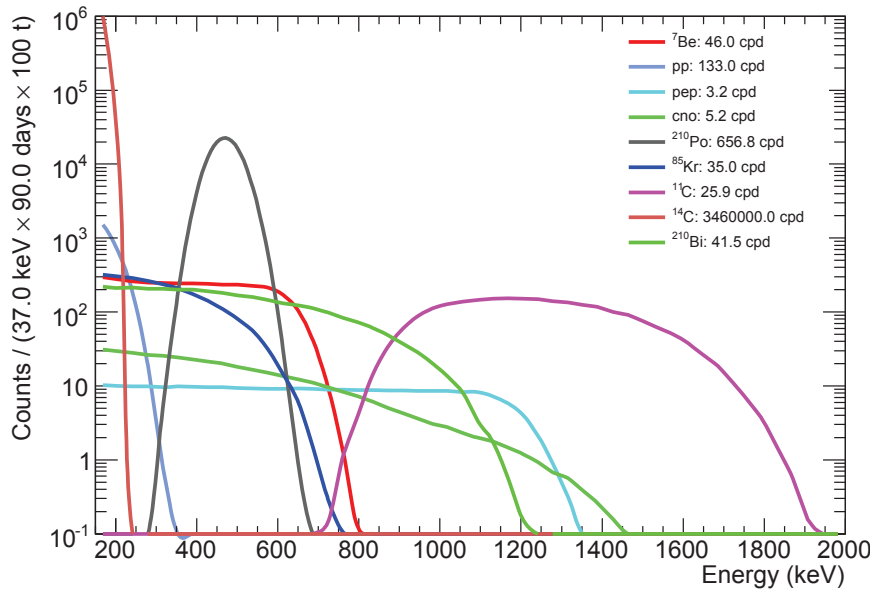


**Figure 7.3:** Simulated background for a possible deployment of a neutrino source near BOREXINO. Practically, the precise background numbers can be measured before and after the source deployment. Due to the short exposure time, the background level is expected to be stable.

### 7.2.2 Background for SOX+Cr Phase

With respect to the  $^{51}\text{Cr}$  analysis, three different background categories have been identified, i.e. radioactive, solar neutrino and cosmogenic background. A dedicated study was already performed during the analysis of solar neutrinos and is documented in several references (see especially [66]). In consideration of the  $^{51}\text{Cr}$  source characteristics (see chapter 5) and in the light of the similarities between the  $^7\text{Be}$  decay in the Sun and the radioactive decay of the  $^{51}\text{Cr}$ -neutrino source, the upcoming analysis and background levels are expected to be similar. Especially the expected recoil spectrum of the  $^{51}\text{Cr}$ -neutrinos is similar to the recoil spectrum of the  $^7\text{Be}$  neutrinos.

Throughout this section the different background components are classified according to Ref. [66] as follows:

- **External and surface background:** This background is caused by the radioactivity of the material surrounding the scintillator, e.g. PMTs, light cones, vessel support structure and hardware mounted on the stainless steel sphere. Background reaching the IV may therefore be  $\gamma$ -rays. To suppress this background, the position reconstruction is used and the fiducial volume is selected accordingly. With the specified fiducial volume, the contribution of the external background is expected to be negligible for the  $^{51}\text{Cr}$ -neutrino measurement.
- **Internal background:** Radioactive isotopes contaminating the scintillator are classified as internal background. These  $\alpha$ ,  $\beta$  and  $\gamma$  emitters have been carefully measured during the first phase of data taking in BOREXINO [66]. In addition to this, some of the backgrounds have been reduced by purification [66] for the second solar phase of BOREXINO. These rates have been reported in Ref. [67]. A detailed description of all internal background sources can be found in Ref. [66]. Here we particularly focus on the most important isotopes with respect to the  $^{51}\text{Cr}$ -neutrino analysis:

- $^{14}\text{C}$  is a  $\beta$  emitter with an end-point of 156 keV and a mean half-life of 5730 years. It is chemically identical to  $^{12}\text{C}$ . Therefore it is impossible to remove  $^{14}\text{C}$  from the organic scintillator. This isotope is constantly produced by the cosmic-ray flux. In order to reduce this specific contamination, BOREXINO has derived its scintillator from deep-underground. By this strategy, the level of contamination was reduced by six order of magnitude [66] compared to other organic materials. The CTF has measured a  $^{14}\text{C}/^{12}\text{C}$  content as low as  $10^{-18}$  [33].

- $^{85}\text{Kr}$  is a radioactive isotope with a half-life of 10756 years and an end-point of 687 keV. With a branching ratio of 99.57%, it mostly undergoes beta decay. The second most common decay is beta particle emission with an end-point energy of 173 keV followed by the emission of a 514 keV  $\gamma$ -ray. The spectral shape is similar to the  $^7\text{Be}$  decay and is therefore considered to be one of the most important backgrounds.

The natural production rate of  $^{85}\text{Kr}$  by interaction of cosmic rays with stable  $^{84}\text{Kr}$  in the atmosphere is small compared to the actual measured content. However, its presence can be attributed to anthropogenic sources [29, 199]. According to Ref. [29, 203, 186], the most important source is nuclear fuel reprocessing. To a large amount the gaseous  $^{85}\text{Kr}$  is released to the atmosphere when the spent nuclear fuel is dissolved [199]. As of 2000, the total amount released by this process has been estimated as 10600 PBq [203].

Other man-made sources include nuclear weapon tests (111 – 185 PBq [203]) and reactor incidents like the Chernobyl (35 PBq [29, 203]) and Fukushima (44–84 PBq [149]) accidents.

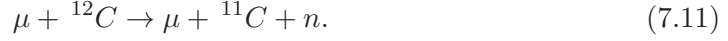
The average concentration in the atmosphere is  $1.3 \text{ Bq/m}^3$  as of 2005 [199]. Any detector operation like the detector-filling may therefore be a serious source of contamination [66].

The  $^{85}\text{Kr}$  content is determined by fitting the energy spectrum. A second and independent measurement can be performed by using the coincident signal of the ( $\beta, \gamma$ ) emission.

- $^{210}\text{Pb}$  is a  $\beta$  emitter with a mean life-time of 32 years. It has an tendency to lay on surfaces. While  $^{210}\text{Pb}$  is not a direct problem for BOREXINO ( $Q = 63.5 \text{ keV}$ ), its daughters,  $^{210}\text{Bi}$  and  $^{210}\text{Po}$ , are major backgrounds [66].
- $^{210}\text{Bi}$  undergoes beta particle emission and has a mean life-time of 7.23 days with a maximum energy of 1160 keV [66]. This makes  $^{210}\text{Bi}$  one of the dominant backgrounds for all solar neutrino analyses and for the  $^{51}\text{Cr}$ -neutrino measurement. The contamination is derived through the spectral fit. During past analyses an increase of the  $^{210}\text{Bi}$  content was observed [66]. This may be the result of detector operations and a huge effort is currently underway to control this background with respect to the CNO measurement. However, for the short time period of the  $^{51}\text{Cr}$  source exposure the rate is expected to be stable.
- $^{210}\text{Po}$  is a  $\alpha$  emitter and has a mean half-life of 200 days. The mono-energetic 5300 keV  $\alpha$  is strongly quenched in the BOREXINO scintillator and its energy spectrum is shifted to the region of  $^7\text{Be}$ -neutrino recoil spectrum [66]. For the  $^7\text{Be}$  and  $^{51}\text{Cr}$  analysis it may be possible to reduce this background via pulse shape discrimination. In general,  $^{210}\text{Po}$  is one of the most abundant backgrounds in BOREXINO and the actual measured value is higher than expected considering the  $^{210}\text{Bi} \rightarrow ^{210}\text{Po}$  decay chain. The off-equilibrium effect results probably from the contact of the scintillator with the storage tanks and pipelines [66].

- **Cosmogenic background:**  $^{11}\text{C}$  is the dominant muon-induced background in BOREX-

INO [66]. The effective energy spectrum of the  $\beta$  decay has only a small overlap with the  ${}^7\text{Be}$  and  ${}^{51}\text{Cr}$  energy region of interest. However,  ${}^{11}\text{C}$  is one of the most important backgrounds for the pep and CNO analysis. The production of this isotope which has a mean life-time of  $\tau = 29.4$  min is given by the following reaction:



${}^{11}\text{C}$  decays under the emission of a positron and electron-neutrino:



The neutron produced by reaction (7.11) is captured with a mean life-time of  $(254.4 \pm 1.8) \mu\text{s}$  [59] on Hydrogen in the scintillator. The  ${}^{11}\text{C}$  content can be reduced by the TFC method (see section 4.3.3). However, for the  ${}^{51}\text{Cr}$ -neutrino analysis this background is expected to be negligible.

- **Neutrino background:** The primary goal of BOREXINO is the study of solar neutrinos. In case of the  ${}^{51}\text{Cr}$ -neutrino analysis, solar neutrinos are a major source of background. The dominant background are the  ${}^7\text{Be}$ -neutrinos which induce a similar electron recoil spectrum as the  ${}^{51}\text{Cr}$ -neutrinos. pp-neutrinos are mostly below the lower energy boundary of 250 keV. CNO and pep neutrinos are only minor backgrounds. Nevertheless, these backgrounds have normally been included in all studies.

### 7.3 Event Selection

The analysis of the  ${}^{144}\text{Pr}$ -antineutrinos will be performed searching for coincident signals. By using this technique, most of the background can be suppressed allowing a nearly background-free analysis. The selection cuts are summarized in section 7.3.1.

The event selection for the  ${}^{51}\text{Cr}$ -phase will be very similar to the  ${}^7\text{Be}$ -neutrino measurement. All relevant cuts are summarized throughout the following section 7.3.2.

#### 7.3.1 IBD Selection for SOX+Ce

The  $\bar{\nu}_e$  selection procedure is similar to the one used for the geo-neutrino analysis [63]. The first edition of this selector was developed by the author in context of the DOUBLE CHOOZ experiment (for more details about DOUBLE CHOOZ see appendix C) and was validated with real and simulated data. Results of this antineutrino selector have already been shown in section 6.5 in context of the Monte Carlo validation. The IBD signature is provided by the prompt event followed by the delayed signal from the neutron capture. The time difference  $\Delta T$  is defined as the time difference between the prompt event time  $t_p$  and delayed signal time  $t_d$ . The following selection cuts have been applied to all events in order to select IBD interactions:

- **Prompt Trigger:**  $0.7 \text{ MeV} < E_p < 3 \text{ MeV}$ , as illustrated in Figure 7.4.
- **Delayed Trigger:**  $1.6 \text{ MeV} < E_d < 2.6 \text{ MeV}$  (Figure 7.4) to select the neutron capture on Hydrogen ( $E \simeq 2.2 \text{ MeV}$ ).
- **Multiplicity Cut:** Only one trigger within  $2 \mu\text{s} < \Delta T < 1000 \mu\text{s}$  after the prompt signal. The aim of this cut is to reduce the correlated background.

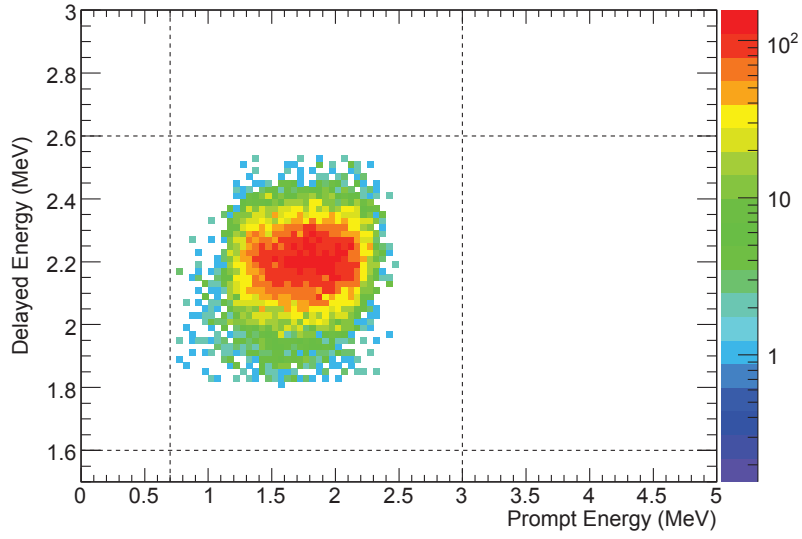


**Figure 7.4:** Antineutrino event selection. The energy window for the prompt signal is indicated by the vertical dashed lines while the delayed energy window is indicated by the horizontal dashed line.

- **Removal of random triggers.** These trigger types are defined within the `echidna` analysis software as trigger type 1.
- **Muon Veto:** Rejection of triggers within a time window of 1 ms following each muon in order to reduce the correlated and cosmogenic backgrounds.
- **Radial Cut:** The distance  $\Delta R$  between the prompt and delayed event has to be smaller than 1.5 m.
- **Fiducial Volume Cut:** The radius of the fiducial volume has to be smaller than 4.25 m or 4.0 m, respectively.

The IBD detection efficiency was determined to be 100%. For the forthcoming analysis, additional cuts might be applied. It should also be noted that some triggers might overlap within their time window. Studies are currently in preparation to recover these events with a high efficiency. The detection efficiency is listed with 100% in Table 7.2. Nevertheless, the duty cycle was assumed conservatively to be 90% to account for any potential efficiency loss for the sensitivity study.

### 7.3.2 $\nu_e e^-$ Scattering Selection for SOX+Cr

The main challenge of the  $^{51}\text{Cr}$  selection is to enlarge the fiducial volume as much as possible while still allowing a precise determination and control of the radioactive background sources. For that purpose an energy selection of  $E_{vis} > 250$  keV is required. This makes it possible to avoid the dominant  $^{14}\text{C}$  background. The lower bound also ensures that pile-up between two  $^{14}\text{C}$   $\beta$  decays ( $Q_\beta = 156$  keV) which might correspond to an energy of  $\sim 250$  keV can be avoided [66]. The higher bound of the energy window is 1250 keV making it possible to exclude the external  $\gamma$ -rays ( $^{208}\text{Tl}$  and  $^{214}\text{Bi}$ ). The overall selection criteria will be identical to the  $^7\text{Be}$  analysis once real data becomes available. The background for the SOX+Cr phase can therefore directly be measured before and after the source exposure.

According to Ref. [66], the following additional selection criteria have been applied:

- **Muon and muon-daughter removal:** The muon rate in BOREXINO is  $\sim 4300$  muons/day crossing the ID [66]. These events have to be identified and removed with respect to the possible cosmogenic isotopes produced by muon interactions in and around the scintillator [66]. Muons crossing close to the edge of the ID may also deposit energy comparable with the energy window of the selection. Further description can be found in Ref. [66] and references therein.
- **Single energy deposition:** The DAQ gate of BOREXINO is approximately  $16 \mu\text{s}$  long. For the analysis only events are used which feature a single energy deposition within this time gate [66].
- **Removal of fast coincident events:** The aim of this cut is to remove Radon correlated  $^{214}\text{Bi}$ – $^{214}\text{Po}$  delayed events, small parts of uncorrelated events and sequences of noise events [66]. This is achieved by the rejection of events with a mutual distance difference of less than 1.5 m and with a time difference of less than 2 ms [66].
- **Charge quality control:** According to the description in Ref. [66], two cuts are applied to suppress noise.
- **Scintillation light isotropy:** In order to reject noise, an isotropic scintillation light emission is required [66]. Details are reported in Ref. [66].
- **Additional noise removal:** Additional noise is rejected by looking at the rms of the cluster start time distribution. The trigger of the cluster has a well defined position within the DAQ gate. Only events are used which start within a specific window [66].

The effects of these cuts have been studied in [66]. The efficiency of these applied cuts have been studied with Monte Carlo simulations and with radioactive sources. Using the Monte Carlo framework as described in chapter 6, the fraction of removed events have been determined. For the  $^7\text{Be}$  the fraction of events is as low as  $(3.3 \pm 0.1) \times 10^{-4}$  and therefore negligible [66]. Similar background levels are expected for a possible SOX+Cr phase. The highest fraction was observed for  $^{210}\text{Po}$ , but is still less than  $(3.3 \pm 0.5) \times 10^{-4}$  [66].

## 7.4 Sensitivity

In order to predict the sensitivity of future experiments it is necessary to have a statistical method for incorporating the experimental parameters [55]. These uncertainties are included by introducing so-called pull terms in the analysis. The sensitivity is calculated using a profile likelihood method. Exclusion limits are set at 95% confidence level (C.L.).

The purpose of the first sub-section is to review the profile likelihood method to compute the sensitivity for the SOX experiment. This section is followed by a calculation of the exclusion limits for the SOX+Ce phase including a discussion about different experimental parameters.

The section ends with a summary of the sensitivity for a possible SOX+Cr phase and a comparison of the SOX experiment to other experiments.

### 7.4.1 The Profile Log-Likelihood Method

The likelihood ratio is a statistical test to compare two different hypotheses [55],  $H_0$  and  $H_1$ . In the context of exclusion limits, the null hypothesis  $H_0$  is compared to an alternative hypothesis  $H_1$ . In order to set exclusion limits the no-oscillation hypothesis ( $H_0$ ) is compared

to the different oscillation scenarios ( $H_1$ ) with specific mixing parameters ( $\sin^2 2\theta_{14}, \Delta m_{41}^2$ ). The ratio of the profile likelihood then grows as the alternative hypothesis further rejects the null hypothesis [55].

For an observable  $X$  with a given probability density function  $f(X_i|\pi, b)$  the likelihood function is [152]:

$$\mathcal{L}(\pi, b|X) = \prod_{i=1}^n f(X_i|\pi, b), \quad (7.13)$$

where  $n$  denotes a set of independent observables [152]. The probability density function is assumed to be dependent on  $k$  parameters  $\pi = \{\pi_1, \dots, \pi_k\}$  and  $l$  additional nuisance parameters  $b = \{b_1, \dots, b_l\}$  [152]. Following Ref. [152], “the likelihood ratio statistic is defined as

$$\lambda(\pi_0|X) = \frac{\sup\{\mathcal{L}(\pi, b|X); \pi = \pi_0, b\}}{\sup\{\mathcal{L}(\pi, b|X); \pi, b\}}, \quad (7.14)$$

where the denominator is the likelihood maximized over the whole  $\{\pi, b\}$  space, while the nominator is maximized over the more restrictive null hypothesis space  $\{\pi = \pi_0, b\}$ ”. For the upcoming SOX experiment a “true” set of oscillation parameters are assumed. The data set does not take into account any statistical fluctuation [55]. This is known as the Asimov data set. However, the statistical fluctuations will increase or decrease the profile likelihood of a measurement in 50% of all cases. In this way the median sensitivity is given [55]. In practice, the logarithmus naturalis of the likelihood ratio is taken to avoid machine precision errors [55]. For large statistics the likelihood ratio is linked to  $\chi^2$  distribution, so that  $\chi^2 = -2 \ln \mathcal{L}$ . For the SOX+Ce sensitivity analysis the likelihood is defined as

$$-\ln \mathcal{L} = \sum_i \text{Pois}(N_{data}(L/E_\nu) | (1 + \alpha) \times N_S(L/E_\nu | \sin^2 2\theta_{14}, \Delta m_{41}^2, A_0)), \quad (7.15)$$

where  $N_{data}$  is the simulated data without oscillation,  $N_S$  the expected signal for a given oscillation scenario while  $\alpha$  denotes the nuisance parameter to account for the normalization uncertainty. The sum runs over the  $L/E_\nu$  bins of the given data sets.

### Confidence Level Intervals

In order to obtain the allowed parameter regions of the best fit point ( $\sin^2 2\theta_{14,bf}, \Delta m_{41,bf}^2$ ), the profile likelihood is calculated for the full  $P = (\Delta m_{41}^2, \sin^2 2\theta_{14})$  parameter space surface [141]. The resulting  $\chi^2$  surface (e.g. in Figure 7.5) depending on the oscillation parameter set  $\sin^2 2\theta_{14}$  and  $\Delta m_{41}^2$  is used to determine the allowed regions by using the  $\Delta\chi^2$  definition (see also [141])

$$\Delta\chi^2 = \chi_P^2 - \chi_{bf}^2 \quad (7.16)$$

The index  $bf$  indicates the  $\chi^2$  value of the best fit. For exclusion plots the best fit corresponds to the null hypothesis,  $bf = (\Delta m_{41}^2 = 0 \text{ eV}^2, \sin_{14}^2 = 0)$ .

The confidence intervals are obtained by drawing the  $\chi^2$  values over the full parameter space (see Figure 7.5) [141]. The corresponding regions allowed by  $\alpha$  confidence level (C.L.) are those which satisfy  $\Delta\chi^2 \leq \Delta\chi_\alpha^2$ .  $\Delta\chi_\alpha^2$  are the  $\chi^2$  cut values assuming two degrees of freedom (*d.o.f.*) [141]. This is done by looking at the  $\chi^2$  distribution depending on one parameter while the other parameter is kept fixed. The resulting picture is the well known  $\chi^2$  parabola. It may be worthwhile to emphasize that for other neutrino oscillation studies correlations between the fit parameters may exist so that  $\Delta\chi^2 = \Delta\chi^2(\sin^2 2\theta, \Delta m^2)$ . The effective *d.o.f.* may then change over the  $(\sin^2 2\theta, \Delta m^2)$  space. A unified approach incorporating small

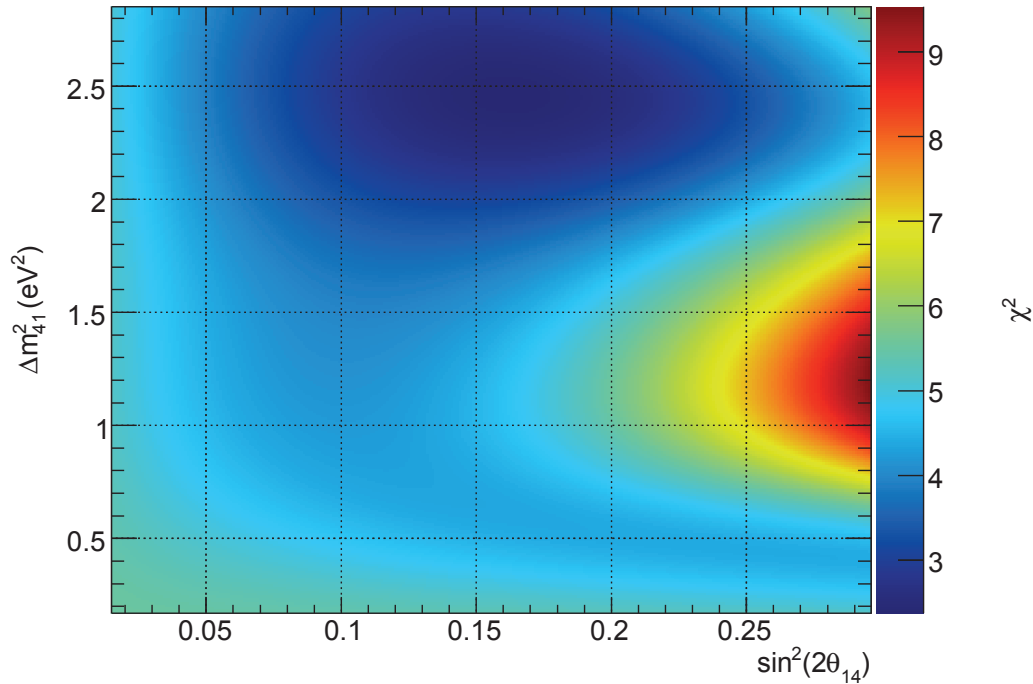


**Figure 7.5:** Parameter scanning. In order to set confidence intervals, the  $(\sin^2 2\theta_{14}, \Delta m_{41}^2)$  – plane is scanned. For each point in the grid the profile likelihood is calculated and converted to the corresponding  $\chi^2$ . In this example plot, the minimum can be found at  $\Delta m_{41}^2 \approx 2.5 \text{ eV}^2$  and  $\sin^2 2\theta_{14} \approx 0.15$ . The confidence interval (for the exclusion limits shown later) is drawn by using the  $\Delta\chi^2 < \Delta\chi_\alpha^2$  condition, where  $\Delta\chi_\alpha^2$  corresponds to a certain value depending on the  $\alpha$  confidence level (see text for details).

signals is known as Feldman-Cousins approach, a frequentist study which can be found in Ref. [103]. In case of the Cerium source with high statistics this is however expected to play only a minor role in the analysis.

### Systematic Uncertainties

For complete sensitivity studies systematic uncertainties have to be incorporated into the profile likelihood and  $\chi^2$  analysis, respectively. The main uncertainties arise normally from the flux, neutrino cross-section and detector effects. Uncertainties from neutrino mixing parameters in the matrix elements of the  $3 \times 3$  mixing matrix and the associated squared mass differences can safely be neglected at the given short baselines. To estimate non-oscillation systematic uncertainties resulting from the source activity uncertainty, cross-section and detector effects (fiducial volume uncertainty), a 1.5% normalization error on the signal events is used.

### Rate+Shape vs Shape Only Analysis

As outlined above, the profile likelihood can be directly linked to a  $\chi^2$  distribution. Taking into account the normalization uncertainty in a rate+shape analysis this becomes

$$\chi^2 = -\ln \mathcal{L} + (\alpha/\sigma_N)^2, \quad (7.17)$$

Parameter	Central value	Uncertainty	Reference
<b>Source</b>			
Source geometry	(cylindrical)		
Capsule diameter	0.14 m	-	
Capsule height	0.14 m	-	
$^{144}\text{Ce}$ distribution	(homogeneous)		
$^{144}\text{Ce}$ half-life	285 d	0.06	
$^{144}\text{Pr}$ $\bar{\nu}_e$ spectrum	...	...	see section 5.2.2
Activity $A_0$	100 kCi	$\pm 1.5\%$	
Source distance <sup>1</sup>	8.51, 7.15 m	$< 1$ cm	
Transportation time	30 d	-	
Measurement time	1.5 y	-	
<b>Detector</b>			
Fiducial volume geometry	(spherical)	...	
Fiducial volume radius	4.0 m		
Proton density in inner vessel	$5.264 \cdot 10^{28} \text{ m}^{-3}$	$< 0.1\%$	
IBD detection efficiency	100%	$< 0.1$ (stat.) %	see section 7.3.1
Overall detection efficiency <sup>2</sup>	90%	-	
Position resolution	$15 \text{ cm}/\sqrt{E}$	...	
Energy resolution	$5\%/\sqrt{E}$	...	Ref. [36]

**Table 7.2:** Input for sensitivity studies using the toy MC generator. Data was taken from Ref. [25], [26] and [36].

<sup>1</sup>Source distance: Distance from source center to detector center.

<sup>2</sup>The overall detection efficiency includes the IBD detection efficiency and the duty cycle efficiency for 1.5 years.

where the normalization is varied within its associated uncertainty  $\sigma_N$ . The last term is called pull term and  $\alpha$  is the corresponding nuisance parameter. Setting the normalization uncertainty to  $\infty$  allows to conduct a sensitivity study which is mostly driven by the distortion of the detected spectral shape and distance dependence due to  $L/E_{\bar{\nu}_e}$  dependence of oscillation to sterile neutrinos. This is referred to as the shape only analysis. The underlying test variable of the study is  $L/E_{\bar{\nu}_e}$  which is composed of the reconstructed baseline<sup>1</sup>  $L$  and the reconstructed antineutrino energy  $E_{\bar{\nu}_e}$ . This means that the null hypothesis is profiled using a PDF with a given  $\Delta m_{41}^2$  and  $\sin^2 2\theta_{14}$  set. Since  $L \ll l_{12}, l_{13}$  ( $l_{ij}$  denotes the oscillation length for a corresponding  $\Delta m_{ij}^2$ ), the two flavor approximation was used. The exclusion contours are computed in the  $(\sin^2 2\theta_{14}, \Delta m_{41}^2)$  space. 95% C.L. corresponds to  $\Delta\chi^2 = \chi^2(\sin^2 2\theta_{14}, \Delta m_{41}^2) - \chi_{min}^2 < 6.0$ .

The analysis was written within the ROOT framework and uses the CernLib package Minuit for the minimization. Additional smoothing of the shown contours was achieved by fitting a second-order polynomial to the  $\chi^2(\sin^2 2\theta_{14})$  distribution for a fixed  $\Delta m_{41}^2$  value. The scanning of the squared mass difference was performed logarithmically.

#### 7.4.2 Sensitivity of the SOX+Ce Project

The sensitivity to the neutrino oscillation parameters  $\sin^2 2\theta_{14}$  and  $\Delta m_{41}^2$  will be explored in

<sup>1</sup>The reconstructed baseline  $L$  is defined as the distance between the reconstructed interaction position and the center of the source. Any smearing resulting from the source geometry is incorporated by this definition.

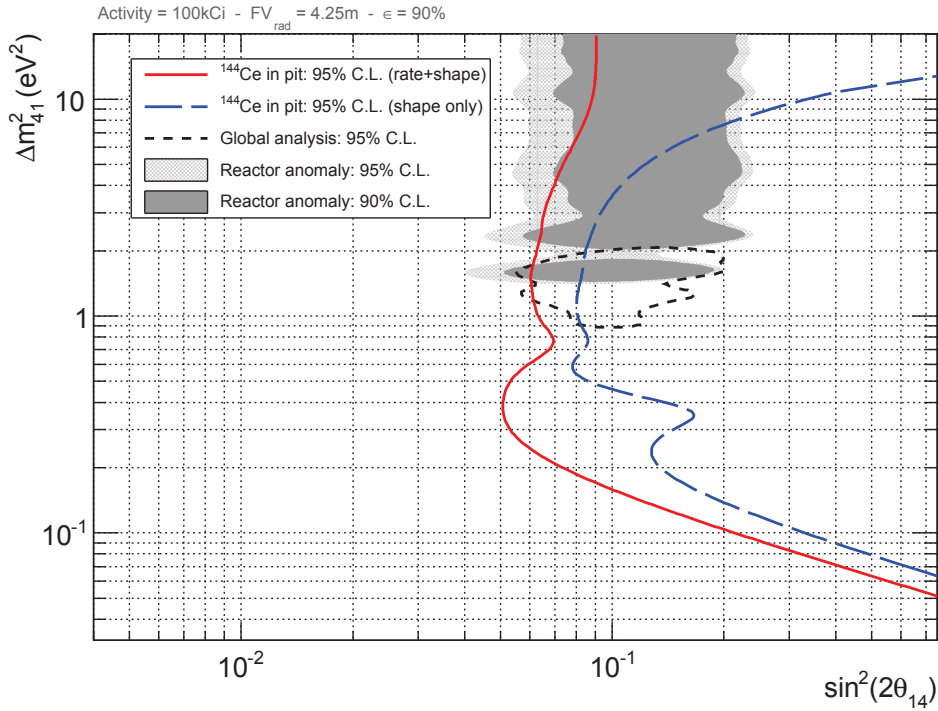


**Figure 7.6:** Sensitivity of  $\bar{\nu}_e$  search at BOREXINO to the oscillation parameters  $\sin^2 2\theta_{14}$  and  $\Delta m_{41}^2$  assuming a 100 kCi  $^{144}\text{Ce}$  source in the pit underneath the detector. The 95% C.L. contours of the rate+shape (red solid) and shape only (blue dashed) analysis are shown. As a comparison the allowed 95% and 90% C.L. contours of the reactor anomaly and the 95% C.L. contours of the global analysis are shown. Input parameters of the analysis are listed in Table 7.2.

this section. Input variables are listed in Table 7.2. The PDFs were created using a toy MC approach similar to the one presented in chapter 6. The source geometry was fixed during the preparation of this thesis.<sup>2</sup> Important parameters like the  $\bar{\nu}_e$  spectrum have already been outlined in chapter 5. To achieve the best possible sensitivity, the source activity should be as high as possible. The exact activity which will be delivered by Mayak is still unknown, but the aimed strength is in the order of 100 kCi. The influence of a higher source activity to the sensitivity will be discussed later as well. The listed activity  $A_0$  in Table 7.2 refers to the value before transportation. To be conservative a transportation time of 30 days was assumed. Under the assumption listed in Table 7.2 about 7100 IBD interactions are expected.

Considering the standard source position (8.51 m from the detector center) at BOREXINO, the sensitivity in the 3+1 model was investigated. The result of this study is shown in Figure 7.6. The allowed regions from the reactor anomaly [155] and from the global 3+1 fit presented in Ref. [116] are shown in comparison. The rate+shape analysis covers mostly these regions at 95% C.L.

The shape of these sensitivity contours is linked to the oscillation formula in the two flavor approximation. It depends primarily on the detector size and characteristics like energy and vertex resolution. The oscillation length is inverse proportional to the squared mass difference  $\Delta m_{41}^2$ . Thus the oscillation length becomes larger at small  $\Delta m_{41}^2$  values and the sensitivity decreases as soon as the oscillation length substantially exceeds the detector diameter. At larger values,  $\Delta m_{41}^2 > 5 \text{ eV}^2$ , the oscillation frequency rapidly increases and energy and

<sup>2</sup>Since the source geometry is known precisely, no studies were performed to investigate the sensitivity dependence on the source geometry.

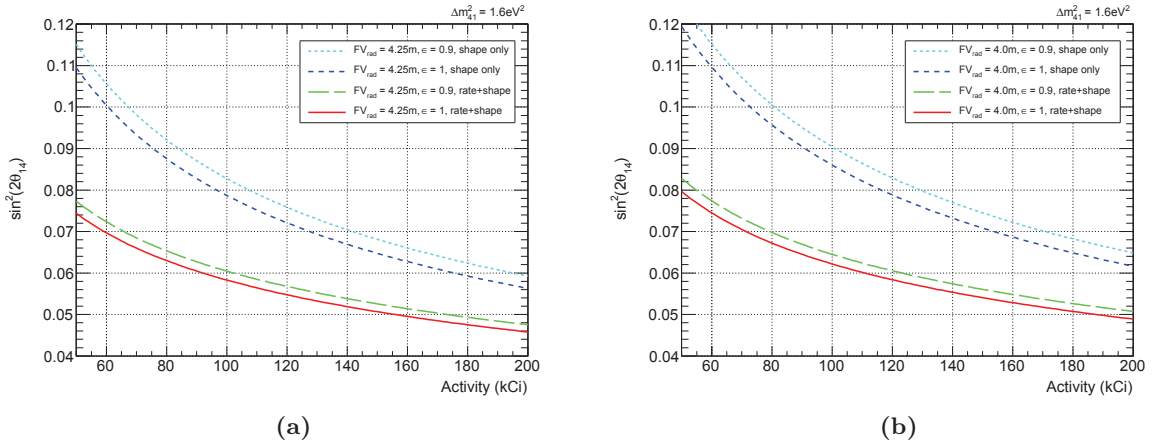


**Figure 7.7:** Sensitivity to the mixing parameter  $\sin^2 2\theta_{14}$  depending on the initial activity. The squared mass difference  $\Delta m_{41}^2 = 1.6 \text{ eV}^2$  was fixed to the global best fit value of Ref. [116]. Two scenarios have been investigated. The fiducial volume is assumed as a sphere with the radius  $FV_{rad}$ . The results for an enhanced fiducial volume is shown on the left side. The more realistic assumption is shown on the right side. In both cases the sensitivity is shown for two different detection efficiencies  $\epsilon$  of 100% and 90%. The final sensitivity is expected to be between the two corresponding lines.

vertex resolution of the detector are no longer sufficient to resolve the oscillation pattern. This primarily affects the shape-only analysis. In the rate+shape analysis, the rate deficit can be used to infer the  $\sin^2 2\theta_{14}$  mixing parameter while it is independent from the squared mass difference. [112]

To test the sterile neutrino hypothesis optimally one would like to place the  $\bar{\nu}_e$  source near the first oscillation maximum at the distance

$$L_{optim} = \frac{L_{osc} [\text{m}]}{2} = 1.24 \frac{E_{\bar{\nu}_e} [\text{MeV}]}{\Delta m_{41}^2 [\text{eV}^2]} \quad (7.18)$$

and observe the  $L/E_{\bar{\nu}_e}$  variation of the observed signal [96]. In the given experimental setup, the optimal sensitivity is achieved for  $\Delta m_{41}^2 \approx 0.4 \text{ eV}^2$ . In case, the  $\bar{\nu}_e$  source is inside the water tank of the detector the optimal sensitivity is only slightly shifted.

### Influence of the Source Activity and Fiducial Volume

Two important experimental parameters that impact the sensitivity of SOX+Ce are the initial activity  $A_0$  and the accessible fiducial volume. For the fiducial volume radius 4.25 m and 4.0 m were assumed. Figure 7.7 shows the sensitivity to the mixing parameter  $\sin^2 2\theta_{14}$  for a squared mass difference of  $\Delta m_{41}^2 = 1.6 \text{ eV}^2$  which corresponds to the best fit value of Ref. [116]. For both Figures (a) and (b), curves are shown for a detection efficiency of 0.9 and 1. The overall detection efficiency in BOREXINO was determined to be 0.87. However, this includes several phases of hardware upgrades and other maintenance work. The aim of the SOX experiment is to achieve a duty cycle of 95%. Therefore an actual sensitivity between the two lines,  $\epsilon = 1$  and  $\epsilon = 0.9$ , can be expected. A fiducial volume radius of 4.25 m might be too optimistic. A fiducial volume radius of 4 m shown in Figure 7.7b is considered to be realistic. In this context it should be highlighted that the actual nylon vessel is not perfectly symmetric and any deformation at the lower part of the vessel, where most of the events are accumulated, may influence the sensitivity significantly.

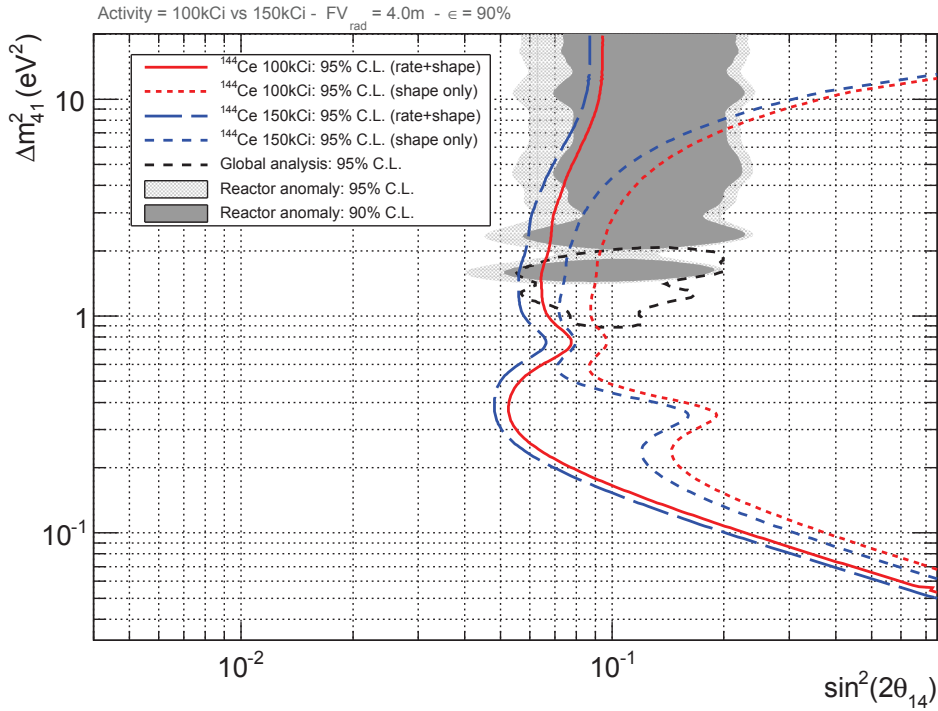


**Figure 7.8:** Comparison of a 100 kCi (red) source and a 150 kCi  $^{144}\text{Ce}$  (blue) source in the pit underneath the BOREXINO detector. The 95% C.L. contours of the rate+shape and shape only analysis are shown. As a comparison the allowed 95% and 90% C.L. contours of the reactor anomaly and the 95% C.L. contours of global analysis are shown. Input parameters of the analysis are listed in Table 7.2.

The lowest expected activity delivered by Mayak is about 70 kCi while it may be possible to get a source activity of 150 kCi. In this case the rate+shape sensitivity of  $\sin^2 2\theta_{14}$  is improved from  $\sim 0.068$  to  $\sim 0.052$  ( $\epsilon = 0.9$ ,  $FV_{rad} = 4.25$  m) and from  $\sim 0.073$  to  $\sim 0.058$  for the more realistic scenario ( $\epsilon = 0.9$ ,  $FV_{rad} = 4.0$  m). The overall influence of the initial source activity over the full  $(\sin^2 2\theta_{14}, \Delta m_{41}^2)$  space is shown in Figure 7.8. Increasing the source activity from 100 kCi to 150 kCi has only little effects in the low  $\Delta m_{41}^2$  region. As expected, the biggest influence is observed in the intermediate region,  $0.3 \text{ eV}^2 < \Delta m_{41}^2 < 3 \text{ eV}^2$  where the sensitivity is driven by the oscillation pattern [112]. Therefore the difference between oscillated and unoscillated signal is strongly depending on total events in a specific  $L/E$  bin (see also [112]). The sensitivity in the high  $\Delta m_{41}^2$  region is dominated by the source normalization uncertainty of 1.5% (see also Figure 7.9).

The expected normalization uncertainty of the SOX project is as low as 1.5%. This error incorporates an activity uncertainty of 1% and a fiducial volume uncertainty of about 1%. The effect of different normalization uncertainties was studied as well and is depicted in Figure 7.9. The study includes the exclusion limits for the so-called shape only analysis which corresponds to an infinite normalization uncertainty.

### Impact of the Energy and Position Resolution on the Sensitivity

For the presented sensitivity study an energy resolution of  $5\%/\sqrt{E}$  and a position resolution of 15 cm were assumed. These numbers have already been reported in the literature and are considered to remain unchanged for the SOX analysis. However, a generic study was

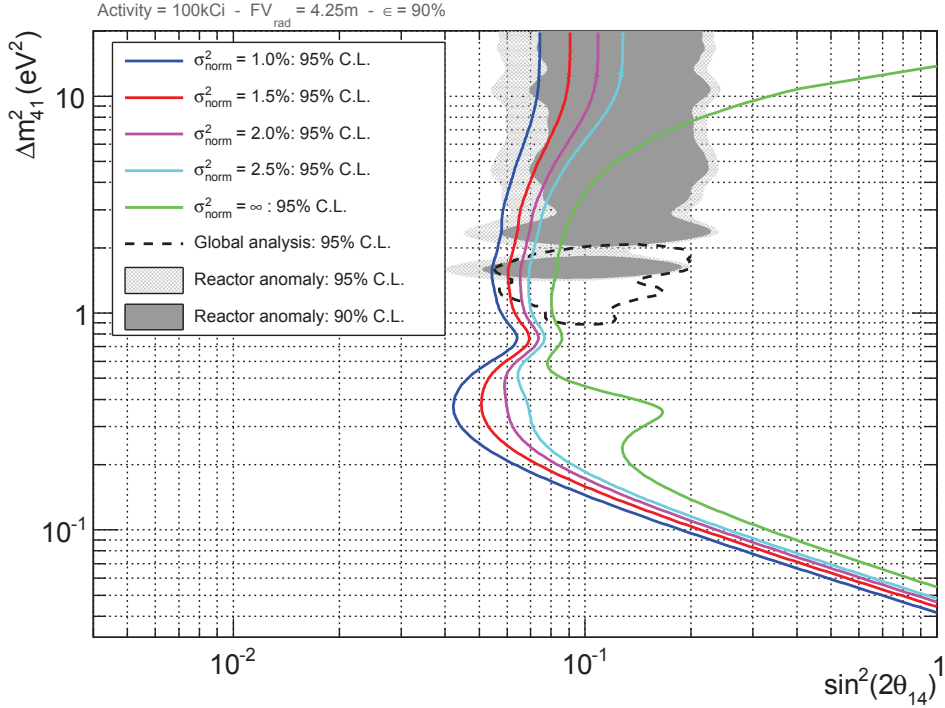
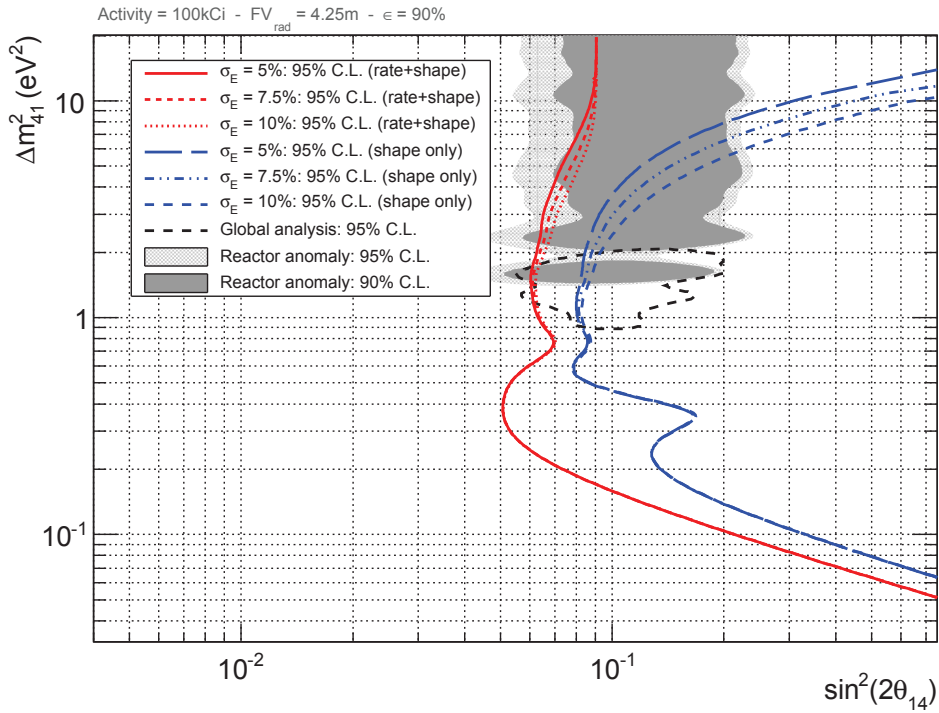


**Figure 7.9:** Exclusion limits for different normalization uncertainties. For this study a 100 kCi source in the pit underneath the BOREXINO detector was assumed. The 95% C.L. contours of the rate+shape analysis are shown. A normalization uncertainty of  $\sigma_{norm}^2 = \infty$  corresponds to the so-called shape only analysis. As a comparison the allowed 95% and 90% C.L. contours of the reactor anomaly and the 95% C.L. contours of the global analysis are shown. Input parameters of the analysis are listed in Table 7.2.

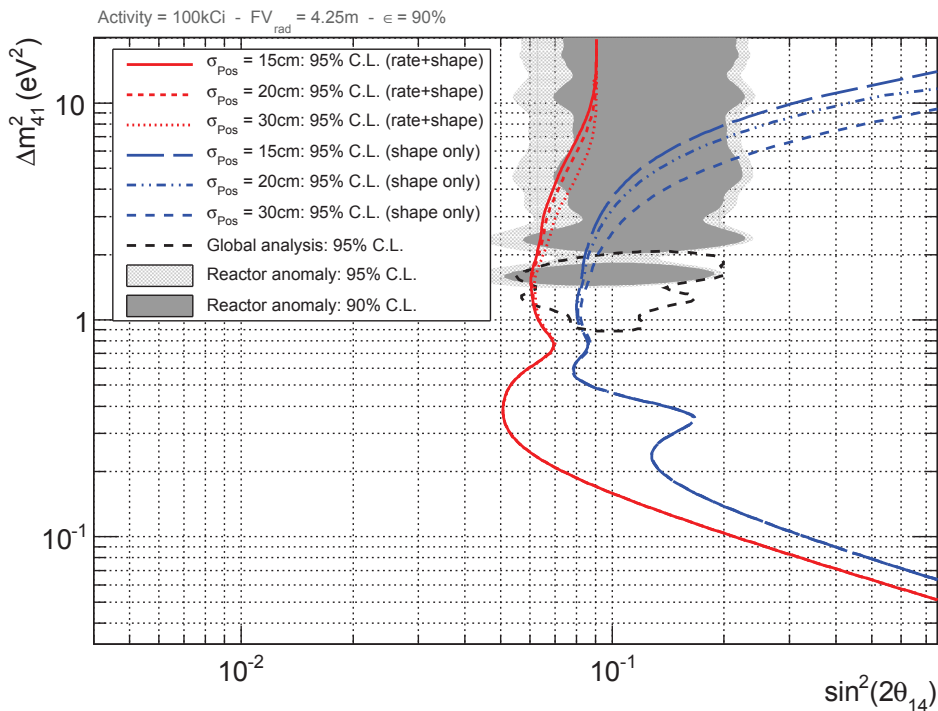
undertaken to investigate the effect of these parameters. The energy resolution was varied between  $5\%/\sqrt{E}$  and  $10\%/\sqrt{E}$ . The results are shown in Figure 7.10a. In the low  $\Delta m_{41}^2 < 1 \text{ eV}^2$  regime the effect is negligible since no actual oscillation pattern can be observed in this region. At larger values of  $\Delta m_{41}^2$  the sensitivity space is degraded. This is especially valid for the shape only analysis. In the global best fit area only minor effects have been observed. For high  $\Delta m_{41}^2 > 10 \text{ eV}^2$ , the rate+shape analysis is not affected, since in this region the sensitivity is dominated only by the rate deficit. The effect of the position (vertex) resolution is similar and shown in Figure 7.10b.

### Possible $\bar{\nu}_e$ Source Locations

During the first phase of the experimental setup, the  $\bar{\nu}_e$  source will be deployed underneath the detector (8.51 m from the detector center). A position closer to the detector center would be particularly advantageous. The only possibility is to open the BOREXINO detector and to install the source within the water tank or even in the center of the detector. Although this concept was originally proposed in Ref. [87] and also discussed in Ref. [65] this has to be considered unrealistic, unless one is willing to destroy and contaminate the unique BOREXINO detector. This will only be considered after the end of the solar program. However, it might be possible to place the  $\bar{\nu}_e$  source inside the water tank. Assuming a fiducial volume radius of 4.0 m and a detection efficiency of  $\epsilon = 0.9$ , an increase of about 58% of IBD interaction rate could be expected. In this concept, the sensitivity could be slightly enlarged, as shown in Figure 7.11. In comparison to a 150 kCi source inside the pit (see Figure 7.8), the sensitivity is



(a) Study of the detector energy resolution impact on the sensitivity.



(b) Study of the detector vertex resolution impact on the sensitivity.

**Figure 7.10:** Study of the detector energy (a) and position resolution (b) impact on the sensitivity. For the study a 100 kCi source in the pit underneath the BOREXINO detector was assumed. The 95% C.L. contours of the rate+shape and shape only analysis are shown. As a comparison the allowed 95% and 90% C.L. contours of the reactor anomaly and the 95% C.L. contours of the global analysis are shown. Input parameters of the analysis are listed in Table 7.2.

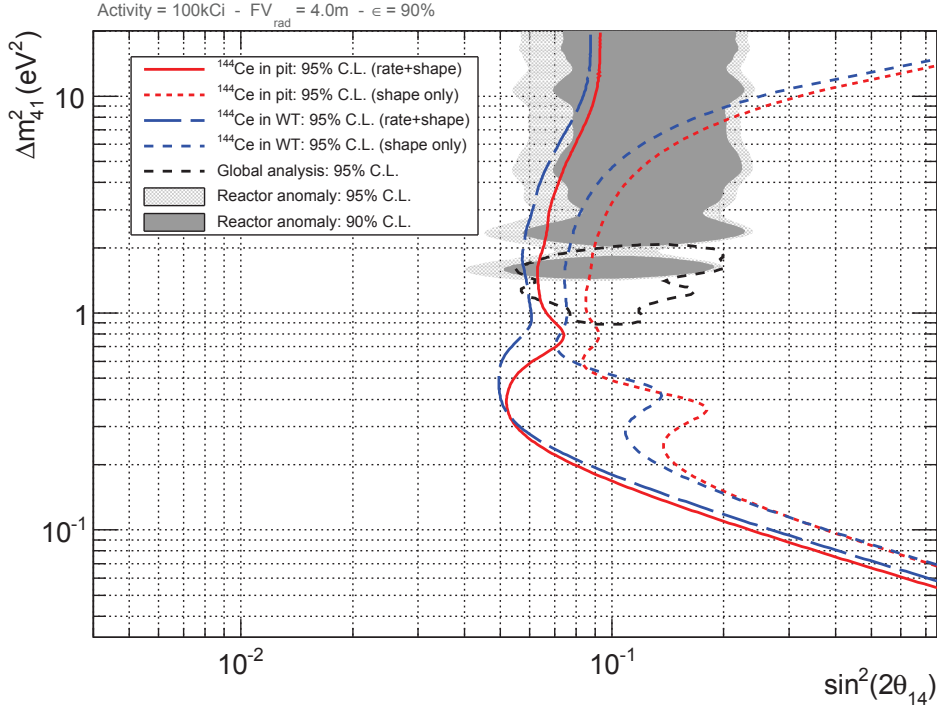


**Figure 7.11:** Comparison of a 100 kCi (red) source in the pit and a 100 kCi  $^{144}\text{Ce}$  (blue) source in the water tank of the BOREXINO detector. The 95% C.L. contours of the rate+shape and shape only analysis are shown. As a comparison the allowed 95% and 90% C.L. contours of the reactor anomaly and the 95% C.L. contours of the global analysis are shown. Input parameters of the analysis are listed in Table 7.2.

almost the same, especially in the parameter space of interest,  $\Delta m_{41}^2 \simeq 1.6 \text{ eV}^2$ . Therefore it might be more convenient to use a 150 kCi  $\bar{\nu}_e$  source in the pit. Other options might include increasing the fiducial volume by putting liquid scintillator inside the buffer. The fiducial volume radius would be then increased to 5.5 m. This concept study was already reported in Ref. [65]. However, a shorter baseline might lead to an increase in the source-induced background [112, 114]. Anyhow, other innovative concepts might be an alternative. A first study and outlook is given in chapter 8.

### Summary of the SOX+Ce Sensitivity

Figure 7.12 shows the influence of the measurement time to the sensitivity of the mixing parameter  $\sin^2 2\theta_{14}$ . First results can be expected after 0.5 years, assuming a fiducial volume radius of 4.25 m. In the region favored by global fits ( $\Delta m_{41}^2 \sim 1.6 \text{ eV}^2$ ) energy and vertex resolution play no significant role. The determination of the fiducial volume by means of an extensive calibration campaign will be one of the critical parts for the upcoming SOX project. The deployment of the source inside the detector is technically demanding. The studies presented in this chapter demonstrate that placing the source inside the water tank volume of the OD is equivalent to an increase of the source activity in the SOX pit by 50%. Other possibilities are outlined in the following chapter.

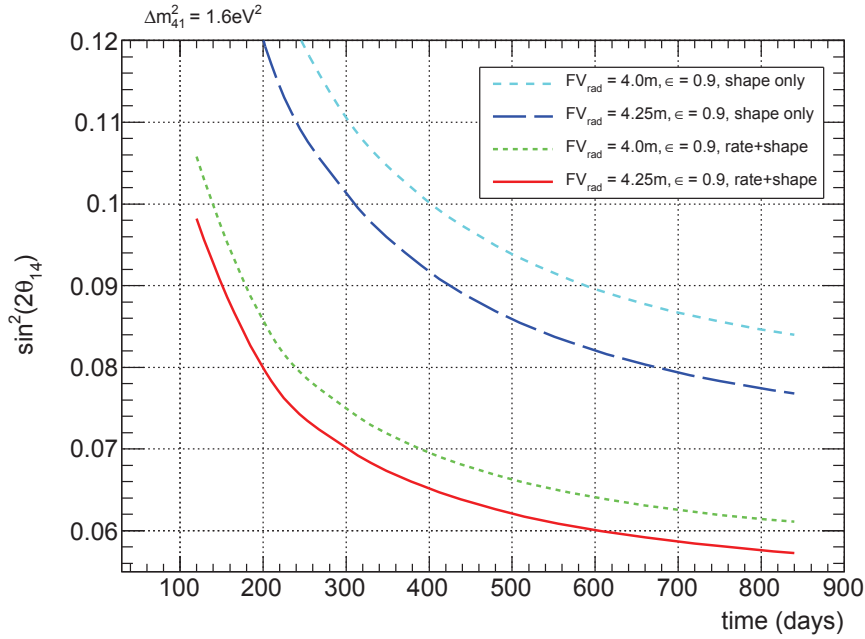


**Figure 7.12:** Sensitivity for the  $\sin^2 2\theta_{14}$  over time. The squared mass difference was fixed in the analysis to  $\Delta m_{41}^2 = 1.6 \text{ eV}^2$ .

### 7.4.3 Sensitivity of the SOX+Cr Project

The sensitivity of the SOX+Cr phase was already previously studied by numerous authors [136, 134, 135, 65, 109], including a study performed by the author of this thesis [158]. After the Saclay group joined the SOX project, the main focus was shifted towards the SOX+Ce phase of the experiment. Due to that fact and the many references available only the most recent study [109] is shortly summarized for completeness. The study is based on a profile likelihood analysis with three different variables (neutrino rate vs time, reconstructed baseline and electron recoil energy). The likelihood function incorporates nuisance parameters to account for systematic effects due to the fiducial volume uncertainty ( $\sigma_{FV}^2 = 1\%$ ), source uncertainty ( $\sigma_A^2 = 1\%$ ) and background uncertainty ( $\sigma_B^2 = 1\%$ ). The background level is derived from current measurements and varied within its uncertainty. For the sensitivity study a source activity of  $A_0 = 10 \text{ MCi}$  and a fiducial volume radius of 3.3 m was assumed. The vertex and energy PDFs were created using the sterile neutrino generator within the G4Bx framework. The resulting sensitivity obtained from these assumptions is shown in Figure 7.13. The sensitivity curves for the first phase SOX+Ce are shown for comparison. At the region of interest at  $\Delta m_{41}^2 \approx 1.6 \text{ eV}^2$ , both setups result in similar sensitivity levels. Compared to the Cerium source, the sensitivity is retained at lower squared mass differences ( $\Delta m_{41}^2 \approx 0.1 \text{ eV}^2$ ), accounting for the slightly lower neutrino energy and the associated neutrino survival probability. For the Cerium source the first oscillation maximum is at  $\Delta m_{41}^2 \approx 0.4 \text{ eV}^2$ . It may be worthwhile to mention that similar results can be obtained by performing the experiment twice with a slightly lower activity of 7 MCi.

### 7.4.4 Sensitivity Comparison

Over the past years many authors have proposed experiments to search for possible light sterile neutrinos. Figure 7.14 shows a compilation of the expected sensitivity contours in comparison with the allowed regions of the reactor anomaly and the global analysis presented

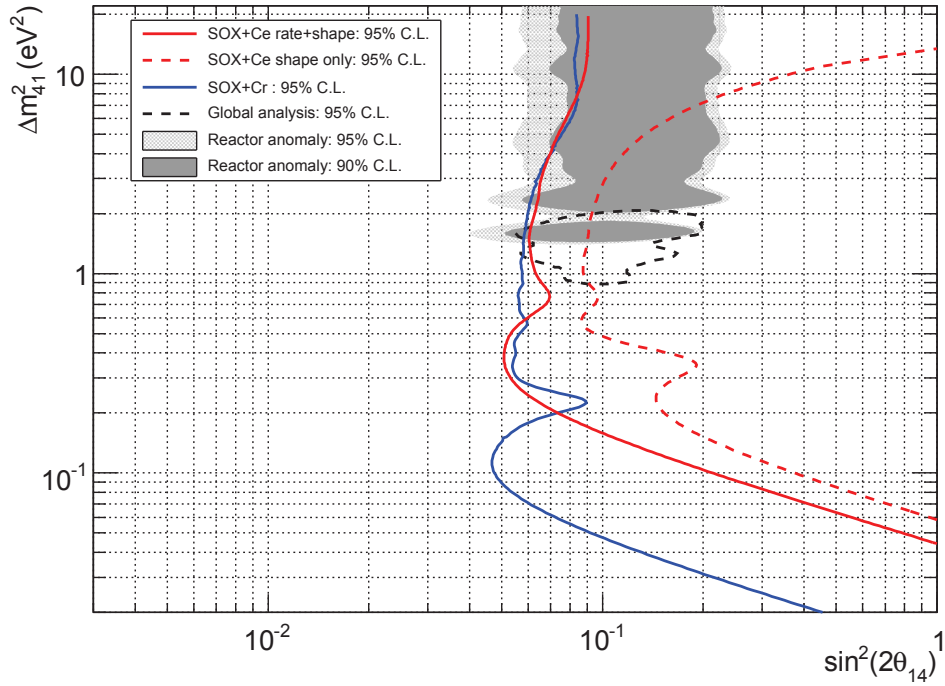


**Figure 7.13:** Sensitivity of the  $\nu_e$  and  $\bar{\nu}_e$  search at BOREXINO to the oscillation parameters  $\sin^2 2\theta_{14}$  and  $\Delta m_{41}^2$  assuming a 100 kCi  $^{144}\text{Ce}$  (red line) or 10 MCi  $^{51}\text{Cr}$  source (blue line) in the pit underneath the detector. The 95% C.L. contours of the rate+shape (red solid) and shape only (blue dashed) are shown. For the Chromium source only a rate+shape analysis was conducted [109]. As a comparison the allowed 95% and 90% C.L. contours of the reactor anomaly and the 95% C.L. contours of the global analysis are shown. The Chromium source has a superior sensitivity at low squared mass differences of  $\Delta m_{41}^2 \leq 0.1 \text{eV}^2$  accounting for the slightly lower neutrino energy and the associated neutrino survival probability. At the global best fit region of about  $\Delta m_{41}^2 \approx 1.6 \text{eV}^2$  both sources exhibit similar sensitivities.

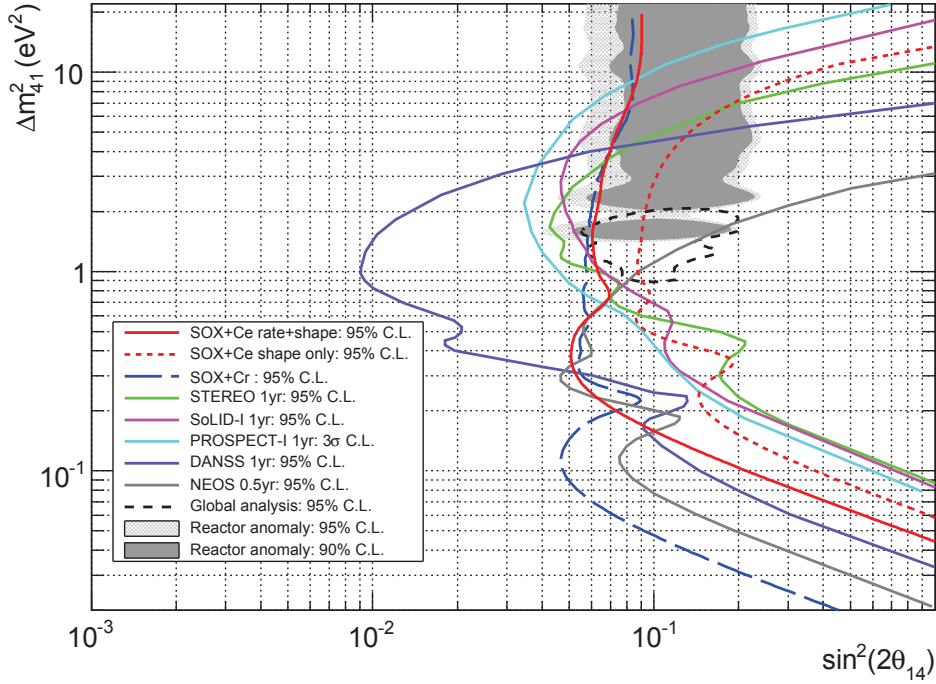


**Figure 7.14:** Sensitivity of the  $\nu_e$  and  $\bar{\nu}_e$  search at BOREXINO to the oscillation parameters  $\sin^2 2\theta_{14}$  and  $\Delta m_{41}^2$  assuming a 100 kCi  $^{144}\text{Ce}$  and 10 MCi  $^{51}\text{Cr}$  source in the pit underneath the detector. As a comparison the allowed 95% and 90% C.L. contours of the reactor anomaly and the 95% C.L. contours of the global analysis are shown. Input parameters of the analysis are listed in Table 7.2 for the SOX+Ce phase. Details about the SOX+Cr phase are reported in Ref. [109]. Following Ref. [117] the sensitivities for the STEREO [171], SoLID [173], PROSPECT [49], DANSS [90] and NEOS [143] are shown for comparison.

in Ref. [116]. All experiments, except for NEOS are able to cover the allowed parameter space at 95% C.L.. Among these experiments, only the SOX+Ce and the short-baseline reactor experiment at the ILL Grenoble (STEREO) are expected to deliver results within the near future (around 2017/2018). Similar to the STEREO experiment, PROSPECT will use a nuclear reactor. Data taking is expected to start in early 2017. During the first phase of the experimental setup, PROSPECT will be located at HFIR at ORNL. The corresponding exclusion limit at  $3\sigma$  for three years of data taking is shown in Figure 7.14 as well. Considering the time-schedule and sensitivity level, PROSPECT has to be regarded as the most competing experiment succeeding SOX+Ce and STEREO. The by far best sensitivity was predicted for the DANSS experiment which will be performed near a nuclear reactor complex in Russia. However, the precise time-schedule is still unknown.

To conclude, many experiments using different approaches are currently under preparation. The exclusion of light sterile neutrinos is within reach at the current parameter space of interest. The detection would open a new window of neutrino physics.

The potential of the SOX concept was presented in detail in the previous chapter. However, at the same time the limitations for small mixing parameter studies and further investigations have been worked out. For a long time the deployment of the source in the center of the detector together with an enlargement of the fiducial volume radius to 5.5 m was discussed. Results of these studies have been published in the original SOX study [65]. The disadvantages are, however, numerous and this scenario has to be considered unrealistic. Besides the great technical challenges, the large amount of background events might be a serious problem. Without the buffer, the accidental rate will be significantly higher and the source-induced neutron background might be difficult to handle since the space for shielding is greatly limited. Simultaneously, any work on the detector will contaminate the unique BOREXINO detector. Other scientific studies, particularly the measurement of solar neutrinos, might become impossible. An alternative to the source internal SOX phase might be the ISODAR concept.

## 8.1 The IsoDAR Concept

The Isotope Decay-at-Rest experiment (ISODAR) is part of the DAE $\delta$ ALUS design study. The primary goal of the DAE $\delta$ ALUS program is the search for  $CP$  violation in the leptonic sector using newly developed cyclotrons [184]. As part of the IsoDAR project, 60 MeV protons will be injected from a 600 kW resistive cyclotron [184] and directed towards a  ${}^9\text{Be}$  target surrounded by  ${}^7\text{Li}$  to produce a large flux of neutrons emanating from the target [184]. These neutrons will decelerate and eventually be captured by the surrounding  ${}^7\text{Li}$  [17, 184],  $\text{Li} + \text{n} \rightarrow {}^8\text{Li}$ .  ${}^8\text{Li}$  eventually decays into an electron and anti-electron neutrino with a peak antineutrino energy of 9 MeV. The compact target can therefore be considered to be an antineutrino factory. Similar to the SOX concept, these antineutrinos can be detected by a large liquid scintillator detector via the IBD,  $\bar{\nu}_e + \text{p} \rightarrow e^+ + \text{n}$ , making it possible to search for sterile neutrino oscillations. The anticipated layout consisting of an ion source, cyclotron and target would allow to cover the mostly unexplored parameter space at  $\Delta m^2 \sim 1 \text{ eV}^2$ .

### 8.1.1 Ion Source and Injection System

Before  $H_2^+$  ions can be accelerated towards the target, they have to be produced and injected into the cyclotron. Ion sources have already been developed by several institutes and are commercially available. A first test of the IsoDAR  $H_2^+$  transport and injection system was reported by *J. Alonso et al.* in Ref. [38]. As part of the experimental setup a versatile ion source (VIS), a 2.45 GHz non-resonant microwave ECR ion source was constructed. This source is the successor of the so-called TRIPS source ([38] and references therein).

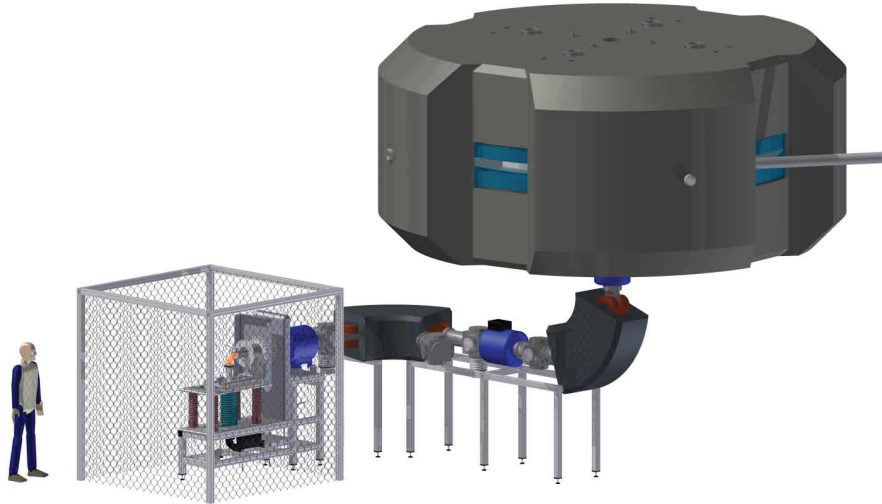


**Figure 8.1:** IsoDAR injection system and cyclotron.  $H_2^+$  are accelerated in this compact cyclotron and directed towards the Beryllium target to produce antineutrinos. The target might be 50 m downstream. Figure taken from [38].

Ions are produced by collision with electrons resonantly heated by 2.45 GHz microwaves [38].  $H_2^+$  in a plasma ion source is produced and lost through the following reactions:



The ratio of  $H_2^+$  and the  $H^+$  ions strongly depends on the electron density and the ion life-time in the plasma (see [211, 38]). Especially the increase of the ion life-time inside the plasma increases the probability that  $H^+$  and  $H_2^+$  might collide with electrons which might result in  $H_2^+$  break-up. From the technical perspective this can be controlled via changes in the magnetic field and by varying the dimension of the plasma chamber. More details can be found in Ref. [38].

The ions are then directed towards the cyclotron via the low-energy beam line transport system and the spiral inflector. The experimental layout of this system is shown in Figure 8.1. The purpose of the spiral is an axial injection of an ionized beam into the cyclotron. This system is built from two curved electrode deflectors to bend the beam  $90^\circ$  from the axial line to the median plane of the cyclotron. [38]

### 8.1.2 Cyclotron

The key to the program is the cyclotron which is currently developed in the framework of the DAE $\delta$ ALUS experiment where it will serve as the injector cyclotron for the two-cyclotron DAE $\delta$ ALUS system [17]. The compact design is one of the greatest advantages of this acceleration system and will allow construction and installation in a fast and inexpensive way. For the DAE $\delta$ ALUS program two different types of cyclotrons will be manufactured, namely the so-called injector cyclotron and a large super-conducting cyclotron. For the IsoDAR program only the injection cyclotron will be used. The first cyclotron was invented by Ernest O. Lawrence in 1932. Lawrence was awarded the 1939 Nobel Prize in Physics for the “*invention and development of the cyclotron and for results obtained with it, especially*”

with regard to artificial radioactive elements” [167]. The basic cyclotron design is still valid today.

First tests with a small prototype cyclotron have already been carried out by members of the IsoDAR project and have been published in Ref. [38]. The goal is to use the injector cyclotron both as a stand-alone accelerator for the IsoDAR sterile neutrino search [17] and as an injector for the DAE $\delta$ ALUS  $CP$  violation search. Preliminary design parameters can be found in [17]. It may be noted that an alternative design study is under consideration where the cyclotron may run with deuterons instead of  $H_2^+$  which may also effect the design of the target.

The IsoDAR cyclotron will accelerate the protons to 60 MeV on the target.

### 8.1.3 Target Design and $\bar{\nu}_e$ Production

The design of the IsoDAR target and the surrounding material used for this study was reported in [17]. The cylindrical target consists of  $^7\text{Be}$ , has a length of 20 cm and a diameter of 20 cm. The primary purpose of the  $^7\text{Be}$  target is to provide a high neutron flux for the isotope production. The  $^7\text{Be}$  target is surrounded by a 5 cm thick layer of  $\text{D}_2\text{O}$  for neutron moderation and multiplication. Furthermore, the heavy water serves as a cooling device for the target. These components are the centerpiece of a cylinder with a diameter of 200 cm and a length of 150 cm made of  $^7\text{Li}$ . For the IsoDAR program the relative content will be about 99.99% compared to the natural abundance of 92.4%. As described in [17] this kind of material is widely used in the industry and is available from a number of sources. The isotope  $^8\text{Li}$  can be produced by the following reactions:



The main  $^8\text{Li}$  production is via thermal neutron capture on  $^7\text{Li}$  and to a lesser extent by primary proton interaction in the  $^9\text{Be}$  target [17]. For enhanced production the Lithium sleeve is surrounded by graphite and steel serving as a neutron reflector [17].

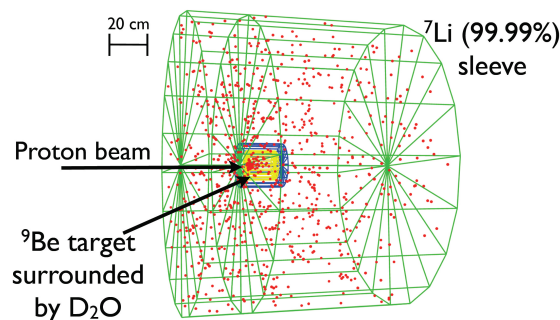
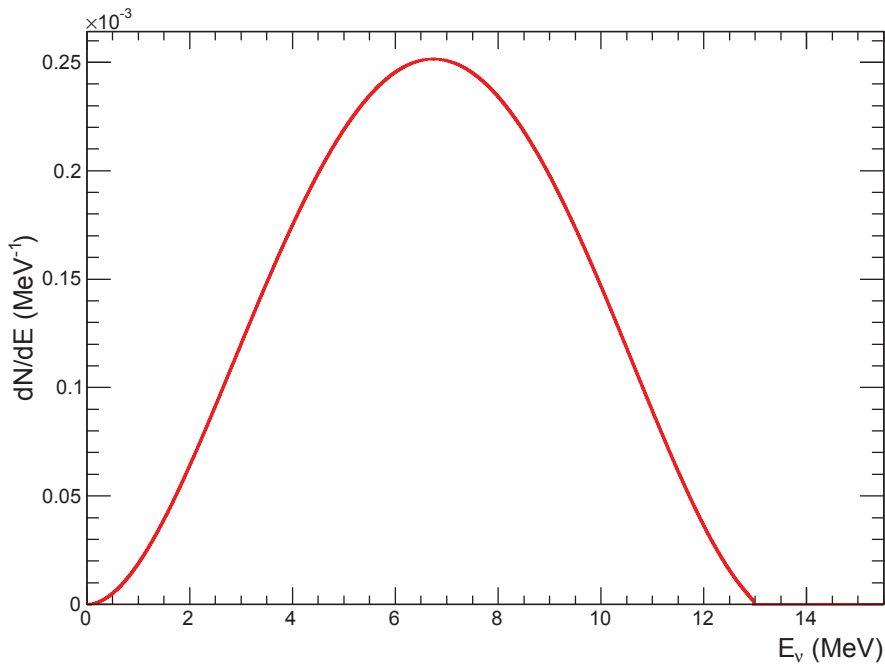


Figure 8.2: IsoDAR target. Figure taken from [17].

The antineutrinos are produced by the decay of  $^8\text{Li}$  inside the target and Lithium sleeve:





**Figure 8.3:** Antineutrino spectrum from the  $\beta^-$  decay of  ${}^8\text{Li}$ . The theoretical modeling of the antineutrino spectrum is based on the formalism as outlined in section 5.2.2 and includes several sub-leading corrections.

${}^8\text{Li}$  has a half-life of 840.3 ms and decays with a branching ratio of 100% into  ${}^8\text{Be}$ . The end-point of the  $\beta^-$  decay is at 12.9645 MeV with a mean released energy of about 7 MeV. The theoretical modeling of the antineutrino spectrum was performed as outlined in section 5.2.2 and includes several sub-leading corrections such as finite size, screening and radiative effects. The corresponding spectrum is shown in Figure 8.3. The  $\bar{\nu}_e$  spectrum was treated as an allowed transition without weak magnetism. However, an accurate modeling of the  $\bar{\nu}_e$  spectrum is not as important as for the Cerium source. The normalization uncertainty for the ISODAR concept will mainly depend on the isotope production and beam parameters. Any analysis of the ISODAR program will therefore be performed as a *shape only* analysis.

## 8.2 Event Prediction and Sensitivity

The expected number of events depends mainly on the IBD cross-section,  $\bar{\nu}_e$  spectrum, detector parameters such as the density of free neutrons and geometry as well as the neutron flux and the associated isotope production of  ${}^8\text{Li}$ . The isotope prediction rate was determined using a dedicated `Geant4` simulation together with the `QGSP-BIC-HP` physics package and reported in [17]. The hadronic processes include elastic scattering, inelastic scattering, neutron capture, neutron fission, lepton-nuclear interactions, capture-at-rest, and charge exchange [17]. Most of the  ${}^8\text{Li}$  isotopes are produced inside the sleeve. According to Ref. [17], about  $1.29 \times 10^{23}$  antineutrinos are expected assuming a 90% duty cycle and five-year run period. For the current study a source distance of 16 m from the detector center was assumed.

The sensitivity is computed using the profile likelihood method as described in section 7.4.1. Important input parameters for this study are listed in Table 8.1. Events were generated using a toy Monte Carlo approach and include energy and vertex information. Under the assumptions listed in Table 8.1 about 158,603 IBD interactions are expected. With respect

Parameter	Central value	Uncertainty	Reference
<b>Accelerator</b>	60 MeV/amu of $H_2^+$	-	
Current	10 mA of protons on target	-	
Power	600 kW	-	
Target	$^9\text{Be}$ surrounded by $^7\text{Li}$	-	
$^8\text{Li}$ distribution	(homogeneous)	-	
$\bar{\nu}_e$ flux	$1.29 \cdot 10^{23} \bar{\nu}_e$	-	
$^8\text{Li}$ $\bar{\nu}_e$ spectrum	...	...	see section 5.2.2
Source distance <sup>1</sup>	16 m	< 1 cm	
Run period	5 years		
<b>Detector</b>			
Fiducial volume geometry	(spherical)	...	
Fiducial volume radius	4.0 m		
Proton density in inner vessel	$5.264 \cdot 10^{28} \text{ m}^{-3}$	< 0.1%	
IBD detection efficiency	100%	< 0.1%	
Overall detection efficiency <sup>2</sup>	90%	-	
Position resolution	$15 \text{ cm}/\sqrt{E}$	...	
Energy resolution	$5\%/\sqrt{E}$	...	Ref. [36]

**Table 8.1:** Input for sensitivity studies using the toy MC generator. Data was taken from [17] and [36].

<sup>1</sup>Source distance: Distance from target center to detector center.

<sup>2</sup>The overall detection efficiency includes the IBD detection efficiency and the duty cycle efficiency for 5 years.

to the sterile neutrino search, the sensitivity for the 3+1 model was investigated. The results are shown in Figure 8.4. The sensitivity reached by the BOREXINO+ISODAR concept is compared to the reactor anomaly and the global best fit of Ref. [116]. Additionally, the exclusion line of the SOX+Ce phase with a source activity of 100 kCi and an exposure time of 1.5 y is shown. Other forthcoming experiments are shown as well. In this context it should be highlighted that an activity of 100 kCi is the most realistic value which might be achieved by the Mayak reactor processing plant. Compared to the allowed region, the potential of the BOREXINO+IsoDAR concept is clearly visible. In contrast to the SOX+Ce phase where a rate+shape analysis is foreseen, the ISODAR exclusion limit was calculated using the “shape only” approach. This technique relies predominantly on the reconstructed energy and position. Any distortion in the reconstructed  $L/E$  distribution due to the oscillation of sterile neutrinos may therefore significantly affect the sensitivity. However, in Ref. [17] it was shown that a normalization uncertainty  $\sigma_N = 5\%$  only affects the exclusion limit at high squared mass differences,  $\Delta m_{41}^2 > 10 \text{ eV}^2$  (see also section 7.4.2 for more explanations). Considering the global best fit at  $\Delta m_{41}^2 = 1.6 \text{ eV}^2$  the sensitivity is enhanced from  $\sim \sin^2 2\theta_{14} = 0.6$  (SOX+Ce,  $A_0 = 150 \text{ kCi}$ ) to  $\sim \sin^2 2\theta_{14} = 0.02$  (BOREXINO+ISODAR) at 90% C.L..

### 8.3 Summary and Discussion of the Borexino+IsoDAR Project

From the physics point of view the BOREXINO+ISODAR project should be seriously discussed as an alternative to the internal SOX+Ce phases with the source inside the water tank or detector. The BOREXINO+ISODAR project would not need any changes of the detector. This is an important advantage, allowing the unique BOREXINO detector to remain fully operational at the achieved low-background levels. Furthermore, the  $^8\text{Li}$  production

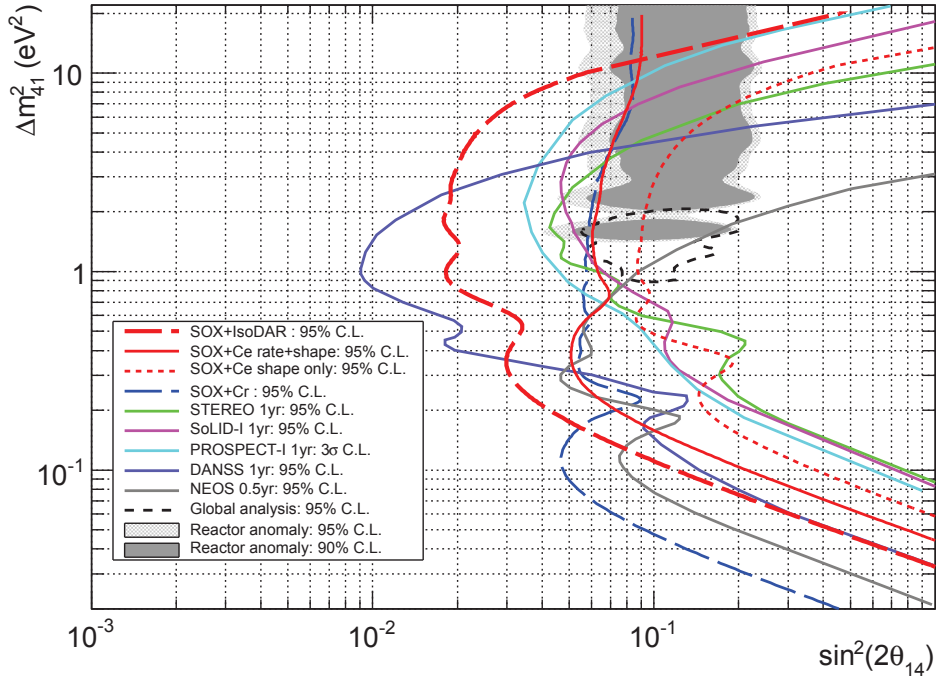


**Figure 8.4:** Comparison of a 100 kCi (red solid line) source in the pit and the BOREXINO+IsoDAR (red dashed line) concept at the BOREXINO detector. The 95% C.L. contours of the rate+shape and shape only analysis are shown. As a comparison the allowed 95% and 90% C.L. contours of the reactor anomaly (gray area) and the 95% C.L. contours of global analysis are shown. Input parameters of the analysis are listed in Table 8.1 for BOREXINO+IsoDAR concept and in Table 7.2 for the SOX+Ce concept, respectively. Following Ref. [117] the sensitivities for the STEREO [171], SoLID [173], PROSPECT [49], DANSS [90] and NEOS [143] are shown for comparison.

is essentially only dependent on the running-time of the cyclotron. The collected statistic is therefore expected to be at least four times larger than what could be expected from the Cerium source inside the center of the detector. This would also allow an excellent differentiation between 3+1 and 3+2 sterile neutrino models. Other physics investigations could include the analysis of  $\bar{\nu}_e e^-$  scattering interactions. Similar to the SOX project, this would allow to test the coupling constants  $g_R$  and  $g_L$  as well as the correlated Weinberg angle  $\sin \theta_W$  at low  $Q^2$ . Any deviation from the standard model prediction would automatically point to the existence of physics beyond the standard model. It may be worth highlighting that at these low-energies higher order loop corrections can be neglected making the analysis easy while conducting a “pure” measurement of the SM parameters. At the same time, the background may be constrained by beam-off periods. A flux normalization of the  $\bar{\nu}_e e^-$  interactions can be achieved by the parallel analysis of the IBD interactions pushing the uncertainty to lower levels. Other physics include cross-section measurement and the production of isotopes which might also be relevant and interesting for the medical industry.

The injector cyclotron planned for the ISODAR project is relatively small. BOREXINO is located in Hall C of the LNGS. Taking into account that the OPERA detector located at the same hall is currently dismantled, space might be available for the injector cyclotron. For the presented study a distance from the target to the detector center of 16 m was assumed. A much closer location might be possible, if the pit is suitable for the target. From the technical point of view, it must, however, be admitted that the necessary shielding for an underground laboratory might be problematic. Although the location might be possible, the high neutron

---

flux emerging from the target might be a serious problem and the key element in the decision to build such an apparatus near BOREXINO or not. Similar to the SOX+Ce phase with the source in the center, neutrons and possible isotope production in the environment could lead to background processes. This may not only be relevant for BOREXINO, but also for other experiments at the LNGS, especially for the DarkSide experiment which uses the old counting test facility of the BOREXINO project and is located near BOREXINO. Dedicated background simulations are therefore necessary to address this challenge forming a basis for further discussions.

In summary, the BOREXINO+IsoDAR project is technically feasible, from the physics point of view superior to the internal Cerium source, but may be challenging considering the background for other low-counting experiments. The upcoming external SOX+Ce phase is the next logical step in the search for sterile neutrinos. Depending on the results a possible SOX+Ce internal phase, a BOREXINO+ISODAR phase might be discussed and lead to a better understanding of neutrino physics.



Neutrino oscillations have been well established over the past decades and have recently been awarded the Nobel Prize in Physics. Although most of the experimental data can be explained within the three-active neutrino flavors picture, some anomalies might be explained by the existence of a fourth sterile neutrino with a relatively large squared mass difference of about  $1 \text{ eV}^2$  to the three other standard neutrinos. The main goal of the SOX experiment is to test these anomalies. For that purpose a highly intense artificial antineutrino source will be deployed underneath the BOREXINO detector.

Assuming the parameter space  $(\sin^2 2\theta_{14}, \Delta m_{41}^2)$  currently favored by global analyses and the source characteristics, an oscillation length of a few centimeters to meters is expected. The BOREXINO detector has the almost unique capability to resolve the distinct oscillation pattern. Filled with ultra-pure liquid scintillator, BOREXINO provides both energy resolution and vertex resolution to observe an energy and distance-dependent antineutrino flux variation within the detector volume.

Within the framework of this thesis, a detailed study to evaluate the performance of the SOX project has been conducted. The prediction of the antineutrino interaction is linked to the calorimetric measurement of the source activity. Therefore the spectral form of the antineutrino source and, associated to that, the mean-released energy has to be known precisely. The theoretical modeling of the antineutrino spectrum, which was performed within this thesis, includes several sub-leading corrections particularly such as finite size, radiative and screening corrections of the atomic electrons. Since this modeling is restricted to allowed transitions, further experimental studies are currently under preparation. The combination of both theoretical and experimental studies, will allow to achieve the highest possible accuracy.

The  $^{144}\text{Ce}-^{144}\text{Pr}$  spectrum serves also as an input parameter for the newly developed Monte Carlo generator to simulate the inverse beta decay reaction. The generator was designed and developed within the work of this thesis and is now part of the official BOREXINO Monte Carlo framework. The generator is complemented by an additional generator to simulate the elastic  $\nu_e e^-$  and  $\bar{\nu}_e e^-$  scattering. The last part might become relevant for future solar analyses at BOREXINO. All future analyses are expected to be performed with these simulation tools.

Part of the developed code was used to build a stand-alone and fast toy Monte Carlo generator which has already been used for sensitivities studies. Investigations performed within this thesis confirm that the neutrino anomalies can be tested at 95% C.L. at the parameter space currently favored by global fits.

An alternative and complementary concept was presented as an outlook of this thesis. The BOREXINO+IsoDAR project is a cyclotron based experiment which utilizes a Beryllium target and the decay-at-rest of  $^9\text{Li}$ . The expected  $\bar{\nu}_e$  rate is expected to be four times larger in five years than compared to the Cerium source inside the center of BOREXINO.

The deployment of a  $^{51}\text{Cr}$  neutrino source was discussed since the beginning of the BOREXINO experiment. It seems reasonable that future analyses should focus on the combination of

the results of both sources which would allow to study other low-energy effects like the measurement of the axial and vector coupling constants as well as the measurement of the Weinberg angle. Another research possibility is the measurement of the magnetic moment by studying the recoil spectrum of the  $\nu_e e^-$  elastic scattering. The foundations for these analyses have already been laid.

The SOX experiment is expected to start data taking at the end of 2017. The developed analysis tools and simulation packages will also serve as a foundation for the upcoming analysis of real data. First results are expected in 2018 and may help to clarify whether sterile neutrinos really exist or not.

*What's past is prologue*  
-William Shakespeare



# Appendix



# A

## THEORETICAL ANTINEUTRINO MODELING

---

### A.1 Tables for the Antineutrino Spectrum Modeling

	$b_1$	$b_2$	$b_3$	$b_4$	$b_5$	$b_6$
$a_{-1}$	0.115	-1.8123	8.2498	-11.223	-14.854	32.086
$a_0$	-0.00062	0.007165	0.01841	-0.53736	1.2691	-1.5467
$a_1$	0.02482	-0.5975	4.84199	-15.3374	23.9774	-12.6534
$a_2$	-0.14038	3.64953	-38.8143	172.137	-346.708	288.787
$a_3$	0.008152	-1.15664	49.9663	-273.711	657.629	-603.703
$a_4$	1.2145	-23.9931	149.972	-471.299	662.191	-305.68
$a_5$	-1.5632	33.4192	-255.133	938.53	-1641.28	1095.36

**Table A.1:** Coefficients for the finite size corrections. Table was taken from [132]. Original data from Ref. [202].

$\tilde{Z}$	1	8	13	16	23	27	29	49	84	92
$N(\tilde{Z})$	1.000	1.420	1.484	1.497	1.52	1.544	1.561	1.637	1.838	1.907

**Table A.2:**  $N(\tilde{Z})$  values for the screening correction. Table was taken from [132]. Original data from Ref. [56].

	End-point energy (keV)	Energy (keV)	Intensity (%)	Dose (keV / Bq)
<hr/> <sup>144</sup> Ce $\beta$ branches				
	318.7 (8)	91.1 (7)	76.5 (5)	69.7 (7)
	238.6 (8)	66.1 (6)	3.90 (20)	2.58 (13)
	185.2 (8)	50.2 (6)	19.6 (4)	9.84 (23)
Total			100	82.1 (11)
<hr/> <sup>144</sup> Ce $\gamma$ lines				
		133.515 (2)	11.09 (19)	14.8 (3)
		99.961 (15)	0.04 (4)	0.04 (4)
		80.12 (5)	1.36 (6)	1.09 (5)
		59.03 (3)	0.0004 (5)	0.00058 (3)
		53.395 (5)	0.1 (8)	0.053 (4)
		40.98 (10)	0.257 (16)	0.105 (7)
		33.568 (10)	0.2 (22)	0.067 (8)
Total				16.2 (4)
<hr/> <sup>144</sup> Pr $\beta$ branches				
	2997.5 (24)	1222 (11)	97.9 (4)	1196 (5)
	2301 (24)	895 (11)	1.04 (20)	9.31 (18)
	1436.5 (24)	526.27 (99)	0.0014 (3)	0.0074 (16)
	924.7 (24)	322.85 (92)	0.00062 (5)	0.002 (16)
	913 (24)	306.77 (96)	0.0067 (10)	0.0206 (3)
	811.8 (24)	267.19 (93)	1.05 (4)	2.81 (11)
	342.6 (24)	98.9 (78)	0.00015 (3)	0.00015 (3)
	322.2 (24)	92.33 (77)	0.00087 (9)	0.0008 (8)
	254.6 (24)	71.11 (76)	0.0003 (10)	0.00021 (7)
Total			100	1208.2 (53)
<hr/> <sup>144</sup> Pr $\gamma$ lines				
		2654.9 (2)	0.00015 (3)	0.0039 (7)
		2368.3 (3)	$5.4 \cdot 10^{-5}$ (13)	0.0013 (3)
		2185.66 (7)	0.694 (15)	15.2 (3)
		2072.9 (2)	0.00023 (3)	0.0047 (6)
		2046.3 (2)	0.00027 (5)	0.0055 (11)
		1978.82 (10)	0.00087 (8)	0.0173 (16)
		1560.97 (10)	0.00020 (3)	0.0031 (4)
		1489.17 (5)	0.278 (5)	4.14 (7)
		1388.02 (10)	0.00672 (9)	0.0933 (12)
		1376.27 (10)	0.00039 (4)	0.0054 (6)
		1182 (3)	$5.37 \cdot 10^{-5}$	$6.34 \cdot 10^{-4}$
		864.45 (10)	0.0024 (3)	0.0209 (23)
		814.1 (10)	0.0032 (3)	0.0262 (22)
		696.51 (3)	1.342	9.35
		674.95 (10)	0.003 (3)	0.0199 (18)
		624.7 (1)	0.00113 (3)	0.00704 (18)
Total				28.9 (4)
<hr/>				
Total $\beta$ branches				1290.3 (64)
Total $\gamma$ lines				45.1 (8)
Total X lines				3.2 (1)
Total CE and Auger lines				9.5 (3)
Grand total				1348.0 (75)

**Table A.3:** Characteristics of the <sup>144</sup>Ce–<sup>144</sup>Pr source. The table is a reproduction from Ref. [114].

# B

## ADDITIONAL INFORMATION FOR SOX

---

### B.1 $\chi^2$ Distribution and $\chi_{n,\alpha}^2$ Quantile

The probability density function is given by

$$\chi_n^2(x) = \frac{1}{2^{n/2}\Gamma(n/2)} x^{n/2-1} e^{-x/2} \quad (\text{B.1})$$

## B.2 Old Gallex Source

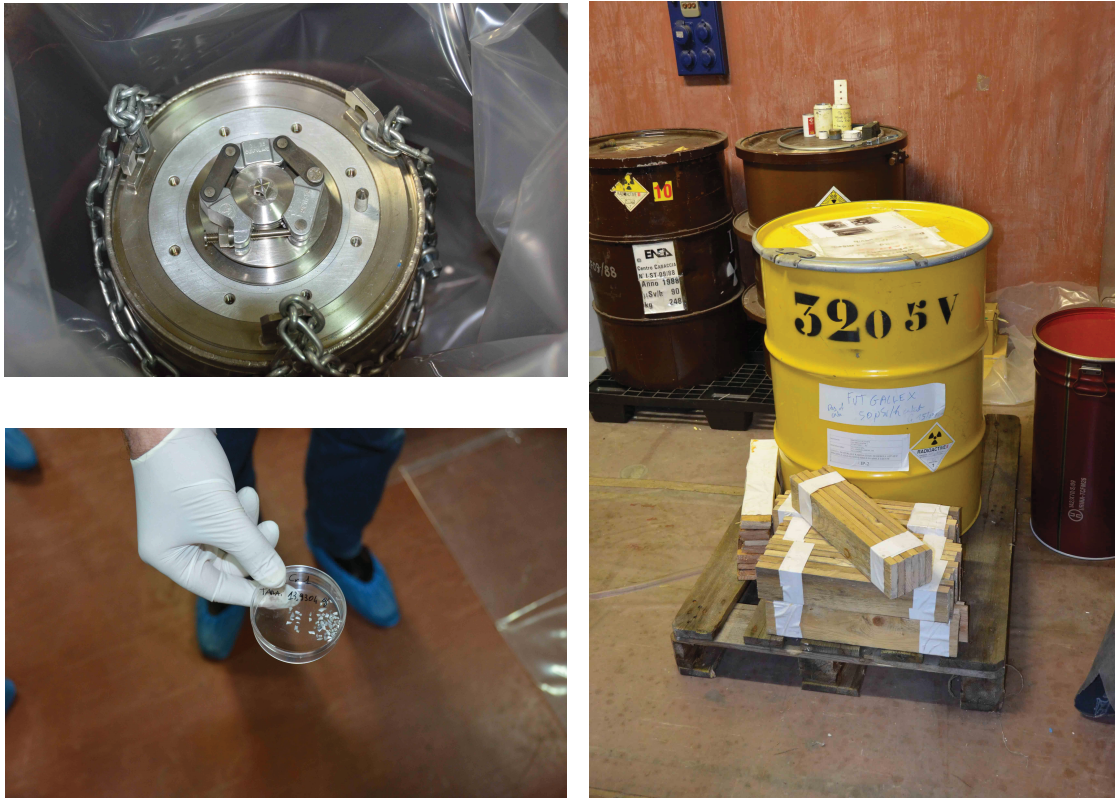
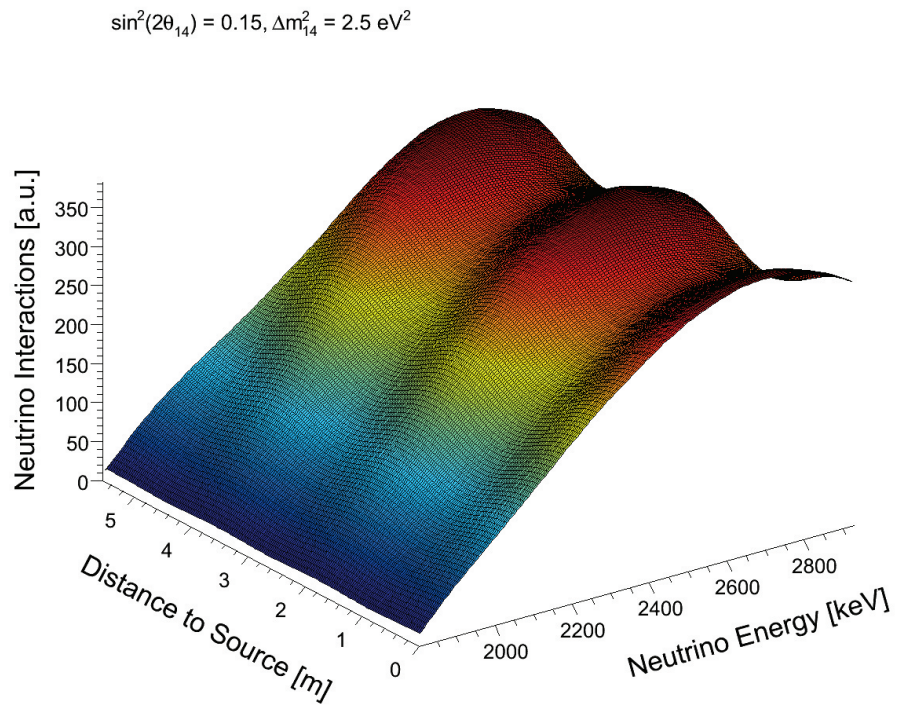


Figure B.1: GALLEX Source. Photos taken from [170].

## B.3 Cerium Source in the Center of Borexino



**Figure B.2:** Expected oscillation pattern for the  $^{144}\text{Ce}$ - $^{144}\text{Pr}$  source deployed in the center of the BOREXINO detector. For this plot the fiducial volume radius was enlarged to 5.5 m. The plot was already published by the author in Ref. [161].



In this chapter, the detector layout and experimental concept of the DOUBLE CHOOZ experiment is described. Furthermore, the data analysis and physical achievement is summarized. This chapter is meant as a supplement to section 2.4.5.2.

The first section is devoted to the reactor physics and the description of the  $\bar{\nu}_e$  production in such an environment. The structure and argumentation line of this section follows Ref. [126] and [12].

### C.1 Reactor Physics and $\bar{\nu}_e$ Production

The Double Chooz (DC) experiment is located at the French-Belgium border in northern France. Two reactor cores, each providing 4.25 GW<sub>th</sub> thermal power are responsible for the  $\bar{\nu}_e$  production. The fuel components which contribute to the  $\bar{\nu}_e$  flux consist mainly of the four isotopes  $^{235}\text{U}$ ,  $^{239}\text{Pu}$ ,  $^{238}\text{U}$ ,  $^{241}\text{Pu}$ . [126]

For the accurate determination of the mixing parameter  $\theta_{13}$ , a precise knowledge of the fuel composition, thermal power and energy spectrum are of utmost importance [126]. To the present date (2015/2016), any analysis performed by the DC experiment had to rely on theoretical predictions of the  $\bar{\nu}_e$  flux due to the absence of the near detector. To reduce the flux normalization uncertainty to a relative error as low as 3% the precise BUGEY4 flux measurement was used as an anchor-point.

In absence of oscillation, the expected number of  $\bar{\nu}_e$  interactions can be expressed as [12, 126]

$$N^{exp} = \sum_{R=1,2} \frac{\epsilon N_p}{4\pi L_R^2} \times \frac{P_{th,R}}{\langle E_f \rangle_R} \langle \sigma_f \rangle_R, \quad (\text{C.1})$$

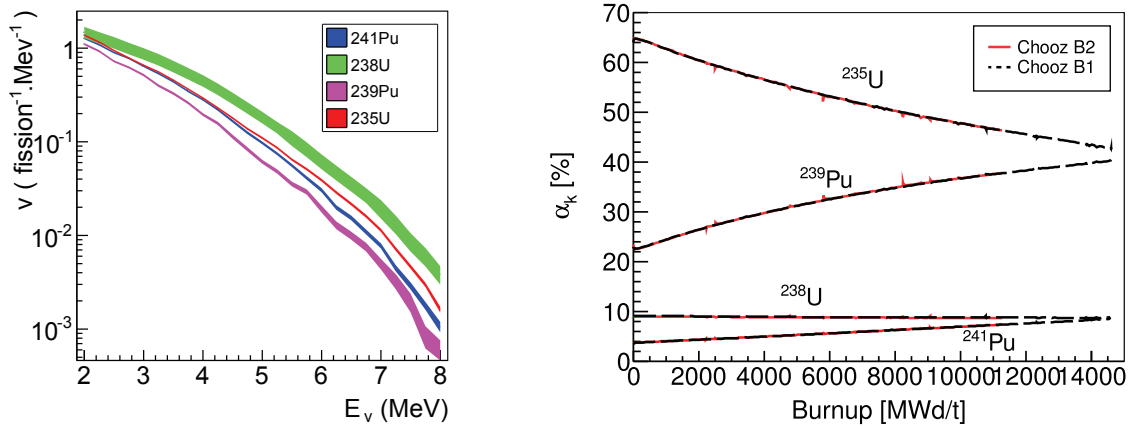
where  $N_p$  denotes the number of protons in the fiducial volume,  $\epsilon$  the detection efficiency,  $L_R$  the baseline between reactor  $R$  and the detector,  $P_{th,R}$  the thermal power,  $\langle E_f \rangle$  the mean released energy per fission and  $\langle \sigma_f \rangle$  the mean interaction cross-section. Some of the parameters ( $P_{th}$ ,  $\langle E_f \rangle$  and  $\langle \sigma_f \rangle$ ) are time dependent (see Figure C.1) and rely on data sets provided by the DC nuclear power plant operator, Electricité de Frances.

The reactor model is based on these informations combined with simulations performed with the MURE [156, 12] and DRAGON [137, 138, 204, 12] packages.

The thermal power is determined every minute by EDF [126] and the 1- $\sigma$  uncertainty of  $P_{th,R}$  is stated to be as low as 0.5% at full nominal power [12].

The mean released energy  $\langle E_f \rangle$  per fission for reactor  $R$  is computed according to [12]

$$\langle E_f \rangle_R = \sum_{a_k} a_k \langle E_f \rangle_k. \quad (\text{C.2})$$



(a) Antineutrino spectra for the different isotopes. Figure taken from [148].

(b) Evolution of the fission fragments of the four isotopes. Figure taken from [101]

**Figure C.1:** Antineutrino spectra and time evolution of fission fragments.

The mean released energy per fission for a specific isotope is weighted with the so-called fractional fission rate  $a_k$  for each isotope. The correct time-dependent modeling of these factors is one of the most important aspects in the reactor core simulation performed with the two complementary reactor codes MURE (3D core simulation) and DRAGON (2D simulation for the modeling of the individual fuel assemblies). Details of the core geometries and materials comprising the core have been fully implemented, including the exact fuel composition for each reactor cycle [12].

The mean cross-section per fission  $\langle \sigma_f \rangle = \sum_{a_k} a_k \langle \sigma_f \rangle_k$  is given by

$$\langle \sigma_f \rangle_k = \int dE S_k(E) \sigma_{IBD}(E), \quad (\text{C.3})$$

where  $S_k$  contains the  $\bar{\nu}_e$  spectrum of the  $k$ th-isotope [126, 12]. The inverse beta decay cross-section can be calculated analytically, following Ref. [194]. Effectively the mean cross-section per fission is equal to a spectrum averaged cross-section [12].

The  $\bar{\nu}_e$  spectrum for each fission isotope is the sum of many beta decays. For  $^{235}\text{U}$ ,  $^{239}\text{Pu}$  and  $^{241}\text{Pu}$  the  $\bar{\nu}_e$  spectra have been obtained from  $\beta$  spectroscopy measurements at the ILL research reactor [12, 177, 195, 123]. The conversion of the measured electron spectrum to the antineutrino spectra was performed following Ref. [132] and the corrections have been used as outlined in Ref. [163]. The conversion was performed assuming only allowed transitions (see also section 5.2.1). As pointed out by *Hayes et al.* [130] many of the involved transitions might be forbidden which introduces additional form factors that alter the  $\bar{\nu}_e$  spectrum.

To minimize the normalization uncertainty during the current phase with only the far-detector being operational<sup>1</sup>, the cross-section per fission of each reactor core is anchored to the BUGEY4 rate measurement at 15 m [12]:

$$\langle \sigma_f \rangle = \langle \sigma_f \rangle^{Bugey} + \sum_k \left( \alpha_k^R - \alpha_k^{Bugey} \right) \langle \sigma_f \rangle_k. \quad (\text{C.4})$$

This approach includes corrections due to the different fuel compositions of the BUGEY4 and DC reactor cores and reduces the uncertainty to 0.2% [12, 126]. In addition, the DC

<sup>1</sup>DOUBLE CHOOZ recently started data taking with the near detector. The first publication is expected soon within the year of 2016.

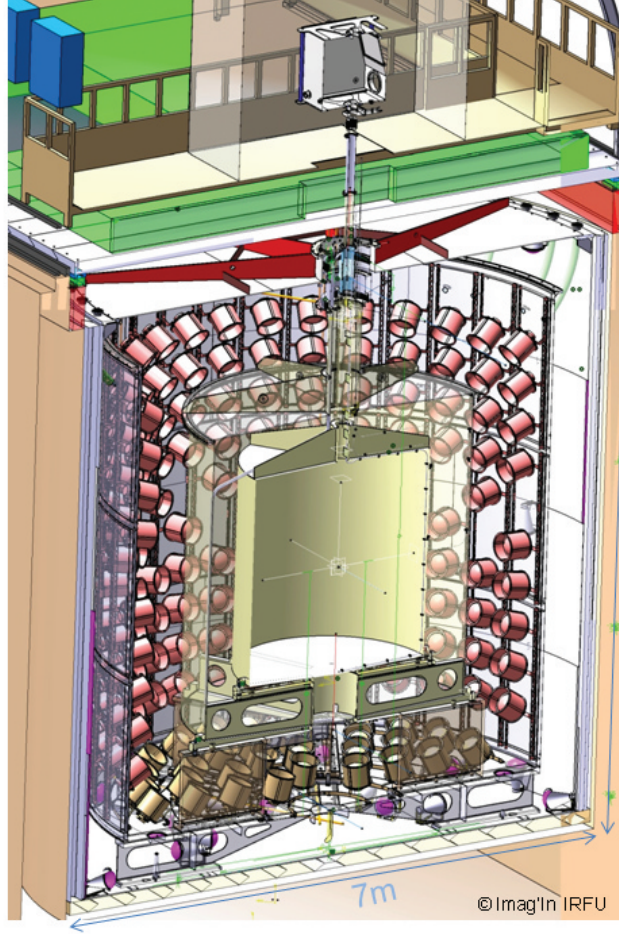


**Figure C.2:** DOUBLE CHOOZ detector. Image credit: Imag'In IRFU.

$\theta_{13}$  measurement is not affected by possible short baseline oscillations introduced by sterile neutrinos with a squared mass difference of about  $1 \text{ eV}^2$ . The expected neutrino flux is then given by

$$N^{\nu,exp} = \sum_{R=1,2} \frac{\epsilon N_p}{4\pi L_R^2} \times \frac{P_{th,R}}{\langle E_f \rangle_R} \left( \sum_k \alpha_k^R \langle \sigma_f \rangle_k^i \right) \left( \frac{\langle \sigma_f \rangle_R}{\sum_k \alpha_k^R \langle \sigma_f \rangle_k} \right), \quad (\text{C.5})$$

if potential  $\theta_{13}$  driven neutrino oscillations are neglected.

## C.2 Double Chooz Detector

The DOUBLE CHOOZ detector consists of several sub-units including the cylindrical main detector, an outer-veto and calibration devices [12]. The main detector is made of four concentric cylindrical tanks, all filled with different liquids, depending on their specific purpose [12, 126]. The innermost target is filled with Gadolinium doped liquid scintillator and is surrounded by the  $\gamma$ -catcher and the buffer (Figure C.2). The buffer contains only mineral oil to shield against external radioactivity originating from photomultiplier tubes (PMTs) and the surrounding rock. These innermost volumes form the so-called inner detector (ID). An additional volume surrounding the ID is called inner veto [12].

In total 390 10-inch PMTs are installed to collect light from the inner volumes [12]. The Inner veto has 78 10-inch PMTs to collect light from penetrating muons and spallation neutrons

Uncertainty (%)	Gd-I	Gd-II	H-II	Gd-III
Reactor flux	1.8	1.8	1.8	1.7
Detection efficiency	1.4	1.0	1.6	0.6
Detector response	1.7	0.3	0.3	-
${}^9\text{Li}+{}^8\text{He}$ BG	2.9	1.5	1.6	+1.1/-0.4
Fast-n, Stopping- $\mu$ BG	0.9	0.5	0.6	0.1
Accidental BG	0.07	0.01	0.2	0.01
Light Noise	-	-	0.1	-
Statistics	1.6	1.1	1.1	0.8
Total	4.4	2.8	3.1	+2.3/-2.0

**Table C.1:** Uncertainties for the DC analysis. Data taken from summary presented in [126].

produced outside the detector [12]. Further information, including details about the liquid scintillator can be found in Ref. [12].

### C.3 Oscillation Analysis

To extract the neutrino oscillation parameter  $\theta_{13}$  the predicted number of IBD candidates was compared to the actual measurement. The data deficit is accordingly directly linked to the neutrino oscillation parameter  $\theta_{13}$  assuming the two flavor approximation framework and a squared mass difference of  $\Delta m_{31}^2 = 2.44_{-0.1}^{+0.009} \times 10^{-3} \text{ eV}^2$ . DC has used three different data analysis techniques: *Rate+Shape*, *rate only* and the *Reactor Rate Modulation* (RRM). In total, three data sets (based on the Gd-channel) have been used to determine  $\theta_{13}$ . These analyses are complemented by two hydrogen-channel analyses. The first publication using the near detector is expected to be published within this year (2016). Depending on the IBD selection channel and procedure, different amounts of background events are expected. Table 2.2 summarizes the expected background levels for the different analyses.

#### Systematic Uncertainties

The normalization uncertainty for the different phases of the DC experiment is given in Table C.1. Without the near detector (ND), the relative uncertainty is dominated by the  $\bar{\nu}_e$  flux prediction ( $\sim 1.7\%$ ), the  ${}^9\text{Li}+{}^8\text{He}$  background measurement and the detector efficiency and response. The two latter uncertainties were greatly reduced over time, especially the detector response, due to dedicated calibration campaigns and improvements in the MC modeling.

#### Rate+Shape Analysis

Within the rate+shape analysis framework the energy dependence of the neutrino oscillation deficit is studied (e.g. in [126]). For that purpose the prompt energy spectrum (which is directly linked to the  $\bar{\nu}_e$  energy) is divided into several bins of variable size. The predicted  $\bar{\nu}_e$  interactions for a given oscillation set is then given by

$$N_i^{pred} = \sum_{R=1,2} P_{\bar{\nu}_e \rightarrow \bar{\nu}_e}(\theta_{13}) \cdot N_i^{exp,R} + \sum_b^{Backgnds} N_i^b, \quad (\text{C.6})$$

where  $P_{\bar{\nu}_e \rightarrow \bar{\nu}_e}(\theta_{13})$  denotes the survival probability while the last sum incorporates the different background components. The spectral shape of these components was measured for the

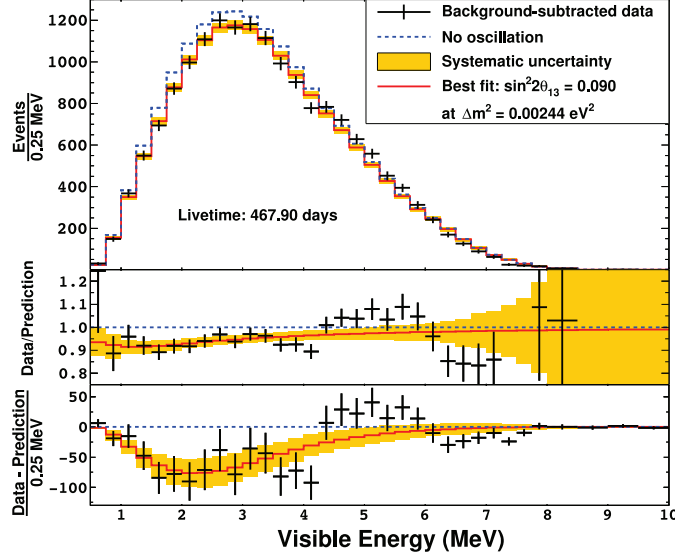


**Figure C.3:** Rate+Shape analysis to extract the mixing angle  $\theta_{13}$ . The Figure was reproduced in Ref. [126].

	$\sin^2 2\theta_{13}$	Null-Hypothesis excluded at	$\chi^2/\text{ndf}$
<b>Gd-I</b>	$0.086 \pm 0.041(\text{stat}) \pm 0.030(\text{syst})$	94.6% C.L.	23.7/17
<b>Gd-II</b>	$0.109 \pm 0.030(\text{stat}) \pm 0.025(\text{syst})$	99.8% C.L. ( $2.9\sigma$ )	42.1/35
<b>H-II</b>	$0.097 \pm 0.034(\text{stat}) \pm 0.034(\text{syst})$	97.4% C.L. ( $2.0\sigma$ )	38.9/30
<b>Gd-III</b>	$0.090^{+0.032}_{-0.029}(\text{stat+syst})$	99.9% C.L. ( $3.2\sigma$ )	52.2/40

**Table C.2:**  $\theta_{13}$  best fit values for the different phases and channels of the DOUBLE CHOOZ experiment. Taken from [126]. Details are reported in Ref. [126, 11, 12, 16, 18].

accidentals, extrapolated in case of the stopping- $\mu$  and fast-n and simulated for the  ${}^9\text{Li}+{}^8\text{He}$  component.

Statistical and systematic uncertainties are incorporated using a covariance matrix [12]:

$$M_{ij} = \sum_A^{Uncert} M_{ij}^A + \sum_b^{Backgnds} M_{ij}^b, \quad (\text{C.7})$$

where  $M_{ij}^A$  denotes the covariance matrix related to the reactor flux uncertainty and  $M_{ij}^b$  is the background covariance matrix. The  $\chi^2$  distribution is given by

$$\chi_{R+S}^2 = \sum_{i,j}^{bins} \left( N_i - N_i^{pred} \right) (M_{ij})^{-1} \left( N_j - N_j^{pred} \right)^T + \chi_{puls}^2 + \chi_{off}^2. \quad (\text{C.8})$$

Systematic uncertainties are incorporated using so-called pull terms where a given parameter such as the background rate or  $\Delta m_{31}^2$  is varied within the associated uncertainty. The last term of Eq. (C.8) includes the reactor off phases. This was only recently included in the last Gd analysis. The pulled parameters mostly cover fully correlated normalization uncertainties between the energy bins. Any uncertainties associated with the shape are included in the matrices [126]. The best fit value for  $\sin^2 2\theta_{13}$  is obtained by minimizing the  $\chi^2$  function. Table C.2 summarizes the best fit values.

### Rate Only Analysis

The rate only fit does not use any information of the spectral deformation. In fact, it takes only the event deficit into account. The result obtained in Gd-III is consistent with the rate+shape analysis and is given by  $\sin^2 2\theta_{13} = 0.090^{+0.036}_{-0.037}$  [16]. However, the uncertainties are slightly larger.

### Reactor Rate Modulation Analysis

A further possibility to extract  $\theta_{13}$  is to take advantage of the unique DC setup with only two reactors. In the reactor rate modulation analysis  $\sin^2 2\theta_{13}$  is extracted by assuming a linear correlation between the reactor-off, one reactor running and two reactors on IBD rate. According to Ref. [15] a result of  $\sin^2 2\theta_{13} = 0.090$  is given. Treating the background as a free parameter lowers the value to  $\sin^2 2\theta_{13} = 0.060 \pm 0.039$ .

## C.4 Summary and Conclusion

DOUBLE CHOOZ successfully measured the mixing angle  $\theta_{13}$ . Three different approaches have been carried out (rate+shape, rate only and RRM) yielding all consistent results within their associated errors. The most precise value is based on a rate+shape analysis and is given by  $\sin^2 2\theta_{13} = 0.090$  [16]. An increase in the sensitivity is expected in the years following 2016 when both detectors are fully operational.

# D

## CROSS-SECTION OVERVIEW

---

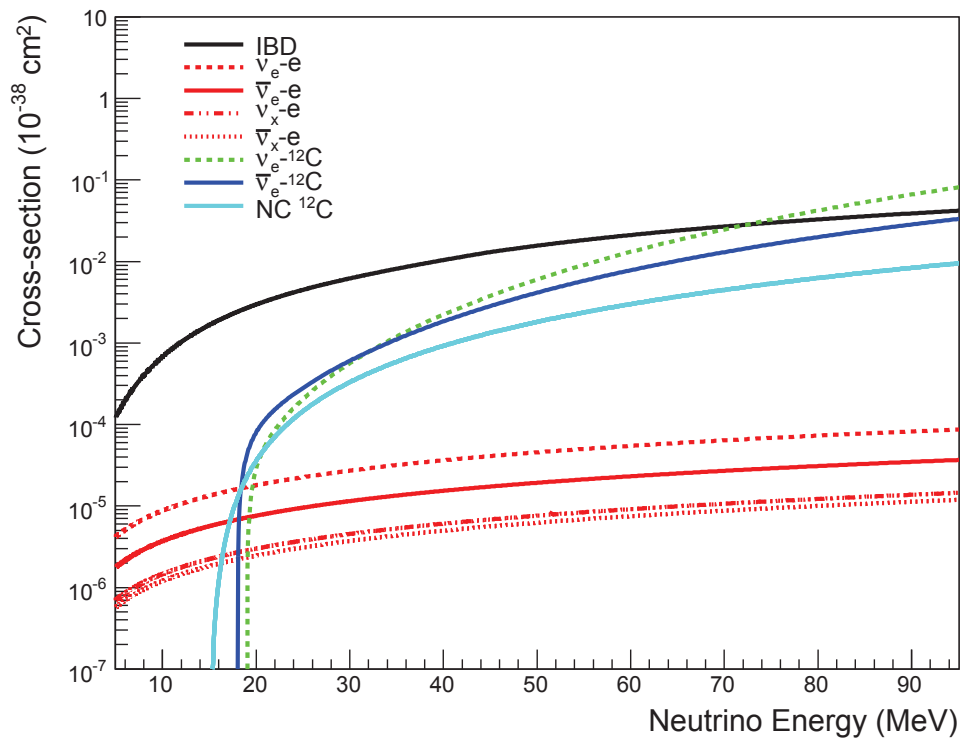


**Figure D.1:** Overview of the different detection channels in liquid scintillator detectors. The plot was created using SNOWGLOBES [4].



BIBLIOGRAPHY

---

- [1] *Beta Decay* - <http://socrates.berkeley.edu/~phylabs/adv/ReprintsPDF/>, online accessed on November 10, 2015.
- [2] *Chapter 8 Beta Decay* - <http://oregonstate.edu/instruct/ch374/ch418518/Chapter8BetaDecay-rev.pdf>, online accessed on July 19, 2016.
- [3] <http://www.wiley-vch.de/books/info/0-471-35633-6/toi99/www/struct/beta.pdf>, online accessed on November 15, 2014.
- [4] *Snowglobes*, <http://www.phy.duke.edu/~schol/snowglobes/>, accessed: 2016-07-19.
- [5] Georges Aad et al. Observation of a new particle in the search for the Standard Model Higgs boson with the ATLAS detector at the LHC. *Phys. Lett.*, B716:1–29, 2012.
- [6] K. N. Abazajian et al. Light Sterile Neutrinos: A White Paper. <http://arxiv.org/abs/1204.5379>, April 2012.
- [7] D.N. Abdurashitov et al. The Russian-American gallium experiment (SAGE) Cr neutrino source measurement. *Phys. Rev. Lett.*, 77:4708–4711, 1996.
- [8] J. N. Abdurashitov et al. Measurement of the response of the Russian-American gallium experiment to neutrinos from a Cr-51 source. *Phys. Rev.*, C59:2246–2263, 1999.
- [9] J. N. Abdurashitov et al. Measurement of the response of a Ga solar neutrino experiment to neutrinos from an Ar-37 source. *Phys. Rev.*, C73:045805, 2006.
- [10] Y. Abe et al. First Test of Lorentz Violation with a Reactor-based Antineutrino Experiment. *Phys. Rev.*, D86:112009, 2012.
- [11] Y. Abe et al. Indication for the disappearance of reactor electron antineutrinos in the Double Chooz experiment. *Phys. Rev. Lett.*, 108:131801, 2012.
- [12] Y. Abe et al. Reactor electron antineutrino disappearance in the Double Chooz experiment. *Phys. Rev.*, D86:052008, 2012.
- [13] Y. Abe et al. Direct Measurement of Backgrounds using Reactor-Off Data in Double Chooz. *Phys. Rev.*, D87(1):011102, 2013.
- [14] Y. Abe et al. First Measurement of  $\theta_{13}$  from Delayed Neutron Capture on Hydrogen in the Double Chooz Experiment. *Phys. Lett.*, B723:66–70, 2013.
- [15] Y. Abe et al. Background-independent measurement of  $\theta_{13}$  in Double Chooz. *Phys. Lett.*, B735:51–56, 2014.

- [16] Y. Abe et al. Improved measurements of the neutrino mixing angle  $\theta_{13}$  with the Double Chooz detector. *JHEP*, 10:086, 2014. [Erratum: *JHEP*02,074(2015)].
- [17] C. Aberle et al. Whitepaper on the DAE $\delta$ ALUS Program. In *Community Summer Study 2013: Snowmass on the Mississippi (CSS2013) Minneapolis, MN, USA, July 29-August 6, 2013*, 2013.
- [18] T. Abrahao et al. Measurement of  $\theta_{13}$  in Double Chooz using neutron captures on hydrogen with novel background rejection techniques. 2015.
- [19] T. Adam et al. Measurement of the neutrino velocity with the OPERA detector in the CNGS beam using the 2012 dedicated data. *JHEP*, 1301:153, 2013.
- [20] P. A. R. Ade et al. Planck 2015 results. XIII. Cosmological parameters. 2015. arXiv:1502.01589.
- [21] N. Agafonova et al. Determination of the muon charge sign with the dipolar spectrometers of the OPERA experiment. 2014. arXiv:1404.5933 [physics.ins-det].
- [22] N. Agafonova et al. Observation of tau neutrino appearance in the CNGS beam with the OPERA experiment. *PTEP*, 2014(10):101C01, 2014.
- [23] N. Agafonova et al. Discovery of  $\tau$  Neutrino Appearance in the CNGS Neutrino Beam with the OPERA Experiment. *Phys. Rev. Lett.*, 115(12):121802, 2015.
- [24] M. Agostini et al. A test of electric charge conservation with Borexino. *Phys. Rev. Lett.*, 115:231802, 2015.
- [25] M. Agostini et al. List of parameters and facts for SOX analysis . SOX-internal document. SOX-doc-91-v1, 2015.
- [26] M. Agostini et al. Spectroscopy of geoneutrinos from 2056 days of Borexino data. *Phys. Rev.*, D92(3):031101, 2015.
- [27] A. Aguilar-Arevalo et al. Evidence for neutrino oscillations from the observation of anti-neutrino(electron) appearance in a anti-neutrino(muon) beam. *Phys. Rev.*, D64:112007, 2001.
- [28] A.A. Aguilar-Arevalo et al. The miniboone detector. *Nuclear Instruments and Methods in Physics Research Section A: Accelerators, Spectrometers, Detectors and Associated Equipment*, 599(1):28 – 46, 2009.
- [29] Jochen Ahlswede, Simon Hebel, J. Ole Ross, Robert Schoetter, and Martin B. Kalinowski. Update and improvement of the global krypton-85 emission inventory. *Journal of Environmental Radioactivity*, 115:34 – 42, 2013.
- [30] J. K. Ahn et al. Observation of Reactor Electron Antineutrino Disappearance in the RENO Experiment. *Phys. Rev. Lett.*, 108:191802, 2012.
- [31] Evgeny Kh. Akhmedov and Alina Wilhelm. Quantum field theoretic approach to neutrino oscillations in matter. *JHEP*, 01:165, 2013.
- [32] G. Alimonti et al. A large scale low-background liquid scintillation detector: The counting test facility at Gran Sasso. *Nucl. Instrum. Meth.*, A406:411–426, 1998.
- [33] G. Alimonti et al. Measurement of the C-14 abundance in a low-background liquid scintillator. *Phys. Lett.*, B422:349–358, 1998.

- [34] G. Alimonti et al. Light propagation in a large volume liquid scintillator. *Nucl. Instrum. Meth.*, A440:360–371, 2000.
- [35] G. Alimonti et al. Science and technology of BOREXINO: A Real time detector for low-energy solar neutrinos. *Astropart. Phys.*, 16:205–234, 2002.
- [36] G. Alimonti et al. The Borexino detector at the Laboratori Nazionali del Gran Sasso. *Nucl.Instrum.Meth.*, A600:568–593, 2009.
- [37] G. Alimonti et al. The liquid handling systems for the Borexino solar neutrino detector. *Nucl. Instrum. Meth.*, A609:58–78, 2009.
- [38] J. Alonso, S. Axani, L. Calabretta, D. Campo, L. Celona, J. M. Conrad, A. Day, G. Castro, F. Labrecque, and D. Winklehner. The IsoDAR High Intensity  $H_2^+$  Transport and Injection Tests. *JINST*, 10(10):T10003, 2015.
- [39] K. Altenmueller et al. Ce-Pr past spectral measurements and impact on SOX. *sox public note. SOX-doc-72-v1*, 2015.
- [40] F. P. An et al. Observation of electron-antineutrino disappearance at Daya Bay. *Phys. Rev. Lett.*, 108:171803, 2012.
- [41] F. P. An et al. New Measurement of Antineutrino Oscillation with the Full Detector Configuration at Daya Bay. *Phys. Rev. Lett.*, 115(11):111802, 2015.
- [42] Fengpeng An et al. Neutrino Physics with JUNO. 2015. arXiv:1507.05613 [physics.ins-det].
- [43] P. Anselmann et al. First results from the Cr-51 neutrino source experiment with the GALLEX detector. *Phys. Lett.*, B342:440–450, 1995.
- [44] M. Apollonio et al. Search for neutrino oscillations on a long base-line at the CHOOZ nuclear power station. *Eur. Phys. J.*, C27:331, 2003.
- [45] S. Appel et al. Measurement of the spectral shape for the cerium-praseodymium. SOX-public document. SOX-doc-187-v1, 2016.
- [46] F. Ardellier et al. Double Chooz: A Search for the neutrino mixing angle  $\theta_{13}$ . 2006.
- [47] C. Arpesella et al. Direct Measurement of the Be-7 Solar Neutrino Flux with 192 Days of Borexino Data. *Phys. Rev. Lett.*, 101:091302, 2008.
- [48] C. Arpesella et al. First real time detection of Be-7 solar neutrinos by Borexino. *Phys. Lett.*, B658:101–108, 2008.
- [49] J. Ashenfelter et al. The PROSPECT Physics Program. 2015.
- [50] C. Athanassopoulos et al. The liquid scintillator neutrino detector and lampf neutrino source. *Nuclear Instruments and Methods in Physics Research Section A: Accelerators, Spectrometers, Detectors and Associated Equipment*, 388(1):149 – 172, 1997.
- [51] D. Autiero et al. Large underground, liquid based detectors for astro-particle physics in Europe: Scientific case and prospects. *JCAP*, 0711:011, 2007.
- [52] John Bahcall. John Bahcall website <http://www.sns.ias.edu/~jnb/> online accessed on July 10, 2016, 2005.

- [53] John N. Bahcall. Gallium solar neutrino experiments: Absorption cross-sections, neutrino spectra, and predicted event rates. *Phys. Rev.*, C56:3391–3409, 1997.
- [54] V. Barger, Yuan ben Dai, K. Whisnant, and Bing-Lin Young. Neutrino Mixing, CP/T Violation and Textures in Four-Neutrino Models. *Rev. D*, 59:991051–6, 1999.
- [55] Matthew Bass. *Neutrino Oscillation Parameter Sensitivity in Future long-baseline Experiments*. PhD thesis, Colorado State University, 2014.
- [56] H. Behrens and H. Bühring. *Electron Radial Wave Functions and Nuclear Beta-Decay*. International Series of Monographs on Physics Series. Clarendon Press, 1982.
- [57] G. Bellini et al. Measurement of the solar  $^8\text{B}$  neutrino rate with a liquid scintillator target and 3 MeV energy threshold in the Borexino detector. *Phys. Rev.*, D82:033006, 2010.
- [58] G. Bellini et al. Observation of Geo-Neutrinos. *Phys. Lett.*, B687:299–304, 2010.
- [59] G. Bellini et al. Muon and Cosmogenic Neutron Detection in Borexino. *JINST*, 6:P05005, 2011.
- [60] G. Bellini et al. Precision measurement of the  $^7\text{Be}$  solar neutrino interaction rate in borexino. *Phys. Rev. Lett.*, 107:141302, Sep 2011.
- [61] G. Bellini et al. First evidence of pep solar neutrinos by direct detection in Borexino. *Phys. Rev. Lett.*, 108:051302, 2012.
- [62] G. Bellini et al. Search for solar axions produced in the  $p(d,^3\text{He})\text{A}$  reaction with Borexino detector. *Phys. Rev. D*, 85:092003, May 2012.
- [63] G. Bellini et al. Measurement of geo-neutrinos from 1353 days of Borexino. *Phys.Lett.*, B722:295–300, 2013.
- [64] G. Bellini et al. New limits on heavy sterile neutrino mixing in  $^8\text{B}$  decay obtained with the Borexino detector. *Phys. Rev.*, D88(7):072010, 2013.
- [65] G. Bellini et al. SOX: Short distance neutrino Oscillations with BoreXino. *JHEP*, 1308:038, 2013.
- [66] G. Bellini et al. Final results of Borexino Phase-I on low energy solar neutrino spectroscopy. *Phys.Rev.*, D89:112007, 2014.
- [67] G. Bellini et al. Neutrinos from the primary proton-proton fusion process in the Sun. *Nature*, 512(7515):383–386, 2014.
- [68] G. Bellini, A. Ianni, L. Ludhova, F. Mantovani, and W. F. McDonough. Geo-neutrinos. *Prog. Part. Nucl. Phys.*, 73:1–34, 2013.
- [69] J. Benziger et al. The Scintillator Purification System for the Borexino Solar Neutrino Detector. *Nucl. Instrum. Meth.*, A587:277–291, 2008.
- [70] J. Beringer et al. Particle data group, 2012.
- [71] H. A. Bethe. Energy production in stars. *Phys. Rev.*, 55:434–456, 1939.
- [72] H. A. Bethe and C. L. Critchfield. The formation of deuterium by proton combination. *Phys. Rev.*, 54:248–254, 1938.

- [73] F. Boehm et al. Final results from the Palo Verde neutrino oscillation experiment. *Phys. Rev.*, D64:112001, 2001.
- [74] Kalpana Bora, Debajyoti Dutta, and Pomita Ghoshal. Probing Sterile Neutrino Parameters with Double Chooz, Daya Bay and RENO. *JHEP*, 12:025, 2012.
- [75] J.P. Both, A. Mazzolo, Y. Penelieu, O. Petit, and B. Roesslinger. User manual for version 43 of the tripoli-4 monte-carlo method particle transport computer code (cear-6044). france, 2003.
- [76] D. Bravo. SOX-Cr update (melt and recast, irradiation, D<sub>2</sub>O core). SOX-public document. SOX-doc-60-v1, 2014.
- [77] Margherita Buizza Avanzini. *The <sup>8</sup>B Solar Neutrino Analysis in Borexino and Simulations of Muon Interaction Products in Borexino and Double Chooz*. PhD thesis, Milan U., 2011.
- [78] R. L. Burman. Neutrino flux calculations for the ISIS spallation neutron facility. *Nucl. Instrum. Meth.*, A368:416–424, 1996.
- [79] Benjamin Büttner. Beidseitige Auslese an OPERA-Driftröhren zur Rekonstruktion des Durchgangsortes entlang der Rohre. Diplomarbeit, Universität Hamburg, August 2011.
- [80] Benjamin Büttner, Joachim Ebert, Caren Hagner, Annika Hollnagel, Jan Lenkeit, Mikko Meyer, and Björn Wonsak. The Muon-Tracking-System of the OPERA Experiment. *PoS*, NEUTEL2015:065, 2015.
- [81] C. Arpesella. Borexino at Gran Sasso. Proposal for a real time detector for low energy solar neutrinos. 1991. Online available: <http://borex.lngs.infn.it/papers/>.
- [82] Erica Caden. Studying Neutrino Directionality with Double Chooz. 2012. arXiv:1208.3628[physics.ins-det].
- [83] Serguei Chatrchyan et al. Observation of a new boson at a mass of 125 GeV with the CMS experiment at the LHC. *Phys. Lett.*, B716:30–61, 2012.
- [84] J. H. Christenson, J. W. Cronin, V. L. Fitch, and R. Turlay. Evidence for the 2 pi Decay of the k(2)0 Meson. *Phys. Rev. Lett.*, 13:138–140, 1964.
- [85] Glen Cowan, Kyle Cranmer, Eilam Gross, and Ofer Vitells. Asymptotic formulae for likelihood-based tests of new physics. *The European Physical Journal C*, 71(2), 2011.
- [86] M. Cribier et al. Production of a 62-PBq Cr-51 low-energy neutrino source for GALLEX. *Nucl. Instrum. Meth.*, A378:233–250, 1996.
- [87] M. Cribier et al. Proposed Search for a Fourth Neutrino with a PBq Antineutrino Source. *Phys. Rev. Lett.*, 107:201801, Nov 2011.
- [88] Michel Cribier, Maximilien Fechner, Thierry Lasserre, Alain Letourneau, David Lhuillier, Guillaume Mention, Davide Franco, Vasily Kornoukhov, and Stefan Schonert. A proposed search for a fourth neutrino with a PBq antineutrino source. *Phys. Rev. Lett.*, 107:201801, 2011.
- [89] Eve Curie. *Madame Curie: Eine Biographie*. FISCHER Taschenbuch; Auflage: 29 (1. Oktober 1983), 1983.

- [90] Mikhail Danilov. Sensitivity of DANSS detector to short range neutrino oscillations. 2014.
- [91] Stefano Davini. *Measurement of the pep and CNO solar neutrino interaction rates in Borexino*. PhD thesis, INFN, Genoa, 2012.
- [92] P. C. de Holanda, Wei Liao, and A. Yu. Smirnov. Toward precision measurements in solar neutrinos. *Nucl. Phys.*, B702:307–332, 2004.
- [93] A. Derbin and V. Muratova. Energy calibration with  $^{241}\text{Am}^9\text{Be}$  neutron source (Borexino internal note), 2009.
- [94] M. Durero, M. Meyer, and M. Vivier. Ce-144/Pr-144 Spectrum Modeling and Uncertainties. *sox internal note. SOX-doc-62-v1*, 2014.
- [95] Mathieu Durero. Beta spectrum modeling for the CeLAND experiment antineutrino source. Master’s thesis, Kungliga Tekniska Högskolan, Stockholm, October 2013.
- [96] D. A. Dwyer, K. M. Heeger, B. R. Littlejohn, and P. Vogel. Search for Sterile Neutrinos with a Radioactive Source at Daya Bay. *Phys. Rev.*, D87(9):093002, 2013.
- [97] Steve Dye. Geo-neutrinos and the Radioactive Power of the Earth. *Rev. Geophys.*, 50:3007, 2012.
- [98] Steve Dye. Geo-neutrinos: recent developments. 2014. arXiv:1412.3520[physics.geo-ph].
- [99] Gösta Ekspong, editor. *Nobel Lectures, Physics 1991-1995*, Singapore, 1997. World Scientific Publishing Co. Nobel lecture given by F. Reines on December 8, 1995. The Neutrino: From Poltergeist to Particle.
- [100] L.R.B. Elton. A semi-empirical formula for the nuclear radius. *Nuclear Physics*, 5:173 – 178, 1958.
- [101] M. Fallot and A. Onillon. Reactor plots, Double Chooz Internal Document, DC-doc-3377-v1. 2011.
- [102] Yasaman Farzan, Thomas Schwetz, and Alexei Yu Smirnov. Reconciling results of LSND, MiniBooNE and other experiments with soft decoherence. *JHEP*, 07:067, 2008.
- [103] Gary J. Feldman and Robert D. Cousins. A Unified approach to the classical statistical analysis of small signals. *Phys. Rev.*, D57:3873–3889, 1998.
- [104] E. Fermi. An attempt of a theory of beta radiation. 1. *Z. Phys.*, 88:161–177, 1934.
- [105] Vincent Fischer. *Beta-decay emitted electronic antineutrinos as a tool for unsolved problems in neutrino oscillation physics*. PhD thesis, UPMC, Paris (main), 2015.
- [106] D. V. Forero, M. Tortola, and J. W. F. Valle. Neutrino oscillations refitted. *Phys. Rev.*, D90(9):093006, 2014.
- [107] J. A. Formaggio and G. P. Zeller. From eV to EeV: Neutrino Cross Sections Across Energy Scales. *Rev. Mod. Phys.*, 84:1307, 2012.
- [108] Tore Frängsmyr [Nobel Foundation], editor. *Les Prix Nobel. The Nobel Prizes 1995*, Stockholm, 1996.
- [109] D. Franco, G. Ranucci, and M. Wurm. Studies on CrSOX Sensitivity. SOX-public document. SOX-doc-30-v1, 2014.

- [110] H. Fritzsch and J. Plankl. Mixing of quark flavors. *Phys. Rev. D*, 35:1732–1735, Mar 1987.
- [111] J. Gaffiot. Source induced backgrounds, spectrum modelling and sample measurements. SOX-public document. SOX-doc-43-v2, 2014.
- [112] J. Gaffiot, T. Lasserre, et al. Experimental Parameters for a Cerium 144 Based Intense Electron Antineutrino Generator Experiment at Very Short Baselines. *Phys. Rev.*, D91(7):072005, 2015.
- [113] A. Gando et al. Partial radiogenic heat model for Earth revealed by geoneutrino measurements. *Nature Geo.*, 4:647–651, 2011.
- [114] A. Gando et al. CeLAND: search for a 4th light neutrino state with a 3 PBq  $^{144}\text{Ce}$ - $^{144}\text{Pr}$  electron antineutrino generator in KamLAND. 2013.
- [115] A. Gando et al. Reactor on-off antineutrino measurement with KamLAND. *Phys. Rev. D*, 88:033001, Aug 2013.
- [116] C. Giunti, M. Laveder, Y.F. Li, Q.Y. Liu, and H.W. Long. Update of Short-Baseline Electron Neutrino and Antineutrino Disappearance. *Phys.Rev.*, D86:113014, 2012.
- [117] Carlo Giunti. Light Sterile Neutrinos: Status and Perspectives. *Nucl. Phys.*, B908:336–353, 2016.
- [118] Carlo Giunti and Marco Laveder. Short-Baseline Electron Neutrino Disappearance, Tritium Beta Decay and Neutrinoless Double-Beta Decay. *Phys. Rev.*, D82:053005, 2010.
- [119] M. C. Gonzalez-Garcia, Michele Maltoni, Jordi Salvado, and Thomas Schwetz. Global fit to three neutrino mixing: critical look at present precision. *Journal of High Energy Physics*, 2012(12):1–24, 2012.
- [120] M. Gronau, R. Johnson, and J. Schechter. On parametrizing the  $N$ -generation quark mixing matrix. *Phys. Rev. D*, 32:3062–3065, Dec 1985.
- [121] Michael Gronau and Joseph Schechter. Constraints on the mixing of a fourth family of quarks. *Phys. Rev. D*, 31:1668–1675, Apr 1985.
- [122] Nils-Holger Haag. *Experimental Determination of the Antineutrino Spectrum of the Fission Products of  $^{238}\text{U}$* . PhD thesis, Technische Universität München, 2013.
- [123] A. A. Hahn, K. Schreckenbach, G. Colvin, B. Krusche, W. Gelletly, and F. Von Feilitzsch. Anti-neutrino Spectra From  $^{241}\text{Pu}$  and  $^{239}\text{Pu}$  Thermal Neutron Fission Products. *Phys. Lett.*, B218:365–368, 1989.
- [124] W. Hampel et al. Final results of the Cr-51 neutrino source experiments in GALLEX. *Phys. Lett.*, B420:114–126, 1998.
- [125] Manuel Harder. Messung des Ladungsverhältnisses kosmischer Myonen im OPERA-Detektor. Diplomarbeit, Universität Hamburg, February 2012.
- [126] Julia Haser. *Neutron Detection Uncertainties in the  $\theta_{13}$  Analysis of the Double Chooz Experiment*. PhD thesis, Ruprecht-Karls-Universität, Heidelberg, 2015.
- [127] Naoya Hata and Wick Haxton. Implications of the GALLEX source experiment for the solar neutrino problem. *Phys. Lett.*, B353:422–431, 1995.

- [128] W. C. Haxton. Cross-section uncertainties in the gallium neutrino source experiments. *Phys. Lett.*, B431:110–118, 1998.
- [129] Wick Haxton. Neutrino physics: What makes the Sun shine. *Nature*, 512(7515):378–380, 2014.
- [130] A. C. Hayes, J. L. Friar, G. T. Garvey, Gerard Jungman, and Guy Jonkmans. Systematic Uncertainties in the Analysis of the Reactor Neutrino Anomaly. *Phys. Rev. Lett.*, 112:202501, 2014.
- [131] Kathrin A. Hochmuth, Franz von Feilitzsch, Brian D. Fields, Teresa Marrodan Undagoitia, Lothar Oberauer, Walter Potzel, Georg G. Raffelt, and Michael Wurm. Probing the Earth’s interior with a large-volume liquid scintillator detector. *Astropart. Phys.*, 27:21–29, 2007.
- [132] Patrick Huber. On the determination of anti-neutrino spectra from nuclear reactors. *Phys. Rev.*, C84:024617, 2011. [Erratum: *Phys. Rev.*C85,029901(2012)].
- [133] A. Ianni, L. Ludhova, and A. C. Re. pp-nu: theoretical expectations and experimental values for solar flux, survival probability, and interaction rate, Borexino internal note, 2014.
- [134] A. Ianni and D. Montanino. The Cr-51 and Sr-90 sources in BOREXINO as tool for neutrino magnetic moment searches. *Astropart. Phys.*, 10:331–338, 1999.
- [135] A. Ianni, D. Montanino, and G. Scioscia. Test of nonstandard neutrino properties with the BOREXINO source experiments. *Eur. Phys. J.*, C8:609–617, 1999.
- [136] Aldo Ianni. *Studio di proprietà non convenzionali per il neutrino mediante sorgenti artificiali di alta intensità in BOREXINO*. PhD thesis, L’Aquila U.
- [137] C. L. Jones. Simulation of the SONGS Reactor Antineutrino Flux Using DRAGON. 2011.
- [138] C. L. Jones, A. Bernstein, J. M. Conrad, Z. Djurcic, M. Fallot, L. Giot, G. Keefer, A. Onillon, and L. Winslow. Reactor Simulation for Antineutrino Experiments using DRAGON and MURE. *Phys. Rev.*, D86:012001, 2012.
- [139] Markus Kaiser. Supernova Neutrinos in LENA - Towards a Time- and Flavor-Resolved Analysis. Master’s thesis, Universität Hamburg, December 2012.
- [140] G. Karagiorgi, A. Aguilar-Arevalo, J. M. Conrad, M. H. Shaevitz, K. Whisnant, M. Sorel, and V. Barger. Leptonic  $CP$  violation studies at MiniBooNE in the  $(3 + 2)$  sterile neutrino oscillation hypothesis. *Phys. Rev. D*, 75:013011, Jan 2007.
- [141] Georgia S. Karagiorgi. *Searches for New Physics at MiniBooNE: Sterile Neutrinos and Mixing Freedom*. PhD thesis, MIT, 2010.
- [142] Boris Kayser. On the quantum mechanics of neutrino oscillation. *Phys. Rev. D*, 24:110–116, Jul 1981.
- [143] Ba Ro Kim et al. Development and Mass Production of a Mixture of LAB- and DIN-based Gadolinium-loaded Liquid Scintillator for the NEOS Short-baseline Neutrino Experiment. 2015.
- [144] K.S. Krane and D. Halliday. *Introductory nuclear physics*. Wiley. 1987.

- [145] T. Lachenmaier et al. Physics with the large liquid-scintillator detector LENA. *Prog. Part. Nucl. Phys.*, 64:381–383, 2010.
- [146] T. Lasserre. Testing the Reactor and Gallium Anomalies with Intense (Anti)Neutrino Emitters. *Nucl.Phys.Proc.Suppl.*, 235-236:214–219, 2013.
- [147] Thierry Lasserre. Light Sterile Neutrinos in Particle Physics: Experimental Status. *Phys. Dark Univ.*, 4:81–85, 2014.
- [148] L. Lhuillier et al. Reactor plots and macros, Double Chooz Internal Document, DCdoc-3373-v4. 2011.
- [149] W. Lin, L. Chen, W. Yu, H. Ma, Z. Zeng, J. Lin, and S. Zeng. Radioactivity impacts of the fukushima nuclear accident on the atmosphere. *Atmospheric Environment*, 102:311 – 322, 2015.
- [150] A. Longhin, A. Paoloni, and F. Pupilli. Large-angle scattering of multi-GeV muons on thin Lead targets. *IEEE Trans. Nucl. Sci.*, 62:2216, 2015.
- [151] L. Ludhova and S. Zavatarelli. Studying the Earth with Geoneutrinos. page 425693, 2013.
- [152] J. Lundberg, J. Conrad, W. Rolke, and A. Lopez. Limits, discovery and cut optimization for a Poisson process with uncertainty in background and signal efficiency: TRolke 2.0. *Comput. Phys. Commun.*, 181:683–686, 2010.
- [153] M. Vivier for the Borexino/SOX collaboration. SOX: short baseline neutrino oscillations with Borexino (Talk given at the TAUP 2015 conference in Torino), 2015.
- [154] Werner Maneschg. *Low-energy solar neutrino spectroscopy with Borexino: Towards the detection of the solar pep and CNO neutrino flux*. PhD thesis, Heidelberg U., 2011.
- [155] G. Mention, M. Fechner, Th. Lasserre, Th.A. Mueller, D. Lhuillier, et al. The Reactor Antineutrino Anomaly. *Phys.Rev.*, D83:073006, 2011.
- [156] Meplan et al. in ENC 2005: European Nuclear Conference; Nuclear power for the XXIst century: from basic research to high-tech industry. 2005.
- [157] S. Mertens, T. Lasserre, S. Groh, G. Drexlin, F. Glueck, A. Huber, A. W. P. Poon, M. Steidl, N. Steinbrink, and C. Weinheimer. Sensitivity of Next-Generation Tritium Beta-Decay Experiments for keV-Scale Sterile Neutrinos. *JCAP*, 1502(02):020, 2015.
- [158] M. Meyer. General Meeting presentation (MC Simulations and Sensitivity Studies for SOX). SOX-doc-12-v1, 2013.
- [159] Mikko Meyer. Analyse von CC Ereignissen beim OPERA Experiment. Diplomarbeit, Universität Hamburg, June 2011.
- [160] Mikko Meyer. Search for Sterile Neutrinos with the Borexino Detector. In *Proceedings, 20th International Conference on Particles and Nuclei (PANIC 14)*, pages 317–320, 2014. DOI: 10.3204/DESY-PROC-2014-04/7.
- [161] Mikko Meyer. SOX: Neutrino Oscillometry in Borexino. *PoS*, NEUTEL2015:075, 2015.
- [162] S.P. Mikheyev and A. Yu. Smirnov. . *Sov. J. Nucl. Phys.*, 42, 1985.

- [163] Th. A. Mueller et al. Improved Predictions of Reactor Antineutrino Spectra. *Phys. Rev.*, C83:054615, 2011.
- [164] B. Ricci N. Ferrari, G. Fiorentini. The Cr-51 neutrino source and Borexino: a desirable marriage. *Phys. Letters B*, 387:427–431, 1996.
- [165] B. Neumair. Sensitivity studies and systematics of the SOX project. SOX-internal document. SOX-doc-145-v1, 2015.
- [166] B. Neumair. Systematic uncertainties: interplay between heat power and shape factor. Borexino Collaboration Meeting in Cagliari, 2015.
- [167] Nobel Foundation. nobelprize.org, 2015. [Online; accessed 4-August-2015].
- [168] Christian Oldorf. *Operation of CdZnTe Semiconductor Detectors in Liquid Scintillator for the COBRA Experiment*. PhD thesis, U. Hamburg, Dept. Phys., 2015.
- [169] M. Pallavicini. The SOX project: a search for sterile neutrinos with BoreXino. *PoS, Neutel2013:026*, 2013.
- [170] M. Pallavicini and P. Lombardi. First sampling process of GALLEX’s old source. SOX-public document. SOX-doc-14-v8, 2014.
- [171] M. Pequignot. The Nucifer and Stereo reactor antineutrino experiments. *Nucl. Part. Phys. Proc.*, 265-266:126–128, 2015.
- [172] Alessandra Carlotta Re. *The Borexino Impact in the global Analysis of Neutrino Data*. PhD thesis, University of Milano, 2012.
- [173] Nick Ryder. First results of the deployment of a SoLid detector module at the SCK-CEN BR2 reactor. *PoS, EPS-HEP2015:071*, 2015.
- [174] S. Schael et al. Precision electroweak measurements on the  $Z$  resonance. *Phys. Rept.*, 427:257–454, 2006.
- [175] J. Schechter and J. W. F. Valle. Neutrino masses in  $SU(2) \otimes U(1)$  theories. *Phys. Rev. D*, 22:2227–2235, Nov 1980.
- [176] N. Schmitz. *Neutrino Physik*. Teubner Studienbücher, 1997.
- [177] K. Schreckenbach, G. Colvin, W. Gelletly, and F. Von Feilitzsch. Determination of the anti-neutrino spectrum from U-235 thermal neutron fission products up to 9.5-mev. *Phys. Lett.*, B160:325–330, 1985.
- [178] Anne Schukraft. *Search for a diffuse flux of extragalactic neutrinos with the IceCube neutrino observatory*. PhD thesis, RWTH Aachen U., 2013-06-07.
- [179] Silvan S. Schweber. Nuclear Forces. The making of the physicist Hans Bethe. *Harvard University Press. Cambridge, Massachusetts and London, England*, 2012.
- [180] Aldo Serenelli. Alive and well: A short review about standard solar models. *The European Physical Journal A*, 52(4):1–13, 2016.
- [181] Aldo M. Serenelli, W. C. Haxton, and Carlos Pena-Garay. Solar models with accretion. I. Application to the solar abundance problem. *Astrophys. J.*, 743:24, 2011.

- [182] Hardy Simgen. *Hochempfindlicher Nachweis radioaktiver Edelgasnuklide und natürlicher Radionuklide aus der Uran-Zerfallsreihe*. PhD thesis, Ruprecht-Karls-Universität, Heidelberg, 2003.
- [183] A. Sirlin. Radiative Correction to the  $\bar{\nu}_e(\nu_e)$  Spectrum in  $\beta$ -Decay. *Phys. Rev.*, D84:014021, 2011.
- [184] Joshua Spitz. IsoDAR and DAE $\delta$ ALUS. In *Proceedings, 20th International Conference on Particles and Nuclei (PANIC 14)*, pages 351–354, 2014.
- [185] Alessandro Strumia and Francesco Vissani. Precise quasielastic neutrino/nucleon cross-section. *Phys. Lett.*, B564:42–54, 2003.
- [186] K. Telegadas and G. J. Ferber. Atmospheric Concentrations and Inventory of Krypton-85 in 1973. *Science*, 190(4217):pp. 882–883, 1975.
- [187] Felicitas A. Thorne. Spectral Analysis of Neutrino and Background Events in the solar Neutrino Experiments Borexino and Lena. Diplomarbeit, Technische Universität München, December 2010.
- [188] J. K. Tuli. Evaluated Nuclear Structure Data File. Technical report, Brookhaven National Laboratory, 1987.
- [189] T. Marrodan Undagoitia, F. von Feilitzsch, M. Goger-Neff, C. Grieb, K. A. Hochmuth, L. Oberauer, W. Potzel, and M. Wurm. Search for the proton decay  $p \rightarrow K^+ \text{ anti-}\nu$  in the large liquid scintillator low energy neutrino astronomy detector LENA. *Phys. Rev.*, D72:075014, 2005.
- [190] Shawn M. Usman, Glenn R. Jocher, Stephen T. Dye, William F. McDonough, and John G. Learned. AGM2015: Antineutrino Global Map 2015. *Sci. Rep.*, 5:13945, 2015.
- [191] L. Vanhoefer. Muon Tracking at Double Chooz. Master’s thesis, Universität Hamburg, April 2013.
- [192] F. L. Villante, A. Ianni, F. Lombardi, G. Pagliaroli, and F. Vissani. A Step toward CNO solar neutrinos detection in liquid scintillators. *Phys. Lett.*, B701:336–341, 2011.
- [193] F. L. Villante, A. Ianni, F. Lombardi, G. Pagliaroli, and F. Vissani. A method to extract the CNO solar neutrino signal in ultrapure liquid scintillator detectors. *J. Phys. Conf. Ser.*, 375:042035, 2012.
- [194] P. Vogel and John F. Beacom. The angular distribution of the neutron inverse beta decay,  $\text{anti-}\nu/e + p \rightarrow e^+ + n$ . *Phys. Rev.*, D60:053003, 1999.
- [195] F. Von Feilitzsch, A. A. Hahn, and K. Schreckenbach. Experimental beta spectra from pu-239 and u-235 thermal neutron fission products and their correlated anti-neutrinos spectra. *Phys. Lett.*, B118:162–166, 1982.
- [196] Alan A. Watson. The Discovery of Cherenkov Radiation and its use in the detection of extensive air showers. *Nucl. Phys. Proc. Suppl.*, 212-213:13–19, 2011.
- [197] Wikipedia. Americium — wikipedia, the free encyclopedia, 2015. [Online; accessed 23-November-2015].
- [198] Wikipedia. Borexino — wikipedia, die freie enzyklopädie, 2015. [Online; accessed 8-February 2016].

- [199] Wikipedia. Krypton-85 — wikipedia, the free encyclopedia, 2015. [Online; accessed 4-August-2015].
- [200] Wikipedia. Carl Friedrich von Weizsäcker — Wikipedia, The Free Encyclopedia, 2016. [Online; accessed 20-July-2016].
- [201] D.H. Wilkinson. Evaluation of beta-decay: I. The traditional phase space factors. *Nuclear Instruments and Methods in Physics Research Section A: Accelerators, Spectrometers, Detectors and Associated Equipment*, 275(2):378 – 386, 1989.
- [202] D.H. Wilkinson. Evaluation of beta-decay: II. Finite mass and size effects. *Nuclear Instruments and Methods in Physics Research Section A: Accelerators, Spectrometers, Detectors and Associated Equipment*, 290(2-3):509 – 515, 1990.
- [203] K. Winger, J. Feichter, M.B. Kalinowski, H. Sartorius, and C. Schlosser. A new compilation of the atmospheric  $^{85}\text{Kr}$  inventories from 1945 to 2000 and its evaluation in a global transport model. *Journal of Environmental Radioactivity*, 80(2):183 – 215, 2005.
- [204] L. Winslow. Simulation of Reactors for Antineutrino Experiments Using DRAGON. 2011. arXiv:1109.6632[nucl-ex].
- [205] L. Wolfenstein. Neutrino oscillations in matter. *Phys. Rev. D*, 17(9):2369–2374, May 1978.
- [206] Bjorn S. Wonsak. *The reconstruction of tracks with the drift tubes in the muon spectrometers of the neutrino experiment OPERA*. PhD thesis, DESY, 2007. Thesis in German. Available online: <http://www-library.desy.de/cgi-bin/showprep.pl?thesis07-035>.
- [207] Michael Wurm. *Cosmic Background Discrimination for the Rare Neutrino Search in BOREXINO and LENA*. PhD thesis, Munich, Tech. U., 2009.
- [208] Michael Wurm et al. Spectroscopy of Solar Neutrinos. 2010. [Astron. Nachr.331,512(2010)].
- [209] Michael Wurm et al. The next-generation liquid-scintillator neutrino observatory LENA. *Astropart. Phys.*, 35:685–732, 2012.
- [210] Michael Wurm, F. von Feilitzsch, M. Goeger-Neff, K. A. Hochmuth, T. Marrodan Undagoitia, L. Oberauer, and W. Potzel. Detection potential for the diffuse supernova neutrino background in the large liquid-scintillator detector LENA. *Phys. Rev.*, D75:023007, 2007.
- [211] H. Zhang. *Ion Sources, vol. 1*. Springer-Verlag Berlin Heidelberg. 1999.
- [212] K. Zuber. *Neutrino physics, Boca Raton: USA: CRC Pr. (2012) 448p*. 2004.

## DANKSAGUNG

---

Abschließend möchte ich allen danken, die zur Fertigstellung dieser Arbeit beigetragen haben.

Frau Prof. Caren Hagner danke ich für die Möglichkeit meine Doktorarbeit in der Forschungsgruppe Neutrino-Physik anzufertigen sowie den interessanten Diskussionen zur aktuellen und mittlerweile historischen Neutrino-Physik. Prof. Walter Schmidt-Parzefall und Dr. Björn Wonsak möchte ich für die Durchsicht des Manuskriptes danken. Björn Wonsak möchte ich darüber hinausgehend für seine stete Bereitschaft zu fachlichen Diskussionen danken. Ich möchte außerdem den Mitgliedern der Prüfungskommission, Prof. Caren Hagner, Prof. Peter Hauschildt, Prof. Dieter Horns, Dr. Björn Wonsak und Prof. Michael Wurm, danken.

Für weitere Kommentare und Verbesserungshinweisen möchte ich mich bei Prof. Michael Wurm bedanken. Desweiteren danke ich der gesamten Neutrino-Physik-Arbeitsgruppe.

Meinem Bürogenossen Benjamin Büttner möchte ich für die jederzeit qualifizierten Diskussionen und Anmerkungen zur Physik sowie programmiertechnischen Angelegenheiten danken (es ist immer praktisch *den* Informatiker der Gruppe im gleichen Büro zu haben). Außerdem möchte ich Stefan Dahmke danken, der, seines Zeichens Astronom (und nebenberuflich beinahe der persönliche Butler der *Queen*), sich immer wieder als kompetenter Hobby-Neutrino-Physiker ausgewiesen hat und wertvolle Verbesserungen zur Arbeit beigetragen hat. Ganz besonders möchte ich mich auch bei Laura Vanhoefer für die vielen kompetenten Diskussionen zur Physik und anderen Themen, für die Verbesserungshinweise zur Arbeit sowie für die sonstige Unterstützung bedanken. Bei unserem Techniker Hans-Jürgen („Hajo“) Ohmacht möchte ich mich für seine immer hilfsbereite Art (am Teststand, beim F-Praktikum-Versuchsaufbau und bei sonstigen Angelegenheiten) sowie für die netten Gespräche bedanken. Seine pragmatische und vernünftige Sicht der Dinge ist immer wohltuend. Markus Kaiser möchte ich für das BOREXINO-Kollegen-Dasein und für die netten gemeinsamen Fahrten zu den Treffen der Kollaboration nach Mailand danken.

Furthermore, I would like to thank all colleagues from the BOREXINO experiment. Special thanks goes to the SOX working group and all people involved<sup>1</sup>. I want to warmly thank Alessio Caminata for his work on the new Monte Carlo framework and his very nice manner and help. Bei Birgit Neumair möchte ich mich für die Studie zum Einfluss des *verbotenen Formfaktors* auf die Sensitivität bedanken, die das richtige Einordnen meiner theoretischen Rechnungen ermöglicht hat.

I also would like to thank Dr. Carlo Giunti for kindly providing the compilation of the exclusion limits of the other experiments.

Zu guter Letzt möchte ich mich bei meiner Familie für die Unterstützung bedanken. Meinem Neffen Philipp (“scientist in progress”) danke ich für die gute Laune und Ablenkung, die er uns allen bereitet.

---

<sup>1</sup>Including the *three Mathieus*: Mathieu, Matthieu and Mateo (©by Livia Ludhova). I still have to laugh thinking of *that* phone call.

*Let's light this candle.*  
-Alan Shepard (1961)

## List of Publications

(Publications linked to the work of the dissertation)

1. OPERA Collaboration (N. Agafonova et al.), **Determination of the muon charge sign with the dipolar spectrometers of the OPERA experiment**, JINST 11 P07022, 2016  
(M.M. correspondig author)  
arXiv:1404.5933
2. Mikko Meyer et al., **SOX: Neutrino Oscillometry in Borexino**, PoS NEUTEL2015 (2015) 075
3. Benjamin Büttner, Joachim Ebert, Caren Hagner, Annika Hollnagel, Jan Lenkeit, Mikko Meyer, Björn Wonsak, **The Muon-Tracking-System of the OPERA Experiment**, PoS NEUTEL2015 (2015) 065
4. OPERA Collaboration (N. Agafonova et al.), **Observation of  $\nu_\tau$  appearance in the CNGS beam with the OPERA experiment**, Prog. Theor. Exp. Phys. (2014) 101C01.  
<http://dx.doi.org/10.1093/ptep/ptu132>
5. Mikko Meyer et al., **Search for Sterile Neutrinos with the Borexino Detector**, DESY proceedings (PANIC 2014)  
<http://dx.doi.org/10.3204/DESY-PROC-2014-04/7>
6. BOREXINO/SOX Collaboration (G. Bellini et al.), **SOX: Short distance neutrino Oscillations with BoreXino**, JHEP 1308 (2013) 038.  
<http://arxiv.org/abs/1304.7721>
7. Double Chooz Collaboration (Y. Abe et al.), **First Measurement of  $\theta_{13}$  from Delayed Neutron Capture on Hydrogen in the Double Chooz Experiment**, Phys. Lett. B723 (2013) 66-70.  
<http://arxiv.org/abs/1301.2948>.
8. Double Chooz Collaboration (Y. Abe et al.), **Direct Measurement of Backgrounds using Reactor-Off Data in Double Chooz**, Phys. Rev. D87 (2013) 011102.  
<http://arxiv.org/abs/1210.3748>.

In addition, there are several other publications whose co-author I am as a member of the BOREXINO collaboration.

## **Eidesstattliche Versicherung**

Hiermit erkläre ich an Eides statt, dass ich die vorliegende Dissertationsschrift selbst verfasst und keine anderen als die angegebenen Quellen und Hilfsmittel benutzt habe.

Hamburg, den

Mikko Meyer